THE UNIVERSITY of ADELAIDE

Development of an Er:YAG laser for Range-finding

by

Lachlan Harris

A thesis submitted for the degree of

Doctor of Philosophy

in

The University of Adelaide

School of Physical Sciences

January 2018

Statement of originality

I certify that this work contains no material which has been accepted for the award of any other degree or diploma in my name, in any university or other tertiary institution and, to the best of my knowledge and belief, contains no material previously published or written by another person, except where due reference has been made in the text.

In addition, I certify that no part of this work will, in the future, be used in a submission in my name, for any other degree or diploma in any university or other tertiary institution without the prior approval of the University of Adelaide and where applicable, any partner institution responsible for the joint-award of this degree.

I give permission for the digital version of my thesis to be made available on the web, via the University's digital research repository, the Library Search and also through web search engines, unless permission has been granted by the University to restrict access for a period of time.

I acknowledge the support I have received for my research through the provision of an Australian Government Research Training Program Scholarship.

Signed: .. ..

Date: 19/7/2018

Supervisors: Prof. Peter Veitch, Prof. David Ottaway

Abstract

Long distance, high precision range-finding requires high energy, short duration laser pulses that exceed 1 MW peak power, as specified by defence companies. However, eye safety is a particularly important consideration for a laser system that will be used outdoors. Currently, this is often achieved by frequency shifting the 1064 nm output from a Q-switched Nd:YAG laser to the 'eye-safe' band (1.5 μm to 1.8 μm). A 1617 nm or 1645 nm Er:YAG laser operating on the $^4I_{13/2}$ to $^4I_{15/2}$ transition can satisfy this need without additional frequency shifting systems. Although this transition has long been used in a variety of erbium-doped gain media, advancements in diode pumping have made these lasers more compact and efficient.

The lower level of the 1.6 μm transition in erbium is within the ground state manifold, making it a quasi-three-level system, leading to re-absorption from the lower laser level. It also suffers from low gain due to Stark splitting of the upper laser level. The gain is further reduced by up-conversion that depletes ions from the upper laser level.

Er:Glass and Er:YAG lasers previously constructed by our research group were useful for coherent laser radars (CLR's) and Doppler wind-field mapping. This project aimed to build an Er:YAG laser with higher pulse energy and shorter (< 10 ns) pulse duration. This was expected to be a serious challenge based on the outcomes of all previous work.

Our approach was to use a Co-Planar Folded zig-zag Slab (CPFS) architecture to provide a sufficiently long path length in the gain medium to compensate for the low inherent gain. The CPFS geometry was first demonstrated using Nd:YAG in the mid 1990's, but was never previously attempted with Er:YAG.

In this thesis, I describe the design and construction of Q-switched Er:YAG lasers for this purpose, followed by a more powerful cavity-dumped Er:YAG laser. Both lasers were resonantly pumped using 1.47 μm laser diode bars. To the best of our knowledge these are the first CPFS Er:YAG lasers demonstrated.

Our first Q-switched laser produced 15.5 mJ pulses with FWHM duration of less than 25 ns, corresponding to a peak power of 620 kW, from 60 W peak pump power. The final version of the Q-switched laser used a shorter crystal and resonator to reduce the pulse duration, and produced 6 mJ pulses with pulse durations of less than 15 ns, but with a peak power of only 400 kW. These are the equal shortest duration pulses from an actively Q-switched Er:YAG laser at the present time. The results from both lasers are compared with the theoretical predictions adapted from a model of the dynamics of a quasi-three-level laser. These investigations demonstrate the difficulties in building a Q-switched Er:YAG laser capable of safely meeting the project requirements.

This thesis also describes the development and characterisation of a cavity-dumped CPFS Er:YAG laser. Cavity-dumped lasers are generally capable of shorter pulse durations and can therefore produce higher peak powers. This laser produced 10 mJ pulses with 4.5 ns duration, corresponding to a peak power of over 2 MW. This represents the highest peak power at 1645 nm reported at the present time.

Acknowledgements

First and foremost, I would like to thank my supervisors Prof. Peter Veitch and Prof. David Ottaway for their guidance and patience in supervising me and reviewing this work. Prof. Jesper Munch also kindly provided feedback on my work.

I would also like to thank BAE Systems Australia for providing project funding and technical support, in particular A/Prof. Martin O'Connor for his advice.

I appreciate the members of the Optics/IPAS group: Dr. Miftar Ganija, Dr. David Hosken, and Dr. Richard White for their help at the start of my project, when building a laser seemed an impossible task. Myles Clark for exchanging ideas (and laser parts) and constantly being cheerful, and my other friends in the Optics/IPAS group: Ori, Josh, Keiron, Ka, Muddassar, Eleanor, Nikita, Cao and Seb.

I would also like to thank the Physics workshop personnel for providing technical support and advice, particularly Blair Middlemiss, Bob Chivell and Trevor Waterhouse, who built parts for my lasers and even let me handle some of the machines. I also thank Neville Wild for his assistance with electronics and the friendly staff at the School of Physics office: Jeanette Roulston, Katie Burton, Sharon Leech, Mary Odlum, Carol Maelzer, Katja Gomulka and Ramona Rogers.

I also acknowledge friends who have contributed to my life outside of university, especially neighbours at college and my mates at 10/27 RSAR.

Finally, I am particularly grateful to my Mum for taking the time to travel from Melbourne to visit and cook for me, read my work and support me throughout my scientific endeavours. Postcards and words of encouragement from my Dad and sister are much appreciated too.

Table of Contents

List of Symbols

α	Pump absorption
δ	Resonator loss
δ_s	Slab loss
Δt	Elapsed time
ΔD	Range resolution
η_C	Coupling efficiency
η_S	Stokes efficiency
η_{slope}	Slope efficiency
θ_B	Brewster's angle
θ_n	Slab nose angle
λ	Wavelength
σ	Cross section
τ	Pulse duration
τ_f	Fluorescence lifetime
Ω	Solid angle
A	Beam area
B	Beam overlap factor
c	Speed of light
C_{up}	Up-conversion parameter

D	Distance
E	Pulse energy
f	Focal length
f_1	Boltzmann factor
F_{abs}	Fraction of power absorbed
g_0	Small signal gain
G	Round trip gain
h	Planck's constant
I	Intensity
k_B	Boltzmann constant
l	Slab length
l_i	Energy level wavenumber
L	Optical gain length
n	Refractive index
N_C	Erbium ion concentration
N_T	Laser threshold upper level erbium ion concentration
P	Pump power
P_{cav}	Intra-cavity power
P_{out}	Output power
q	Complex beam parameter
R	Output coupler reflectivity
T	Absolute temperature
T_i	Transmission factor

T_{rt}	Round trip transmission
t_r	Round trip time
w_0	Beam waist
z	Propagation distance
AOM	Acouso-optic modulator
AR	Anti-reflective
BP	Brewster plate
CCD	Charge-coupled device
CPFS	Co-planar folded zig-zag slab
CW	Continuous wave
DIAL	Differential absorption lidar
EDFL	Erbium-doped fibre laser
EOM	Electro-optic modulator
ETU	Energy transfer up-conversion
FWHM	Full width half maximum
GGG	Gadolinium gallium garnet ($Gd_3Ga_5O_{12}$)
HeNe	Helium-neon laser
HR	High reflectivity
HV	High voltage
HWP	Half-wave plate
IC	Input coupler
IR	Infrared
LDD	Laser diode driver

LIDAR	Light detection and ranging
LoD	Likelihood of damage
MPE	Maximum permissible exposure
NEP	Noise equivalent power
OC	Output coupler
OPO	Optical parametric oscillator
PC	Pockels cell
PD	Photodetector
PM	Power meter
PRF	Pulse repetition frequency
QCW	Quasi continuous wave
QWP	Quarter-wave plate
RTP	Rubidium titanyl phosphate ($RbTiOPO_4$)
SNR	Signal to noise ratio
TEM	Transverse electromagnetic mode
TFP	Thin film polariser
TIR	Total internal reflection
UV	Ultraviolet
YAG	Yttrium aluminium garnet ($Y_3Al_5O_{12}$)
YGG	Yttrium gallium garnet ($Y_3Ga_5O_{12}$)
YLF	Yttrium lithium fluoride ($YLiF_4$)

List of Figures

List of Tables

Chapter 1: Introduction

1.1 Range-finding using LIDAR

Range-finding of hard targets for military and navigation purposes was among the first practical applications of the laser [1][2]. Light Detection and Ranging (LIDAR) has since expanded to include remote sensing of diffuse targets for atmospheric studies [3]. For example, coherent LIDAR can be used for wind sensing and cloud studies [4]. In this application, the pulsed laser is injection seeded by a single frequency master oscillator to yield transform-limited pulses. The radial velocity of the target is then determined from the Doppler shift of light back-scattered from dust particles in the moving air [5].

Differential Absorption LIDAR (DIAL) is used for the remote detection of gases such as methane and carbon dioxide [6]. DIAL works by alternately emitting two pulsed probe beams of slightly different wavelength, for which the scatter loss in the atmosphere and reflection coefficient of aerosols and dust is the same, except one wavelength is partially absorbed by a target gas [7]. The time dependent difference in return signal strength is then analysed to determine the range-resolved concentration of the gas.

Advances in laser development have opened up new applications and possibilities thanks to ever-increasing output powers. For laser range-finders designed to be mounted on modern weapons platforms, a peak power of 1 MW appears to be the benchmark.

A laser "range-finder" measures the "range" or distance *D* to a target by firing a laser pulse at the target and measuring the time elapsed Δt until the arrival of the back-scattered light:

$$D = \frac{c\Delta t}{2} \tag{1.1}$$

where *c* is the speed of light. The greatest distance measured using this technique is the roughly 400,000 km distance to the moon, for which Δ*t* is around 2.5 seconds.

For a diffuse or "soft" target, the uncertainty in the measured range Δ*D* or "range resolution/confusion" is determined mainly by the pulse duration τ:

$$\Delta D < c\tau \tag{1.2}$$

where $c\tau$ is the spatial extent of the pulse, assuming a detector rise time of < τ/2, so short pulses are therefore preferred, provided a wide bandwidth photodetector is used.

For a "hard" target, the range uncertainty can be reduced by using matched filtering, assuming an adequate signal to noise ratio (SNR) for the return pulse. For example, if using a matched filter in which the reference shape is that of the transmitted pulse, then the centre of the pulse can be determined to less than 5% of the pulse width [8].

To prevent confusion, pulses must be distinguishable. One way is to have a system of identifying each pulse by means of encoding/decoding the pulse train. This has been done using a 40 MHz pulse train from a mode-locked laser, however the 12.5 nJ pulse energy limited this system to close range targets [9]. Otherwise each pulse should return to the detector before the next one is transmitted. This requires the maximum pulse repetition frequency (PRF), denoted by f_{max}, to be less than the inverse of the time of flight:

$$f_{max} < \frac{c}{2D} \tag{1.3}$$

For example, if D = 30 km then f_{max} = 5 kHz. In practice, the PRF of a laser range-finder is much lower, in order to allow sufficiently energetic pulses to be produced.

Ranging a remote target requires a high peak power because the laser pulse invariably scatters off the target over a large angle [10]. For a Lambertian scatterer, the intensity of back-scattered light varies as the cosine of the angle between the observer-target line and the target-scatter line, as shown in Figure 1.1. While the radiance of the surface remains unchanged when viewed from any angle and the highest proportion of light per unit area is back-scattered, only a small proportion of the transmitted light will be intercepted by the detection system because its area covers a tiny fraction of the solid angle:

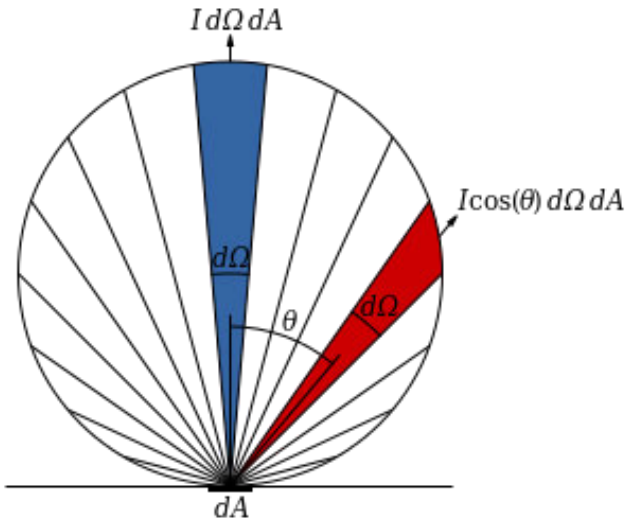

FIGURE 1.1: Lambertian scattering where I denotes the intensity of the probe beam and dA is the area of the scatterer [11]. The highest proportion of light is back-scattered.

In practice this means that a high pulse energy is necessary for range-finding, since a fast detector is required to pick up the leading edge of the returning pulse. The detector bandwidth is inversely proportional to the rise time, however a large detector bandwidth lets in more noise, which reduces the SNR. While a detector with a small noise-equivalent power (NEP) is more sensitive, having a lower noise floor, achieving an adequate SNR with laser range-finding requires a high energy pulse to begin with.

Since high pulse energies are required, eye safety is a crucial consideration, especially for a laser that will be deployed outdoors. The hazard to the eye depends strongly on the laser wavelength. The blink reflex provides some protection against visible light, but cannot protect the eye from ultraviolet or infrared light. The 1500 – 1800 nm band is relatively "eye-safe" because the light is mostly absorbed in the vitreous humour of the eyeball before reaching the retina [12]. The maximum permissible exposure (MPE) in terms of fluence in this wavelength range is generally over 1000 times that at 1064 nm, and a factor of 10 times larger than at 2 μm, as shown in Figure 1.2:

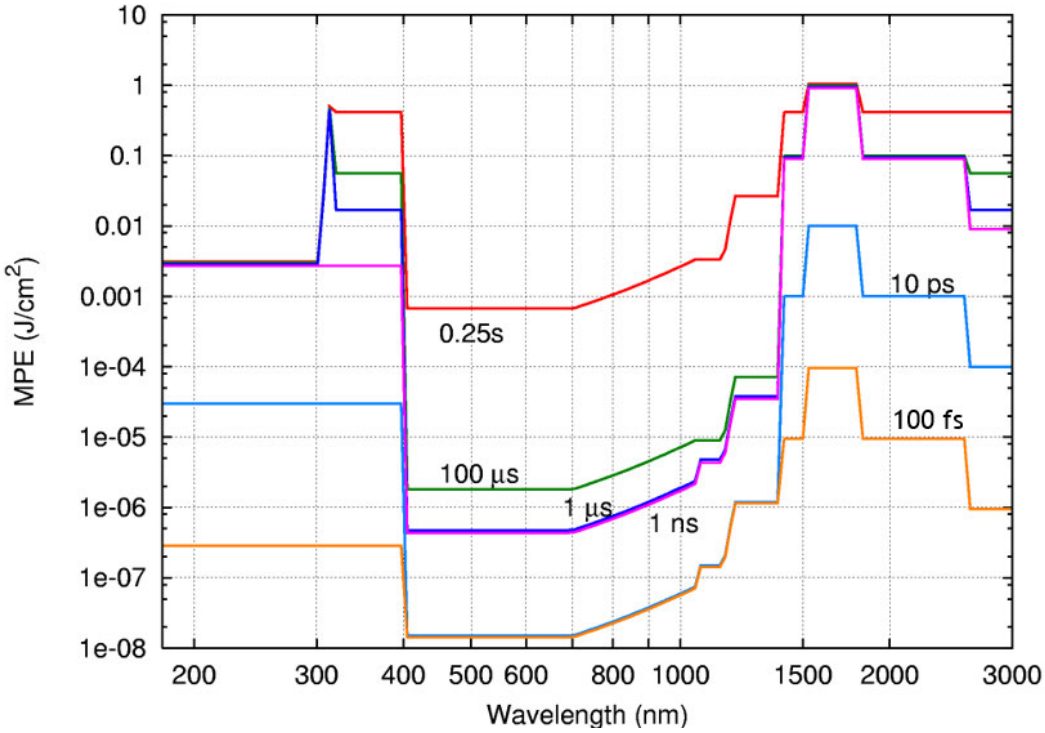

FIGURE 1.2: MPE in terms of fluence versus wavelength for different pulse durations. Note the significantly higher MPE in the 1500 – 1800 nm wavelength band [13].

To summarise, a laser range-finding system requires the following characteristics:

- "Eye-safe" output wavelength between 1500 – 1800 nm
- High pulse energy and peak power to detect distant targets
- Short pulse duration to provide high range resolution
- PRF that ensures only one pulse is "in flight" at any time

1.2 Eye-safe laser systems

1.2.1 Wavelength-shifted systems

High power Nd:YAG lasers emitting at 1064 nm are a mature technology; for decades they have provided a quick and accurate means of measuring distance [14]. Some existing laser range-finders frequency-shift the 1064 nm output of a Q-switched Nd:YAG laser to the eye-safe band using an Optical Parametric Oscillator (OPO) [15]. This arrangement is depicted in Figure 1.3:

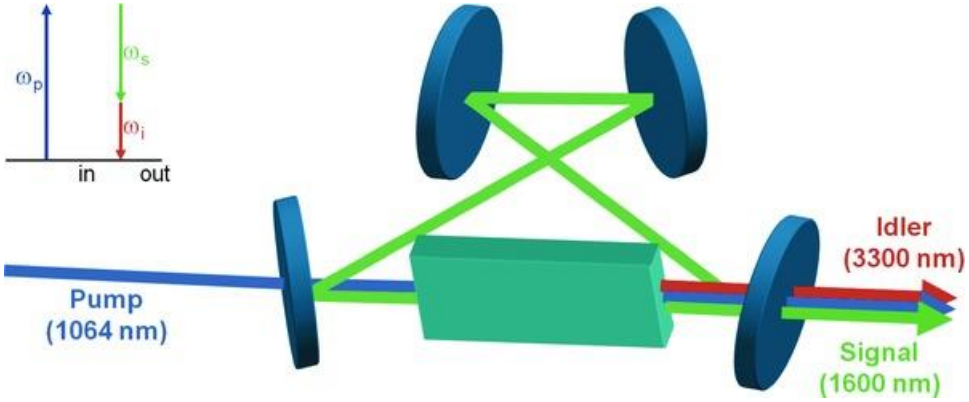

FIGURE 1.3: A schematic of an Nd:YAG laser frequency-shifted using an OPO [16]. The non-linear crystal converts the pump beam into two beams of longer wavelength (signal and idler).

Another wavelength-shifting method is Raman scattering in high pressure methane or hydrogen gas to produce 1.54 μm pulses [17][18]. Raman wavelength-shifting to 1.49 μm has also been demonstrated in diamond, with peak output powers exceeding 1 MW [19][20]. These approaches can reduce the overall efficiency and increase the bulk and complexity of the laser system, which may be a hindrance to field deployment.

An alternative is to use a gain medium that lases directly in the eye-safe band as discussed in §1.2.2. Erbium has transitions in the "eye-safe" band and can be incorporated into different host materials, including silica and phosphate glass hosts as discussed in §1.2.3 and YAG and other crystalline hosts as discussed in §1.2.4.

1.2.2 Erbium laser systems

Erbium-doped gain media can produce laser output between 1.5 μm and 1.7 μm. The doping level is generally expressed as an atomic percentage (often abbreviated to at.% or simply % throughout this thesis unless stated otherwise). The energy levels of a laser medium are mostly determined by the electron configuration of the doping ion, with a slight influence from the laser host. The spectroscopic properties of an erbium-doped host are a direct consequence of these energy levels.

An overview of the energy levels of the Er^{3+} ion (in this case in YAG) is shown in Figure 1.4:

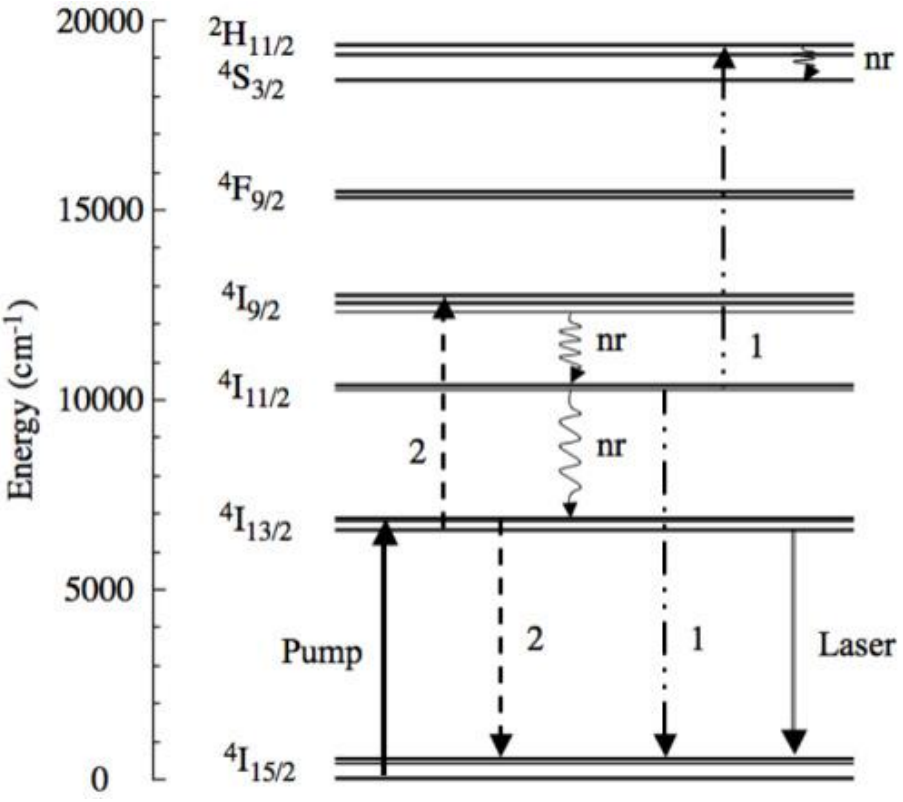

FIGURE 1.4: The seven lowest energy bands of Er^{3+} (in YAG) [21]. The pumping scheme shown is referred to as resonant or 'in-band' pumping. Other pump schemes are discussed further in the text. The processes (1) and (2) represent up-conversion, which is discussed in §2.2.4. The term 'nr' denotes a non-radiative transition to a lower energy level.

Erbium lasing at around 1.6 μm occurs due to transitions between levels in the two lowest bands of energy levels. While the upper laser level has a relatively long fluorescence lifetime that helps with energy storage, the lower laser level is very close to the ground state. It is thus referred to as a quasi-three-level system, and as will be discussed further in Chapter 2, there are several problems:

- Since the lower laser level is within the ground state manifold, it has a significant population density at room temperature, leading to potential re-absorption of laser photons.
- The evenly spaced energy levels result in up-conversion losses due to energy transfer between excited Er^{3+} ions depleting the upper laser level [22].
- Erbium has a small upper laser level Boltzmann factor and therefore suffers from low gain, compared to Nd:YAG.
- Erbium has a low absorption cross-section, meaning that high doping and/or long absorption length is required.

All of these problems increase the lasing threshold and reduce overall efficiency. Erbium-doped lasers therefore require high reflectivity output coupling mirrors and large pump powers to overcome these issues. The heating associated with the inefficiency has been overcome to some extent by the development of improved pumping methods.

Solid-state lasers were initially pumped using flash lamps [23]. While the emitted power from a flash lamp is high, it is very spectrally broad, resulting in a poor overlap with the absorption bands. This results in low efficiency since most of the incident lamp light is not absorbed by the gain medium. It can also cause excess heating which is undesirable in most laser hosts. Lamp pumping has largely been surpassed by more efficient pumping systems that selectively target various absorption transitions.

Pumping using narrow-band sources that directly access the upper energy bands is inherently more efficient. Absorption at 647 nm ($^4I_{15/2} \rightarrow {}^4F_{9/2}$), 790 nm ($^4I_{15/2} \rightarrow {}^4I_{9/2}$) and 970 nm ($^4I_{15/2} \rightarrow {}^4I_{11/2}$) has been exploited [24][25]. The latter generally uses co-doping with high levels of ytterbium to improve pump absorption at low erbium doping levels, and rely on cross-excitation to transfer energy to the erbium (see §1.2.3), compensating for the lower absorption cross section at that wavelength [26].

Resonant pumping, in which the pump and laser transitions occur between energy levels in the same two energy manifolds (see Figure 1.4), is the most efficient pumping method as it has the smallest quantum defect. There are two approaches:

- A 1532 nm erbium/ytterbium doped fibre laser (EDFL), which is itself often pumped by a 980 nm laser diode [27].
- A high power InGaAsP (Indium-Gallium-Arsenide-Phosphorus) laser diode emitting at either 1470 nm or 1532 nm.

1.2.3 Er:Glass lasers

Er:Glass lasers were initially lamp-pumped, and were co-doped with chromium to improve pump absorption [28]. The development of 980 nm laser diodes enabled the development of more efficient diode-pumped Er:Glass lasers. Since the absorption cross section of erbium is low, high levels of ytterbium dopants were added to increase pump absorption, without increasing the erbium doping [29]. These co-doped gain media used an energy transfer (ET) process (shown in Figure 1.5) to transfer the ytterbium excitation to erbium. This reduced the lasing threshold and up-conversion losses as ytterbium does not suffer from up-conversion.

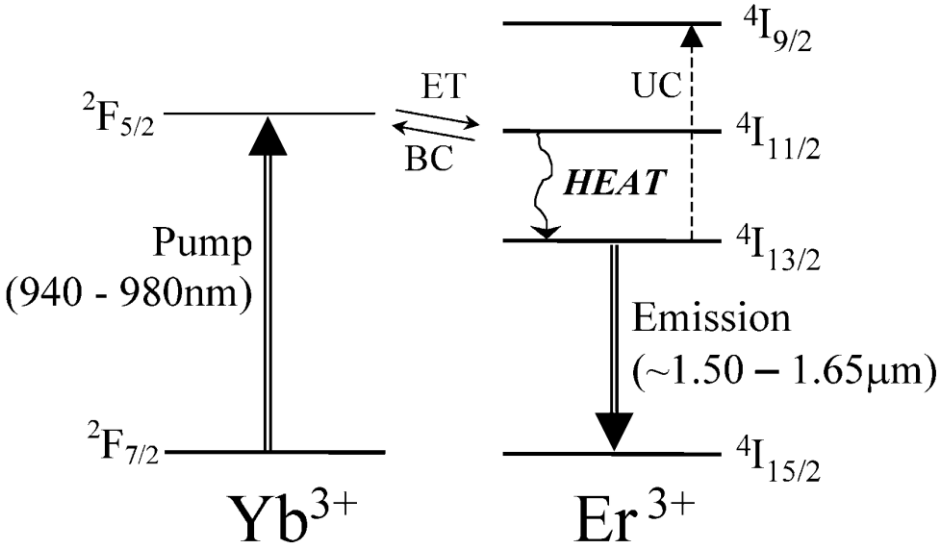

FIGURE 1.5: Energy transfer in Er:Yb:Glass using a 980 nm pump [30]. The acronyms are ET = energy transfer, BC = back-conversion and UC = up-conversion.

The cross sections of ytterbium and erbium (in ZBLAN glass) are shown in Figure 1.6:

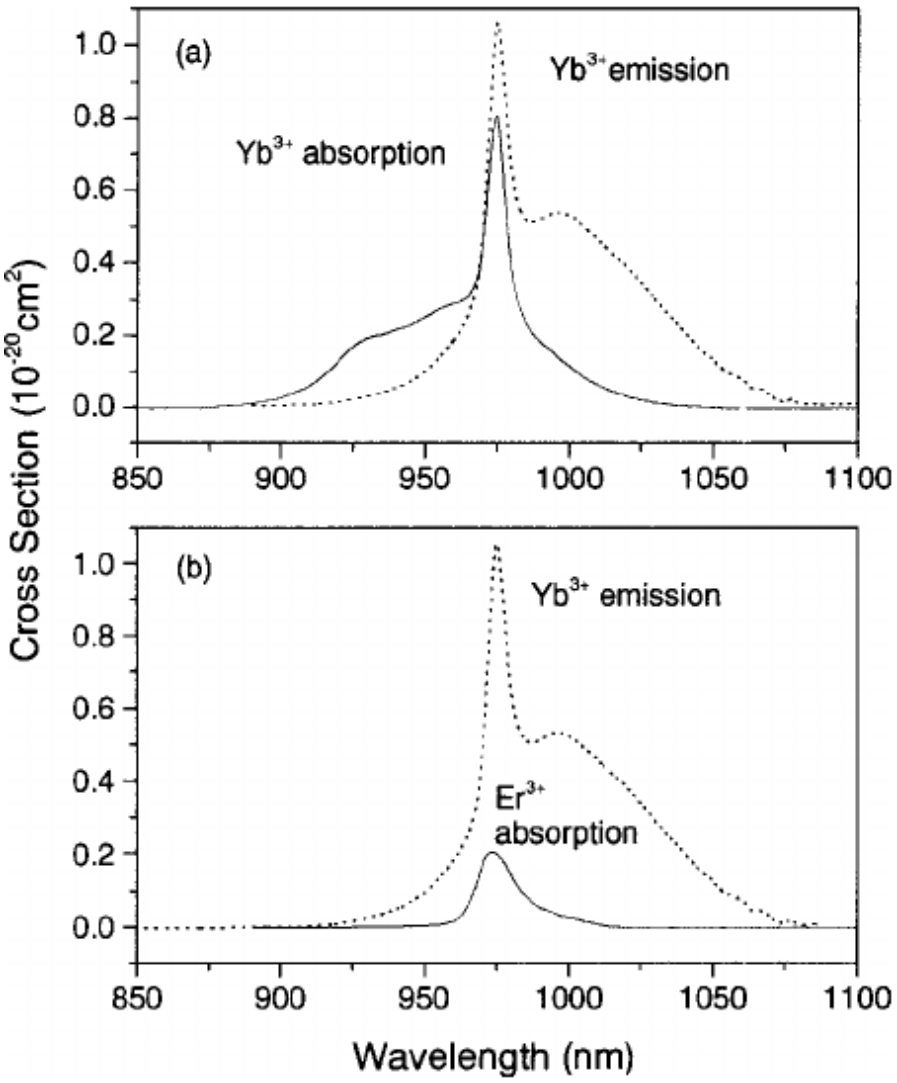

FIGURE 1.6: Cross section vs. wavelength for ytterbium compared to erbium (in this case in ZBLAN glass) [31]. Note the considerably higher cross section of ytterbium.

An erbium, ytterbium co-doped silica glass solid-state laser emitting at 1.54 μm was first reported in 1964 [32]. The first Er/Yb co-doped fibre laser was demonstrated in 1986 and has since been used in erbium doped optical fibre lasers (EDFL) and amplifiers (EDFA) for telecommunications systems [33]. Er/Yb co-doped phosphate glass has also been used to generate 1.5 μm light [34]. Eye-safe Er:ZBLAN (fluoride glass) [35] and Er:Tellurite [36] glass laser systems have also been demonstrated.

Glass is far from an ideal bulk laser host because it has poor thermal conductivity compared to crystalline hosts, as shown in Table 1.1. Combined with the high lasing threshold of erbium-doped lasers, the thermal gradients resulting from the heating cause thermal lensing and the low strength of glass can lead to gain medium fracture. Consequently, Er:Glass laser systems are limited to a low PRF [37]. For high average power applications, glass has since been supplanted by YAG and other hosts.

1.2.4 Er:YAG lasers

Yttrium Aluminium Garnet ($Y_3Al_5O_{12}$ or YAG) is a cubic structured crystal that can be doped by replacing yttrium atoms with rare earth atoms such as Nd, Er, Yb, Ho or Tm. The notable physical properties of YAG are listed in Table 1.1:

Parameter	Er:Glass	Er:YAG
Density	3.0 g cm^{-3}	4.55 g cm^{-3}
Hardness	5.5	8.25
Thermal conductivity	0.8 W m^{-1} K^{-1}	12 W m^{-1} K^{-1}
Thermal expansion	9.0 x 10^{-6} K^{-1}	6.14 x 10^{-6} K^{-1}
Refractive index	~1.53	~1.81
dn/dT coefficient	–5 x 10^{-6} K^{-1}	7.8 x 10^{-6} K^{-1}
Lasing wavelength(s)	1530 – 1550 nm	1617 nm, 1645 nm

TABLE 1.1: The physical properties of Er:YAG and Er:Glass [37][38]. The exact values for glass generally depend on composition. The refractive indices provided are accurate close to the lasing wavelengths around 1.6 μm and do not vary much in the IR region.

YAG is a better laser host than glass because of its higher thermal conductivity, an important consideration for any laser dealing with high average pump powers. The lower thermal expansion coefficient compared to glass is also an advantage. The relatively high hardness of YAG makes it easier to polish and more resistant to scratching compared to the majority of laser hosts. Scratches on a gain medium not only increase loss where a

laser beam interacts, but can also nucleate fractures and thereby make the gain medium vulnerable to damage from high power laser pulses [39].

Lasing at 1.64 μm in lamp-pumped Er:YAG was first reported in the 1960's [40], however lasing was only achieved with great difficulty and poor efficiency, using low temperatures to produce more favourable spectroscopic conditions [41]. The 1645 nm emission was identified as a means of sensing methane in 1972 using a lamp-pumped laser with an Er/Yb co-doped YAG crystal [42].

Other uses for Er:YAG were also explored. For example, room temperature lasing at 2.94 μm in highly doped (30% erbium doping by weight) Er:YAG was first reported in 1975 [43]. This exploited the up-conversion process to populate the $^4I_{11/2}$ energy level and lases as a four level system using the $^4I_{11/2} \rightarrow {}^4I_{13/2}$ transition. This transition does not suffer from re-absorption if pumped at low repetition rates. The 2.94 μm output has since proven useful for medical and dental applications.

The early Er:YAG lasers used various erbium doping concentrations and sometimes incorporated ytterbium to help with energy transfer, but even so were still inefficient [44]. Other crystalline hosts such as Yttrium Lithium Fluoride (YLF) [45], Yttrium Gallium Garnet (YGG) [46] and Gadolinium Gallium Garnet (GGG) [47] were also trialled. Various "eye-safe" erbium-doped laser systems have since been demonstrated using these hosts. As technology improved with improved crystal polishing as well as brighter and more efficient pump sources, 1.6 μm Er:YAG lasers operating at room temperature were commonly reported by the late 1990's, with steadily increasing output power and efficiency. The next section looks at some of these Q-switched Er:YAG lasers.

1.3 Review of Q-switched Er:YAG lasers

Q-switching is the most commonly used technique for producing energetic laser pulses with pulse durations on the order of tens of nanoseconds. This works by rapidly varying the resonator quality factor (Q). The resonator has high intra-cavity loss (i.e. low Q) while the gain medium is pumped, preventing feedback and allowing a large population inversion to build up without it being depleted by lasing. Rapidly decreasing the intra-cavity loss (switching to high Q) allows lasing to occur, and a giant pulse builds up within the resonator, as shown in Figure 1.7. The energy circulating within the resonator emerges through an "output coupler" over many round trips of the resonator as a 'giant' laser pulse.

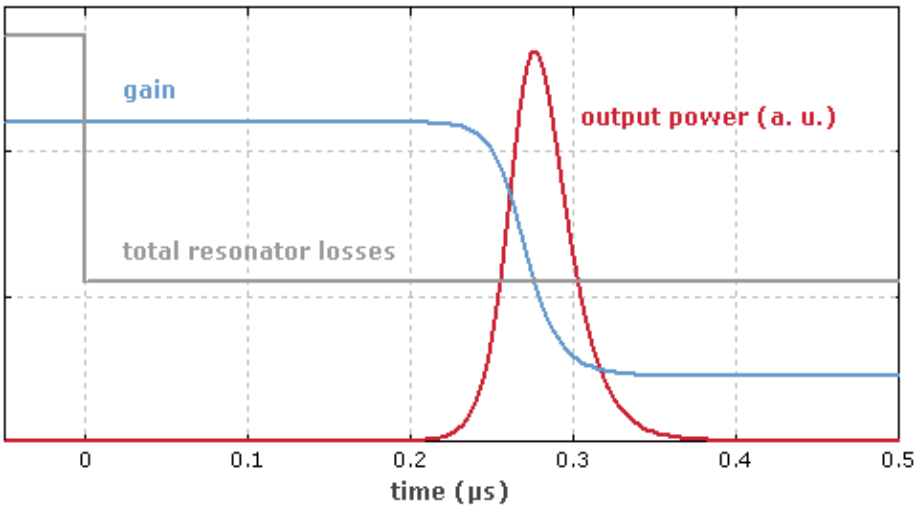

FIGURE 1.7: Representation of active Q-switching [48]. The gain is equal to one at the peak of the pulse, after which the pulse decays. Units and scale on the Y-axis are arbitrary.

There are two types of Q-switching: active and passive. Active Q-switching employs either an electro-optic (EOM) or acousto-optic modulator (AOM) to vary the resonator loss. An electro-optic Q-switch consists of a Pockels cell (PC), which actively cancels the polarisation rotation of a Quarter-wave plate (QWP) [49]. This is sometimes combined with a polarising element such as a Brewster window. An AOM Q-switch adjusts the diffraction within the modulator, thereby changing the out-coupling losses [49]. The pulse can be out-coupled either through the output coupler or via the Q-switch.

Passive Q-switching uses a saturable absorber whose absorption reduces (transmission increases) dramatically at high photon flux [50]. It has the advantage of not requiring an external control system, but timing jitter can be more problematic and saturable absorbers can be more vulnerable to damage at high peak power [51].

The performance of selected Q-switched Er:YAG lasers is listed below in Table 1.2:

Reference	[52]	[53]	[54]	[55]	[56]
Erbium doping	0.5 at.%	1.0 at.%	0.5 at.%	0.5 at.%	0.25 at.%
Pump source	1532 nm EDFL	1532 nm EDFL	1470 nm laser diode	1532 nm EDFL	1532 nm EDFL
Q-switch type	PC	Passive	AOM	AOM	PC
Wavelength	1645 nm	1617 nm	1645 nm	1617 nm	1617 nm
Pulse energy	15 mJ	0.23 mJ	10.5 mJ	3.5 mJ	30.5 mJ
Pulse duration	67 ns	7 ns	27 ns	14.5 ns	20 ns
Peak power	220 kW	33 kW	390 kW	240 kW	1.52 MW
Repetition rate	30 Hz	3.8 kHz	20 Hz	1.5 kHz	20 Hz

TABLE 1.2: Comparison of selected Q-switched Er:YAG lasers. These are described in the text on the following pages. All of these lasers used a rod gain medium.

Many Q-switched Er:YAG lasers operate at 1617 nm, which is favoured when high population inversions are achieved, as explained in Chapter 2.

Pumping has generally employed 1532 nm EDFL's. However 1532 nm laser diodes are now available which can simplify pumping systems [57]. These can be spectrally narrowed using Bragg gratings to efficiently target the absorption transition [58]. This approach was first used in an Er:YAG laser reported in 2012 by M. Wang et. al. that produced 11.8 mJ, 81 ns pulses at 100 Hz PRF when Q-switched using an AOM [59].

Lasers that can produce short-duration pulses require high round-trip gain and a short resonator [60]. Passive Q-switches allow more compact resonators as they occupy less space than a Pockels cell and also eliminate the requirement for a QWP.

A CrZnSe saturable absorber was used by Stultz et. al [53]. Their laser schematic is shown in Figure 1.8:

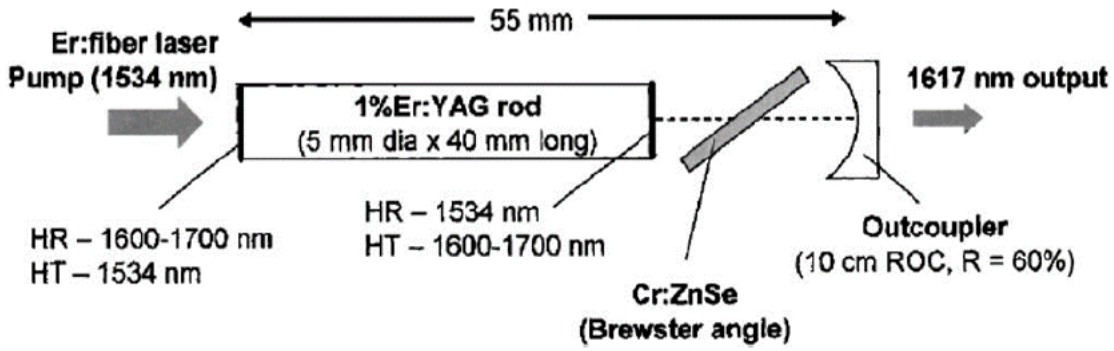

FIGURE 1.8: The passively Q-switched Er:YAG laser constructed by Stultz et. al. [53].

Figure 1.8 illustrates the potential simplicity of a passively Q-switched solid-state laser system. It uses a linear resonator, a rod with dichroic coatings, and a passive Q-switch. The optical length of under 9 cm allowed the generation of 7 ns pulses, but limited the output energy to only 0.23 mJ due to the low damage threshold of ZnSe. This pulse energy and resulting 33 kW peak power is too low for a long distance laser range-finder.

A high-power laser pumped using a 1470 nm laser diode was reported by Kudryashov et. al. in 2010 [54], using the design shown in Figure 1.9:

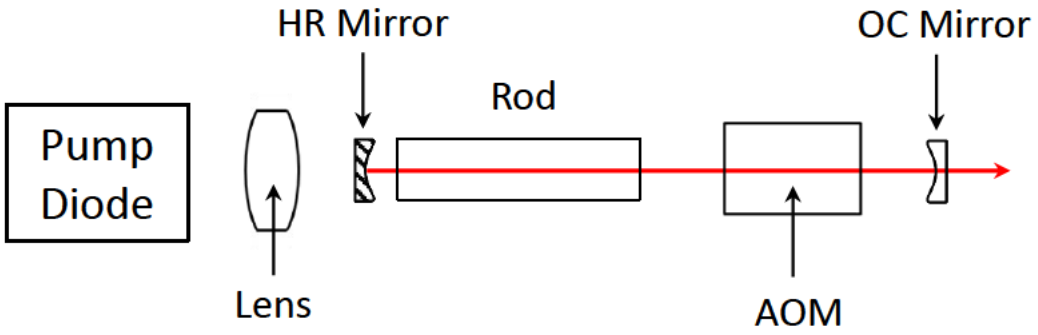

FIGURE 1.9: Schematic of a Q-switched Er:YAG laser capable of 390 kW peak power.

This design used a 40 mm long 0.5% Er:YAG rod, end-pumped with a 1470 nm laser diode and produced 10.5 mJ pulses of 27 ns duration, corresponding to 390 kW peak power at 1645 nm. While this pulse energy would satisfy my requirements, the pulse duration was too long. A similar system, also using an AOM, produced 3.5 mJ, 14.5 ns pulses at 1.5 kHz repetition rate, corresponding to 240 kW peak power [55]. These are the shortest pulses from an actively Q-switched Er:YAG laser so far.

Other actively Q-switched Er:YAG lasers have produced more energetic pulses with higher peak powers but longer duration. The most powerful laser in Table 1.2 was reported by Clarkson et. al. [56]. Pumped by an Er;Yb co–doped fibre laser, it yielded pulse energies of up to 30.5 mJ at 20 ns duration, corresponding to 1.5 MW peak power. A schematic of this laser is shown in Figure 1.10:

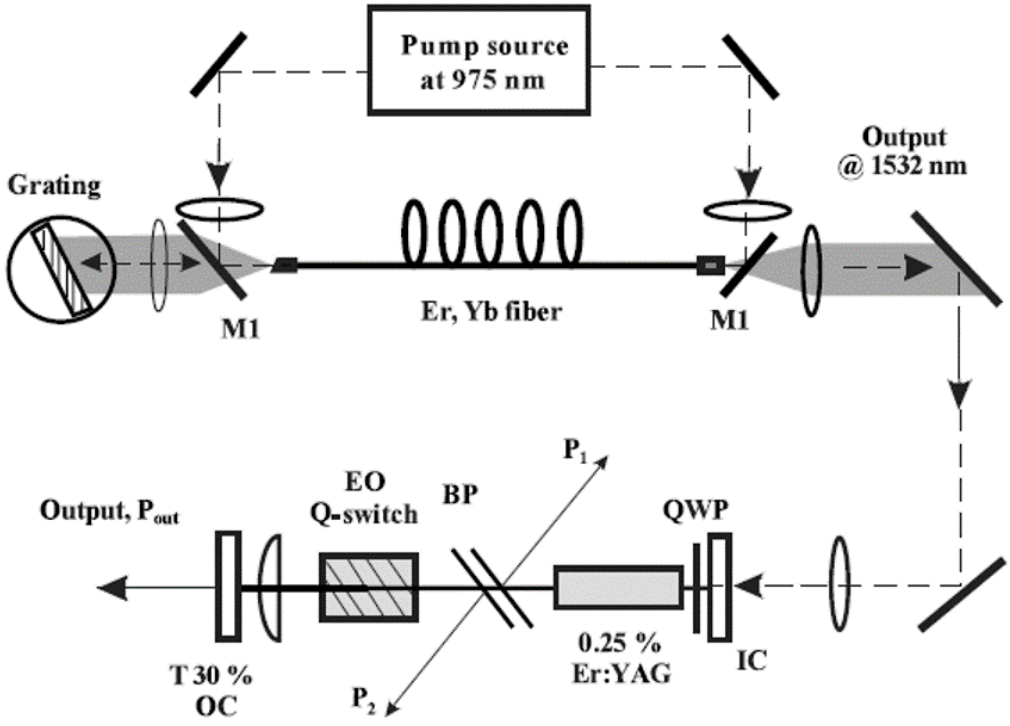

FIGURE 1.10: The 1617 nm Q-switched Er:YAG laser reported by Clarkson et. al. [56]. The components labelled are M1 = mirror, IC = input coupler, QWP = Quarter-wave plate, BP = Brewster plate, OC = output coupler.

Despite producing energetic pulses due to the high pump power and large round trip gain, the resonator round trip time was too long to produce short duration pulses. The dielectric coating on the dichroic input coupler was also susceptible to damage at high powers, which limited the maximum achievable output pulse energy.

Previous work done at the University of Adelaide by Nick Chang et al. produced two Er:YAG slab lasers [61][62]. The more powerful model was end-pumped using a fast-axis collimated 1470 nm laser diode array that was focused into the gain medium using a lens. It produced a maximum continuous wave (CW) power output of 6.1 W using 40 W pump power, with a slope efficiency of 36%. Q-switching experiments yielded 2.3 mJ pulses of 100 ns duration at 250 Hz PRF [62]. A schematic of this laser is shown in Figure 1.11:

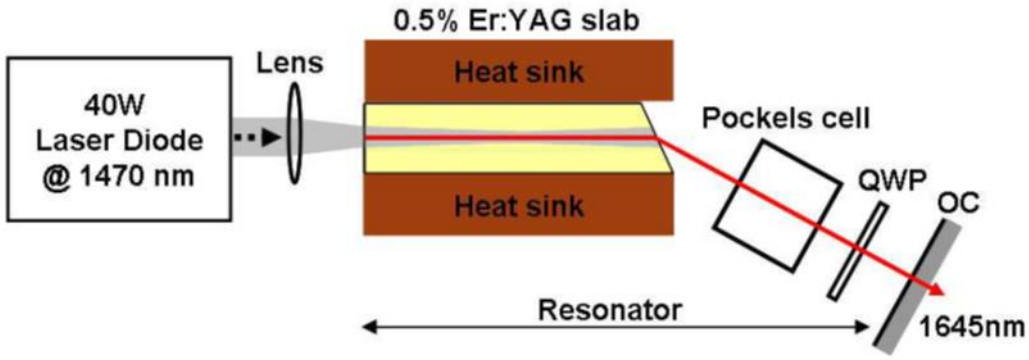

FIGURE 1.11: Q-switched Er:YAG slab laser constructed at the University of Adelaide. The pumped end of the slab required a dichroic coating to transmit pump light, but reflect the laser light. This coating was susceptible to damage at high pulse energies.

All of the lasers in Table 1.2 used a rod gain medium. Compared to the Co-Planar Folded zig-zag Slab (CPFS) geometry used in this project, the path length within the gain medium and therefore gain-length product is lower, which limits the peak power achievable. They also require anti-reflective (AR) coatings on the end faces of the rod, which increases the vulnerability to damage at high peak powers.

Based on the results of these previous works, it appears that the combination of high pulse energy and short duration required to achieve my project requirements would be a challenging task to achieve using a Q-switched Er:YAG laser.

1.4 Review of cavity-dumped Q-switched lasers

Another method of generating short pulses is by using cavity-dumped Q-switching. This also works by allowing no feedback until pumping of the gain medium is complete, so a large population inversion can build up, and then varying the laser out-coupling using either an electro-optical or acousto-optical modulator. The point of difference with cavity-dumping is that all of the out-coupling is via the Q-switch (the resonator mirrors have high reflectivity). Thus the out-coupling fraction can be reduced to 0% once pumping is complete, allowing the giant pulse to build up faster. Once this is achieved, all of the circulating energy is completely dumped out of the laser by rapidly switching the Q to 100% out-couple again, ideally in a time less than the resonator round-trip time. This produces a short pulse, as represented in Figure 1.12:

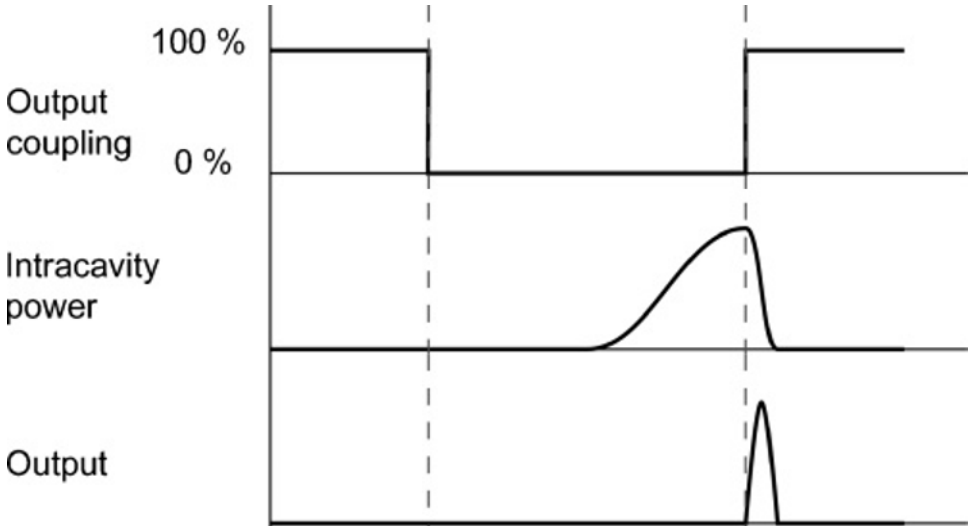

FIGURE 1.12: Representation of cavity-dumped resonator timings and laser output [63].

Technically this is still a form of Q-switching, however for brevity "cavity-dumped Q-switching" will be referred to as "cavity-dumping" and "cavity-dumped Q-switched lasers" will henceforth be referred to as "cavity-dumped lasers" in this thesis.

Cavity-dumped resonators generally require fast switching electronics. They can also be more complicated to align (depending on their design), without always delivering greatly superior results. Consequently, less work has been done in this area, even though the technique, then known as Q-spoiling, was first reported in 1963 in a ruby laser [64].

The performance of selected cavity-dumped laser systems is listed in Table 1.3, only one of which uses the Er:YAG gain medium to produce 1.6 μm pulses:

Reference	[65]	[66]	[67]	[68]	[69]
Gain medium	Nd:YAG	Yb:YAG	Nd:YAG	Tm:YAG	Er:YAG
Q-switch type	PC	PC	PC	AOM	PC
Wavelength	1444 nm	1031 nm	1064 nm	2013 nm	1645 nm
Pulse energy	50 mJ	4.4 μJ	40 mJ	3 μJ	0.22 mJ
Pulse duration	14 ns	15 ns	6 ns	54 ns	1.1 ns
Peak power	3.57 MW	293 W	6.7 MW	55 W	200 kW
Repetition rate	Unknown	100 kHz	10 Hz	200 kHz	10 kHz

TABLE 1.3: Comparison of selected cavity-dumped lasers with different gain media.

A cavity-dumped 1031 nm Yb:YAG laser with an optical to optical efficiency of 56% was reported by H. Hitotsuya et. al. in 2013, although the output pulse energy was limited to less than 5 μJ as the PRF was 100 kHz [66]. In 2012, a cavity-dumped Nd:YAG laser constructed by Y.F. Ma et. al. produced 40 mJ, 6 ns pulses at 10 Hz PRF [67]. It used a Pockels cell and thin film polariser (TFP), relying on polarisation dependent reflectivity/ transmission to dump the beam. The laser schematic is shown in Figure 1.13:

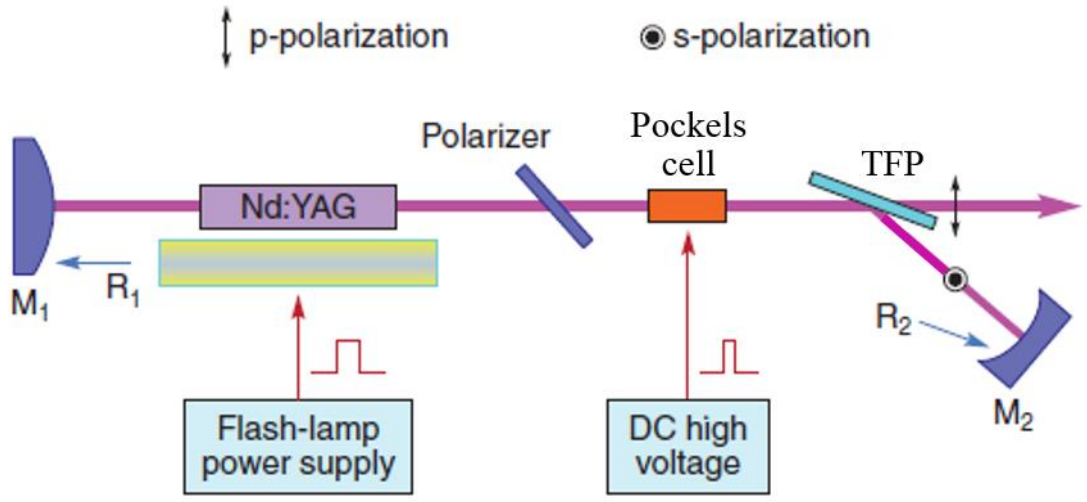

FIGURE 1.13: The cavity-dumped Nd:YAG laser using an electro-optical modulator [67].

More recently in 2014, G. Cai et al. reported a cavity-dumped 2013 nm Tm:YAG laser that produced 595 mW average power with pulses of 54 ns duration, representing 3% efficiency from 20 W pump power [68]. They used an acousto–optical modulator to dump the beam by deflecting it out of the resonator as shown below in Figure 1.14:

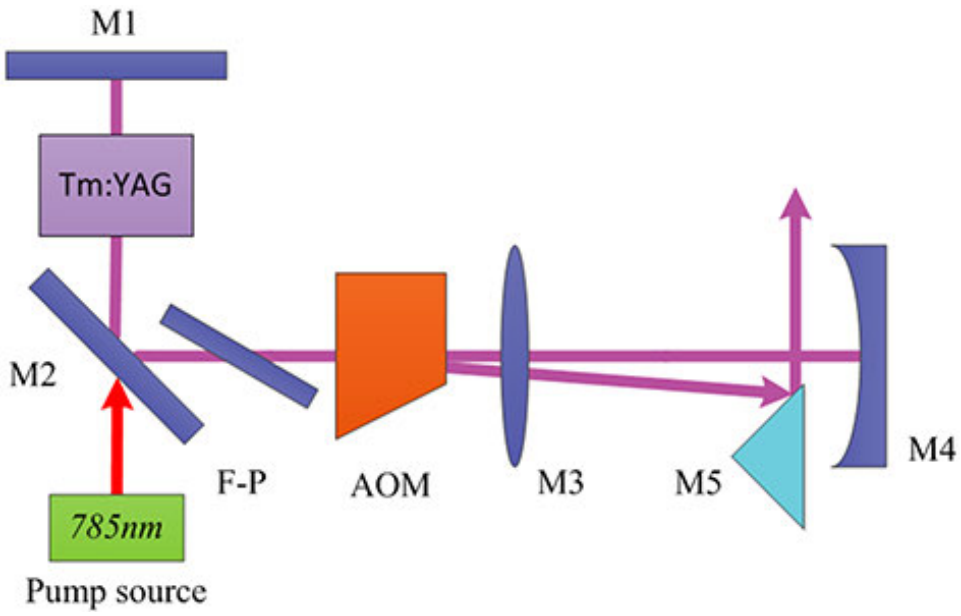

FIGURE 1.14: Cavity-dumped Tm:YAG laser using an acousto-optical modulator to deflect the pulse out [68]. The laser pulse oscillates between the mirrors M1 and M4 in the build-up phase before being deflected by the AOM onto M5 and dumped.

One characteristic of using acousto-optical modulation to deflect the beam out of the resonator is the switching time, which is limited by the speed of sound in the AOM crystal. The minimum pulse duration of 54 ns greatly exceeded the round trip time of the resonator, which had an optical path length of 208 mm. The pulse duration was proportional to the resonator length and the rise-time of the AOM, and inversely proportional to the deflection efficiency of the AOM [68].

Only one cavity-dumped 1.6 μm Er:YAG laser system has been reported so far [69]. A schematic of that laser is shown below in Figure 1.15:

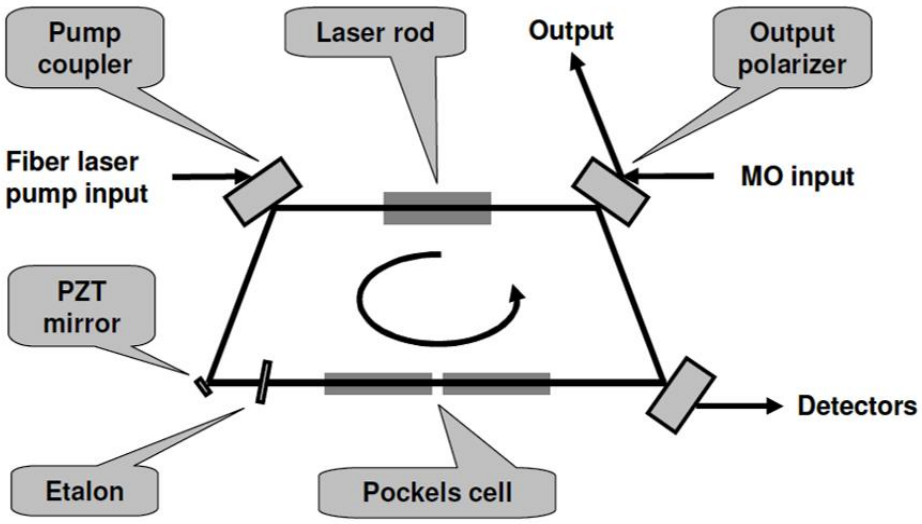

FIGURE 1.15: The 1617 nm cavity-dumped Er:YAG laser that produced 0.22 mJ, 1.1 ns pulses [69]. The output pulse energy increased to 1.6 mJ after amplification.

This resonator has a ring configuration and uses a Pockels cell to perform cavity-dumping. The laser was pumped using a 1533 nm erbium-ytterbium doped fibre laser. It was injection seeded by a 1617 nm laser diode and used an intra-cavity etalon to ensure operation at 1617 nm instead of 1645 nm.

This shows that a cavity-dumped Er:YAG laser system is a realistic approach for my project, offering shorter duration pulses and potentially higher peak powers, however a very fast Pockels cell capable of rapidly switching off high voltages will be required.

1.5 Thesis overview

The aim of my PhD project was to build a Q-switched "eye-safe" Er:YAG laser capable of producing short duration, high peak power pulses for range-finding and remote sensing. The system parameters were specified by BAE Systems as part of an ARC Linkage Project, and they called for a pulsed laser with:

- Peak power exceeding 1 MW
- Pulse energy of 5 to 10 mJ
- Pulse duration of 5 to 10 ns
- Repetition rate of 10 to 20 Hz

No previously reported Q-switched Er:YAG lasers have demonstrated such short pulse durations, while cavity-dumped Er:YAG lasers have so far been limited to much lower pulse energies.

My initial approach was to construct a Q-switched Er:YAG slab laser emitting at 1617 or 1645 nm to investigate the shortest pulse duration achievable, since Q-switching is the more commonly employed technique and is suitable for most pulsed laser applications. The back-up plan was to construct a cavity-dumped Er:YAG laser.

This thesis will describe the development of this laser, the design of which was subsequently adapted in a related project for a methane sensing DIAL system.

While Er:YAG lases directly in the "eye-safe" part of the spectrum, the spectroscopic properties of erbium present many challenges as discussed in Chapter 2. It also promotes the use of an end-pumped Co-Planar Folded zig-zag Slab (CPFS) as the crucial measure taken to overcome these challenges. This architecture increases the path length of the laser beam in the gain medium by a factor of $2\sqrt{2}$ to help achieve the higher round trip gain required for short-duration pulses. A description of the pump assembly and characterisation follows, along with the design of the lens duct. The laser heads used in the Q-switched laser prototypes are also described.

Chapter 3 describes the resonators employed along with the alignment procedure for the telescopic resonator. The results of the initial laser tests in gain-switched mode are compared to predictions of threshold power and slope efficiency. With 60 W peak pump power, it was capable of operating with an output coupler reflectivity of only 40%, previously unheard of in Er:YAG lasers.

Chapter 4 discusses the adaption of the laser to Q-switched operation using the combination of a Pockels cell and Quarter-wave plate. The first prototype Q-switched laser achieved 15 mJ pulses of duration under 25 ns, among the highest peak power ever achieved in Er:YAG lasers. Since shorter pulse durations were required, measures were taken to reduce the resonator length, including using a shorter slab. The best result we subsequently observed was a 6 mJ pulse of 15 ns duration; for 400 kW peak power. This was the equal shortest duration pulse observed in an actively Q-switched Er:YAG laser, but it still fell short of project requirements. The slab was also vulnerable to optical damage due to the high intra-cavity fluence on the surfaces.

In order to achieve shorter pulse durations and higher peak powers, cavity-dumping was investigated. Chapter 5 reports the trials and results of the cavity-dumping, which was able to shorten the pulse duration to approximately equal to the resonator round trip time of 4.5 ns. Pulses of up to 10 mJ thereby achieved a > 2 MW peak power.

Finally, the project outcomes are summarised in Chapter 6 and scope for improvement in the laser system is discussed, along with possible future directions.

Chapter 2: Laser head

2.1 Introduction

The requirement for a short-pulsed Er:YAG laser source with high peak power was discussed in Chapter 1. It comes with unique challenges due to the spectroscopic properties of the Er:YAG gain medium.

This chapter covers the considerations for the design of an end-pumped Er:YAG slab laser and highlights the need to use a CPF slab geometry to overcome the low gain of Er:YAG. The spectroscopic properties of the Er:YAG gain medium are examined in Section 2.2, including re-absorption and up-conversion. The equations describing the gain medium are provided. The optimal erbium doping level is also discussed. This is followed by the modelling of a CPFS gain medium using MATLAB simulations in Section 2.3. This allowed the parameters for the slab design to be justified. The angles of the Brewster faces are also calculated since these determine the resonator layout. The dimensions of the initial slab and a shorter version are then provided. The pump assembly, water cooling system and characterisation of the pump diode and spectral output are described in Section 2.4. It also explains the lens duct design and provides measurements of the vertical pump profile. The two laser head designs that were used in the Q-switched laser prototypes are shown in Section 2.5. The chapter is concluded in Section 2.6.

2.2 Er:YAG spectroscopic properties

2.2.1 Energy levels

The two lowest energy manifolds of Er:YAG are shown in detail in Figure 2.1:

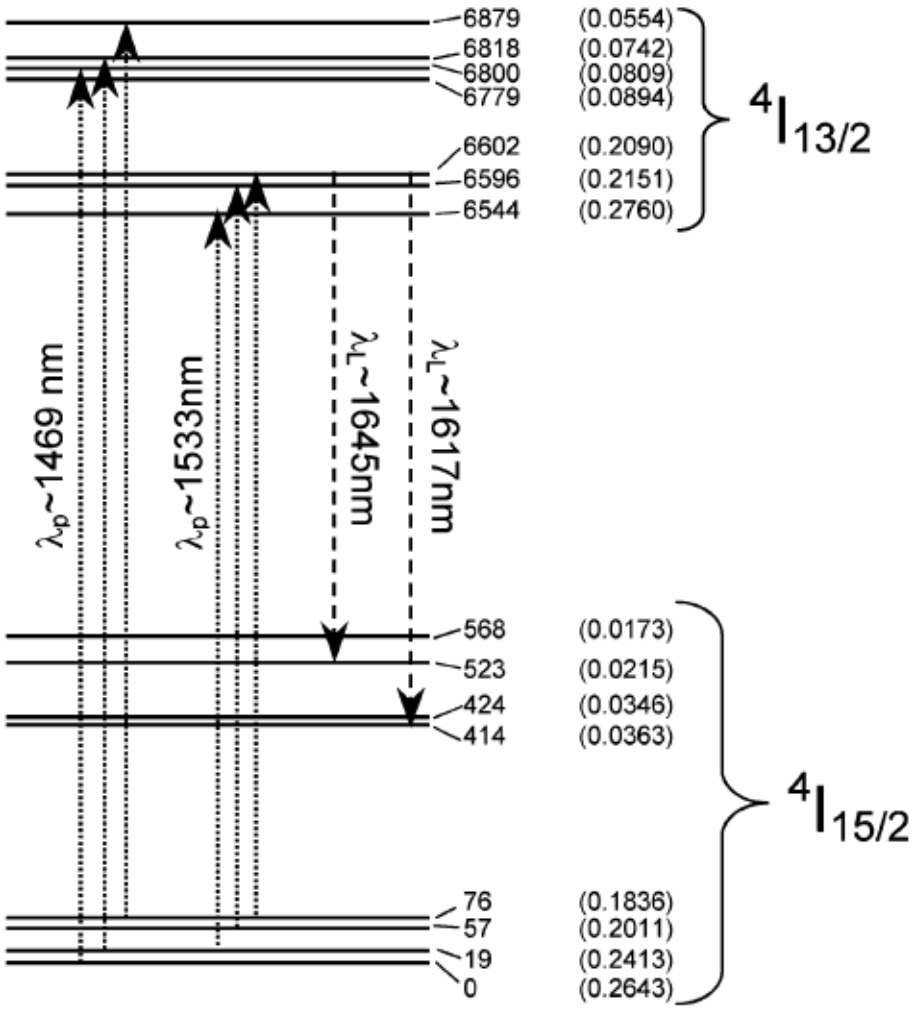

FIGURE 2.1: A detailed diagram of the two lowest energy manifolds along with the most common transition wavelengths in Er:YAG [70]. The left hand column of numbers show the wavenumbers of the sublevels in cm^{-1}. The right hand column shows the Boltzmann factors for the respective levels within each manifold at 300 K.

Er:YAG is referred to as a quasi-three-level system because the lower laser level is one of the sublevels in the ground state manifold.

The absorption/emission wavelengths (in nm) are found from the inverse of the differences between the energy levels:

$$\lambda_{ij} = \frac{10^7}{(l_i - l_j)} \tag{2.1}$$

where l_i is the wavenumber (cm^{-1}) of the corresponding sublevel (labelled i).

The Boltzmann factor (f_i) for each sublevel of an energy manifold is the probability that an ion will occupy that particular sublevel, and is calculated using [71]:

$$f_i = \frac{e^{-hcl_i/k_BT}}{\sum_i e^{-hcl_i/k_BT}} \tag{2.2}$$

where h is Planck's constant (6.63×10^{-34} J s), T is the absolute temperature in Kelvin and k_B is Boltzmann's constant (1.38×10^{-23} J K^{-1}). In this case there is no degeneracy in the energy levels since different electron configurations produce different energy levels.

Virtually all ions will reside in the $^4I_{15/2}$ ground state manifold in the absence of pumping. They will tend to occupy the lowest energy sublevels at low temperatures, but will be distributed more evenly across the sublevels at higher temperatures. Unfortunately, around 2% of the ground state population resides in the lower laser sublevel at room temperature. These ions can re-absorb laser radiation, as discussed in §2.2.3.

2.2.2 Pump absorption

A typical absorption and emission spectrum of Er:YAG is shown in Figure 2.2:

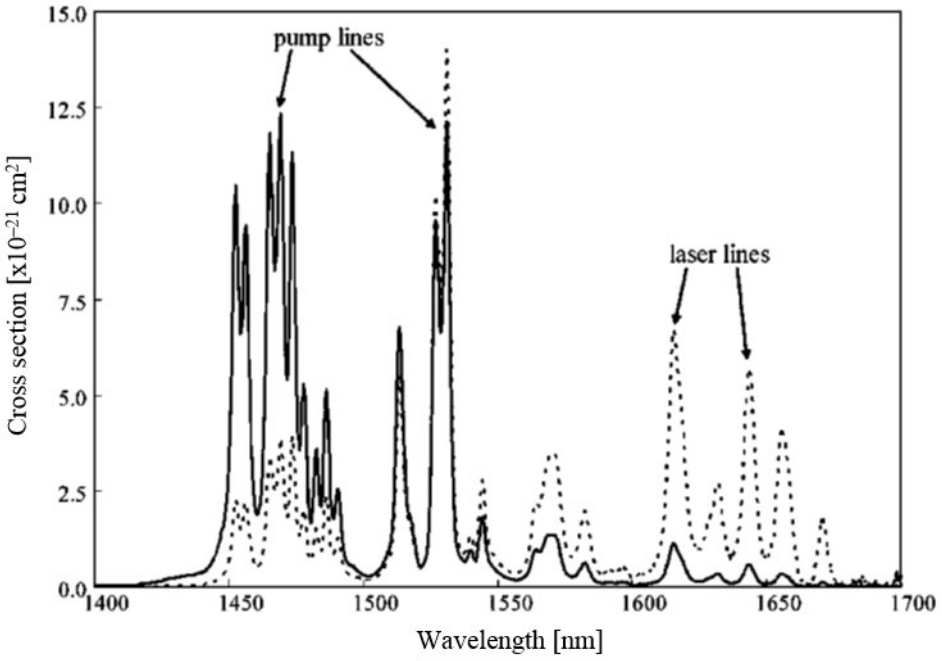

FIGURE 2.2: The absorption (solid line) and emission (dashed line) spectrum of Er:YAG at room temperature [70].

The two groups of absorption lines are shown in Figures 2.1 and 2.2. The group centred around 1.47 μm consists of sixteen possible absorption wavelengths between the four lowest sublevels of the $^4I_{15/2}$ state and the four highest sublevels of the $^4I_{13/2}$ state. The Stokes factor is the ratio of the pump wavelength to laser wavelength:

$$\eta_S = \frac{\lambda_p}{\lambda_l} \tag{2.3}$$

The slope efficiency of a laser is directly proportional to this figure. Thus it is usually desirable that the pump and laser wavelengths are as close together as possible.

The possible absorption wavelengths are listed from shortest to longest in Table 2.1:

Pump absorption transitions (cm^{-1})	**No. of transitions**	**Wavelength**
0 → 6879	1	1454 nm
19 → 6879	1	1458 nm
0 → 6818, 57 → 6879	2	1466 nm
0 → 6800, 19 → 6818, 76 → 6879	3	1470 nm
0 → 6779, 19 → 6800	2	1475 nm
19 → 6779, 57 → 6818	2	1479 nm
57 → 6800, 76 → 6818	2	1483 nm
57 → 6779, 76 → 6800	2	1487 nm
76 → 6779	1	1492 nm

TABLE 2.1: In-band pump transitions in Er:YAG centred around 1.47 μm. Wavelength(s) are rounded to the nearest 1 nm.

The large number of absorption wavelengths ranging from 1454 nm to 1492 nm in this group facilitate absorption of pump light from 1.47 μm laser diodes. These generally have a large (10 nm) bandwidth, but can be tuned to maximise absorption. However the relatively broad emission spectrum of the diode means that a small proportion of the pump power will not be absorbed over any slab length. Er:YAG can also be pumped at 1.53 μm using an EDFL, but we chose a 1.47 μm laser diode for simplicity.

In the absence of significant depletion of the ground state manifold, the pump is exponentially attenuated:

$$P_t = P_0 e^{-\alpha l} \tag{2.4}$$

where P_t is the transmitted pump power, α is the pump absorption coefficient and l is the length. The pump absorption coefficient of 0.5% Er:YAG is around 0.77 cm^{-1} at these

wavelengths [70]. This is fairly low and so end-pumping must be used to allow maximum absorption of pump light.

2.2.3 Small signal gain

The optical gain in a quasi-three-level gain medium such as Er:YAG is determined by two processes: stimulated emission and absorption. The small-signal gain is given by:

$$g_0 = \sigma_e(f_2 N_2 - f_1 N_1) \tag{2.5}$$

where σ_e is the stimulated emission cross section for the transition, f_2 and f_1 are the Boltzmann factors for the upper and lower laser sublevels and N_2 and N_1 are the ion population densities of those respective manifolds [72]. This can be thought of as two separate terms, with $\sigma_e f_2 N_2$ creating laser photons and $\sigma_e f_1 N_1$ absorbing them. The small signal gain of a laser transition in a quasi-three-level system is less than that in a four-level system as the population inversion is reduced by the lower level population.

Both the 1617 nm and 1645 nm transitions have the same upper sublevel; with a Boltzmann factor of 0.21, significantly reducing the gain of these transitions.

If we neglect the population of the higher energy manifolds caused by energy transfer up-conversion, and with the simplifying assumption that all the Er^{3+} ions occupy the two lowest energy levels, then $N_1 + N_2 = N_C$, where N_C is the Er^{3+} concentration. In this case, the small signal gain can be written as:

$$g_0 = \sigma_e\big((f_1 + f_2)N_2 - f_1 N_C\big) \tag{2.6}$$

In addition to reducing the small signal gain, the lower laser level population can also introduce re-absorption losses if the gain medium is not pumped to beyond transparency where stimulated emission is more likely than stimulated absorption: $f_2 N_2 > f_1 N_1$

Thus, for a quasi-three-level gain medium, it is essential that all regions of the gain medium through which the laser mode propagates is pumped to above transparency. The transparency condition ($g_0 = 0$) for each lasing wavelength is given by:

$$N_{tr} = N_C \left(\frac{f_1}{f_1 + f_2} \right) \tag{2.7}$$

where N_{tr} is the minimum N_2 population density required for transparency. N_{tr} is nearly 10% of N_C for 1645 nm lasing and nearly 15% for 1617 nm lasing, assuming the gain medium is in thermal equilibrium at 300 K.

2.2.4 Energy transfer up-conversion

Energy Transfer Up-conversion (ETU) is a cross-relaxation process where two nearby excited erbium ions exchange energy; one moves up and the other moves down. This occurs in Er:YAG since the energy levels are almost evenly spaced [73]. One of the ETU processes in which the upper laser level is depleted is shown in Figure 2.3:

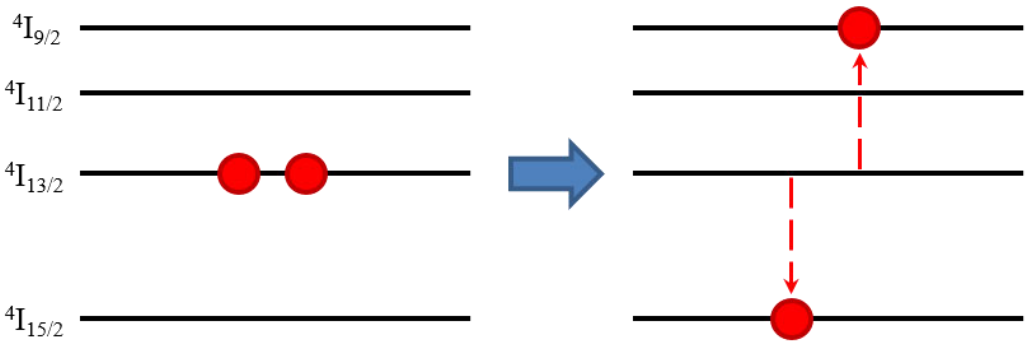

FIGURE 2.3: A depiction of up-conversion in the lower energy levels of Er:YAG. This populates the $^4I_{9/2}$ and $^4I_{15/2}$ levels, but depletes the $^4I_{13/2}$ level of both ions.

ETU thus reduces the upper state population density and populates higher energy levels of Er:YAG.

The ETU processes for Er:YAG are as follows:

- $^4I_{13/2} + {}^4I_{13/2} \rightarrow {}^4I_{9/2} + {}^4I_{15/2}$
- $^4I_{11/2} + {}^4I_{11/2} \rightarrow {}^2H_{11/2} + {}^4I_{15/2}$

The second process leads to a green glow during pumping, resulting from transitions from the $^4S_{3/2}$ level to the ground state [74].

The rate at which ETU depletes the upper state population is proportional to the square of the upper state ion concentration [75]. Therefore, gain media with lower erbium concentrations, which have a smaller upper state population at transparency, are preferred.

The most common Er^{3+} doping concentrations are 0.25% and 0.5%. Experiments with higher erbium concentrations show a strong decrease in 1.6 μm laser efficiency, due to higher threshold power and lower slope efficiency [76]. Reviewing previous work in this field indicates that 0.25% erbium doping is often used as a means of reducing up-conversion losses. However, to provide a balance between adequate pump absorption in a small slab size and limited up-conversion, a doping level of 0.5% was chosen.

The up-conversion parameter for the first process listed above is thought to be directly proportional to the doping concentration [77]. This has been measured at between 5.0 and 8.0 x 10^{-18} cm^3 s^{-1} for 1.0% Er:YAG [76][78]. A C_{up} value of 3.6 x 10^{-18} cm^3 s^{-1} for 0.5% Er:YAG will be used, based on the results of Kim et. al. with 1% Er:YAG [79].

2.2.5 Lasing wavelength

There are twelve possible emission wavelengths according to Figure 2.1: the shortest wavelengths are four transitions around 1617 nm and the longest wavelength is 1673 nm, according to Eqn. (2.1). These correspond to the emission spectrum in Figure 2.2.

The two reported lasing wavelengths of 1617 nm and 1645 nm are the transitions with the highest stimulated emission cross sections, listed in Table 2.2 [80]. The preferred wavelength is largely determined by the population inversion. While both transitions share the same upper laser level, the 1617 nm transition has a higher lasing threshold due to increased re-absorption loss from the higher population density of the lower laser level.

However, as it has a higher stimulated emission cross section than the 1645 nm transition at room temperature, it will lase at a sufficiently high inversion density.

Parameter	Symbol	Value
Doping concentration	N_C	7.0×10^{19} cm^{-3}
Upper level lifetime	τ_f	0.0068 s
Upper Boltzmann factor	f_2	0.21
1617 nm cross section	σ_{1617}	3.2×10^{-20} cm^2
1617 nm Boltzmann factor	$f_{1(1617)}$	0.036
1645 nm cross section	σ_{1645}	2.7×10^{-20} cm^2
1645 nm Boltzmann factor	$f_{1(1645)}$	0.022
Up-conversion parameter	C_{up}	3.6×10^{-18} cm^3 s^{-1}

TABLE 2.2: The spectroscopic parameters of 0.5% Er:YAG at 300 K [79][80].

All other loss factors being equal, the 1617 nm transition will be favoured when its small signal gain exceeds that of the 1645 nm transition:

$$\sigma_{1617}\left(f_2 N_2 - f_{1(1617)} N_1\right) > \sigma_{1645}\left(f_2 N_2 - f_{1(1645)} N_1\right) \tag{2.8}$$

Using the $N_1 = N_C - N_2$ approximation, this can be re-arranged to:

$$N_2 > N_C \left(\frac{\sigma_{1617}\left(f_{1(1617)}\right) - \sigma_{1645}\left(f_{1(1645)}\right)}{\sigma_{1617}(f_1 + f_2)_{1617} - \sigma_{1645}(f_1 + f_2)_{1645}} \right) \tag{2.9}$$

Substituting in the parameter values indicates that N_2 must exceed 35% of N_C for the 1617 nm transition to be favoured over the 1645 nm transition.

2.2.6 Rate equations

The rate equations for the four lowest energy levels in the absence of lasing are [81]:

$$\frac{dN_1}{dt} = -W_p N_1 + \frac{N_2}{\tau_f} + C_{up} N_2^2 + \frac{N_4}{\tau_{41}} + \frac{N_3}{\tau_{31}} \quad (2.10a)$$

$$\frac{dN_2}{dt} = W_p N_1 - \frac{N_2}{\tau_f} - 2C_{up} N_2^2 + \frac{N_4}{\tau_{42}} + \frac{N_3}{\tau_{32}} \quad (2.10b)$$

$$\frac{dN_3}{dt} = \frac{N_4}{\tau_{43}} - N_3 \left(\frac{1}{\tau_{31}} + \frac{1}{\tau_{32}} \right) \quad (2.10c)$$

$$\frac{dN_4}{dt} = C_{up} N_2^2 - N_4 \left(\frac{1}{\tau_{41}} + \frac{1}{\tau_{42}} + \frac{1}{\tau_{43}} \right) \quad (2.10d)$$

where W_p is the pump rate, C_{up} is the up-conversion parameter for the N_2 energy level, and N_3 and N_4 are the populations of the $^4I_{11/2}$ and $^4I_{9/2}$ levels respectively.

The fluorescence lifetime τ_f of the upper laser level at low population densities is around 6.8 ms, however ETU reduces the effective fluorescence lifetime of this level [82].

The other lifetimes in the equations above are listed in Table 2.3:

Symbol	τ_{31}	τ_{32}	τ_{41}	τ_{42}	τ_{43}
Value (ms)	8.5	67	20	18	0.006

TABLE 2.3: Approximate lifetimes of the excited states of erbium ions in YAG [83].

These equations were used in MATLAB code to model the behaviour of the Er:YAG laser gain medium.

2.3 Gain medium

The Er:YAG lasers discussed in Chapter 1 used a rod architecture. Our gain medium is based on the Co-Planar Folded zig-zag Slab (CPFS) design that was first developed by J. Richards and A. McInnes [84]. This offers a longer path length for a given pump absorption length, providing a larger gain-length product. The disadvantage of using a CPF slab is that the resonator round trip time is also increased, along with the slab loss because each TIR bounce is not 100% reflective. The results of the modelling are reported in §2.3.2 and the long and short slabs are described in §2.3.3 and §2.3.4 respectively.

2.3.1 CPF slab architecture

A schematic of the CPF slab is shown in Figure 2.4. The entry and exit faces are Brewster-angled and thus the CPF slab does not require optical coatings.

A CPF slab with a 45° internal bounce angle increases the path length of the beam in the slab by a factor of $2\sqrt{2}$ compared to a rod gain medium, without increasing the length over which the pump light is absorbed. A comparison is shown in Figure 2.4:

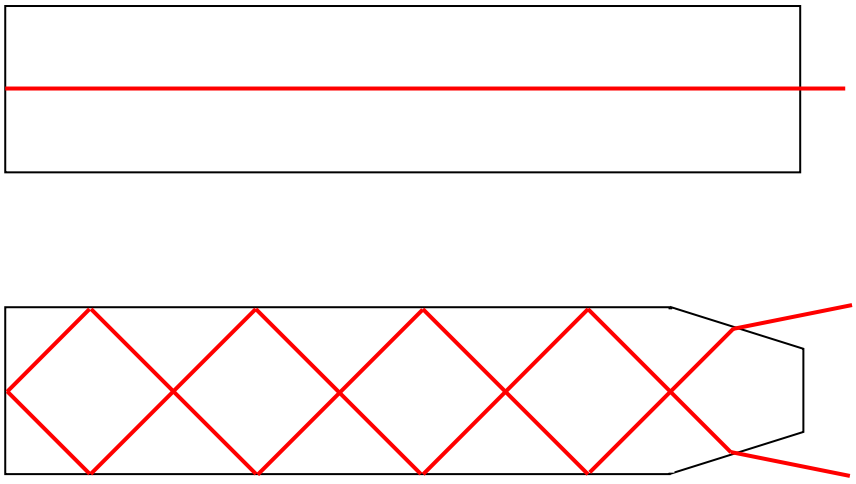

FIGURE 2.4: Comparison between a single pass of a laser beam through a conventional slab (top) and a CPF slab (bottom) of the same length.

There were several competing considerations when designing the CPF slab. It must be long enough to absorb most of the pump light and provide high gain to allow high energy, short duration laser pulses, while being short enough to minimise the slab loss and the resonator round trip time.

The round trip gain G achieved after a double pass of the slab is given by:

$$G = e^{2g_o L} \tag{2.11}$$

where L is the physical path length of the laser beam for a single pass of the slab. This is equal to the slab length for lasers using a rod gain medium and many slab lasers, unless they use a zig-zag geometry. A higher round trip gain helps make pulses shorter.

2.3.2 MATLAB modelling

We designed a CPF slab based on MATLAB simulations of a 0.5% Er:YAG gain medium, taking into account pump power, slab length and width. These programs had previously been used to design other Er:YAG slab lasers built by our research group, and are provided in Appendix C1. They calculated theoretical round trip gain, stored energy and pump absorption from the slab length and pump intensity.

The following simulations use 20 W end pumping because this was anticipated to be the maximum CW pump power available from a 1470 nm laser diode. Then they are repeated with 50 W pump power, which assumed quasi-CW (QCW) pumping.

A plot of the round trip gain for 20 W incident pump power vs. slab length and pumped area is shown in Figure 2.5:

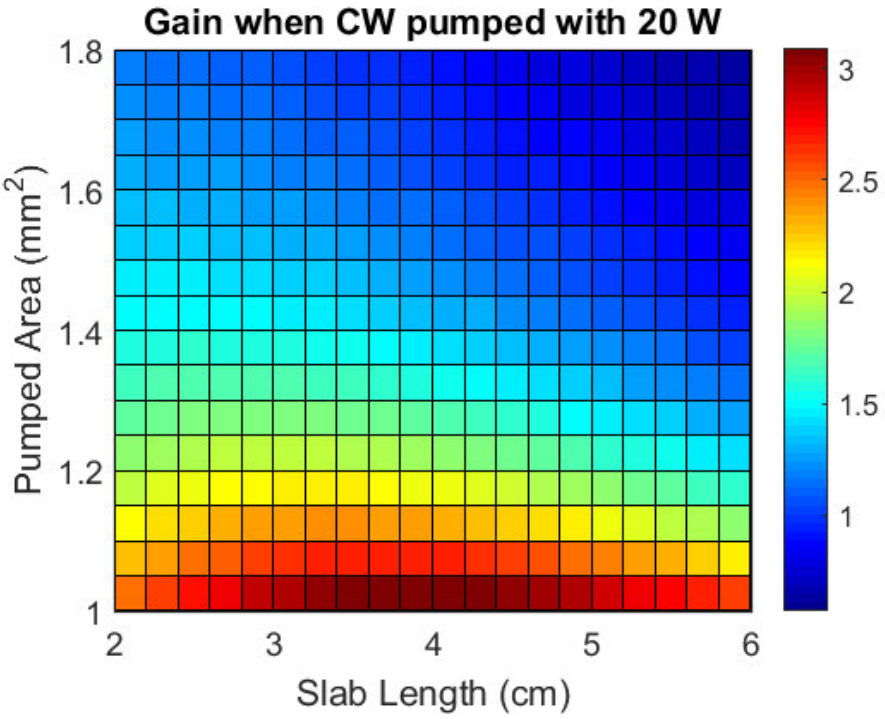

FIGURE 2.5: Round trip gain vs. slab length and pumped area for 20 W pump power.

This shows that a higher gain is achieved with a smaller pump area, and maximised with a 3.5 cm slab length when using 20 W pump power. While a longer slab would increase pump absorption (see Figure 2.7), it does not provide extra gain since the pump attenuation along the slab prevents a population inversion from being created.

Another consideration is the energy storage, which requires both a large upper level population density and pumped volume. A large upper level population density requires a higher pump intensity, which favours a smaller pumped volume. Based on these simulations, we estimated the optimum slab length to be around 3.5 cm, with a pumped area of 1.2 mm^2 to maximise stored energy. Since the height of the pumped region was 0.6 mm (see §2.4.6), we chose a slab width of 2.0 mm. This would allow a high pump intensity and large population inversion, while we knew that higher peak pump powers would be available under pulsed pump conditions.

A plot of the round trip gain for 50 W incident pump power vs. slab length and pumped area is shown in Figure 2.6:

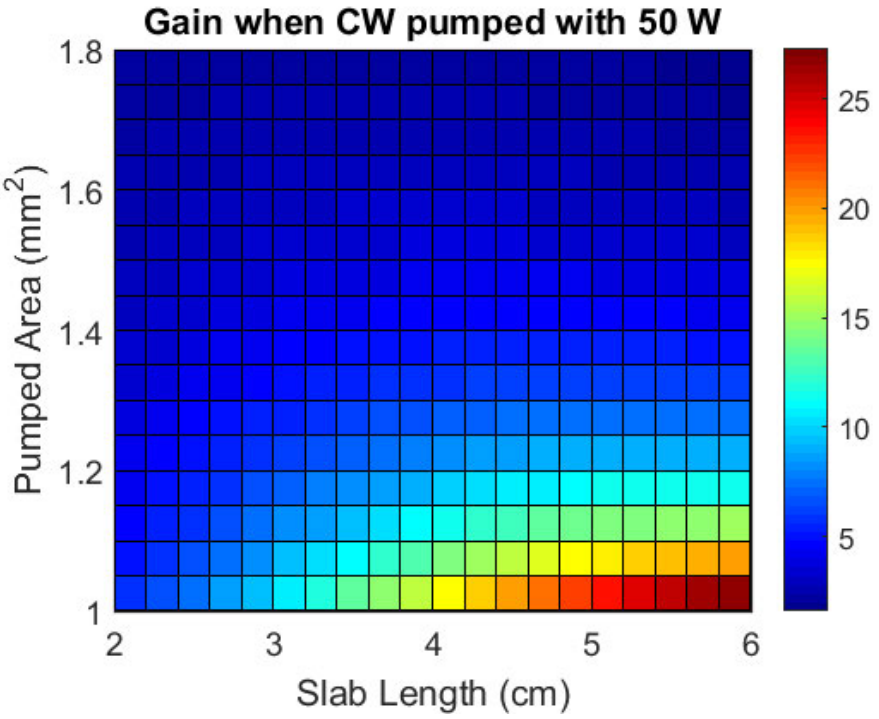

FIGURE 2.6: Round trip gain vs. slab length and pumped area for 50 W pump power.

The round trip gain approaches 7-9 for the chosen slab dimensions, indicating that the laser could easily produce sufficiently energetic pulses with a R = 40% output coupler, even after including additional intra-cavity losses. The reason for using such a low reflectivity output coupler will be explained in Chapter 4.

The plot of transmitted pump power for 20 W incident pump power as a function of slab length and pumped area is shown in Figure 2.7:

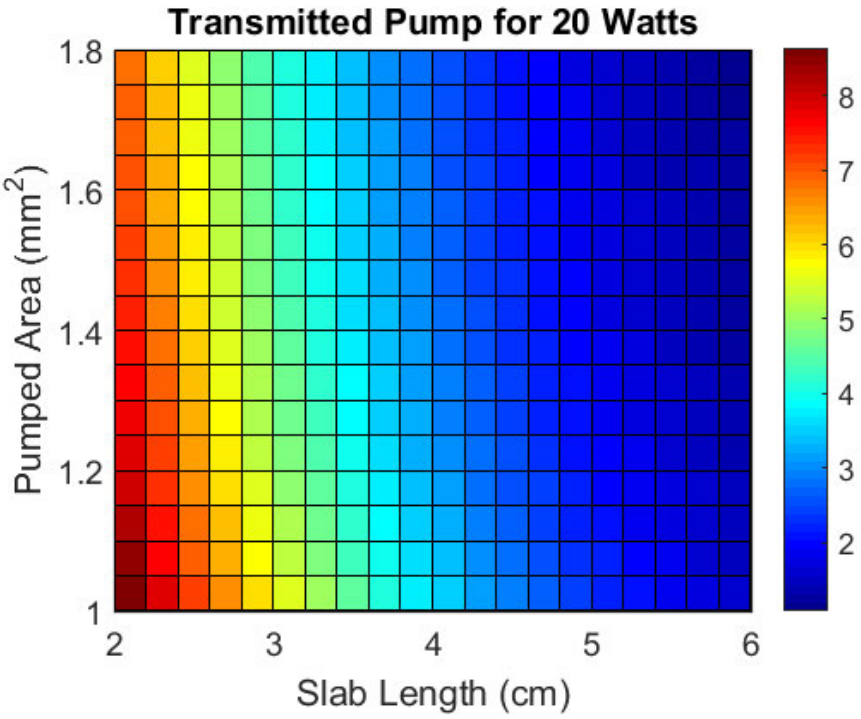

FIGURE 2.7: Transmitted pump vs. slab length and pumped area for 20 W pump power.

A smaller slab width and pumped area corresponds to a higher pump intensity, which can deplete the lower energy levels, resulting in less absorption. However the main factor in pump absorption is the slab length and doping. The above plot indicates that a 2 cm long 0.5% Er:YAG slab will absorb about 60% of the pump power, which rises to around 80% for a 3.5 cm slab. However, both figures are subject to pump wavelength tuning.

The height of the slab was the least important parameter, and was chosen to be 4 mm, although in hindsight a slab of lower height would have been easier to position without toppling over due to the high centre of mass.

Once the approximate slab dimensions were decided on, the slab nose was designed using the refractive index of YAG at the lasing wavelength to calculate the correct shoulder angle for minimal loss at the entry and exit faces.

The refractive index of YAG is 1.813 at 1645 nm. The wavelength dependence of the refractive index is covered in Appendix F. The critical angle is given by:

$$\theta_c = \sin^{-1}\left(\frac{1}{1.813}\right) \approx 33.5° \tag{2.12}$$

This is considerably less than the 45º bounce angle inside the slab.

2.3.3 Long slab

The Er:YAG gain medium with a doping concentration of 0.5% was sourced from Scientific Materials (USA). Slab cutting and polishing was performed by BAE Systems Australia (Holden Hill). The full dimensions of this slab were 35.6 mm long x 2.0 mm wide x 4.0 mm high. The laser mode follows a folded zig-zag path, with 35 TIR bounces (at 45º) on the slab sides and end face. A diagram of the slab is shown in Figure 2.8:

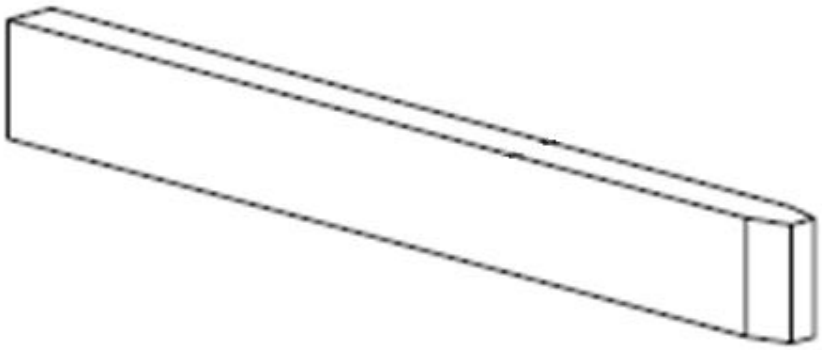

FIGURE 2.8: 3D view of the long Er:YAG CPF slab used in my first Q-switched laser.

The surface flatness was specified to the highest quality, λ/20, due to the large number of TIR bounces while the scratch/dig was specified to 10/5, the highest quality available. This is necessary to minimise loss and reduce the risk of damage at high power. The top and bottom surfaces were fine ground. A technical drawing is provided in Appendix B1.

The slab entry and exit faces are Brewster angled for minimal loss of π-polarisation, the angle being dictated by the refractive index of the slab:

$$\theta_B = \arctan(n) = 61.1^{o} \tag{2.13}$$

The incident angles of the beam inside and outside the slab sum to 90°. The shoulder angle must therefore be 61.1° – 45° = 16.1° (see Figure 2.9). This eliminates the requirement for dielectric coatings, which are vulnerable to damage at high power and difficult to apply to small surfaces. This makes the laser mode π-polarised (with the electric field in the plane of incidence) for minimal loss at the Brewster faces.

The final consideration of the slab design was the clear aperture of the Brewster faces. The horizontal clear aperture is illustrated by the top view of the slab nose in Figure 2.9:

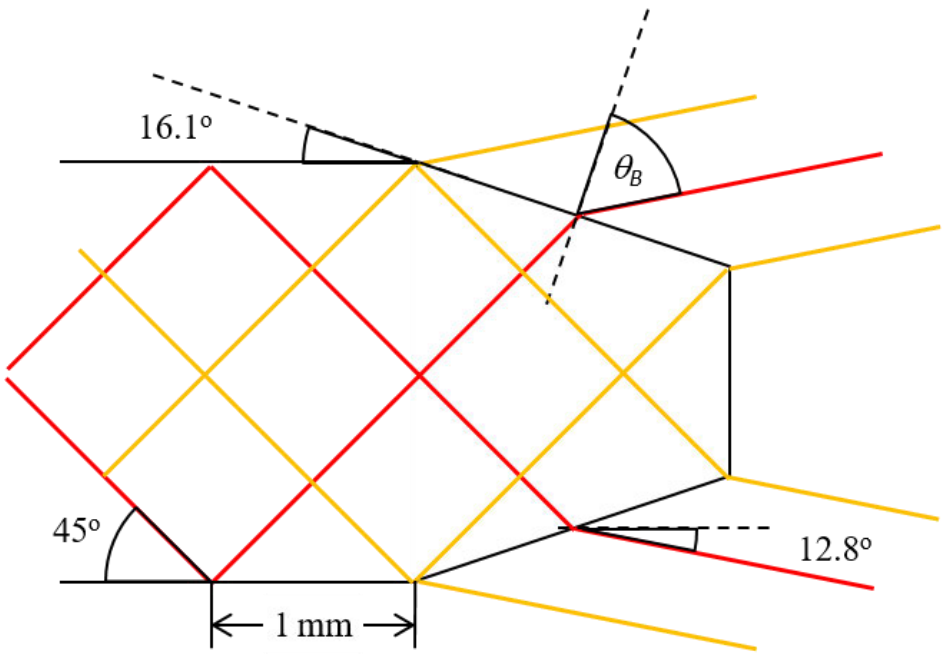

FIGURE 2.9: Top view of the nose of each slab showing the Brewster angled faces. The red lines represent the centre of the beam, with the orange lines being the maximum extent of the beam. The slab nose was intended to be no larger than the latter.

These would restrict the dimensions of the laser mode in the horizontal direction. This constrained the horizontal extent of the beam inside the slab to be 1.4 mm and outside the slab to a diameter of 0.78 mm and therefore a maximum beam radius of 0.39 mm.

The hard aperture can be used to control the mode content in the horizontal direction: if the fundamental mode has a radius of ~60% of 0.39 mm, then clipping losses for the fundamental will be negligible while those for higher-order modes will prevent lasing in those modes. The nose length was kept as short as possible, which was intended to reduce the likelihood of parasitic lasing [85].

2.3.4 Short slab

The Q-switched test results of the long slab, presented in §4.3.2, showed that the Q-switched pulse durations were too long to meet the project requirements. Thus, a shorter slab was designed with 20 mm long sides and 21.6 mm total length. There were 10 TIR bounces per side (21 total). The slab width, height and nose dimensions remained unchanged. The shorter gain length ultimately reduced the maximum attainable pulse energies. A technical drawing of this slab is provided in Appendix B2.

2.4 Pump assembly

A picture of the complete pump module is shown below in Figure 2.10.

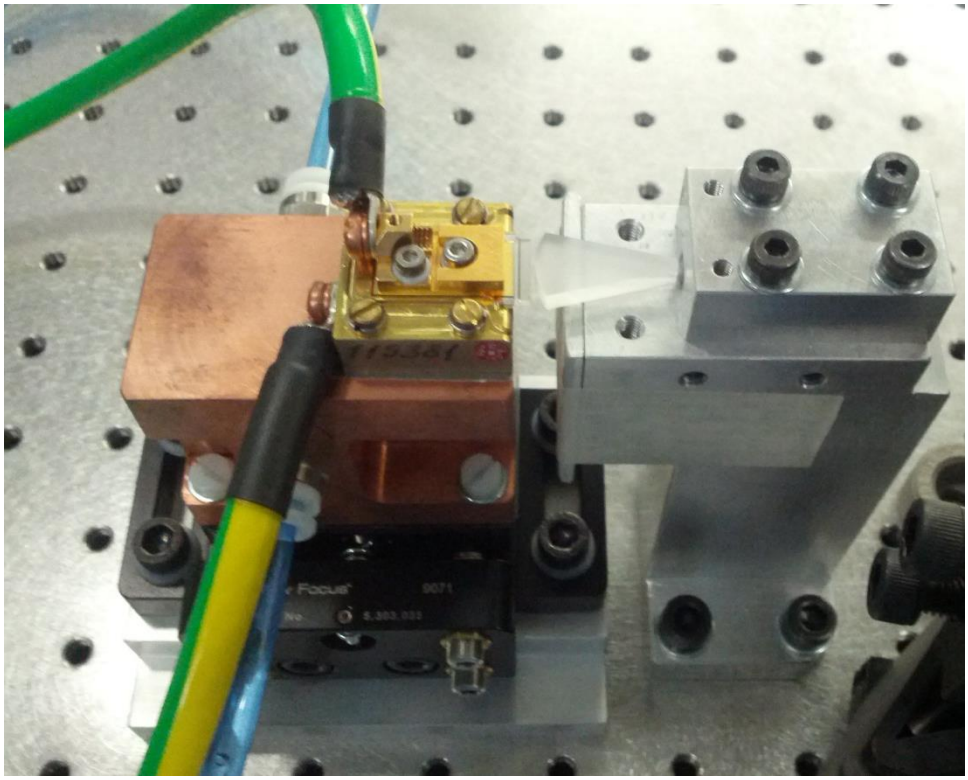

FIGURE 2.10: Mounting of the pump diode (the gold package) on the water-cooled copper block. The black mount is the tilt stage, which is bolted to the aluminium spacer. The light from the diode is guided into the slab by the glass lens duct.

The pump module consisted of a 20 W CW laser diode, described further in §2.4.1, mounted on a water cooled copper block, with a 125 μm thick layer of indium foil placed in between. Indium is malleable at room temperature and can be crushed by around 5% to improve thermal contact and heat conduction. The temperature of the diode was controlled by a water chiller, as discussed in §2.4.2. The light from the pump diode was guided into the slab using a lens duct, which is described further in §2.4.5.

The copper block was attached to a tilt stage in order to control the direction of the pump light. The tilt stage was attached to an aluminium spacer so that the pump emission height was 100 mm above the optical table. The schematics of these components are provided in Appendices B4, B5 and B6.

2.4.1 Pump diode

The pump source was a DILAS 1.47 μm InGAsP laser diode consisting of 19 emitters equally spaced on a 1 cm wide conduction-cooled bar. A fast axis collimation (FAC) lens reduced the full-angle divergence in the vertical direction from 70^{o} to less than 0.5^{o}. The complete specifications of the pump diode are provided in Appendix D.

The CW output power of the laser diode could exceed 20 W. Higher peak powers could be produced when the laser diode was pulsed at low duty cycles; rated up to 80 W using a 2% duty cycle for example. Pulsing the pump diode had the advantage of increasing the pump pulse energies whilst reducing the average power and heat load in the slab.

2.4.2 Water cooling system

The water chiller had an operating temperature range of 15ºC to 35ºC. It circulated cooling water to the pump diode mount, allowing wavelength tuning of the pump diode and preventing it from overheating. A technical drawing of the mount is in Appendix B4. A schematic of the water cooling system is shown in Figure 2.11:

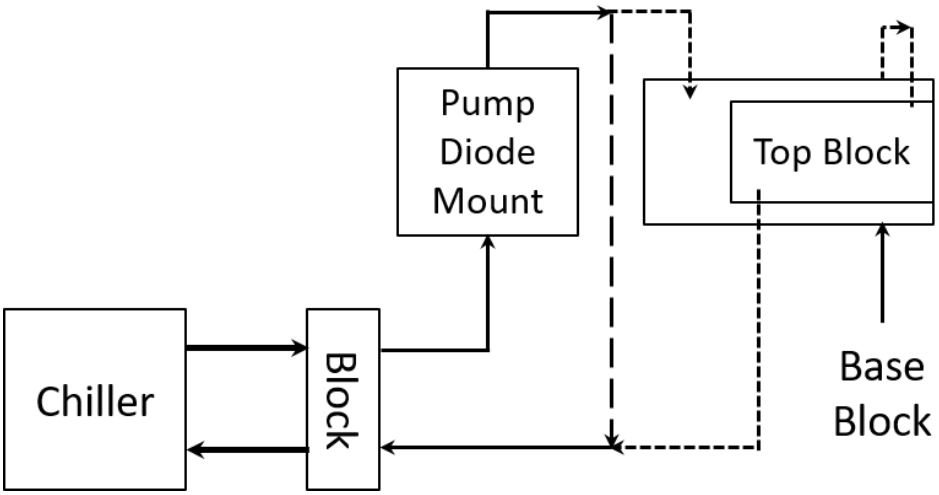

FIGURE 2.11: Schematic of the water cooling system used for the laser. The aluminium block was bolted to the optical table and adapted thick water pipes from the chiller into thin water pipes connected to the pump diode mount (—) and later the laser head (- -).

2.4.3 Pump diode spectra

Two plots of typical output spectra from the pump diode are shown in Figure 2.12:

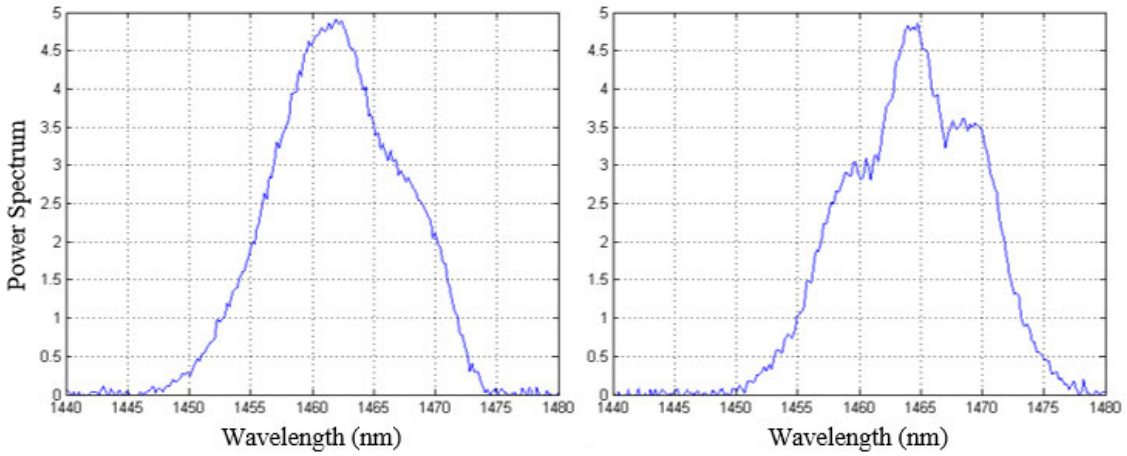

FIGURE 2.12: Plots of pump diode spectra centred on 1462 nm (15°C) and 1464 nm (20°C).

The centre wavelength of the pump emission increased with both pump current and duty cycle because heating caused thermal expansion of the junction. Varying the water temperature controlled the equilibrium temperature of the junction, enabling wavelength tuning of the pump diode. This provided an emission spectrum that would be best absorbed by the slab, maximising the laser power. Emission wavelengths between 1450 nm and 1485 nm were observed, while the centre wavelength of the pump diode red-shifted at an average rate of 0.5 nm/°C.

2.4.4 Laser diode driver

The pump diode was powered by a laser diode driver (LDD) and a control system that was linked to the lab door interlock for safety. The CW laser initially used a 55 A LDD, but this was replaced by one rated to provide 160 A, because a high peak current was required for pulsed lasing using low reflectivity output couplers.

A RIGOL DG1022 waveform generator was used to supply square waveforms into the control system to enable pump diode pulsing. The output was set to 10 ms duration pulses, slightly longer than the lifetime of the upper state, with a PRF of 12 Hz.

The LDD controller could not reliably measure a low frequency pulsed current. Therefore, a Hall effect sensor was used to provide a voltage that was directly proportional to the peak current in the cable and thus related to the peak pump power.

This sensor was calibrated by measuring the average pump diode output power as a function of the peak sensor voltage, enabling the pump power to be accurately determined during laser operation. A plot of peak pump power against Hall probe sensor voltage for the 12% duty cycle is shown in Figure 2.13:

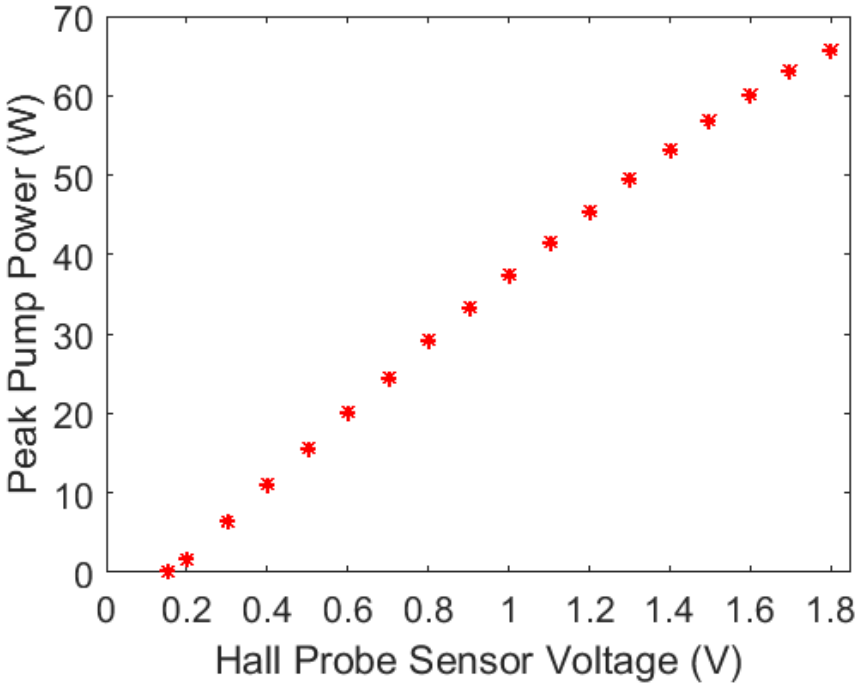

FIGURE 2.13: Peak pump power vs. sensor voltage, at a chiller temperature of 20°C.

Increasing the driver current gradually decreased the efficiency of the pump diode due to heating in the junction [86]. Catastrophic failure of one pump diode occurred at just over 69 W peak power on the 12% duty cycle with the chiller temperature set to 20°C. To prolong the pump diode lifespan, I restricted the driver current so that the sensor voltage did not exceed 1.60 V, corresponding to a peak pump power of just over 60 W (600 mJ pump pulse energy) when the chiller was set to 20°C.

2.4.5 Lens duct design

An uncoated BK7 glass lens duct, sometimes referred to as a waveguide [87], was used to efficiently couple the pump light into the slab. This was the simplest and most effective coupling method, as opposed to using a cylindrical or convex lens, since the 10 mm wide emission strip of the pump diode greatly exceeded the slab width of 2 mm and the full-angle divergence from each emitter in the horizontal direction was almost 18°. The curved front face focused the pump light while TIR confined it as the lens duct width gradually decreased to match the slab width. A schematic of the lens duct is shown in Figure 2.14, and a technical drawing is provided in Appendix B3:

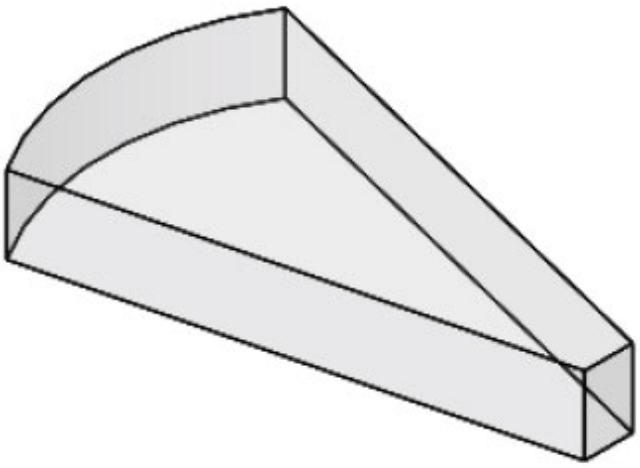

FIGURE 2.14: The lens duct. The front face had a 10.5 mm radius of curvature.

The lens ducts were fabricated from BK7 glass cylinders by BAE Systems Australia; the surface quality was 20/10 scratch-dig and λ/4 figure on the optical surfaces, with fine polish on the curved front face. The top and bottom surfaces were fine ground.

The performance of the lens duct was modelled using ray-tracing in Zemax [88]. The model simulated the path of light rays from the pump emitters to the slab. The primary variables were the parameters of the pump diode; the number and spacing of the emitters and the maximum typical divergence of pump rays in both directions. A 3D Zemax model showing the slow axis of the pump source is shown in Figure 2.15:

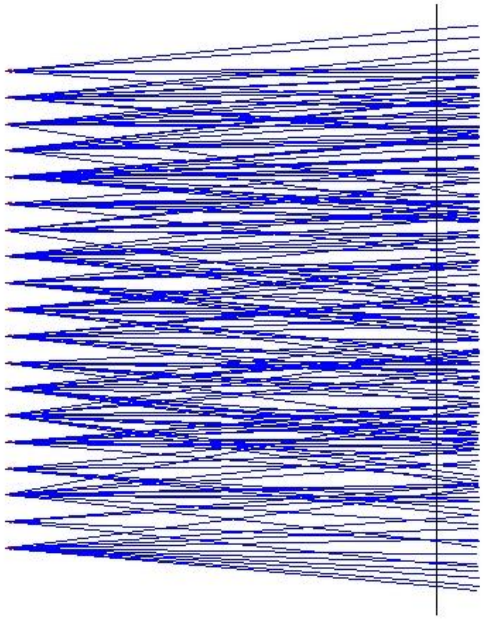

FIGURE 2.15: Top view of the Zemax model showing 100 simulated pump rays from the slow axis of the 19 emitters of the laser diode.

The lens duct and slab were added to complete the simulation. Their refractive indices came from the Zemax materials database. The gap between the pump diode and lens duct was less than 1 mm and the slab placed as close to the lens duct as possible without touching, otherwise TIR of the laser mode would no longer occur.

Each ray was refracted or reflected at the optical surfaces it encountered. The Zemax model showing the top view of the complete system of the pump source and the light entering the lens duct and slab is shown in Figure 2.16:

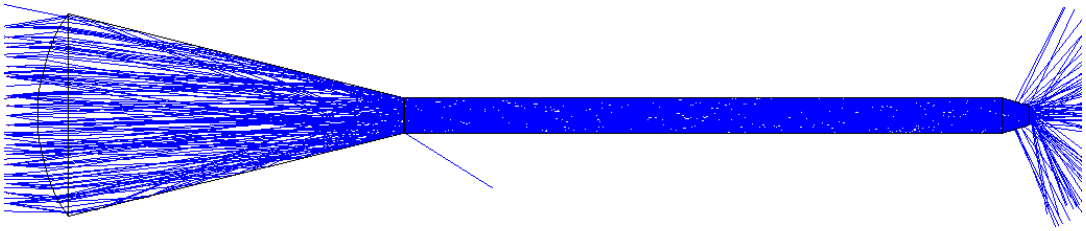

FIGURE 2.16: Top view of the Zemax model showing 100 simulated pump rays from the slow axis of the 19 emitters of the laser diode entering the lens duct and slab. The rays that escape the lens duct are most likely due to Fresnel reflections or from having large incident angles on the front face of the lens duct, particularly towards the edges.

The Zemax model enabled different lens duct dimensions to be trialled to determine which length and curvature radius was able to guide the maximum fraction of light rays into the slab without being “lost”. The maximum length was constrained to slightly less than double the radius of curvature of the front face due to the fabrication technique from 21 mm diameter rods. A gentler constriction angle of the lens duct as it narrowed down was better at preventing sharp reflection angles that could lose rays, but this came with a larger curvature radius which was less effective at focusing horizontally divergent rays.

2.4.6 Vertical pump profile

The pump profile in the vertical direction is critical as a high pump intensity is required to produce a large population inversion. With the pump diode running in CW mode, I measured the power transmitted after the lens duct using an opaque blade that could be moved through the beam, as shown in Figure 2.17:

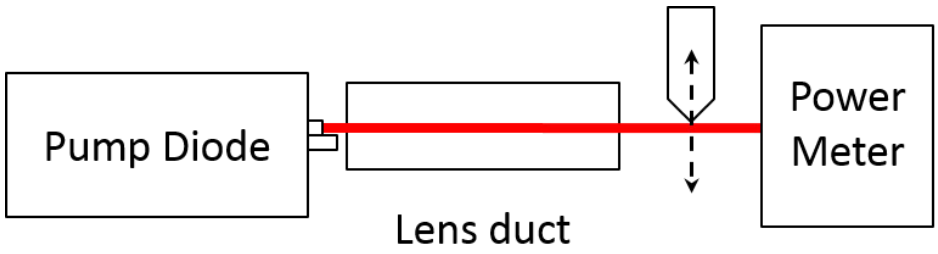

FIGURE 2.17: The setup used to measure the pump power profile in the vertical direction.

The result of this measurement using 5.5 W pump power is shown in Figure 2.18:

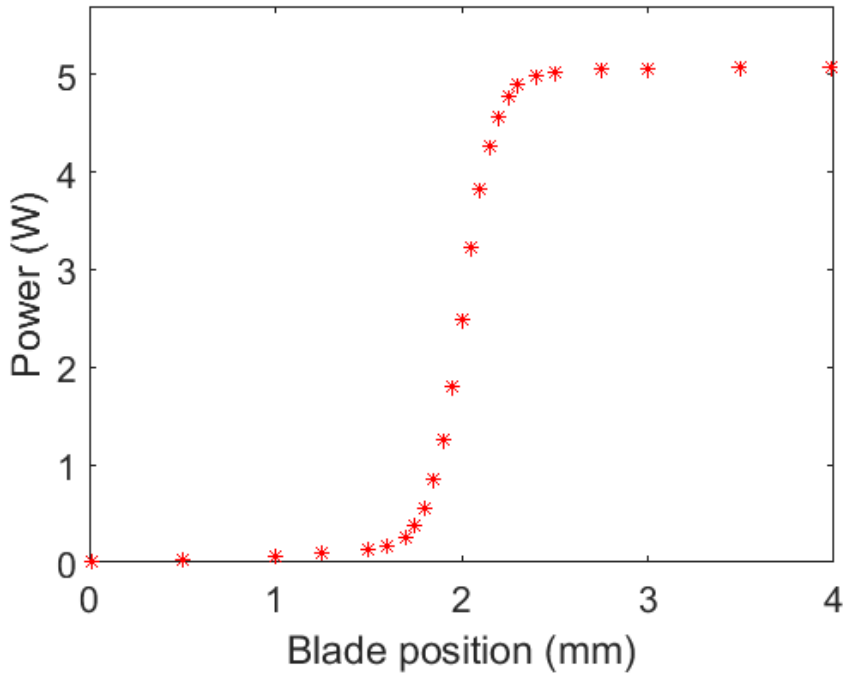

FIGURE 2.18: Pump power readings as a function of the vertical position of the blade.

The location of the centre of the pump beam was determined from the gradient of the above plot with respect to the vertical position of the blade, as shown in Figure 2.19:

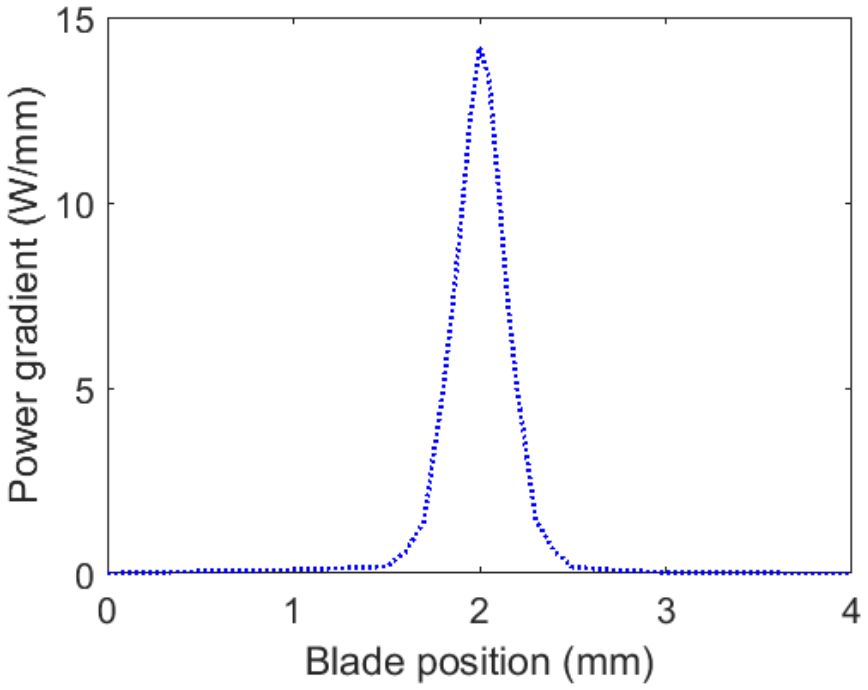

FIGURE 2.19: Pump power gradient as a function of vertical position of the blade.

Poorly fabricated laser diode bars sometimes have a slight curve in the horizontal line connecting the emitters, a characteristic known as the "smile". This spreads the output beam in the vertical direction since the emitters are placed at different heights [89]. The sharp symmetric peak on the plot, as opposed to a flatter peak, proved that the "smile" of the pump diode was negligible, as claimed by DILAS.

It also shows that 80% of the pump power is within a 0.5 mm high region and 90% is within a 0.6 mm high region. As we will see, this overlaps almost perfectly with the vertical extent of the laser mode, assuming the pump diode tilt stage was correctly angled.

2.5 Laser head designs

2.5.1 Initial laser head

The first laser used for the gain-switching and early Q-switching trials had the all–aluminium laser head shown in Figure 2.20. The lens duct rested on the base "platform". A technical drawing for this head is provided in Appendix B7.

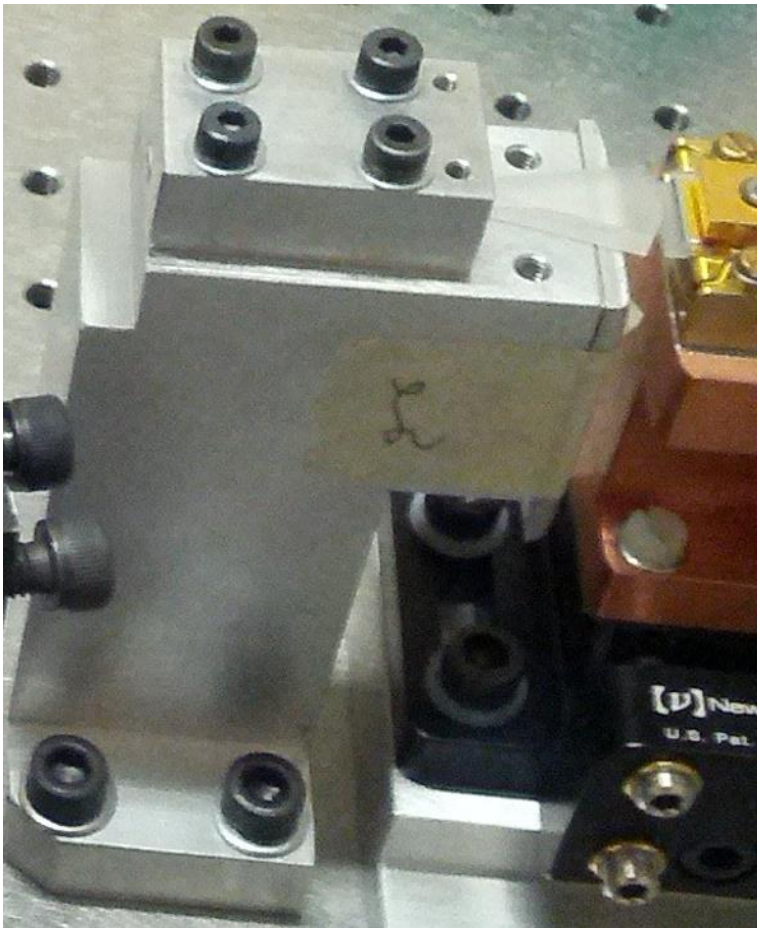

FIGURE 2.20: The initial conduction-cooled aluminium laser head.

The slab was sandwiched between the laser head platform and top block using 125 μm thick indium sheets to allow good thermal contact. The top block had a groove cut in to provide space for the slab. This head relied on conduction of heat away from the slab in anticipation of a minimal heat load due to the low (10%) quantum defect, and it was limited to mounting only long slabs of a specific height.

2.5.2 Water-cooled laser head

Providing water cooling to the laser head as well as being capable of mounting different slabs called for a redesigned laser head that is shown in Figure 2.21:

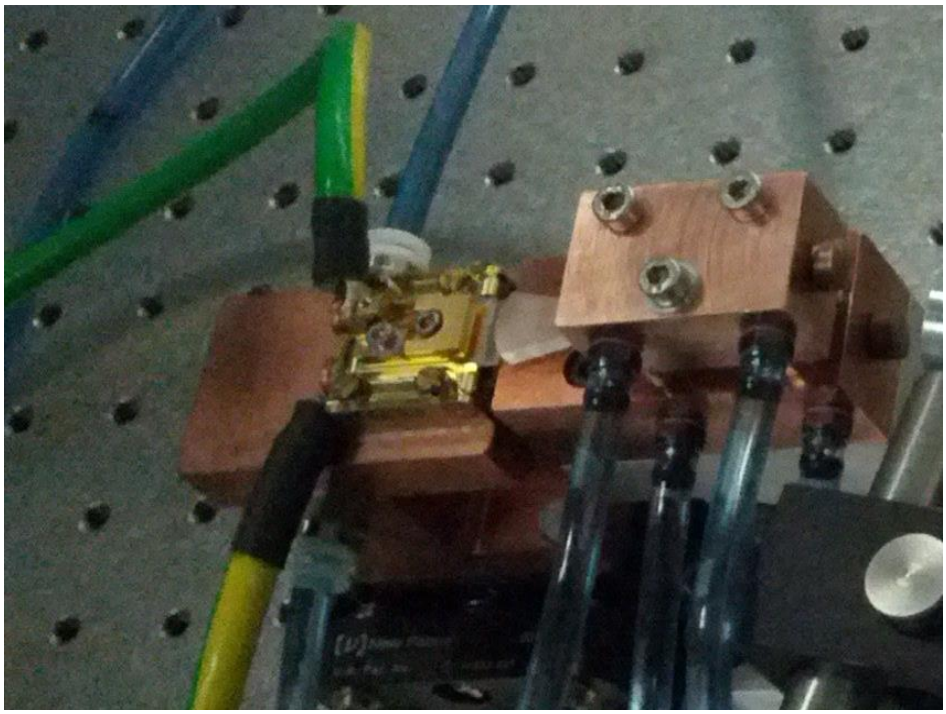

FIGURE 2.21: The improved water-cooled copper laser head. The water pipes operated off the same chiller and were connected as shown in Figure 2.11.

This laser head consisted of two water-cooled copper blocks, allowing improved temperature control of the slab (using the water cooling system shown in Figure 2.11) and mounting slabs of different heights. The top block was secured to the base block using three M4 bolts, with four cylindrical steel spacers to control the crush on the indium sheets. Technical drawings of both blocks are provided in Appendix B8. The base block was mounted on the original aluminium platform which was reduced to 78 mm high. This head was used for the short slab gain-switched results in §3.3.2 and the remainder of the Q-switching experiments, yielding the results presented in Chapter 4.

2.6 Chapter summary

This chapter has reviewed the spectroscopic properties of Er:YAG and its challenges as a laser gain medium. A CPF slab was designed based on MATLAB simulations from several programs. The CPFS architecture compensates for the low gain common to all 1.6 μm Er:YAG lasers and allows operation with lower reflectivity output couplers, an important consideration for high power Q-switched operation. The design of a shorter slab was also covered because this was eventually used as a means of obtaining shorter Q-switched pulses. The pump diode was described next, the mount and the assembly of the pump stage, characterisation of the pump diode and lens duct also explained. Finally both laser heads were described. The next chapter will cover the resonator designs, the laser components and their assembly into the prototype gain-switched lasers which will later be adapted for Q-switching.

Chapter 3: Laser resonator

3.1 Introduction

This chapter describes the development and testing of the lasers used in the Q-switched systems reported in this thesis. The resonator design, optical components and resonator construction are discussed in Section 3.2. The initial resonator suffered from parasitic lasing – the solution to this problem is described in Section 3.3. This section also presents the results of gain-switched testing of both slabs with various output couplers. Intra-cavity losses can significantly reduce the efficiency of a laser. Hence Section 3.4 explains the source of the losses and the measurement of the single-pass slab loss. The threshold and slope efficiency of the gain-switched lasers are compared to theoretical predictions in Section 3.5. The chapter is concluded in Section 3.6.

3.2 Resonator designs

A variety of resonator designs were employed, beginning with a simple symmetric resonator using two curved mirrors to test the alignment (see §3.2.5). This was later adapted to a telescopic resonator that used lenses to expand the beam size for the Q-switch, while ensuring the correct beam size in the slab. The results of resonator modelling using ABCD matrices and the resonator stability conditions are presented in §3.2.2 and §3.2.3. The mirrors and lenses available for the resonator assembly are listed in §3.2.4 and the details of the resonator assembly process are outlined in §3.2.5.

3.2.1 The telescopic resonator

The resonator used to provide the gain-switching results included a telescope to expand the beam. A comparison between the beam size in a simple symmetric resonator and a telescopic resonator is provided on the following page. A similar but more compact layout was used for the shorter slab gain medium. A schematic of the telescopic resonator is shown in Figure 3.1:

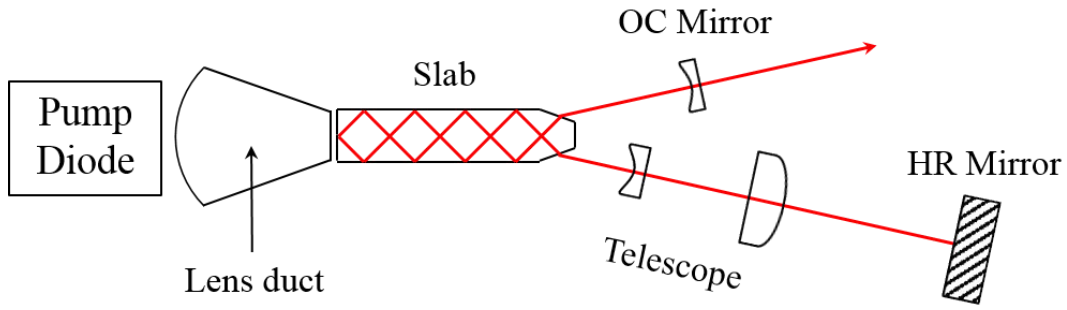

FIGURE 3.1: Schematic of the laser used for gain-switched testing.

3.2.2 Resonator ABCD model

The resonator designs were modelled using a MATLAB code adapted from that written by Dr. Ka Wu (see Appendix C2), which calculated the resonator ABCD matrix from the product of each component matrix in sequential order [90]:

$$\begin{bmatrix} A & B \\ C & D \end{bmatrix} = \prod_i M_i \tag{3.1}$$

where M_i is the matrix associated with the i^{th} optical component or free space. The program also calculated the dimensions of the TEM_{00} eigenmode and plotted the mode size as a function of position in the resonator. This was extremely useful for estimating the best positions for optical components when constructing a resonator, as well as estimating the beam size throughout.

A plot of the mode size in the simple symmetric resonator is shown in Figure 3.2:

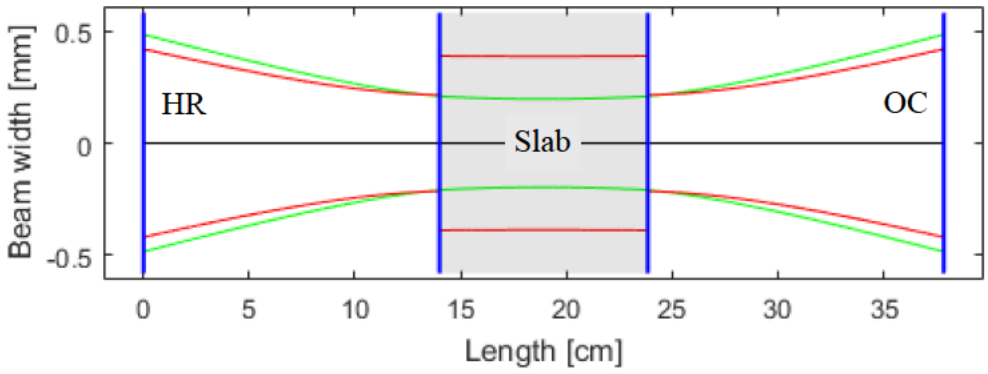

FIGURE 3.2: Plot of the predicted laser mode in the simple symmetric resonator. The slab gain medium is shaded gray. The two mirrors, each with 20 cm curvature radius, are denoted by the left and right blue lines. The red and green curves correspond to the mode size in the horizontal and vertical directions respectively.

A plot of the mode size in the telescopic resonator is shown in Figure 3.3:

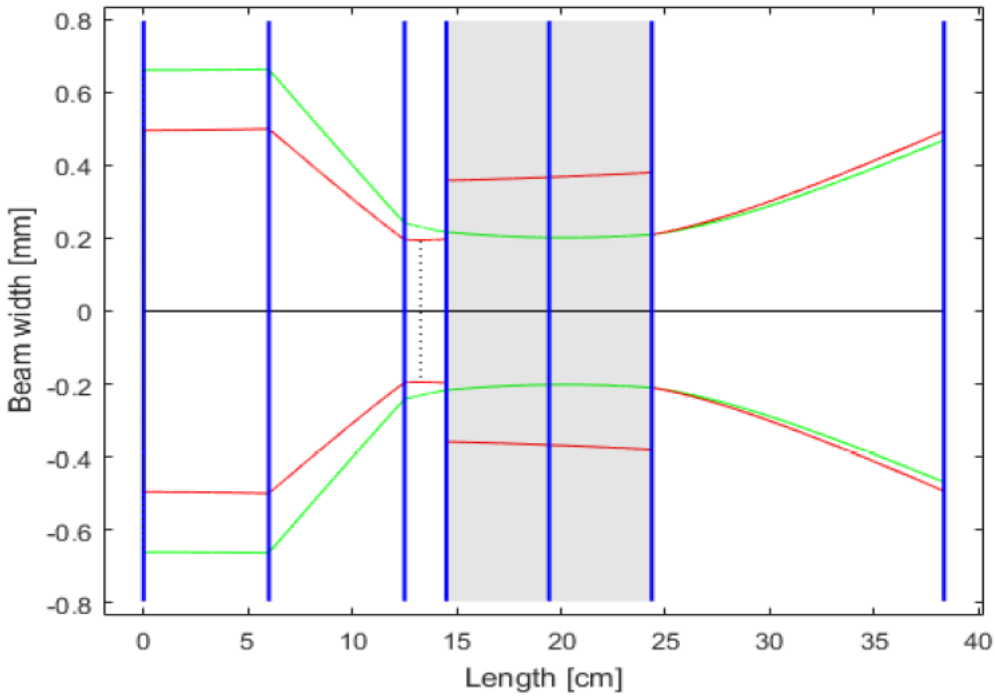

FIGURE 3.3: Plot of the predicted laser mode in a telescopic resonator for the long slab. From left to right, the components are the flat HR mirror, $f = +100$ mm lens, $f = -50$ mm lens and OC mirror. The dotted line designates the location of the horizontal beam waist.

It is apparent from Figure 3.2 that the beam in the simple symmetric resonator is collimated only within the slab. Figure 3.3 shows that a collimated region for the Pockels cell can be obtained using a telescope. Note the larger size of the mode near the HR mirror, where the Q-switch would be placed, compared to that in Figure 3.2.

3.2.3 Resonator stability

The dynamic stability of a laser resonator can be inferred from the half-trace value of the resonator ABCD matrix [90]:

$$-1 < \frac{1}{2}(A + D) < 1 \tag{3.2}$$

For maximum stability, the half-trace should be closer to 0 than ± 1. The mode size in the slab will then be relatively insensitive to the positioning of lenses along the optical axis as well as changes from thermal lensing within the slab.

Different resonator dimensions were trialled. In instances where the half-trace of the resonator ABCD matrix was predicted to be very close to 1, the laser experienced significant power fluctuations.

The stability parameters for the telescopic resonator using the long slab, shown in Figure 3.3, were 0.88 in the horizontal direction and 0.60 in the vertical direction.

3.2.4 Optical components

All cavity mirrors were sourced from Altechna (Vilnius, Lithuania), each 12.7 mm in diameter. They all had curvature radii of either 20 cm or 30 cm, and a scratch-dig specification of 20/10 with λ/10 surface figure (λ = 633 nm). Different coatings resulted in various reflectivities at the anticipated lasing wavelengths of 1617 nm and 1645 nm; the nominal reflectivity values below were guaranteed to be within ±2%. Their flat sides were coated to be anti-reflective. The mirrors used are listed in Table 3.1:

Mirror	**Curvature radius**	**Reflectivity**
Flat-flat	Flat	HR (R > 99.6%)
Plano-concave	200 mm	R = 90%
Plano-concave	200 mm	R = 80%
Plano-concave	200 mm	R = 60%
Plano-concave	200 mm	R = 40%
Plano-concave	300 mm	R = 90%
Plano-concave	300 mm	R = 80%
Plano-concave	300 mm	R = 60%
Plano-concave	300 mm	R = 40%

TABLE 3.1: The inventory of mirrors available for the resonator testing.

The reflectivities of a sample of the mirrors were measured using the 1645 nm laser output as a probe beam. All were found to be accurate to within 1% of the nominal value.

Uncoated negative and positive spherical lenses of various sizes and focal lengths were ordered from CVI Laser Optics. The BK7 substrates were AR-coated for 1.63 μm by BAE Systems Australia. These lenses are listed in Table 3.2:

Lens	Nominal focal length	Diameter
Plano-concave	–30 mm	12.7 mm
Plano-concave	–50 mm	15.0 mm
Plano-concave	–100 mm	25.4 mm
Plano-convex	+50 mm	25.4 mm
Bi-convex	+75 mm	25.4 mm
Plano-convex	+100 mm	25.4 mm
Plano-convex	+200 mm	25.4 mm

TABLE 3.2: The inventory of lenses available for use in the telescopic resonator. The lens scratch-dig and surface figure specifications were 10/5 and λ/10 (λ = 633 nm).

3.2.5 Telescopic resonator alignment

The compact nature of the telescopic resonator and small clear aperture of some components required careful alignment of the resonator components. Recall that the slab nose dimensions were based on the refraction angles at 1645 nm (calculated in §2.3.2). The laser mode is refracted at the Brewster-angled faces on the CPFS and thus its "V" shaped path depends on the refractive index of the slab. Fortunately, the refractive index of YAG is almost independent of wavelength in the infrared region (see Appendix F), dropping from 1.829 at 633 nm to 1.813 at 1645 nm. This meant that a HeNe laser beam could be used for initial resonator alignment. Nevertheless, the separation half angle of the beam from the slab was 11.8° at 633 nm but 12.8° at 1645 nm. Thus, after placing the mounts holding optical components and using HeNe back-reflections to help with positioning, optimal alignment required further fine angular and positional adjustments.

The laser resonator was assembled and aligned using the following steps, maximising the output power at every stage:

(1) Align a simple symmetric resonator with two curved mirrors of 20 cm radius of curvature (HR and R = 90% OC), using a HeNe beam (- -) and pinhole as a guide to see the back-reflection from the HR mirror, as shown below:

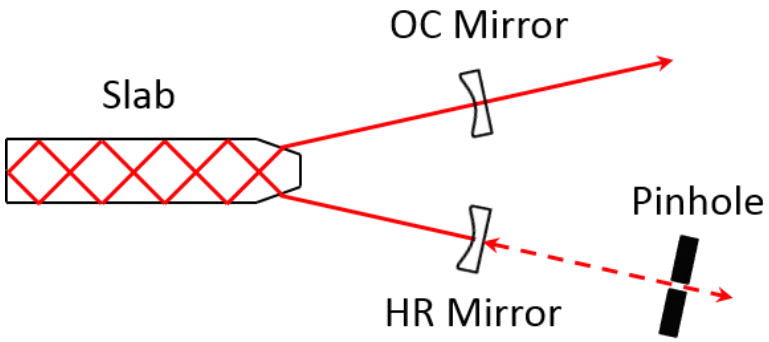

(2) Adjust the angular orientation of the mirrors to achieve lasing at 1.6 μm.

(3) Modify the resonator to a simple telescopic resonator by replacing the curved HR mirror with a flat HR mirror and an f = +100 mm plano-convex lens. Leave enough room to include the QWP and Pockels cell needed later for Q-switching:

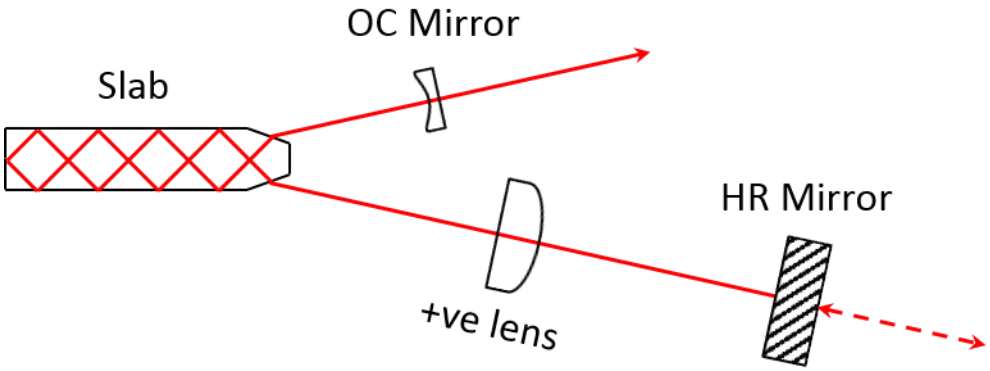

(4) Insert the $f = -50$ mm plano-concave lens into the resonator. While the position of the lens was crucial, the angle was not so important. The telescope spacing should slightly exceed the sum of the focal lengths of the lenses used in order to produce a beam waist inside the slab:

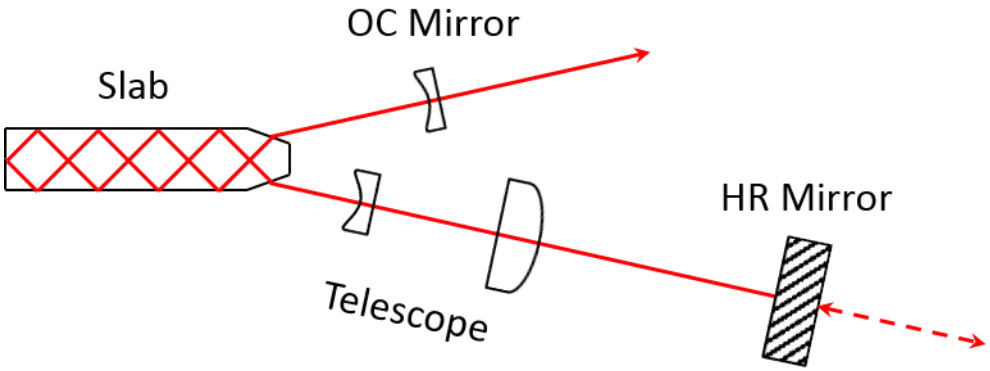

Once the telescopic resonator was assembled with the HR arm optimally aligned, output couplers of varying reflectivity could be easily interchanged by aiming the HeNe reflection from the output coupler near the middle of the slab Brewster face and making slight adjustments until maximum laser power was achieved.

The most sensitive parameter in the resonator was the telescope spacing, which could generally not vary by more than ± 5 mm without causing instability. The distance between the positive lens and flat HR mirror could be varied by up to 20 cm, with only a minimal change in telescope spacing required to compensate.

3.3 Gain-switched testing

The laser was initially aligned in gain-switched mode, with the pump diode output pulsed using the 12% duty cycle described in §2.4.4, to provide high peak pump powers. This had two important advantages: it permitted a high peak pump power while reducing the destabilising effect of unwanted heating. This was necessary because alignment in CW mode was impossible due to excessive heating in the slab from the >10 W of absorbed pump power. CW operation only worked if the laser was already aligned and could not be achieved from an un-aligned laser.

3.3.1 Parasitic lasing

At various stages during testing, parasitic lasing was encountered, in which the laser mode followed an incorrect path in the slab. This was a consequence of the high gain provided by the CPFS architecture and was characterised by lower than expected output power and sometimes by an incorrect exit angle of the laser beam. Parasitic lasing was diagnosed by performing the following tests:

Test 1: Block the HR mirror. Lasing should cease and output power should drop to zero.

Test 2: Misalign the OC mirror. Output power should steadily drop until reaching zero.

A lack of variation in output power with respect to tilting either cavity mirror angle indicated that the lasing mode was parasitic.

The problem was found to be a result of several slabs having an incorrect angle on one of the Brewster faces (16.5^{o} instead of 16.1^{o}). This increased the exit angle of the beam by nearly 1^{o}, resulting in optical component(s) being incorrectly positioned on the arm corresponding to that Brewster face. I eventually solved the parasitic lasing problem by dismantling the resonator, changing the angle of the HeNe alignment beam to match the correct mode, then reconstructing the resonator by repeating the steps in §3.2.5.

3.3.2 Effect of different output couplers

The telescopic resonator from §3.2.2 was used to investigate the output pulse energy vs. pump pulse energy for the long slab using R = 80%, 60% and 40% output couplers. The results are plotted in Figure 3.4.

The highest output power was produced by the long slab using the R = 80% output coupler. The highest slope efficiency of nearly 40% was achieved using the R = 60% output coupler. The increase in slope efficiency at high pump pulse energies is due to the elimination of re-absorption losses, as expected for a quasi-three-level gain medium.

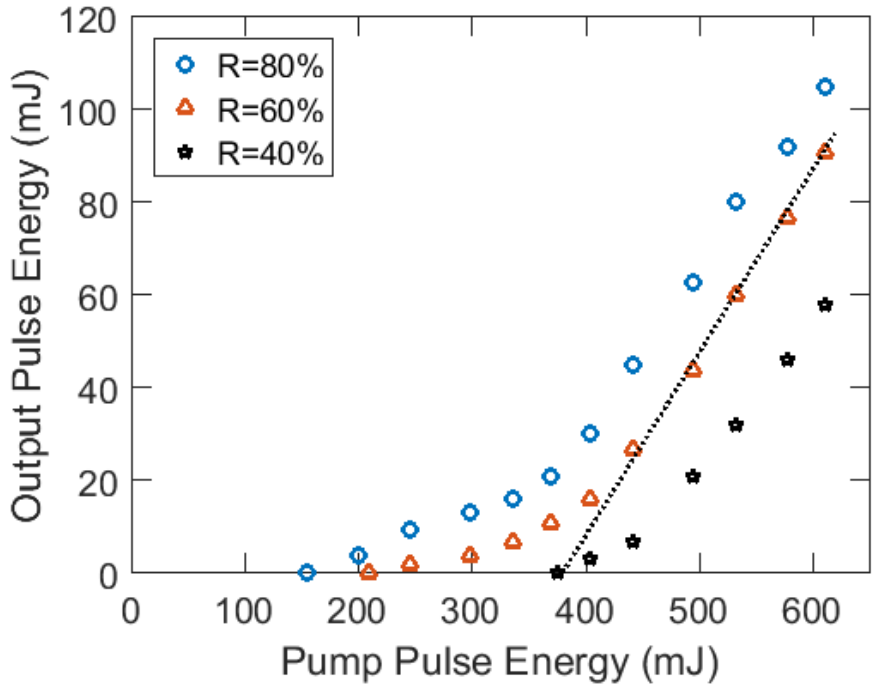

FIGURE 3.4: A plot of output pulse energy vs. pump pulse energy for the long slab. The dashed line represents the 40% slope efficiency with the R = 60% output coupler.

The threshold pump power vs. output coupler reflectivity is shown in Table 3.3:

OC reflectivity	90%	80%	60%	40%
Threshold power	15 W	16 W	21 W	37 W

TABLE 3.3: Threshold pump power (10 ms pulses) vs. OC reflectivity for the long slab.

As expected, the threshold pump power increased to overcome the overall resonator round-trip losses caused by the decrease in output coupler reflectivity.

A plot of output pulse energy vs. pump pulse energy for the short slab using R = 90%, 80%, 60% and 40% output couplers is shown in Figure 3.5:

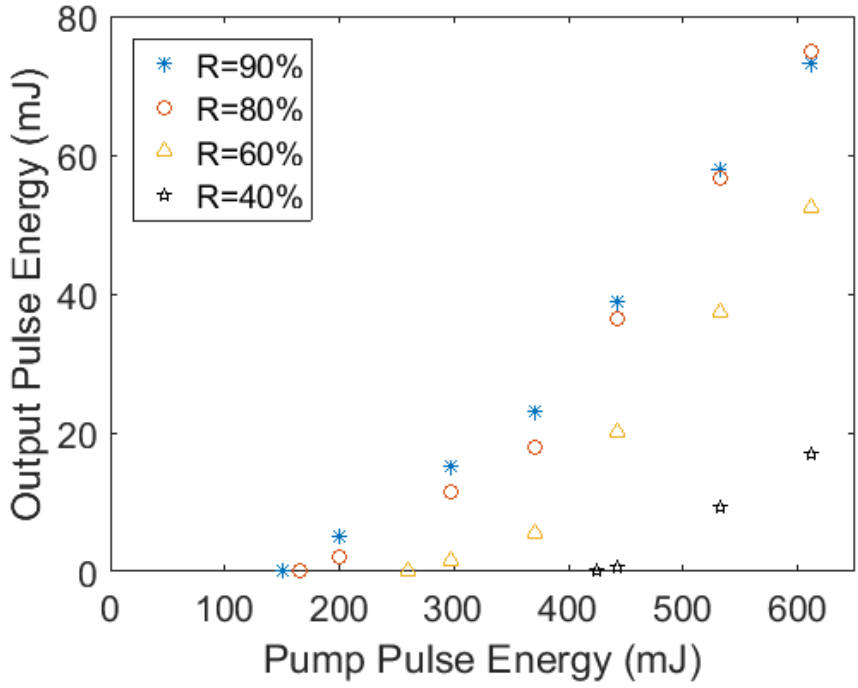

FIGURE 3.5: A plot of output pulse energy vs. pump pulse energy for the short slab.

The threshold pump power vs. output coupler reflectivity is shown in Table 3.4:

OC reflectivity	90%	80%	60%	40%
Threshold power	15 W	17 W	26 W	42 W

TABLE 3.4: Threshold pump power (10 ms pulses) vs. OC reflectivity for the short slab.

The output pulse energies vs. mirror reflectivity for 600 mJ pump pulse energy using output couplers of R = 90%, 80%, 60% and 40% are shown below in Table 3.5:

OC reflectivity	90%	80%	60%	40%
Short slab	73 mJ	75 mJ	53 mJ	17 mJ
Long slab	96 mJ	105 mJ	90 mJ	58 mJ

TABLE 3.5: The maximum output pulse energy vs. OC reflectivity for both slabs.

The optimum output coupling can be estimated by plotting these results, as shown in Figure 3.6, which indicates that the optimum reflectivity is 80% for gain-switched lasing.

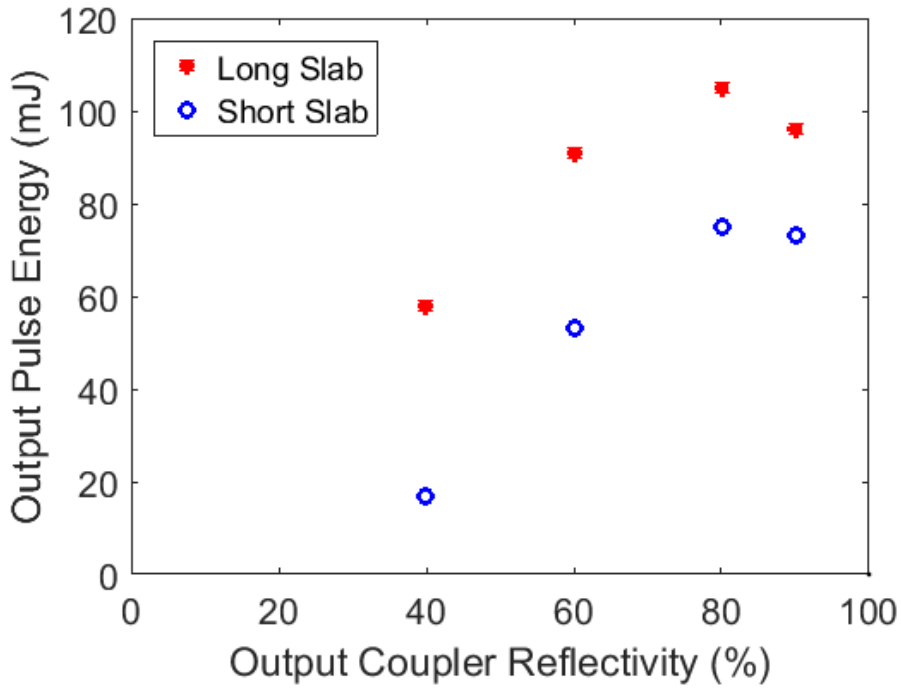

FIGURE 3.6: Output from 600 mJ pump pulse energy for various mirror reflectivities.

The optimum output coupler reflectivity for maximum laser power and efficiency decreases as the pump power increases. The effect of the higher gain of the long slab on the laser efficiency is particularly apparent for the R = 40% output coupler.

3.4 Intra-cavity loss

The efficiency of a laser can be considerably reduced by intra-cavity losses. Defects in the crystal can cause bulk scatter loss while surface polishing imperfections result in TIR scatter loss, increasing the threshold power and reducing slope efficiency. Slab cleanliness was also a critical contributing factor to the laser's operation, as any dust on the slab surfaces would increase losses.

3.4.1 Slab losses

Ideally, a TIR bounce should be 100% reflective. However, surface irregularities such as scratches and dust introduce losses. Even careful polishing techniques cannot eliminate micro scratches on the slab surfaces. These unavoidable surface imperfections cause a scatter loss of 0.1 – 0.2% at each bounce [91]. Assuming an average of 0.15% loss per bounce, the 35 bounces on the long slab can be expected to give 5% loss.

This surface scatter loss produces bright spots on the slab surfaces where the HeNe alignment beam has undergone TIR, as shown in Figure 3.7:

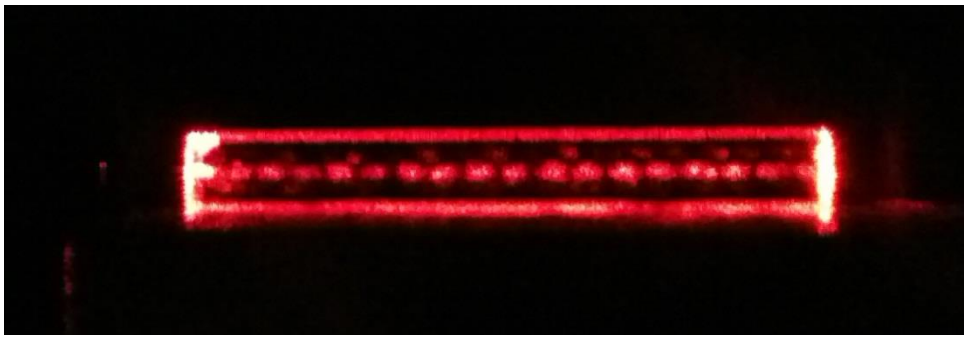

FIGURE 3.7: A side view of the slab with the HeNe beam passing through it. The bright spots show the losses from the TIR bounces of the beam in the slab. The location and number of these spots can be used to assist alignment.

The bulk scatter coefficient for YAG has been reported as 0.002 cm^{-1} [91]. The physical path length of the laser beam in the long slab was nearly 10 cm, giving an overall bulk scatter loss per pass of 2%. The total single pass loss of the slab was thus estimated at 7%.

I determined the single pass loss by measuring the attenuation of a collimated 1319 nm probe beam through the slab, as this wavelength does not correspond to any transition between Er:YAG energy levels. This was done by comparing the voltage registered by a photodetector before and after the slab, using the setup shown in Figure 3.8.

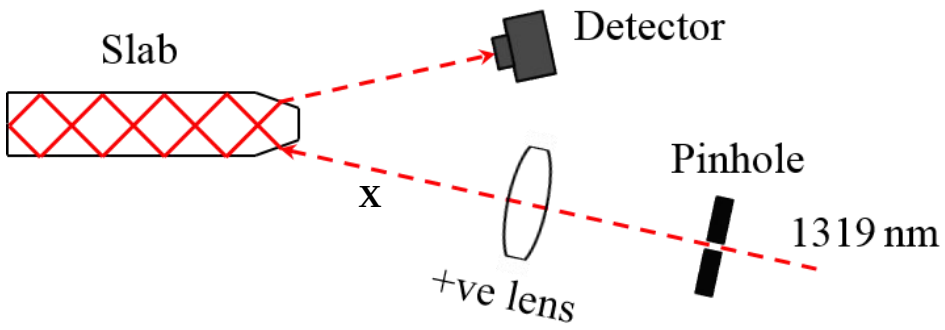

FIGURE 3.8: Measurement of the single pass loss of the slab using a photodetector to compare voltage readings from a 1319 nm beam before (**X**) and after traversing the slab.

The result of the measurement confirmed that the slab loss for a single pass was 7%, and therefore the round-trip loss due to the slab alone, δ_S, was close to 14%.

3.4.2 Component losses

Other intra-cavity losses come from imperfect anti-reflective coatings on lenses and the Q-switching components, which are up to 99.9% transmitting, as well as the slight transmission through the HR mirror. For example, the latter had a nominal reflectivity of $R_{HR} > 99.6\%$. The round-trip loss due to these components was estimated to be 1%, meaning that the vast majority of the resonator loss was due to the slab.

3.5 Comparison of laser performance with theory

A comparison between the laser performance and theoretical prediction, specifically the threshold power and slope efficiency once re-absorption is overcome, is outlined below. The first consideration is the effective transfer of pump energy to the slab.

3.5.1 Pump coupling efficiency

Both the lens duct and slab were uncoated. The Fresnel reflection loss factor R_l for a given angle of incidence and transmission at an interface is given by [92]:

$$R_l = \left(\frac{n_1 \cos\theta_1 - n_2 \cos\theta_2}{n_1 \cos\theta_1 + n_2 \cos\theta_2}\right)^2 \tag{3.3}$$

where n_1 and n_2 are the initial and final refractive indices and θ_1 and θ_2 are the incident and transmission angles respectively. The values of R_l for several incident angles at an interface are listed in Table 3.6:

Interface	0° incident	15° incident	30° incident
Lens duct entry	0.04	0.044	0.057
Lens duct exit	0.04	0.05	0.105
Slab entry	0.085	0.09	0.113

TABLE 3.6: Fresnel reflection loss factors for the pump light at different interfaces.

The transmission coefficient through the lens duct into the slab, η_C, is equal to the average product of the three transmission factors, $T_l = 1 - R_l$. I estimated this to be around 0.83 because most of the rays will have shallow incident angles after undergoing refraction at the interfaces, based on the ZEMAX simulations from §2.4.5. For example, a 15° angle at each interface gives T_l = (1 – 0.044) x (1 – 0.05) x (1 – 0.09) ≈ 0.826.

3.5.2 Threshold power

The lasing threshold was estimated by setting the round-trip gain to 1 and solving [93]:

$$R_{HR}Re^{2g_0L}(1-\delta_S)\prod_i (T_i)^2 \geq 1 \tag{3.4}$$

where R_{HR} is the reflectivity of the HR mirror, R is the reflectivity of the OC mirror, L is the path length of the beam in the gain medium, δ_S the total slab loss and T_i is the one-way transmission of the i^{th} optical element/component. The AR coatings on the components should ensure T_i is nearly 1. The component losses can be rolled into one round-trip transmission factor of the resonator:

$$T_{rt} = R_{HR}(1-\delta_S)\prod_i (T_i)^2 \tag{3.5}$$

and the equation rewritten as

$$T_{rt}Re^{2g_0L} = 1 \tag{3.6}$$

where g_0 is the small signal gain, approximated by:

$$g_0 \cong \sigma_e\big((f_1+f_2)N_2 - f_1N_C\big) \tag{3.7}$$

where σ_e is the stimulated emission cross section and the variables f_1, f_2, N_2 and N_C were defined in Chapter 2. We have assumed that the entire population occupies the two lowest energy levels. Eqn. (3.6) can be re-arranged to

$$g_0 \cong \frac{1}{2L}\log_e\left(\frac{1}{T_{rt}R}\right) \tag{3.8}$$

Combining Eqns. (3.7) and (3.8) allows the threshold N_2 value (N_T) to be determined:

$$N_T = N_C\left(\frac{f_1}{f_1 + f_2}\right) + \frac{1}{2\sigma_e L(f_1 + f_2)}\left(\log_e\left(\frac{1}{T_{rt}R}\right)\right) \tag{3.9}$$

This upper level threshold population must be maintained despite spontaneous emission and up-conversion. The pump rate, W_pN_1, must equal or exceed the depletion of the upper level population:

$$W_pN_1 = \frac{N_2}{\tau_f} + 2C_{up}N_2^2 \tag{3.10}$$

where C_{up}, the up-conversion parameter of 0.5% Er:YAG was 3.6 x 10^{-18} cm^3 s^{-1}, assuming a value directly proportional to the doping concentration.

The rate at which pump photons must be absorbed by the slab is given by $V_pW_pN_1$, where V_p is the pumped volume of the slab. The threshold power is then given by:

$$P = \frac{hc\left(V_pW_pN_1\right)}{\lambda_p F_{abs}\eta_h} \tag{3.11}$$

where F_{abs} represents the estimated fraction of launched pump power absorbed by the slab, as defined in Eqn. (3.12), and η_h is the proportion of pump power that overlaps with the laser mode in the pumped region. Since 90% of the pump light illuminates the 0.6 mm high pumped region, η_h can be estimated at between 0.9 and 1.

The pump absorption was estimated at around 62% for the short slab and nearly 80% for the long slab based on experiments, although this was difficult to determine due to the wide divergence angle of pump light after exiting the Brewster angled faces of the slab. This can be seen from the Zemax simulation of the pump system in Figure 2.16.

For simplicity, the coupling and absorption factors were combined into one factor:

$$F_{abs} = \eta_C \eta_{abs} \tag{3.12}$$

where F_{abs} represents the estimated fraction of launched pump power absorbed by the slab, taking into account the Fresnel losses of the lens duct and slab end face.

The predicted lasing thresholds for the different output couplers were calculated by substituting the values of the parameters listed below into Eqn. (3.11). The parameters for the long 0.5% Er:YAG slab are shown in Table 3.7:

Parameter	**Symbol**	**Value**
Er^{3+} concentration	N_C	7.0×10^{19} cm^{-3}
Up-conversion parameter	C_{up}	3.6×10^{-18} cm^3 s^{-1}
Slab pumped volume	V_p	0.042 cm^3
Optical gain length	L	9.85 cm
Pump absorption fraction	F_{abs}	0.67
Round-trip transmission	T_{rt}	0.85

TABLE 3.7: The values of parameters for the long 0.5% Er:YAG slab.

The measured and predicted lasing thresholds for the long slab using the different output couplers are:

OC reflectivity	90%	80%	60%	40%
Measured threshold	15 W	16 W	22 W	37 W
Theoretical threshold	15 W	17 W	23 W	32 W

TABLE 3.8: The measured and predicted laser threshold power with the long slab.

The parameters for the short 0.5% Er:YAG slab are shown in Table 3.9:

Parameter	Symbol	Value
Er^{3+} concentration	N_C	7.0×10^{19} cm^{-3}
Up-conversion parameter	C_{up}	3.6×10^{-18} cm^3 s^{-1}
Slab pumped volume	V_p	0.025 cm^3
Optical gain length	L	5.88 cm
Pump absorption fraction	F_{abs}	0.52
Round-trip transmission	T_{rt}	0.9

TABLE 3.9: The values of parameters for the short 0.5% Er:YAG slab.

The measured and predicted lasing thresholds for the short slab using the different output couplers are:

OC reflectivity	90%	80%	60%	40%
Measured threshold	15 W	17 W	26 W	42 W
Theoretical threshold	14.5 W	17.5 W	26.5 W	42 W

TABLE 3.10: The measured and predicted laser threshold power with the short slab.

3.5.3 Slope efficiency

The maximum achievable slope efficiency η_{slope} is given by [94]:

$$\eta_{slope} = \eta_C \eta_{abs} \eta_S \left(\frac{\ln\left(\frac{1}{R}\right)}{\ln\left(\frac{1}{R}\right) + \delta} \right) \tag{3.13}$$

where η_C is the proportion of pump light transmitted through the lens duct and into the slab, η_{abs} is the proportion of pump power absorbed in the slab and η_S is the Stokes factor defined in §2.2.2. The final term depends on the output coupler reflectivity, R, and the

total resonator intra-cavity loss factor, δ. This shows that intra-cavity loss is most detrimental to slope efficiency when the output coupler reflectivity is higher.

The predicted slope efficiencies from the various output couplers were calculated using Eqn. (3.13) and compared with the measured values for the long slab in Table 3.11 and the short slab in Table 3.12:

OC reflectivity	90%	80%	60%	40%
Measured slope	25%	36%	40%	36%
Theoretical slope	25%	36%	46%	52%

TABLE 3.11: The measured and predicted laser slope efficiency for the long slab.

OC reflectivity	90%	80%	60%	40%
Measured slope	20%	24%	22%	20%
Theoretical slope	20%	27%	33%	35%

TABLE 3.12: The measured and predicted laser slope efficiency for the short slab.

These predicted threshold power values compare reasonably well with the measured figures, considering the likely errors in the parameters from Tables 3.7 and 3.9. The larger discrepancy with the threshold for the long slab using the R = 40% output coupler was most likely due to a lower pump absorption at that power level. The measured slope efficiencies were lower than expected, particularly for the R = 40% output couplers.

3.6 Chapter summary

This chapter described the development and testing of the telescopic-resonator lasers that will be used for Q-switching and cavity-dumping in the following chapters. The observed pump thresholds and slope efficiencies from gain-switched testing using different output couplers were found to be in reasonable agreement with those predicted using a simple rate-equation model. An optical to optical efficiency of over 17% was obtained using the long slab and R = 80% output coupler. Importantly, the lasers could operate with low reflectivity output couplers, indicating that they had large small signal gains as required for producing short duration Q-switched pulses. The adaption of these lasers for Q-switching and subsequent results will be discussed in the next chapter.

Chapter 4: Q-switched Er:YAG laser

4.1 Introduction

The previous chapter described the construction and testing of a CPFS Er:YAG laser. This laser produced high energy pulses of several milliseconds duration in gain-switched mode. However, the laser had to be adapted for Q-switching to produce pulses with nanosecond order durations required for a laser range-finder. Section 4.2 describes the resonator design, construction and output coupler considerations. Section 4.3 explains the principle of Q-switched operation and summarises the trials and results from the prototype Q-switched laser using the long slab. The problem of intra-cavity damage is discussed in Section 4.4, along with measures taken to reduce this. The steps taken to reduce the resonator size and pulse duration are discussed in Section 4.5. A description of the final version of the Q-switched laser that used the short slab and the results are presented in Section 4.6. Mathematical analysis of pulse duration versus pulse energy is covered in Section 4.7. All findings are summarised in Section 4.8.

The Q-switched laser results reported in this chapter are also provided in the paper *"Short-pulse actively Q-switched Er:YAG lasers"* that was published in Optics Express. A copy of that paper is included in Appendix A.

4.2 Resonator design

Our first Q-switched laser was based on the telescopic resonator described in Section 3.2. A schematic of the completed laser resonator is shown in Figure 4.1:

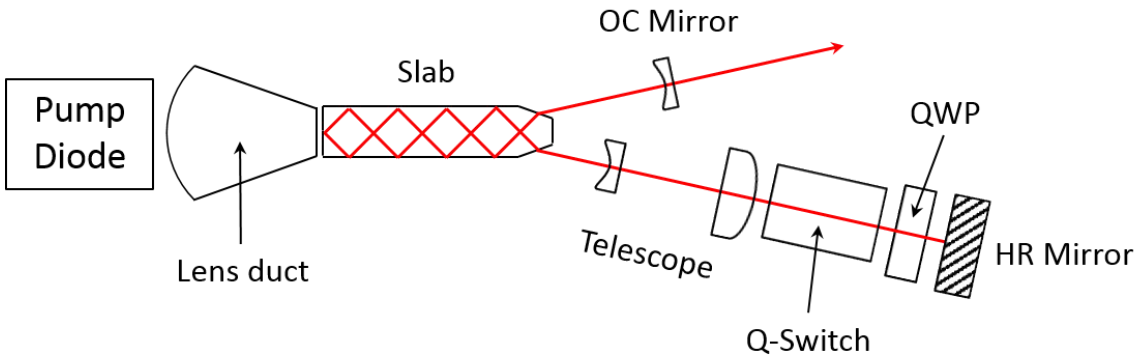

FIGURE 4.1: Schematic of the Q-switched laser.

The telescope consisted of a $f = -50$ mm plano-concave lens and a $f = +100$ mm plano-convex lens, separated by about 65 mm to adjust the size of the laser mode in the slab. This expanded the beam and reduced the power density on the Q-switch, an important factor in reducing the possibility of damage to the surfaces of the Q-switch. The Q-switch and quarter-wave plate (QWP) were both AR-coated for 1.6 μm.

This resonator was successfully tested in gain-switched mode and found to be stable over a period of several minutes (i.e. thousands of pulses), which indicated that thermal lensing was not a serious problem due to the relatively low average pump power.

4.2.1 Resonator model

The prototype Q-switched resonator was modelled using the MATLAB code from §3.2.2. A plot of the predicted mode size in the resonator is shown in Figure 4.2:

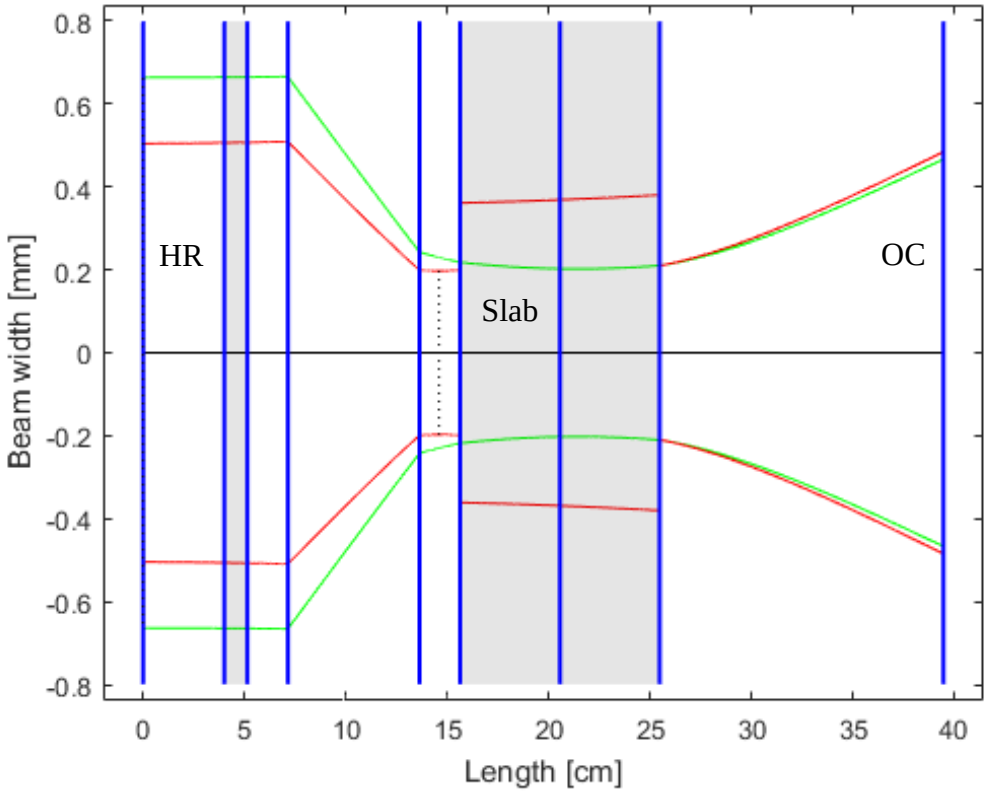

FIGURE 4.2: Simulation of the laser mode in the prototype Q-switched laser. From left to right, the optical components are the flat HR mirror, the Pockels cell, f = +100 mm lens, f = –50 mm lens, slab and OC mirror with 20 cm radius of curvature. The QWP is not depicted as it has flat surfaces and negligible thickness. The red and green lines represent the horizontal and vertical dimensions of the laser mode respectively.

4.2.2 The Q-switch

The Q-switch was a Rubidium Titanyl Phosphate ($RbTiOPO_4$ or RTP) Pockels cell from Raicol Crystals with the general schematic shown in Figure 4.3. Applying a voltage to the RTP crystals induces birefringence, allowing polarisation rotation to occur. RTP has the advantage of not being hygroscopic, unlike other electro-optical crystals such as BBO, and does not suffer from piezoelectric ringing [95][96].

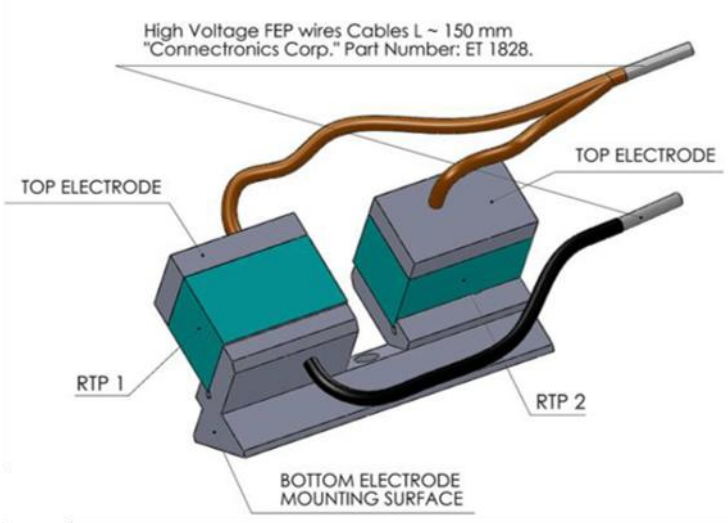

FIGURE 4.3: Schematic of an RTP Q-switch used in the Q-switched laser [97]. The two crystals are mounted 90° apart to compensate for thermally induced birefringence.

Two different Q-switches were used during this project. The first was 25 mm long and had a quarter-wave voltage of 1.4 kV at 1.63 μm, but was too bulky from being mounted under a Perspex cover. The second had a higher quarter-wave voltage of 2.5 kV, but was more compact. The optical faces of both Q-switches were AR-coated for 1645 nm.

4.2.3 Resonator assembly

The resonator was aligned in several stages, optimising output power at every step:

(1) Two curved mirrors (HR and R = 90% OC) were aligned to achieve lasing, using the transmission of a HeNe beam (- -) through the slab as a guide. The mirrors were placed on the beam paths as shown:

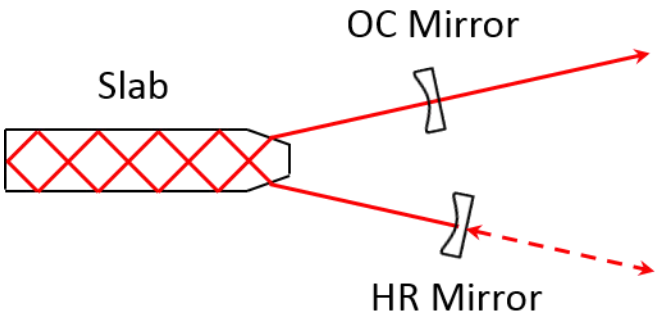

(2) The curved HR mirror was replaced with a flat HR mirror and plano-convex lens with +100 mm focal length, using the back reflections of the HeNe beam from both components as a guide. The transverse position of the lens was critical as incorrect positioning would deflect the beam, reducing the power. The angle of the lens was less important. The alignment was optimised by leaving the OC mirror untouched but concurrently adjusting lens position and HR mirror angle:

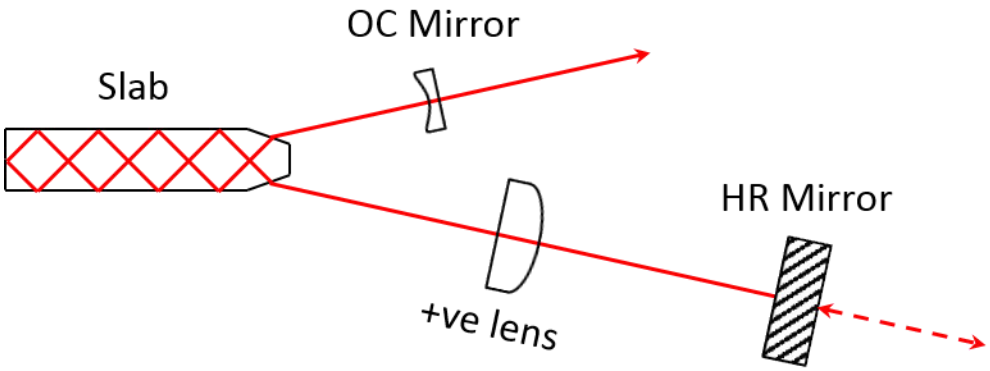

(3) A plano-concave lens with a focal length of –50 mm was inserted into the resonator and the telescope spacing adjusted to maximise power. The position of this lens was also critical while the angle was less important. The best way of optimising the negative lens position was by mounting it on a 3-axis stage, allowing translation in every direction:

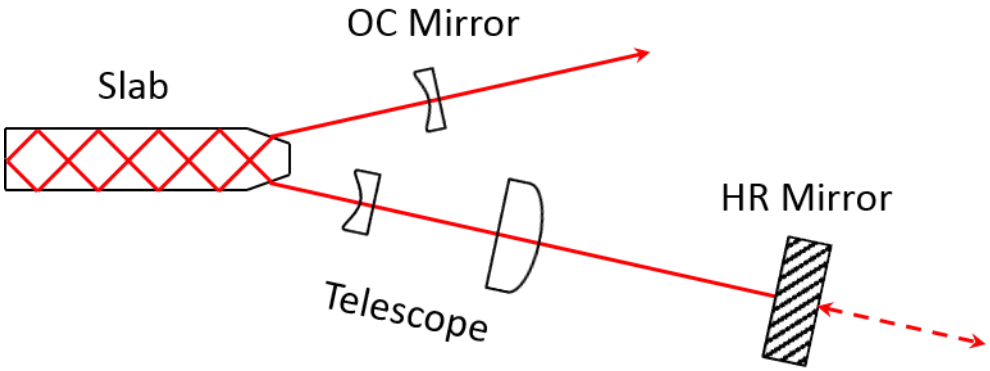

(4) Finally, the Q-switch and QWP were positioned to minimise power loss, with the QWP rotated to maximise the power in the gain-switched pulse:

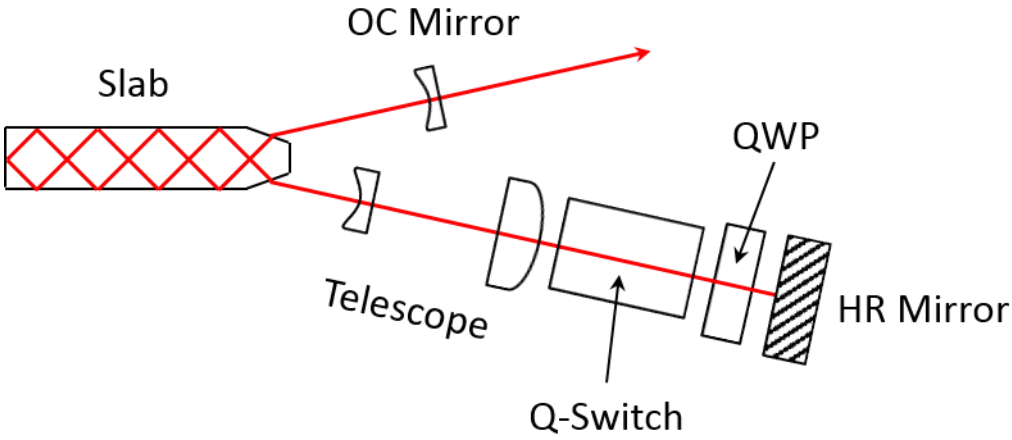

A picture of the prototype Q-switched laser is shown in Figure 4.4:

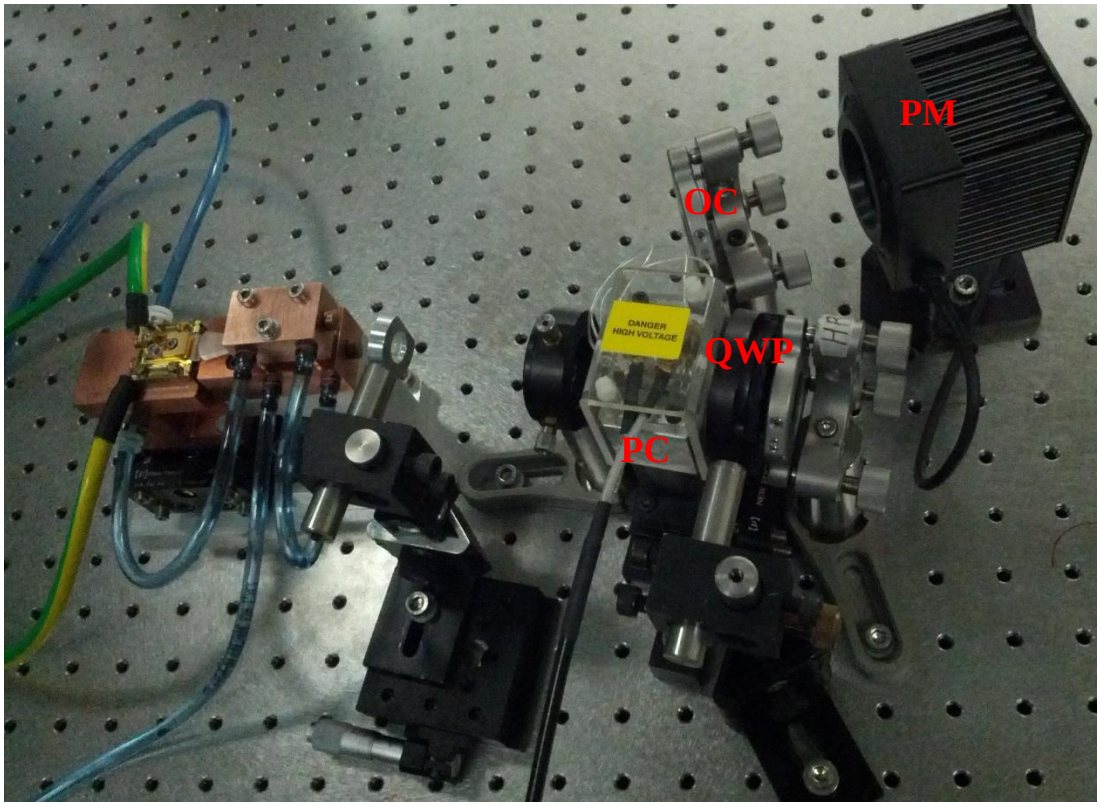

FIGURE 4.4: The Q-switched test laser. The pump assembly is on the left side. Note the output coupler (OC), Q-switch (PC), quarter-wave plate (QWP) and power meter (PM).

4.2.4 Output coupler

The maximum intra-cavity power P_{cav} in a standing wave resonator depends on the output coupler reflectivity according to the equation [98]:

$$P_{cav} = P_{out}\left(\frac{1+R}{1-R}\right) \tag{4.1}$$

where the $(1 + R)$ factor is due to the overlapping beams. Thus the maximum intra-cavity power always exceeds the laser's output power by the factors shown in Table 4.1:

OC reflectivity	90%	80%	60%	40%
P_{cav}/P_{out} ratio	19	9	4	2.33

TABLE 4.1: Ratio of intra-cavity power to output power for the various output couplers.

To reduce the likelihood of damage being inflicted on intra-cavity components, it is clearly desirable to obtain energetic laser pulses with a low reflectivity output coupler. While the highest energy gain-switched pulses were achieved using an 80% reflective output coupler, this could be hazardous to the laser components when Q-switching at anything other than very low pulse energies. With that in mind, most of the Q-switching tests were performed using an $R = 40\%$ output coupler.

4.3 Initial Q-switching trials

4.3.1 Principle of Q-switched operation

For Q-switching, the QWP is rotated by 45^o relative to that used for gain-switched pulsing. When the slab is pumped, no voltage is applied to the Pockels cell. A double pass of the Q-switch and QWP thus rotates the polarisation by 90^o. The high intra-cavity loss of σ-polarisation from the slab Brewster faces prevents lasing and allows a large population inversion to build up in the gain medium.

Applying the quarter-wave voltage to the Pockels cell immediately after the end of the pump pulse means that the Q-switch and QWP collectively function as a half-wave plate; a double pass cancels out the effect of the QWP, preserving the π-polarisation and minimising the intra-cavity loss. The high round-trip gain now allows lasing to occur and a giant pulse builds up exponentially from spontaneous emission. As the intra-cavity power increases, the population inversion decreases, thereby reducing the gain. The amplitude of the pulse is maximised when the instantaneous round-trip gain is equal to one. Thereafter the loss exceeds the gain and the pulse amplitude starts to decay. The intra-cavity power "leaks" out through the output coupler.

To safely test the Q-switched laser, I initially adjusted the pump power to approximately equal the threshold for gain-switched lasing. After applying the quarter-wave voltage to the Q-switch, a slight increase in the pump power produced long duration Q-switched laser pulses.

The Q-switched pulses were measured using a high-speed photodetector positioned behind the flat HR mirror to monitor the power leakage. It was observed that the build-up time was roughly an order of magnitude greater than the pulse duration.

4.3.2 Multiple pulsing

An early problem I encountered was obtaining two or even three Q-switched pulses for each pump pulse. This was caused by a slow rise time on the Q-switch driver, taking 1 μs to reach the quarter-wave voltage, which in turn caused the Pockels cell to take too long to switch the resonator Q from low to high. This allowed the first pulse to develop and decay via gain depletion, and then further loss reduction allowed the second pulse to develop which depleted the gain again, and so on. The result is shown in Figure 4.5:

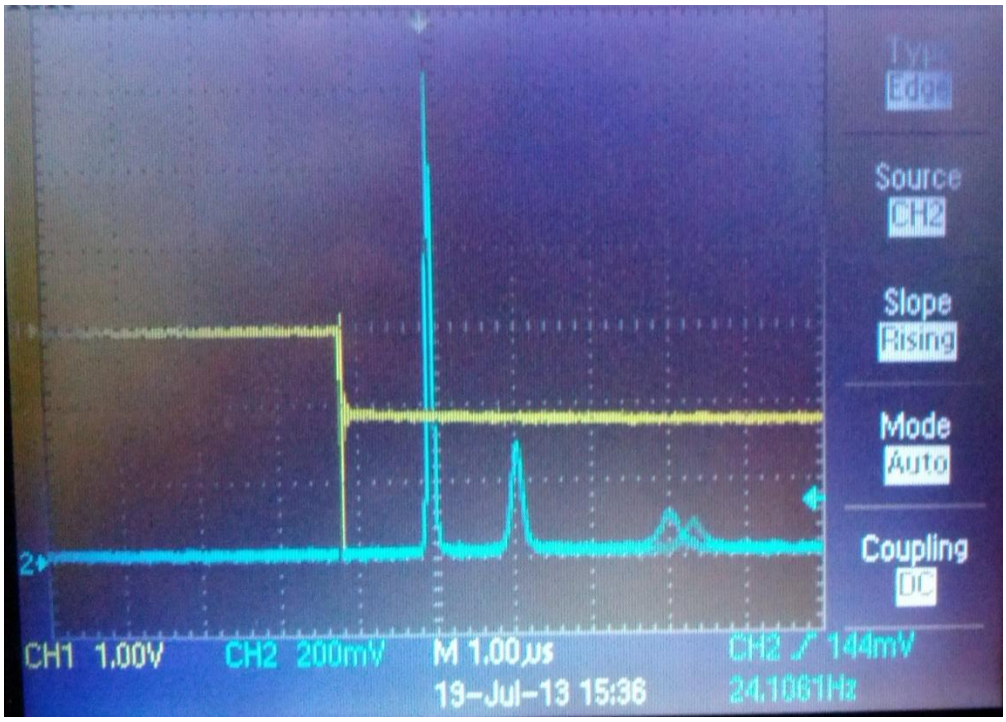

FIGURE 4.5: Three Q-switched pulses (blue) produced from a single pump pulse (yellow).

We solved this problem by replacing the HV driver with a HVP-5LP Quantum Technology pulse generator that had a 12 ns rise-time, which was more than an order of magnitude less than the pulse build-up time.

The early Q-switching tests using 60 W peak pump power (600 mJ pump pulse energy) were able to produce 185 mW average output power (15.5 mJ output pulse energy), corresponding to an optical to optical efficiency of just over 2.5%. The pulses had a minimum FWHM pulse duration of < 25 ns where the temporal resolution was limited by the 5 ns rise time of the photodetector. This was > 600 kW peak output power.

4.3.3 Preliminary observations

A plot of inverse pulse duration vs. pulse energy for different resonator lengths using the R = 40% OC is shown in Figure 4.6:

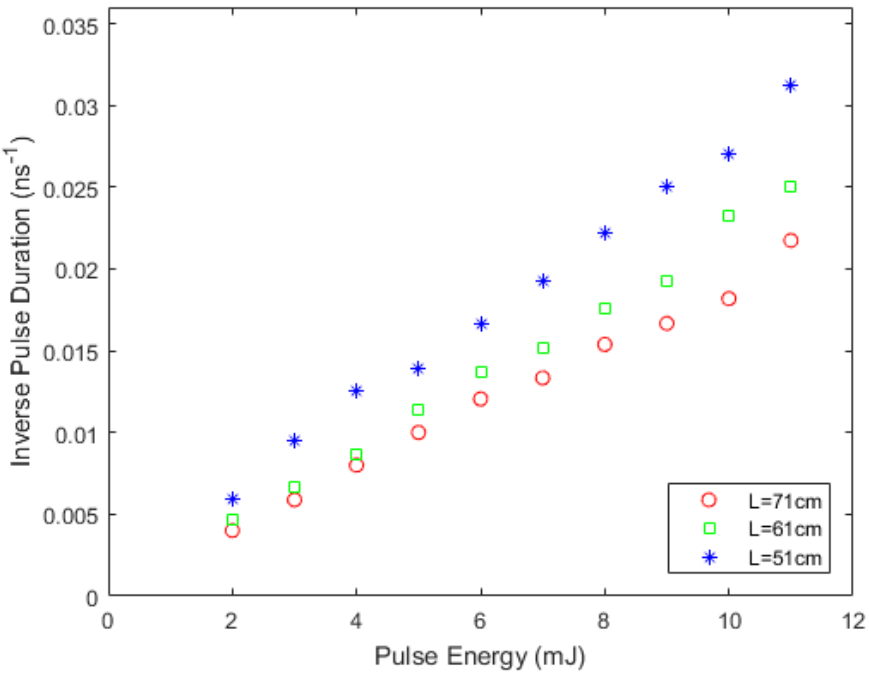

FIGURE 4.6: Inverse pulse duration vs. pulse energy for different resonator lengths.

These results show a roughly inverse relationship between pulse duration (τ) and energy (E) for a given resonator, while the pulse duration was almost directly proportional to the resonator round-trip time as expected [99]. This is summarised by the relation:

$$\tau \propto \frac{t_r}{E} \tag{4.2}$$

where t_r is the round-trip time of the resonator and E is the output pulse energy.

Increasing the pump energy produces a greater population inversion; once lasing is allowed to occur, the higher gain reduces the build-up time. As the pulse builds up faster, the population inversion depletes more rapidly, reducing the pulse duration.

4.4 Slab damage

The early Q-switching tests at full power (600 mJ pump pulses) produced 15.5 mJ output pulses, with a minimum pulse duration of < 25 ns. Sustained Q-switched lasing at full power, however, resulted in optical damage and a marked reduction in output power. While the AR-coated surfaces of the negative lens were predicted to be most vulnerable, the damage was found to be solely on the slab surface where TIR bounce(s) had occurred. A photo of the slab damage and close-up view is shown in Figure 4.7:

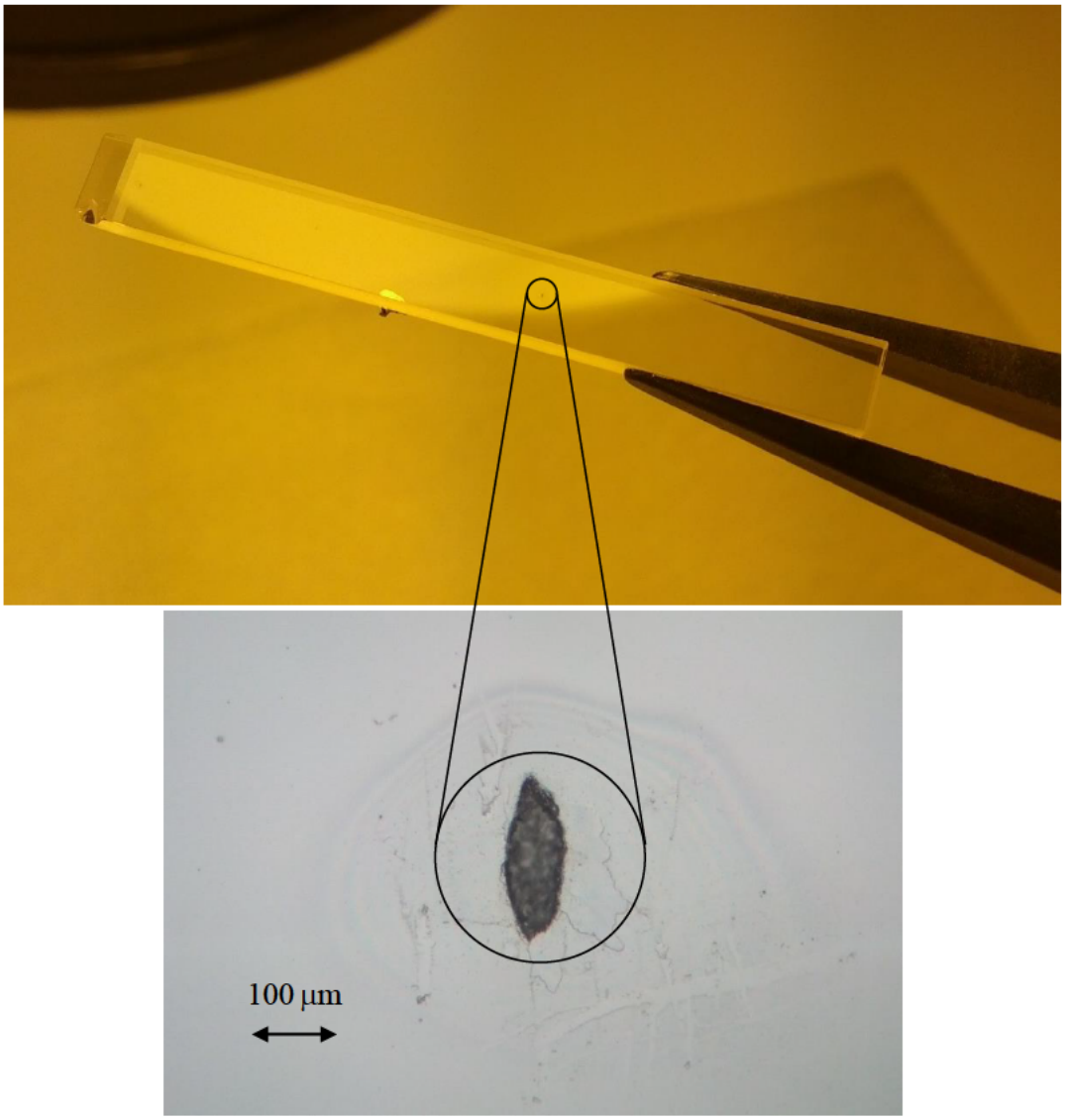

FIGURE 4.7: Slab surface damage caused by 15.5 mJ Q-switched laser pulses showing the damage spot (above) and zoomed in view (below) from a microscope.

4.4.1 Damage mechanism

In the short pulsed regime of 1–100 ns, the optical damage mechanism is most likely to be dielectric breakdown caused by the large electric field of the laser beam, as opposed to overheating which can occur for longer pulses and CW lasers [100].

The bulk damage threshold of YAG has been variously measured as being >1000 J/cm^2 for 10 ns pulses at 1064 nm [101]. The surface damage threshold is considerably lower, at around 100-150 J/cm^2 [102], although the presence of scratches or surface contamination can lower this further [103]. The fact that the CPFS geometry relies on the laser beam doubly overlapping on itself in those locations enhances the risk, but it could also have been a problem with the slab material and/or imperfect polishing creating micro scratches.

Presumably the combination of high intra-cavity power and overlapping fields in the CPF slab caused the damage spot in Figure 4.7. Further experiments with previously damaged and re-polished slabs indicated they had an even lower damage threshold.

4.4.2 Likelihood of damage

The likelihood of damage (LoD) index depends on the intra-cavity fluence of the pulse, along with the pulse duration and wavelength, as summarised by the relation:

$$\mathrm{LoD} \propto \frac{E}{\mathrm{A}\sqrt{\lambda\tau}}\left(\frac{1+R}{1-R}\right) \tag{4.3}$$

where E is the output pulse energy, A is the intra-cavity beam area, λ is the lasing wavelength and R is the output coupler reflectivity. The laser PRF is less important in the short-pulse regime due to the damage mechanism. Note that in the long-pulse regime, the likelihood of thermal damage will also increase in proportion to a higher PRF.

Several wavelength dependences have been reported: sometimes as inversely proportional [104][105], but also as the inverse square root [106], which is assumed here.

Eqn. (4.3) can be rewritten in terms of the peak output power P_{peak} as:

$$\text{LoD} \propto \frac{P_{peak}\sqrt{\tau}}{\text{A}\sqrt{\lambda}}\left(\frac{1+R}{1-R}\right) \tag{4.4}$$

As suggested earlier, it is advantageous to use lower reflectivity output couplers and to attempt to lower both the pulse energy and duration to achieve the same peak power while reducing the risk of damage. For example, a 16 mJ, 16 ns pulse and a 4 mJ, 4 ns pulse have the same peak power, but the LoD index is twice as high for the 16 mJ pulse.

The overlapping beams near the slab surfaces combined with the intra-cavity scaling factor for the R = 40% output coupler increased the fluence by nearly an order of magnitude compared to the output pulse. For the 15 mJ, 23 ns pulses from the prototype Q-switched laser, the fluence is:

$$\frac{2E}{\text{A}}\left(\frac{1+\text{R}}{1-\text{R}}\right) = \frac{2 \text{ x } 15.5}{\pi(0.23 \text{ x } 0.4)} \text{ x } 2.33 = 25 \text{ J/cm}^2 \tag{4.5}$$

The areas of the elliptical spot on the TIR surfaces were calculated from the MATLAB simulation of the mode. Note that the mode area refers to the estimated average where the damage occurred, since the size varies inside the slab. While the figure calculated above is ostensibly less than the anticipated surface damage threshold, the dark damage spot suggests the presence of a dust particle. Subsequent damage spots appeared to be white, although there was no evidence that the damage thresholds were higher.

This experience showed that precautions were necessary when Q-switching at high power. Output pulse energy was subsequently restricted to less than 12 mJ and slab cleaning before laser head assembly was especially thorough. Eqn. (4.4) also shows that the LoD is decreased for a given peak power by reducing the pulse duration, which can be achieved by reducing the resonator round-trip time, as discussed in the next section.

4.5 Reducing the pulse duration

The Q-switched pulse duration is directly proportional to the photon round-trip time in the resonator, which in turn depends on the optical length of the resonator. Reducing the pulse duration involved eliminating as much empty space from the resonator as possible. An early step towards achieving this was moving the output coupler much closer to the slab, while being careful to preserve the stability of the resonator.

4.5.1 Estimating resonator length

The optical length of the resonator is determined by the physical size and refractive indices of the slab and intra-cavity components. The resonator round-trip time is equal to double the optical length divided by the speed of light [107]:

$$t_r = \frac{2\sum_i (n_i d_i)}{c} \tag{4.6}$$

where n_i is the refractive index of the i^{th} optical component and d_i is the physical distance travelled by the laser beam in that component. For example, at 1.63 μm the RTP crystals have a refractive index of 1.76 while the BK7 glass in the lenses has a refractive index of 1.50 [108].

In practice, the easiest way of estimating the optical length of the resonator was by measuring the distances between the Brewster faces of the slab and the cavity mirrors, then adding the extra optical length due to the slab and intra-cavity components:

$$t_r = \frac{2}{c}\left[2n_S l\sqrt{2} + d_1 + d_2 + \sum_i (n_i - 1)d_i\right] \tag{4.7}$$

where l is the length of the slab and d_1 and d_2 are the lengths of the resonator arms. The optical path length of this resonator was 51 cm, corresponding to a t_r of 3.4 ns.

The main limitations on reducing the resonator length were the telescope spacing and the physical size of the Q-switching elements. The significant optical length of the CPF slab, at nearly 18 cm, was also a major factor in pulse durations being longer than desired. The measures taken to address these issues are discussed below, and were implemented when developing the final Q-switched laser described in the next section.

4.5.2 Short telescope

The optical length was reduced by constructing a smaller telescope using $f = -30$ mm and $f = +50$ mm lenses. This removed roughly 4 cm of empty space from the resonator, the main drawback being that the $f = +50$ mm lens had to be held in a smaller mount and fixed in place. Aligning the $f = -30$ mm lens was also more difficult.

The smaller Q-switch was 14 mm long. It was mounted with the QWP (which was removed from its rotation mount) on a single 22 mm long aluminium block. This allowed the space between the HR mirror and the positive lens to be reduced.

4.5.3 Shorter slab

The optical path length of the slab contributed a substantial proportion of the overall resonator length, and so two shorter slabs (21.6 mm long) with 10 TIR bounces per side (21 overall) were fabricated from damaged original slabs by cutting and re-polishing. This decreased the optical path length of the slab to less than 10.7 cm, which reduced the round-trip time, but at the expense of decreased pump absorption, lower round-trip gain and stored energy. These factors limit the maximum achievable pulse energy.

The same laser head was used, despite the slab length being reduced by 14 mm. This increased the gap between the pump diode and lens duct to 15 mm, however the horizontal divergence of the pump diode output was small enough that the beam width did not exceed the 11.5 mm wide entry face of the lens duct.

4.6 Final Q-switched laser

The final Q-switched laser had the same layout as in Figure 4.1, but was designed with the intention of constructing a smaller resonator by eliminating as much empty space as possible. This involved mounting the Q-switch and QWP onto one block and making a modified mount for the output coupler to provide space on the optical bench for posts of other components. The total single pass optical length was estimated at 20 cm, corresponding to a round-trip time of 1.33 ns.

4.6.1 Resonator design

The resonator was modelled using the MATLAB code. The unfolded view of the resonator showing a plot of the mode size in the resonator is shown in Figure 4.8:

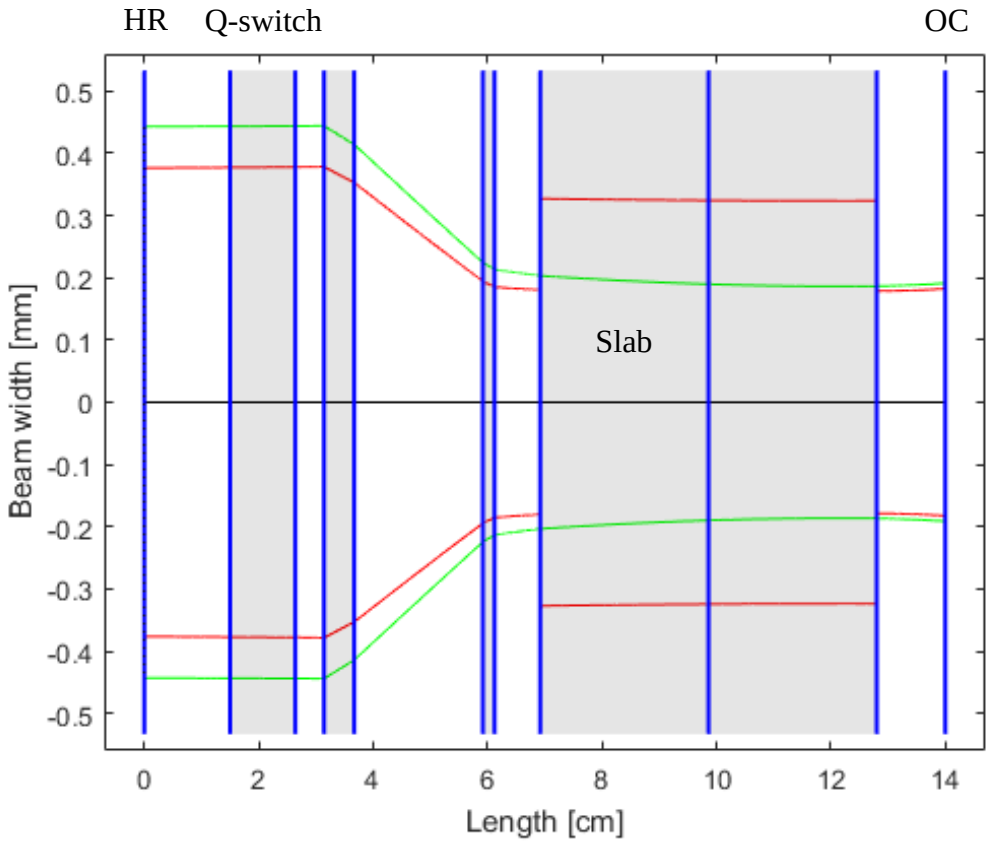

FIGURE 4.8: Simulation of the laser mode in the final version of the Q-switched laser. The telescope lenses are more accurately represented as thick lenses. The output coupler had a curvature radius of 30 cm.

4.6.2 Resonator assembly

The resonator was aligned using the procedure described in §4.2.3. A picture of the completed laser is shown in Figure 4.9:

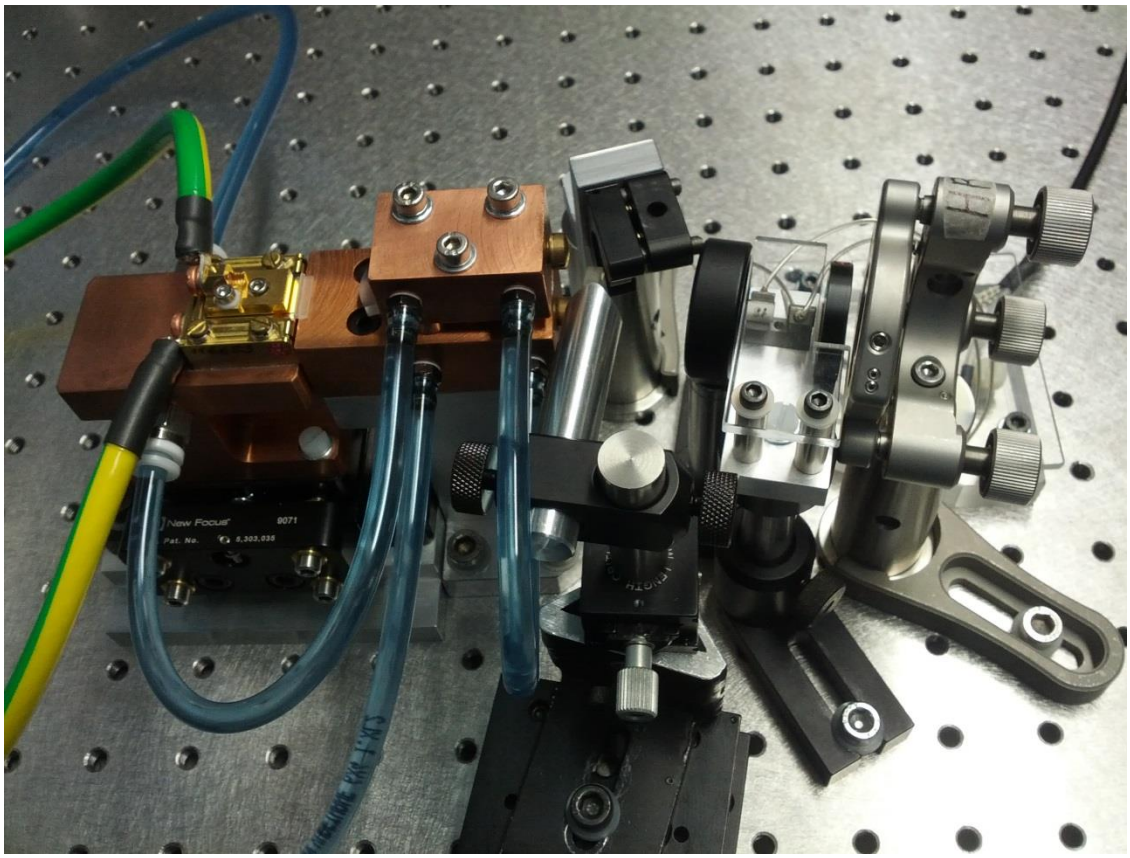

FIGURE 4.9: The final Q-switched laser using the short slab and compacted resonator.

The footprint of this laser on the optical bench was less than 25 cm long x 15 cm wide. The positive lens was fixed in position and could not be adjusted due to space constraints. The negative lens was still adjustable in the vertical and horizontal axes, but not along the optical axis. The rotation stage holding the QWP was discarded because it was too bulky; when unmounted, the rotation angle of the QWP was estimated when changing between gain-switched operation and Q-switched operation. The breakdown voltage of air is ~3000 V/mm, so the 2 mm gap between the PC and QWP was sufficient to prevent sparking from the 2500 V applied to the PC. The photo-detector was replaced with a faster BB-30 detector with a < 200 ps rise time for more accurate pulse measurements.

4.7 Results and discussion

4.7.1 Pulse duration vs. energy

The Q-switched output pulse energy and pulse duration compared to the input pulse energy for the R = 40% output coupler are shown in Figure 4.10:

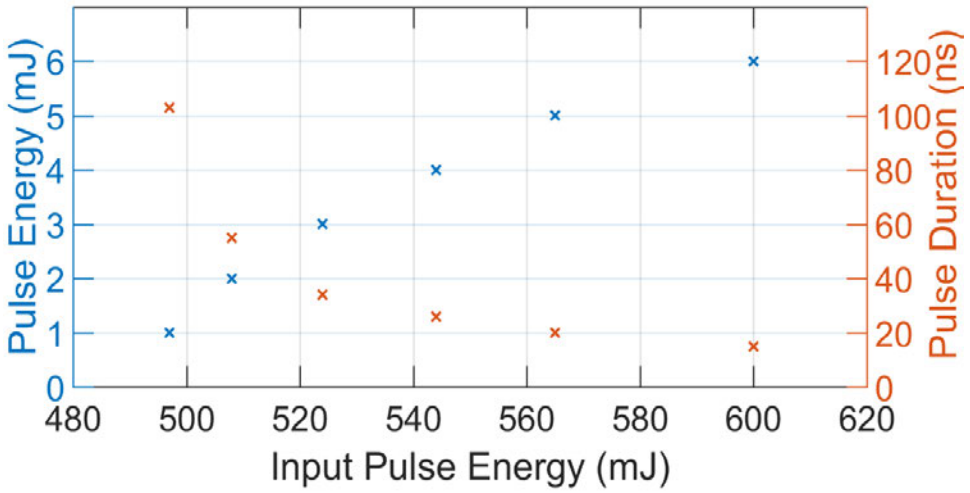

FIGURE 4.10: Output pulse energy and duration compared to input pulse energy.

The operation of this Q-switched laser was modelled as described in the paper "*Short-pulse actively Q-switched Er:YAG lasers*" in Appendix A. The following equation derived by Prof. David Ottaway predicts an inverse relationship between pulse duration and pulse energy if the beam area within the slab is taken into account:

$$\frac{E\tau}{\mathrm{A}} = \frac{8hct_r}{\mathrm{B}\lambda_l\sigma(f_1+f_2)}\left(\frac{\ln\left(\frac{1}{R}\right)}{\ln\left(\frac{1}{R}\right)+\delta}\right) \tag{4.8}$$

where A is the mode area in the slab and B is a factor accounting for the overlap of the laser mode in the slab. This beam overlap factor is related to the number of passes of a gain medium on each round-trip: 1 for a ring resonator, 2 for a standing wave resonator or ring resonator using a CPF slab, and 4 for a standing wave resonator using a CPF slab.

The other parameters are defined below. This complete version of Eqn. (4.2) shows that the pulse energy-duration product divided by the beam area is directly proportional to the resonator round-trip time. If the out-couple losses, $\log_e(1/R)$, are much larger than the scatter losses, δ, then $E\tau$/A will be fairly constant for most output couplers.

The values for the parameters of this laser are shown in Table 4.2:

Parameter	**Symbol**	**Value**
Er^{3+} concentration	N_C	7.0×10^{19} cm^{-3}
1617 nm cross section	σ_{1617}	3.0×10^{-20} cm^2
1617 nm Boltzmann factors	$f_{1(1617)}$ & $f_{2(1617)}$	0.036 & 0.21
1645 nm cross section	σ_{1645}	2.7×10^{-20} cm^2
1645 nm Boltzmann factors	$f_{1(1645)}$ & $f_{2(1645)}$	0.022 & 0.21
Round-trip time	t_r	1.33 ns
Beam area	A	0.002 cm^2
Beam overlap factor	B	4
OC reflectivity	R	0.4
Resonator loss	δ	0.1

TABLE 4.2: The parameters for the final version of the Q-switched laser.

For each resonator, the pulse duration was found to be close to inversely proportional to the pulse energy, for various output couplers, as shown by a linear plot of inverse pulse duration vs. pulse energy for $R = 40\%$, 60% and 80% output couplers in Figure 4.11:

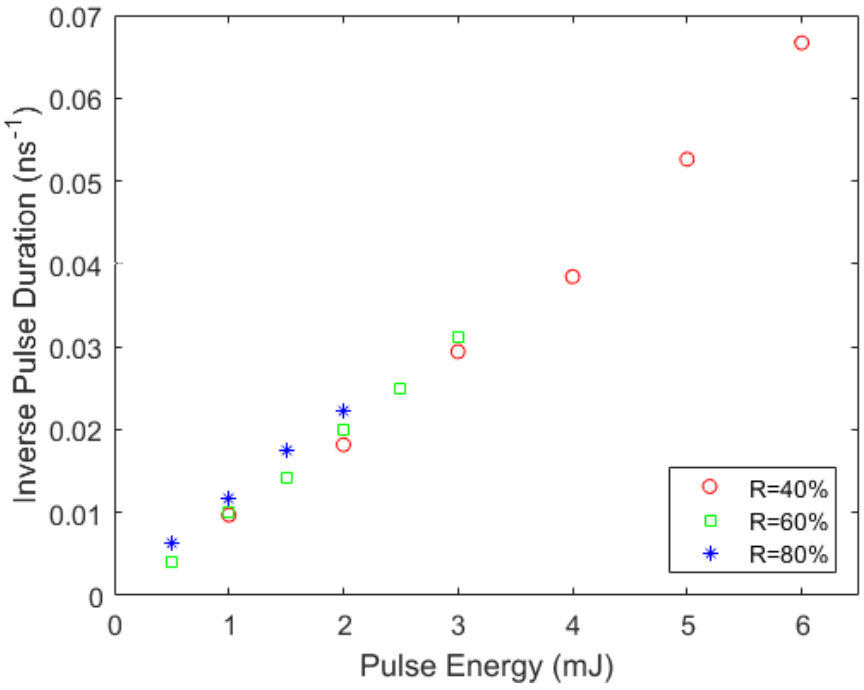

FIGURE 4.11: Inverse pulse duration vs. pulse energy for different output couplers. The pulse energies at $R = 60\%$ and $R = 80\%$ were limited to reduce the risk of slab damage.

A less reflective output coupler increases the threshold power, but has no effect on the mode size due to the resonator geometry remaining unchanged. The lower round-trip gain reduces the pulse energy, but also increases the build-up time and pulse duration. Consequently, the product of pulse energy and pulse duration barely changes between different reflectivity mirrors.

The experimental and theoretical results of both slabs in different resonators can be summarised by the plot of $E\tau$/A vs. resonator round-trip time in Figure 4.12:

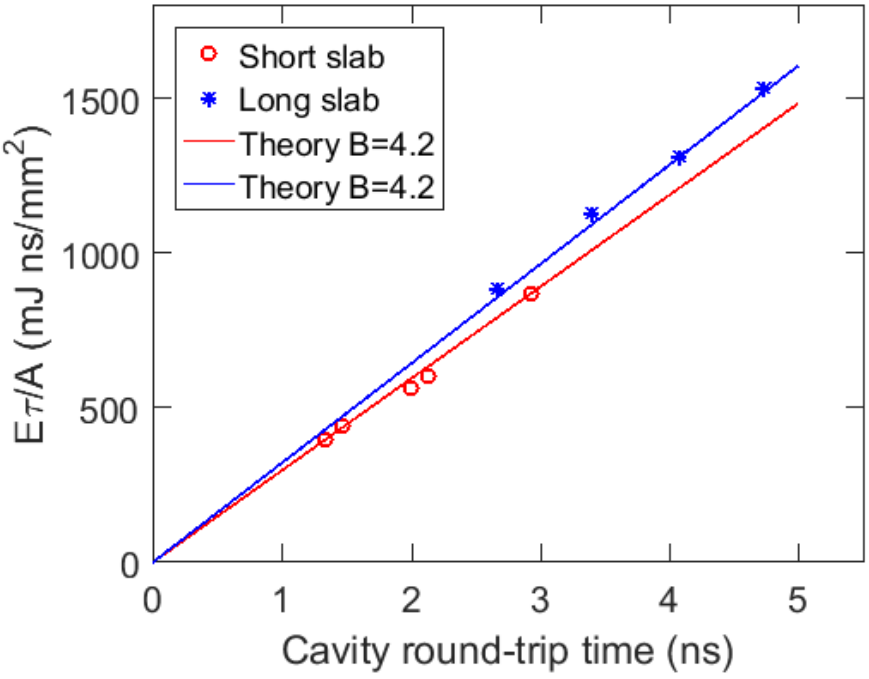

FIGURE 4.12: $E\tau$/A vs. round-trip time for the short and long slabs compared to theory.

The mode area values were estimated using the MATLAB resonator code. The lines for the short and long slabs are slightly different because the increased threshold required for lasing with the short slab actually favoured the 1617 nm transition, whereas the lasing wavelength of the long slab was 1645 nm. The constant B was 5% higher than the expected value, however this could be explained by systematic errors in the emission cross sections, mode areas, or power meter calibration.

Eqn. (4.8) shows the problem with using a Q-switched laser to achieve very short pulses in Er:YAG. Reducing the beam area in the slab will reduce the $E\tau$ product, allowing for shorter pulse durations, but a smaller beam area also results in a higher power density which increases the risk of damage.

4.7.2 Shortest pulse

The shortest duration, highest peak power pulse produced by the Q-switched laser using the short slab is shown in Figure 4.13:

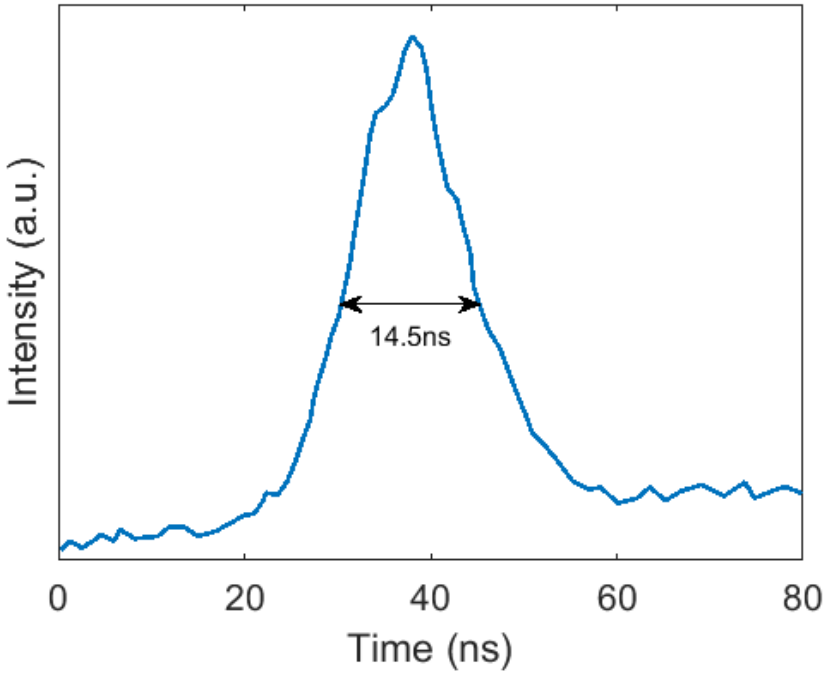

FIGURE 4.13: The 6 mJ, 14.5 ns duration pulse from the Q-switched laser as measured by a 1.5 GHz bandwidth BB-30 photodetector and displayed on a 200 MHz oscilloscope.

The 6 mJ, 14.5 ns pulse corresponded to a peak power of 410 kW at 1617 nm and an optical to optical efficiency of 1% from the 600 mJ pump pulse. This pulse duration is the equal shortest reported from an actively Q-switched Er:YAG laser so far, but was still more than an order of magnitude longer than the resonator round-trip time of 1.33 ns.

4.8 Chapter summary

This chapter has described the design and operation of the Q-switched laser. The results of the Q-switching trials showed that the pulse duration was close to inversely proportional to the pulse energy, which was explained by expanding on the Q-switched laser theory developed by Degnan [109]. While capable of producing high peak powers, the Q-switched laser fell short of the desired specifications. The highest pulse energy observed from the long slab was 15.5 mJ with a < 25 ns duration, corresponding to over 650 kW peak power, however this caused damage on the slab surface. Since the slab was susceptible to damage from sustained high intra-cavity peak powers, it was necessary to reduce both the pulse energy and duration. Trials of a shorter slab and more compact resonator succeeded in reducing the pulse duration to less than 15 ns, however the maximum achievable pulse energy fell to 6 mJ. While 400 kW peak power was still respectable, it fell short of project requirements. This necessitated a change of strategy.

The next chapter will describe the design, construction and operation of the cavity-dumped laser, which was able to safely produce the desired peak power.

Chapter 5: Cavity-dumped Er:YAG laser

5.1 Introduction

We have seen that the Q-switched Er:YAG laser prototypes were unable to produce the short duration, high peak power pulses demanded by this project. Furthermore, the slab was vulnerable to optical damage caused by high intra-cavity peak powers. These obstacles could only be overcome with an alternative approach: a cavity-dumped laser.

This chapter describes the design and construction of a cavity-dumped Er:YAG laser that met the requirements for use in a high precision laser range-finder. The Er:YAG slab and laser head used for this laser are described in Section 5.2. The resonator layout, construction, operating principle, and supporting electrical systems are described in Section 5.3. The threshold power calculation in Section 5.4 is followed by the results in Section 5.5. The cavity-dumped laser performance is compared to that of the Q-switched laser in Section 5.6 and the chapter is summarised in Section 5.7.

The cavity-dumped laser results reported in this chapter are also provided in the paper *"Compact cavity-dumped Q-switched Er:YAG laser"* that was published in Optics Letters. A copy of that paper is included in Appendix A.

5.2 Cavity-dumped laser head

5.2.1 Gain medium

The pulse duration of a cavity-dumped laser is equal to the resonator round-trip time provided the switching time is sufficiently fast, as discussed in Section 1.4, and so the need for an ultra-compact resonator was alleviated. Thus, I chose to use a larger 0.25% Er:YAG slab which was designed by Myles Clark for a methane LIDAR project. This slab was already mounted in a laser head along with a glass lens duct to channel the pump light into the slab. The slab schematic is shown below in Figure 5.1. The slab measured 4.06 mm wide, 3.5 mm high, had a shoulder length of 65 mm and a total length of 68.2 mm. The laser mode had 16 bounces on each side with a 45^{o} angle of incidence, giving a total of 33 TIR bounces:

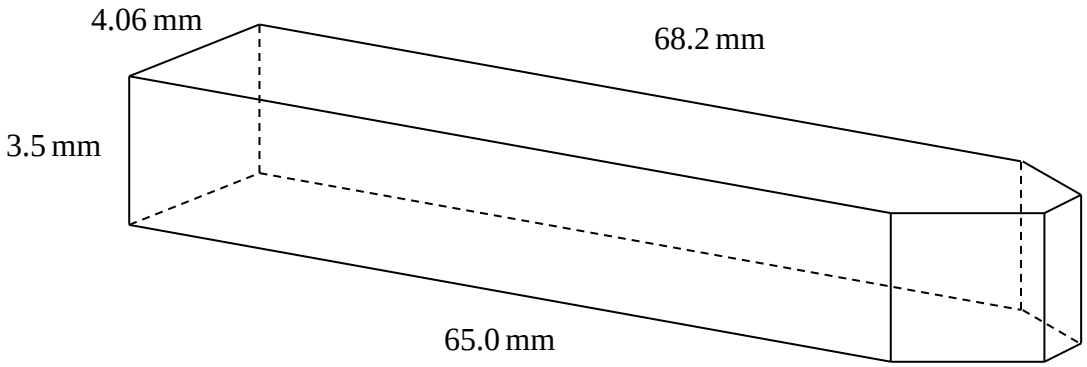

FIGURE 5.1: 3D view of the 0.25% Er:YAG slab used in the cavity-dumped laser.

Compared to the 0.5% Er:YAG slabs used in the Q-switched lasers, this slab provided more even pump absorption and reduced losses from up-conversion. It also meant the gain medium occupied a greater proportion of the total cavity length. The surface finishing was performed to similar standards: top and bottom surfaces were fine ground, while the reflecting slab surfaces were specified to $\lambda/10$ flatness and 10/5 scratch/dig. The detailed slab and lens duct drawings are provided in Appendices B9 and B10.

5.2.2 Laser head

The slab was mounted in a laser head consisting of two copper blocks (Appendix B11) with 125 μm thick indium sheets to provide stress relief and heat conduction. The base block of the laser head was designed to allow for pumping with two pump diodes. The chiller system previously used on the Q-switched laser provided cooling water to the pump diode and laser head. A picture of this arrangement is shown in Figure 5.2:

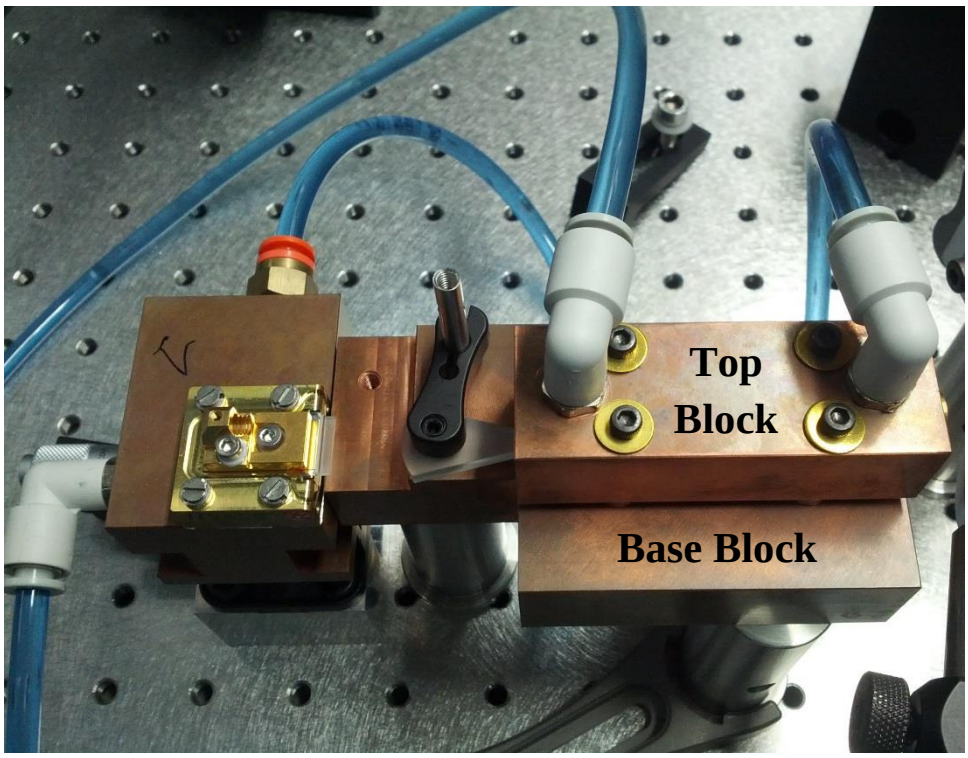

FIGURE 5.2: Picture of the laser head, pump diode, lens duct and water cooling.

A side view of the pumping and slab arrangement is depicted in Figure 5.3. The height of the pumped region, through which 90% of pump light passes, slightly exceeds 0.6 mm.

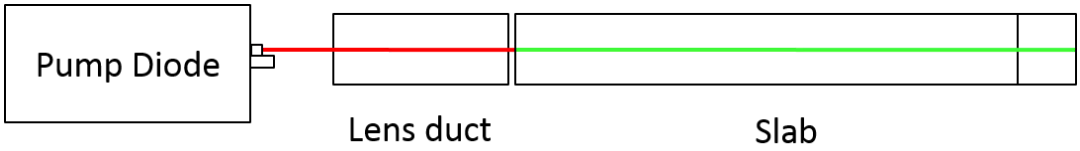

FIGURE 5.3: Side view of the pump and slab arrangement. The green line represents the observed up-conversion in the slab, which indicates the pumped region.

5.3 Laser resonator

5.3.1 Resonator layout

A schematic of the cavity-dumped laser is shown in Figure 5.4A. It used an RTP Pockels cell to electro-optically control the resonator Q-factor. An intra-cavity telescope was used to expand the laser mode, reducing the fluence at the Pockels cell and TFP.

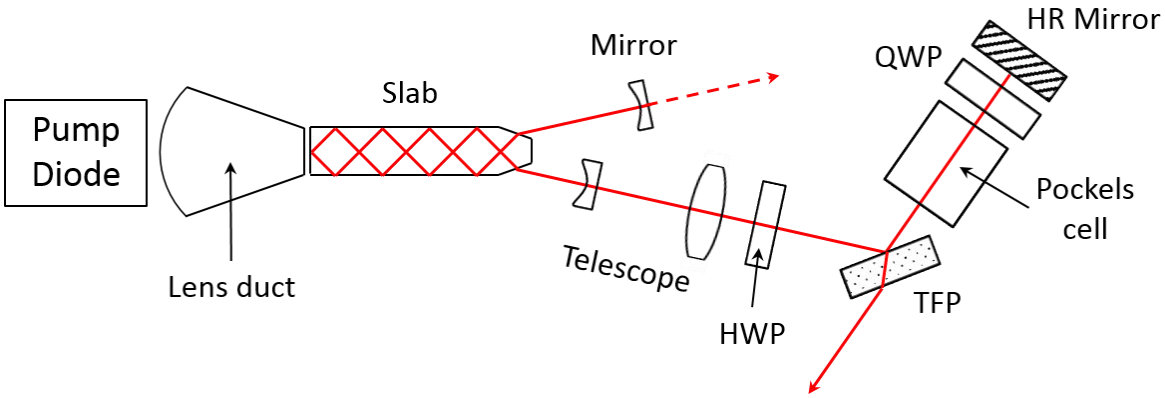

FIGURE 5.4A: Schematic of the cavity-dumped laser. The lenses, half-wave plate (HWP), thin film polariser (TFP), QWP and Pockels cell are all AR-coated for 1645 nm.

Construction of this resonator was complicated by the need to precisely align the thin film polariser (TFP) and "perpendicular" HR arm. However this design benefits from reduced intra-cavity loss during the build-up phase compared to the alternative configuration shown in Figure 5.4B, as the TFP has lower loss reflecting σ-polarisation compared to transmitting π-polarisation [110].

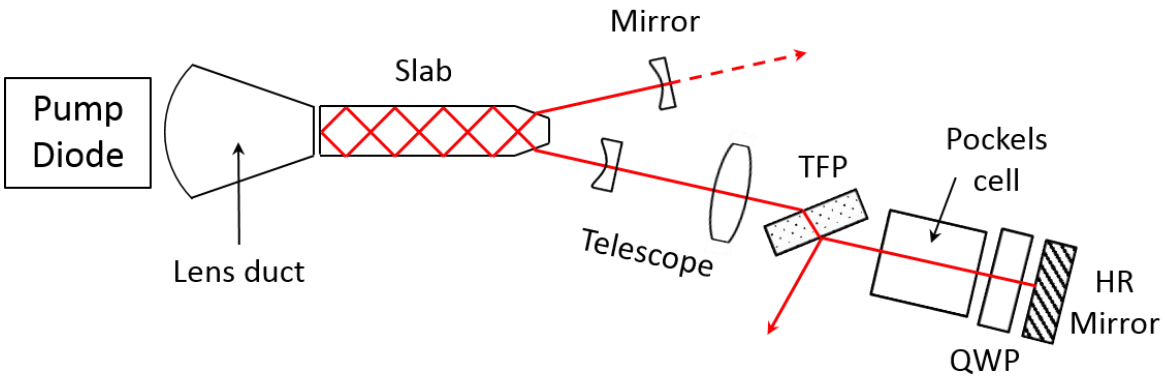

FIGURE 5.4B: Alternative configuration of the cavity-dumped laser.

5.3.2 Resonator model

The resonator dimensions were modelled using the MATLAB code from §3.2.2. A plot of the mode size in the resonator is shown below in Figure 5.5:

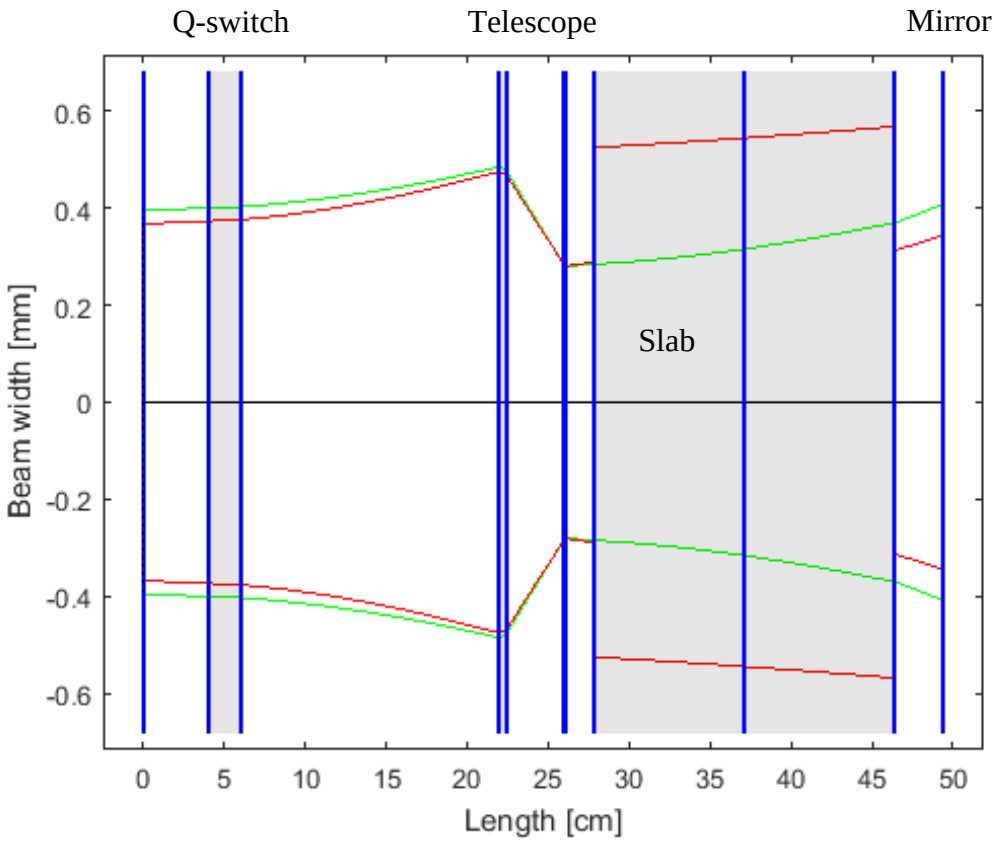

FIGURE 5.5: Simulation of the laser mode in the cavity-dumped resonator. The red curve corresponds to the horizontal direction. From left to right, the optical components are the Q-switch, f = +75 mm lens, f = –50 mm lens, slab and curved 30 cm mirror. The flat surfaces of the TFP, HWP and QWP are not depicted.

Preliminary measurements showed that using an f = +100 mm lens in the telescope expanded the beam too much, causing clipping on the 2.5 mm Pockels cell aperture and a resulting loss in power. Using an f = +75 mm bi-convex lens instead, along with a shorter telescope length, reduced the clipping loss. The one-way resonator optical length was designed to be 67 cm, corresponding to an expected pulse duration of 4.5 ns.

5.3.3 Resonator assembly and testing

I constructed the laser resonator in several stages, the first three of which were exactly the same as used for the prototype Q-switched lasers. At every step, the optical alignment was optimised by gain-switching the laser using the standard duty cycle (10 ms pump pulses at 12 Hz PRF) and maximising the power transmitted through the R = 90% mirror:

(1) Align two curved mirrors (HR and R = 90% OC) to achieve lasing, using a HeNe beam (- -) and pinhole as a guide to see the back-reflection from the HR mirror:

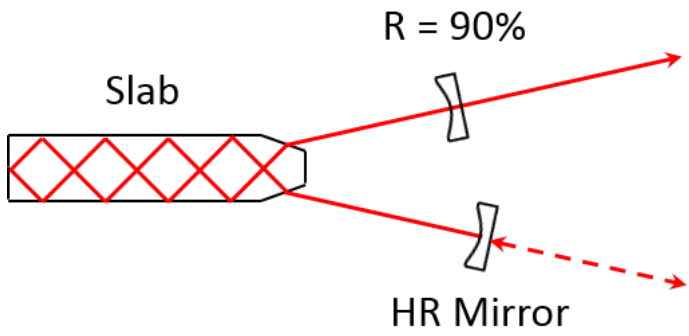

(2) Replace the curved HR mirror with a flat HR mirror and f = +75 mm lens as shown below. Angular mirror alignment is achieved using the back-reflection of the HeNe beam on the pinhole. Translate lens laterally to achieve lasing:

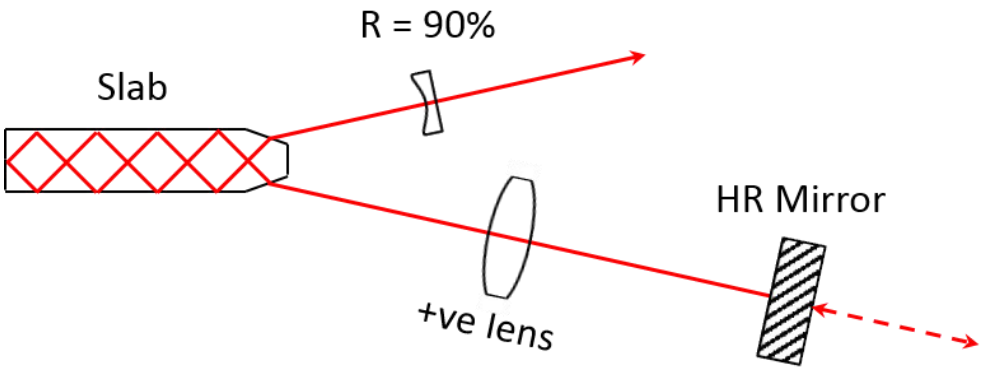

(3) Insert the $f = -50$ mm lens into the resonator. Angular alignment using the HeNe beam. Translate laterally using an improvised 2–axis mount to achieve lasing and adjust telescope spacing to optimise power:

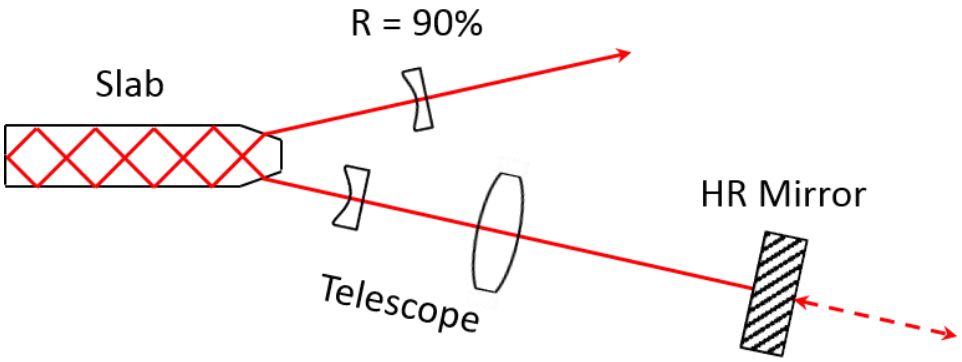

(4) Now the polarisation dependent components can be added. Position the TFP and adjust to Brewster's angle (56° to the normal) to minimise loss. Then insert the HWP and rotate to minimise loss:

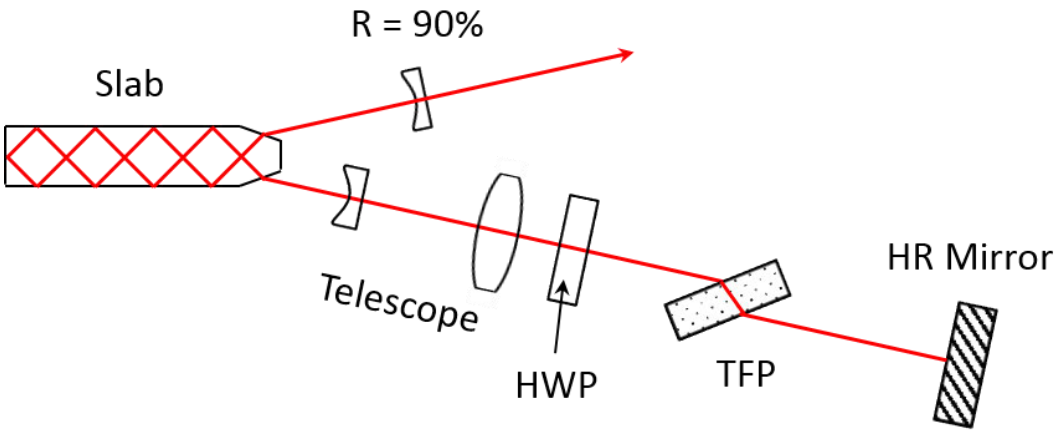

(5) Rotate the HWP slightly to produce a reflection off the TFP, providing the "perpendicular" beam path which is marked with a pinhole. Using a HeNe beam as a guide, align the flat HR mirror to the perpendicular HR arm:

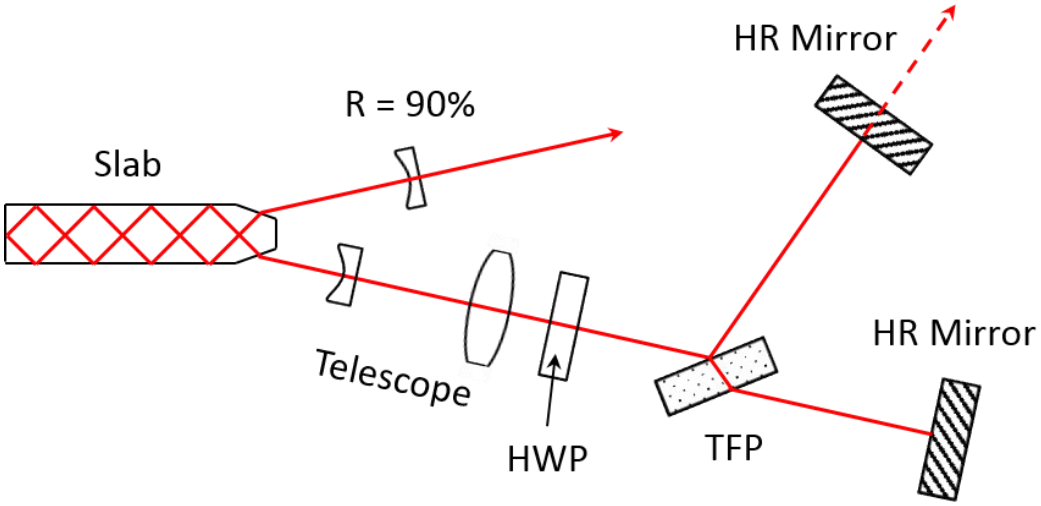

(6) Finally, insert the Pockels cell and QWP into the resonator. Rotate the QWP to maximise the power in the gain-switched pulse:

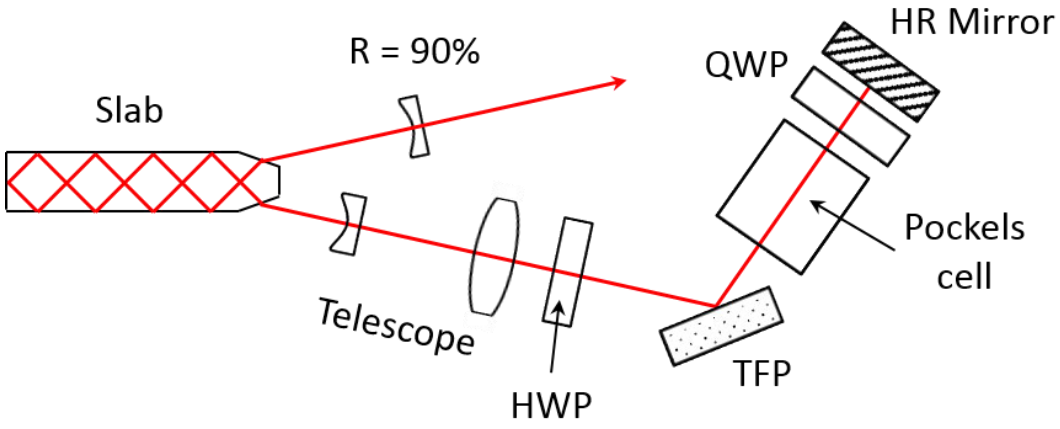

The most difficult parts of the resonator assembly were the positioning of the negative lens, the alignment of the flat HR mirror to the reflection from the TFP and the placement of the Pockels cell to minimise clipping loss. The threshold power in gain-switched mode was observed to be 32 W with the chiller temperature set to 16°C.

A picture of the completed laser is shown below in Figure 5.6:

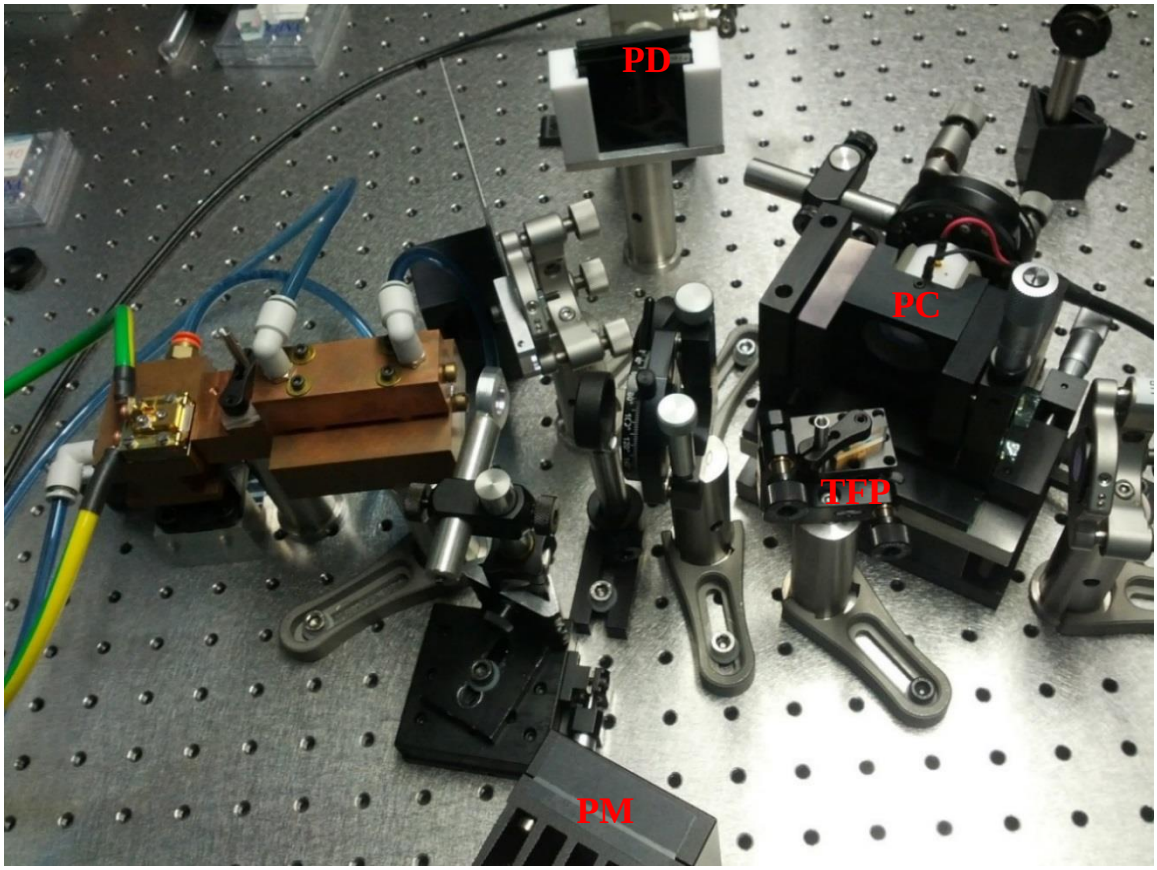

FIGURE 5.6: The completed cavity-dumped laser, showing the Pockels cell (PC) mounted in a bulky 2-axis tilt stage. The power meter (PM) is visible at the bottom of the picture, while the photodetector (PD) for analysing pulse evolution is visible at the top.

5.3.4 Cavity-dumped laser operation

The TFP, when mounted at the Brewster angle, functions as a polarisation controlled output coupler, reflecting the σ-polarisation but transmitting the π-polarisation. The QWP is rotated by 45° to provide high output coupling when the slab is pumped and no voltage is applied to the Pockels cell. The resonator Q is low (i.e. high loss), preventing lasing and allowing a population inversion to build up.

Applying the quarter-wave voltage of 1.1 kV to the Pockels cell at the end of the pump pulse reduces the resonator loss, allowing lasing to occur. The laser pulse builds up and is dumped out through the TFP by rapidly removing the high voltage from the Pockels cell. This requires fast switching electronics to drive the Pockels cell.

5.3.5 Pockels cell driver

The optimum operation of the cavity-dumped laser relies on a HV driver capable of switching off in less than half the resonator round-trip time. This meant a switch-off time of less than 2 ns. The switch-on time, which is not required to be exceptionally fast, was 8 ns. I used a custom Starfire HV pulser from Quantum Technology. It used two input triggers, the rising edge of the first to switch on the high voltage, and the rising edge of the second to switch it off, and had a minimum "on-time" of 200 ns.

I used an SRS DG645 digital delay generator triggering off the pump pulse to provide the trigger for HV-on and an analog DataPulse 101 pulse generator to provide the trigger for HV-off. The latter enabled smooth control of the HV on-time and thereby allowed precise and rapid control of the pulse switch-out time, the importance of which will be seen from the results in §5.5.2. A not-to-scale representation of the timings of the trigger voltages for the cavity-dumped laser is shown in Figure 5.7:

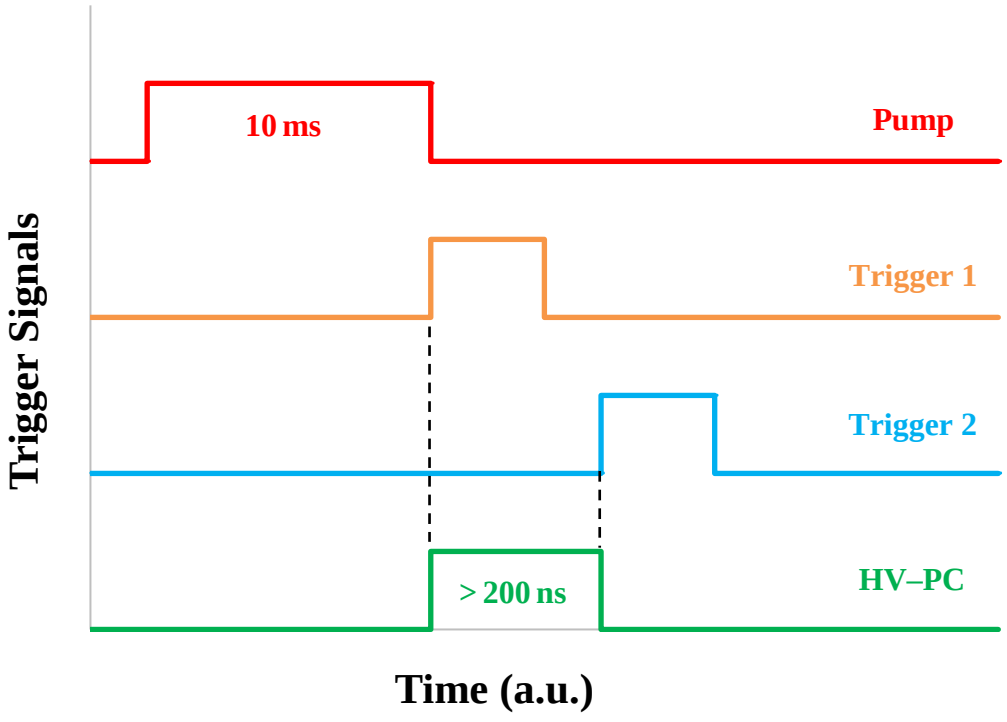

FIGURE 5.7: A timing diagram of the pump, trigger and HV pulses. Trigger 1 is prompted by the falling edge of the pump and trigger 2 is initiated off trigger 1 with a variable delay.

The oscilloscope display with the HV triggers and HV output signal from the driver is shown in Figure 5.8. The latter was measured using a high voltage probe with an attenuation factor of 1000. The “ringing” in both of the trigger signals is caused by interference from the on/off switching of the high voltage. The 100 ns delay between the rise of the triggers and the HV driver response is caused by the response time of the latter. Also note that the apparent 15-20 ns delay between the HV-on/off triggers and the signal response is caused by the latter being transmitted over a 3.8 m long cable, as opposed to the former signals being transmitted over cables of less than 1 m in length.

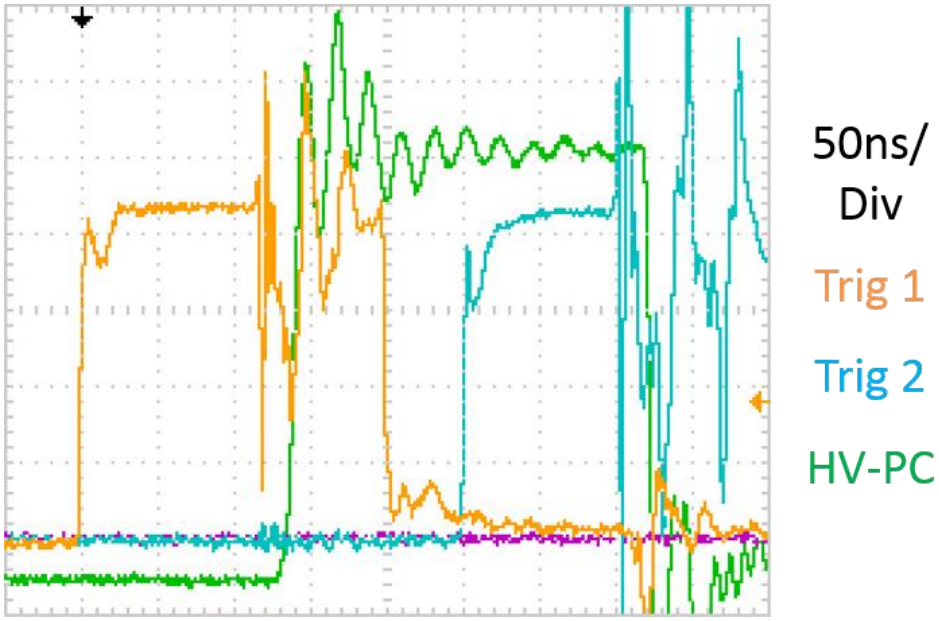

FIGURE 5.8: A screenshot of the HV triggers and HV output monitor on the oscilloscope using a 50 ns time scale. HV-on is the orange trace, HV-off is the blue trace and the HV signal to the Pockels cell is the green trace.

5.4 Theoretical comparison

The measured lasing threshold of 32 W slightly exceeded the predicted lasing threshold of 31 W, which was estimated using the formula derived in §3.5.2:

$$P = \frac{hc\left(V_p W_p N_1\right)}{\lambda_p F_{abs} \eta_h} \tag{5.1}$$

The relevant parameters for the cavity-dumped laser are listed in Table 5.1:

Parameter	Symbol	Value
Er^{3+} concentration	N_C	3.5×10^{19} cm^{-3}
Up-conversion parameter	C_{up}	1.8×10^{-18} cm^3 s^{-1}
Slab pumped volume	V_p	0.165 cm^3
Optical gain length	L	18.8 cm
Pump absorption fraction	F_{abs}	0.65
Round-trip transmission	T_{rt}	0.75
Upper level threshold	N_T	5.0×10^{18} cm^{-3}

TABLE 5.1: The values of parameters for the 0.25% Er:YAG slab. The slab loss was measured at ~12.5% for a round-trip, however there was additional loss caused by clipping at the Pockels cell aperture. Therefore a value of 0.75 for T_{rt} was assumed.

The upper level population density at threshold was found from Eqn. (3.9) and the pump rate from Eqn. (3.10). The predicted threshold power agreed quite well with the measured value, considering the uncertainties in the values of the up-conversion parameter, pump absorption fraction, overlap factor and round-trip transmission.

5.5 Cavity-dumping results

Following the initial testing of the laser in gain-switched mode, cavity-dumping experiments commenced. While in principle cavity-dumped lasers should have no output coupling during the build-up phase, I left the R = 90% mirror in place for diagnostic purposes, at the penalty of a higher threshold power and reduced efficiency.

5.5.1 Initial Q-switching

In order to safely test the cavity-dumped laser, the pump power was initially set to just above the lasing threshold observed in gain-switched mode. The QWP was rotated by 45^{o} to prevent lasing during pumping and the quarter-wave voltage applied to the Pockels cell. The HV on-time was initially set to 200 ns and then gradually increased until lasing was observed. I repeated this process with increasing pump powers and recorded the minimum HV on-time required for detectable lasing. The results are plotted in Figure 5.9:

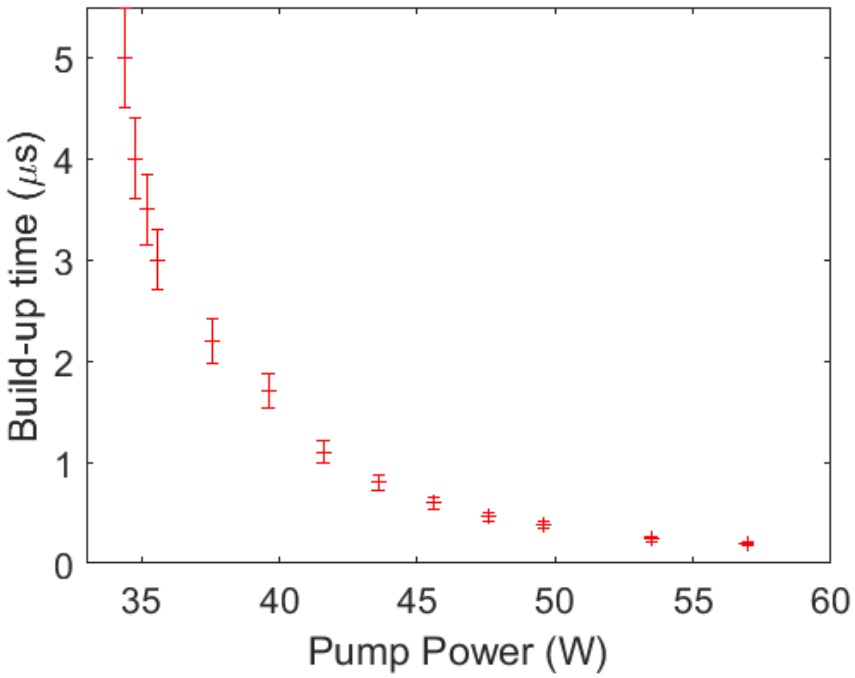

FIGURE 5.9: The HV on-time needed for detectable Q-switched lasing vs. pump power.

As the peak pump power increased, the minimum HV on-time required for lasing decreased. If the efficiency of pump absorption remained constant, we would expect:

$$\tau_{BU} \propto \frac{1}{P} \tag{5.2}$$

based on our Q-switched results, where τ_{BU} is the build-up time and P is the pump power. A plot of inverse build-up time vs. pump power is shown in Figure 5.10:

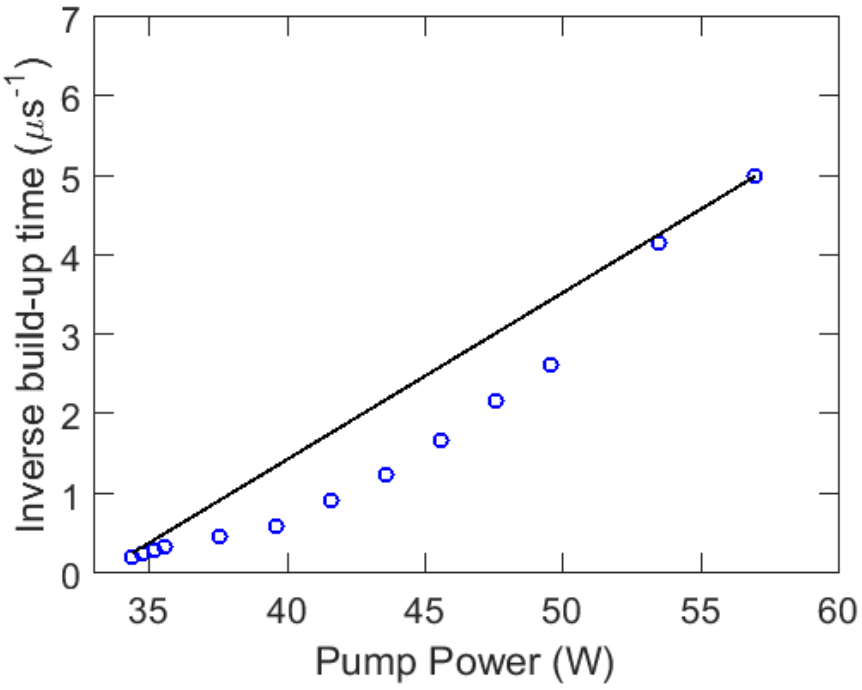

FIGURE 5.10: Plot of the measured inverse build-up time vs. pump power. The solid line represents the expected relationship assuming a constant pump absorption efficiency.

While most of the points on the plot fall below the expected line, it must be noted that the pump diode was tuned for optimal absorption at high powers. At lower powers, the build-up times are longer than expected because the diode junction was cooler and therefore had a blue-shifted emission spectrum. This resulted in less efficient pump absorption in the slab, and consequently lower gain and a slower pulse build-up.

A plot of the evolution of the energy stored in the laser cavity over an extended HV on-time was recorded using the photodetector to monitor the power transmitted through the R = 90% mirror at 52 W pump power. Figure 5.11 shows the evolution of the Q-switched pulse if it is not dumped:

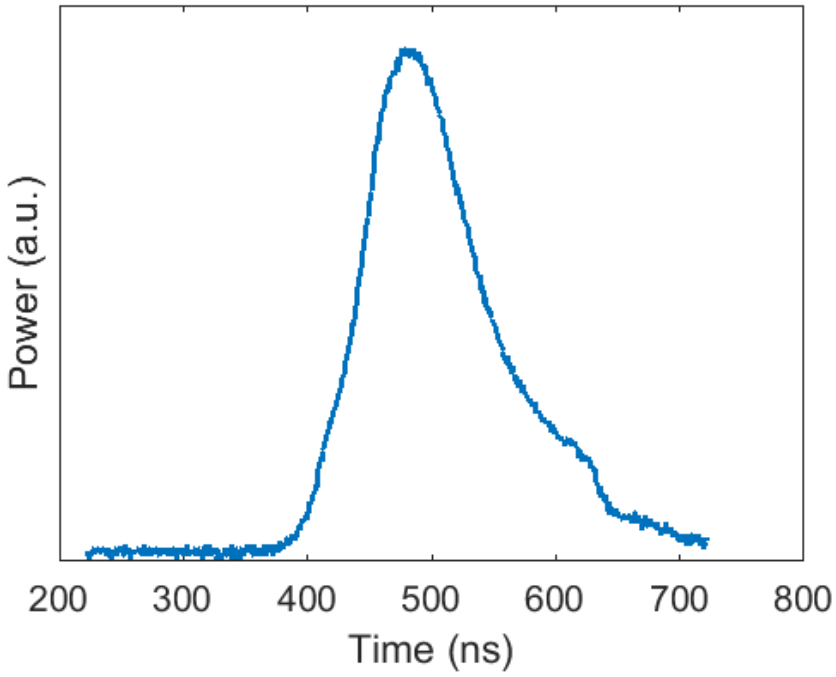

FIGURE 5.11: The evolution of the Q-switched laser pulse as measured by the Newport BB-30 photodetector and displayed on the 200 MHz oscilloscope.

The pulse is not symmetric as the resonator has a low output coupling and thus the pulse builds up quickly but decays slowly due to intra-cavity loss and out-coupling through the R = 90% mirror. The pulse should be dumped at the peak of the curve, when the cavity has the highest stored energy, for optimum laser efficiency but this runs the risk of slab and/or component damage when higher pump powers are used.

When the HV is switched off, the TFP combination functions as a highly transmitting element, so lasing will cease and the erbium ions remaining in the upper laser level will decay via fluorescence. This was confirmed by monitoring the output of the photodetector.

5.5.2 Cavity-dumping

The cavity was dumped by removing the HV from the Pockels cell during the growth of the stored energy. The resulting pulse duration was measured using the BB-30 photodetector. As expected, the pulse duration was approximately equal to the round-trip time of the resonator. A typical output pulse is shown in Figure 5.12:

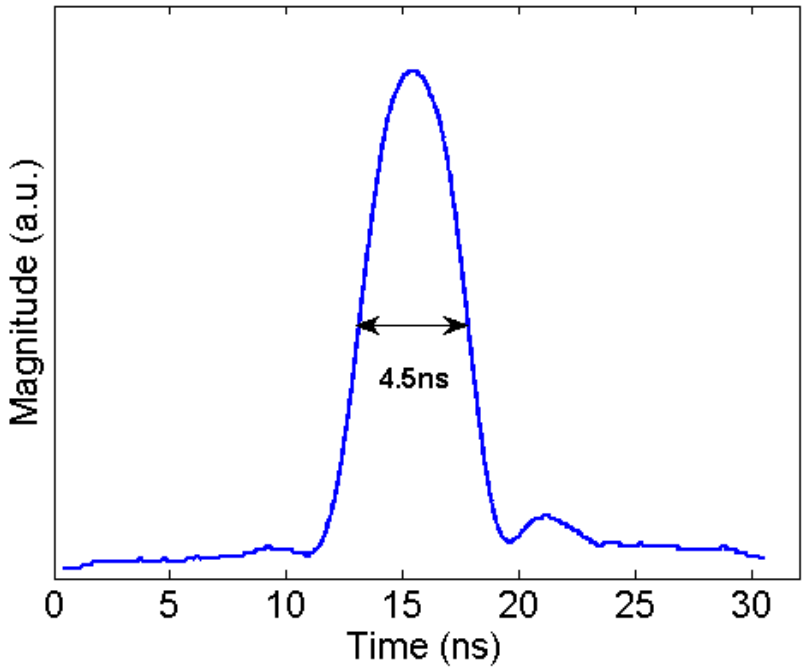

FIGURE 5.12: A typical cavity-dumped laser pulse with 4.5 ns FWHM duration as measured by the BB-30 photodetector and displayed on the 200 MHz oscilloscope. The small trailing lump is believed to be caused by "ringing" in the photodetector.

While the pulse energy and efficiency would be maximised by dumping the cavity at the peak of the stored energy, if the HV on-time was too long, the pulse could be trapped inside the resonator for too long and the risk of damage to components would increase. However high energy pulses could also be produced by increasing the pump power and dumping a partially formed Q-switched pulse by limiting the HV on-time. Although the laser efficiency would be lowered, this would reduce the time over which the resonator components were exposed to high fluence and therefore reduce the risk of optical damage.

The dependence of the output pulse energy vs. HV on-time for various pump powers is plotted in Figure 5.13:

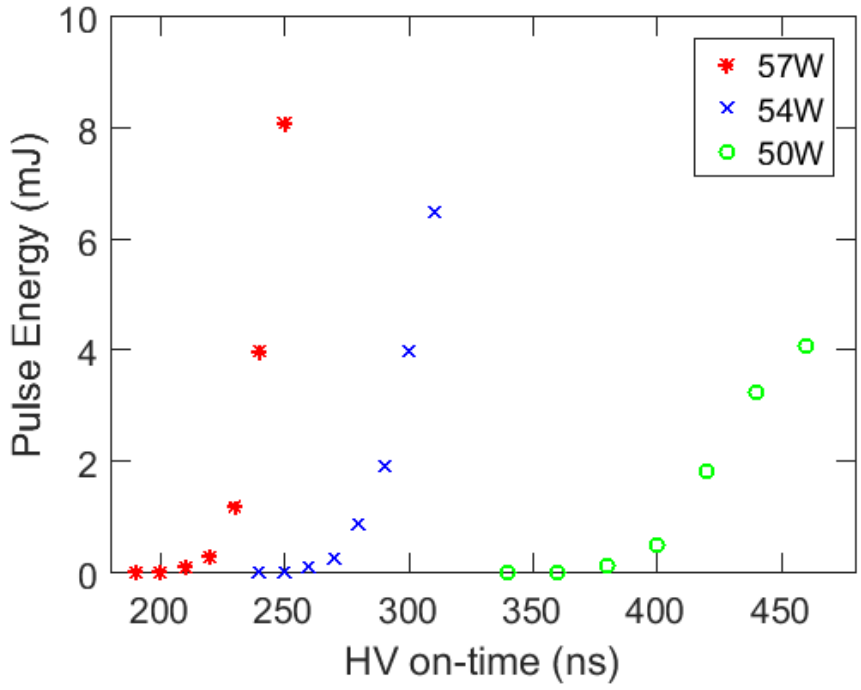

FIGURE 5.13: Cavity-dumped pulse energy vs. HV on-time for different pump powers. The pulse energy was calculated by dividing the average power by the PRF (12 Hz).

The curve for 50 W peak pump power increases noticeably slower and appears to be "rolling over" as the HV on-time increases past 440 ns. This indicates the laser was close to the maximum output energy. The other two curves do not appear to show this.

I later repeated the measurements for 57 W peak pump power with the intention of obtaining higher output pulse energies and exceeding 2 MW peak power. These results are recorded in Table 5.2 and plotted in Figure 5.14:

HV on-time (ns)	200	210	220	230	240	250	260
Laser power (mW)	0	0.3	1.1	8.0	28	72	120
Pulse energy (mJ)	0	0	0.1	0.7	2.3	6.0	10

TABLE 5.2: Output power and pulse energy vs. HV on-time with 57 W peak pump power.

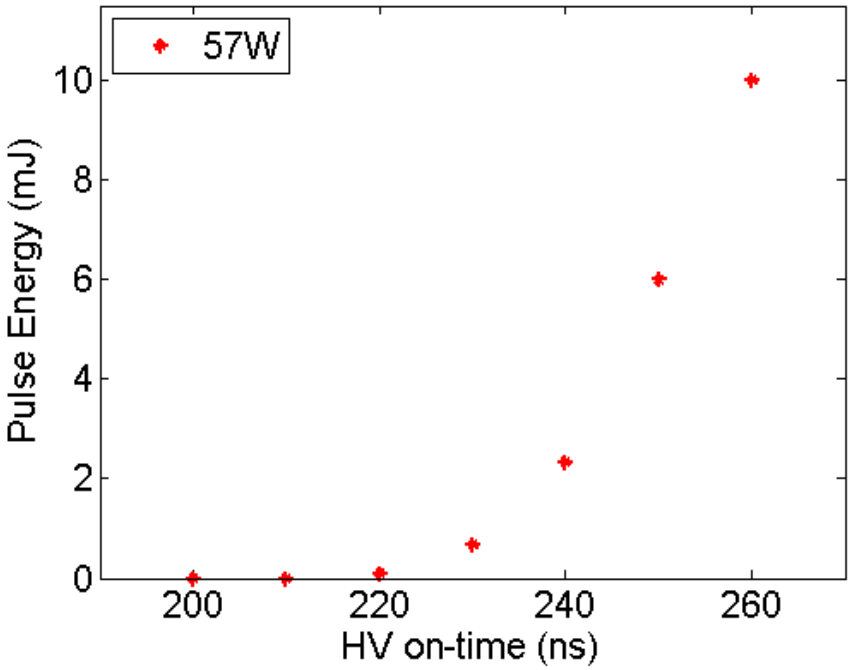

FIGURE 5.14: Cavity-dumped pulse energy vs. HV on-time for 57 W peak pump power.

The highest average output power exceeded 120 mW, corresponding to a pulse energy of 10 mJ, giving an optical to optical efficiency of ~1.7% from the 570 mJ pump pulse. This could be improved by replacing the R = 90% mirror with one of higher reflectivity or increasing the HV on-time, although the increased risk of damage to the slab must be considered. With a pulse duration of 4.5 ns, this was a peak power of more than 2 MW.

The laser wavelength was measured to be 1645 nm, as is consistent with the prediction that the population inversion was too low to yield lasing at 1617 nm:

$$N_2 = N_C \left(\frac{\sigma_{1617}(f_{1(1617)}) - \sigma_{1645}(f_{1(1645)})}{\sigma_{1617}(f_1 + f_2)_{1617} - \sigma_{1645}(f_1 + f_2)_{1645}} \right) \tag{5.3}$$

This shows that lasing at 1617 nm requires N_2 to exceed 1.20 x 10^{19} cm^{-3}, which is more than double the threshold upper level population N_T calculated in Section 5.4, so even 60 W pump power is well below the requirement for 1617 nm lasing.

5.5.3 Beam profile

The beam profile was recorded using a Goodrich SU-320M InGaAs CCD camera located ~60 cm from the flat HR mirror. It was processed using the MATLAB file GaussPictures.m (see Appendix C3). The results are shown in Figure 5.15:

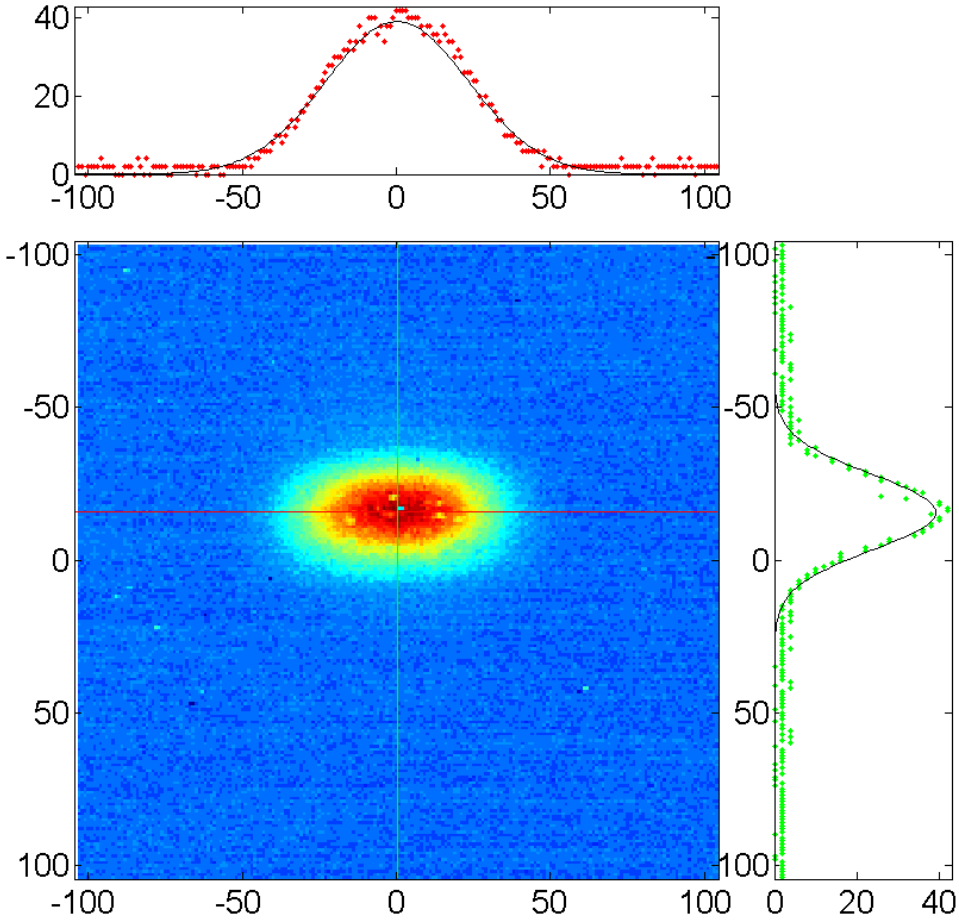

FIGURE 5.15: Plot of the beam profile at the CCD camera, a distance of ~50 cm from the TFP. The axis numbers denote the pixel numbers where each pixel is 40 μm x 40 μm. The solid curves are the best-fit Gaussians in the horizontal (red) and vertical (green) planes.

The picture shows that the beam is elliptical, with the vertical spot radius of the laser mode of 0.9 mm being much less than the horizontal spot radius of 1.6 mm.

The expected spot size of a TEM_{00} beam at the camera can be estimated using ABCD matrices. The matrix for propagation from the beam waist at the flat HR mirror to the camera is given by the product of the propagation matrices:

$$\begin{bmatrix} A & B \\ C & D \end{bmatrix} = \prod_i \begin{bmatrix} 1 & {z_i}/{n_i} \\ 0 & 1 \end{bmatrix} = \begin{bmatrix} 1 & z \\ 0 & 1 \end{bmatrix} \tag{5.4}$$

where z is the propagation length from the beam waist to the camera position:

$$z = \sum_i \frac{z_i}{n_i} \tag{5.5}$$

being the sum of the free space distances divided by their respective refractive indices. The complex beam parameter q can then be used to provide an estimate of beam width:

$$q' = \frac{Aq + B}{Cq + D} = q + z \tag{5.6}$$

where

$$\frac{1}{q} = \frac{1}{R} - \frac{i\lambda}{\pi w^2} = \frac{\lambda}{i\pi w_0^2} \tag{5.7}$$

since the beam has no curvature at the waist. So we can express q' as:

$$q' = \frac{i\pi w_0^2}{\lambda} + z \tag{5.8}$$

The expected beam radius w' at the camera, located at a distance of ~60 cm from the beam waist, can be found by isolating the imaginary part of q' and solving.

Since the resonator model in §5.3.2 predicts a vertical beam waist, w_0, of ~0.40 mm at the flat HR mirror:

$$w' = \frac{\sqrt{\pi^2 w_0^4 + z^2\lambda^2}}{\pi w_0} = 0.88 \text{ mm} \tag{5.9}$$

which compares well with the measured vertical beam radius of ~0.9 mm.

The vertical beam radius at the CCD camera could also have been estimated using

$$w' = w_0\sqrt{1 + \left(\frac{z}{z_R}\right)^2} \tag{5.10}$$

where z_R is the Rayleigh range for the vertical waist, given by:

$$z_R = \frac{\pi w_0^2}{\lambda} \approx 30.5 \text{ cm} \tag{5.11}$$

and therefore

$$w' = 0.40 \text{ x}\sqrt{1 + \left(\frac{60}{30.5}\right)^2} = 0.88 \text{ mm} \tag{5.12}$$

The horizontal beam radius at the camera should be nearly 1.0 mm based on beam divergence from the flat HR mirror (see Figure 5.5), assuming that it is a TEM_{00} beam. The much larger size observed indicates that the laser beam is higher order in the horizontal direction, although there was no requirement for very high beam quality.

The astigmatism of the beam can be attributed to the width of the pumped region greatly exceeding the height and the 3.2 mm clear aperture permitting lasing in a higher order mode. This higher order mode could be removed by altering the resonator design.

5.6 Comparison to Q-switched laser

The performance of the cavity-dumped laser was far superior to that of the Q-switched laser in terms of short pulse duration and peak power. While the minimum FWHM duration of a Q-switched pulse was greater than 10 round trips, the duration of a cavity-dumped pulse was equal to the resonator round-trip time. Both lasers were somewhat comparable in terms of pulse energy, however the Q-switched laser required a progressively greater pump power to achieve a linear increase in pulse energy. Conversely, the cavity-dumped laser was capable of substantially higher pulse energies from relatively modest increases in the pump power and/or build-up time, with the main limitation being the risk of optical damage to the slab surfaces. This was found to occur once the pulse energy exceeded 10.5 mJ, showing that there was room for improvement in the design.

5.7 Chapter summary

A cavity-dumped Er:YAG CPF slab laser was designed and constructed. The threshold power was only slightly above the predicted value of 31 W. The output pulses had a constant FWHM duration of 4.5 ns, while the pulse energy could be controlled by varying the pump power and build-up time. Instability just above threshold meant that the best way to obtain a stable output power was to increase the pump power and reduce the high voltage on-time. Pulses of up to 10 mJ were obtained, corresponding to over 2 MW peak output power at 1645 nm, which is the highest in the world at the present time. However the susceptibility of the CPF slab to optical damage limits the likelihood of reaching higher peak powers. Nevertheless there is still room for improvement in laser efficiency by reducing the resonator loss with a more highly reflective curved mirror.

Chapter 6: Conclusion

6.1 Project summary

The original goal of my project was to develop a short-pulse, high peak power Er:YAG laser that would be capable of replacing existing wavelength-shifted Nd:YAG laser range-finders. The project objectives were achieved, though not as originally planned: both of the Q-switched lasers were found to be inadequate for this task and only a cavity-dumped laser was capable of providing the desired pulse duration and peak power.

Chapter 1 reviewed previous work in eye-safe laser systems, Q-switched Er:YAG lasers and cavity-dumped lasers. Chapter 2 discussed the spectroscopic properties of Er:YAG and the drawbacks in using it as a gain medium. Low gain, re-absorption and up-conversion limit the peak power achievable compared to the more widely used Nd:YAG gain medium. Aided by MATLAB simulations, two CPF slabs were designed with the intention of overcoming these problems. The pump diode mounting and characterisation, lens duct design and laser heads for each slab were also discussed.

Chapter 3 described the design and assembly of a diode-pumped Er:YAG CPF slab laser using both slab designs. It also reported gain-switched lasing measurements and compared the results to theoretical predictions of threshold power and slope efficiency. These generally showed good agreement, although the laser was less efficient than expected when using an $R = 40\%$ output coupler.

Chapter 4 reported the construction and operation of the Q-switched laser, which was built in two main variants. The first used the 35.6 mm long slab and achieved pulses of up to 15.5 mJ with less than 25 ns duration. However as with all Q-switched lasers, the intra-cavity peak power was significantly larger than the output peak power. This resulted in optical damage to the slab surfaces. The second variant used the 21.6 mm short slab and was designed to be as compact as possible. It achieved shorter pulse durations due to the reduced optical length of the cavity. However the lower round trip gain and stored energy limited the pulse energy to a maximum of 6 mJ, with the shortest observed pulse duration being 14.5 ns. The 400 kW peak power fell short of that required for the range-finding laser. The performance of these lasers and a comparison with theoretical predictions were reported in the *Optics Express* publication provided in Appendix A, further developing quasi-three-level Q-switched laser theory.

Chapter 5 described the design, assembly and operation of the cavity-dumped laser. This architecture allowed the generation of pulses of variable energy with duration equal to the resonator round trip time. This overcame the inherent problems of the Q-switched lasers by decoupling the inverse relationship between pulse energy and duration that applies for normal Q-switched lasers. Pulses of up to 10 mJ of 4.5 ns duration at 12 Hz PRF were safely generated, corresponding to over 2 MW of peak power. This is currently the highest peak power achieved from any 1.6 μm Er:YAG laser. These results were reported in the *Optics Letters* publication provided in Appendix A.

As far as we know, these lasers were the first Q-switched and cavity-dumped Er:YAG lasers using CPF slabs. The comparison between them improved our understanding of the advantages and disadvantages of Q-switching compared to cavity-dumping.

6.2 Comparison of Q-switching vs. cavity-dumping

Combining previous knowledge with my project results, a brief comparison of the advantages and disadvantages of Q-switching and cavity-dumping is now provided.

The schematics of the Q-switched (top) and cavity-dumped (bottom) lasers are reproduced in Figure 6.1:

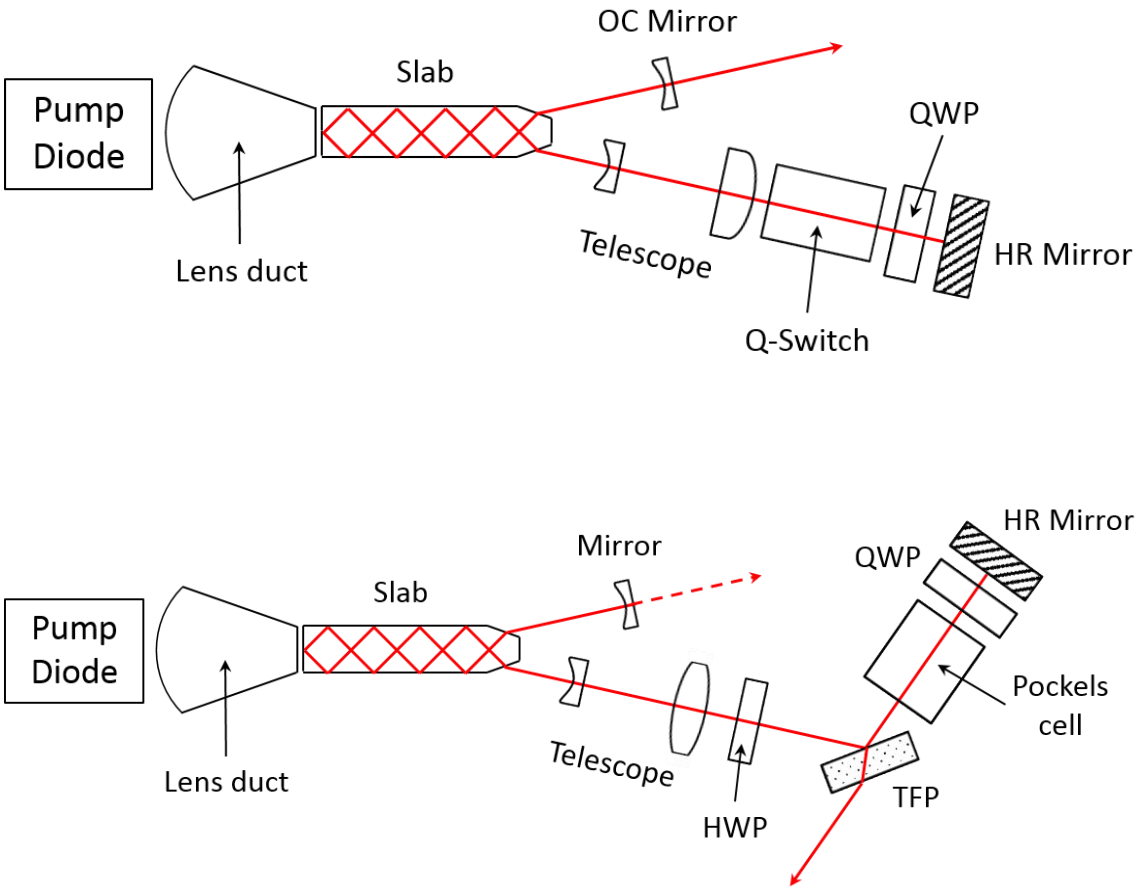

FIGURE 6.1: Comparison of the Q-switched and cavity-dumped Er:YAG lasers.

6.2.1 Advantages and disadvantages of Q-switching

Advantages of Q-switching:

- Q-switching does not require the exceptionally fast HV electronics demanded by a cavity-dumped laser. The HV rise-time must only be less than the pulse build-up time.
- The resonator alignment is easier since it does not include a TFP, half-wave plate and perpendicular HR arm.
- A simpler laser with a smaller parts count has a lower manufacturing cost.

Disadvantages of Q-switching:

- The minimum pulse duration is several times the resonator round trip time, and even longer in Er:YAG lasers due to the low gain.
- Reducing the resonator round-trip time to achieve a shorter pulse duration requires a compact telescopic resonator, which is harder to align.
- The intra-cavity peak power is greater than the peak output power by a factor of $(1 + R)/(1 - R)$. This can lead to optical damage at high peak power.
- Decreasing the output coupler reflectivity reduces the intra-cavity power but increases the threshold power of the laser and increases the pulse duration.

6.2.2 Advantages and disadvantages of cavity-dumping

Advantages of cavity-dumping:

- It is easier to achieve short pulses since pulse duration is set to the resonator round trip time provided the high voltage switching is fast enough.
- Therefore, the resonator can be larger than that for a Q-switched laser.
- Eliminating the out-coupling during the build-up phase reduces threshold power.
- The peak intra-cavity power does not exceed the peak output power of the dumped pulse. This reduces the damage risk if the pulse is dumped at the appropriate time.
- Pulse energy can be controlled by varying pump power and/or dump time.
- Pulse duration can be lengthened without reducing the pulse energy by slowing down the switching time of the Pockels cell, in a process called "throttling" [111].

Disadvantages of cavity-dumping:

- Faster and more expensive HV electronics are required to dump the pulse.
- Alignment of the TFP and perpendicular HR arm is more complicated.
- Appropriate timing of the pulse dumping may be important to prevent damage.

6.3 Further work

The efficiency of our lasers could potentially be improved by spectrally narrowing the pump diode output by using a volume Bragg grating as well as by reflecting some of the un-absorbed pump light back into the slab. Other marginal improvements in efficiency could be achieved through anti-reflective coatings on the entry face of the lens duct.

The efficiency of our cavity-dumped Er:YAG laser could also be improved by reducing losses, namely by increasing the reflectance of the curved mirror and eliminating clipping from the beam on the Pockels cell aperture.

A problem for both lasers, particularly the Q-switched laser, was the tendency of the slab to incur surface damage at high peak powers. This limitation might one day be alleviated by improved polishing techniques that reduce scratch size.

The possibility of increasing the beam size in the slab in order to decrease fluence is worthy of further investigation. This would be achieved by increasing the height of the pumped region in the slab to support a larger fundamental and/or higher order modes, an acceptable solution since range-finding does not require extremely high beam quality. This would also allow the use of more pump power, giving higher pulse energies, although the pulse durations would not decrease.

Using two pump diodes would provide the extra power required to increase the pulse energy with the same PRF, or produce the same pulse energy at higher PRF. For example each pump diode was capable of producing > 40 W peak power on a 20% duty cycle. However these techniques could be more effective for the cavity-dumped laser because the pulse duration is set to equal the resonator round trip time.

Appendix A: Publications

Two papers were published as a direct result of my project:

(1) D. Ottaway, L. Harris and P. Veitch, *"Short-pulse actively Q-switched Er:YAG lasers"*, Optics Express, vol. 24, no. 14, pp. 15341-15350 (2016)

(2) L. Harris, M. Clark, D. Ottaway and P. Veitch, *"Compact cavity-dumped Q-switched Er:YAG laser"*, Optics Letters, vol. 41, no. 18, pp. 4309-4311 (2016)

Research Article | Vol. 24, No. 14 | 11 Jul 2016 | OPTICS EXPRESS 15341

Optics EXPRESS

Short-pulse actively Q-switched Er:YAG lasers

DAVID J OTTAWAY,* LACHLAN HARRIS, AND PETER J. VEITCH

Department of Physics and Institute of Photonics and Advanced Sensing, The University of Adelaide, Adelaide, South Australia, Australia
*david.ottaway@adelaide.edu.au

Abstract: We report the shortest duration pulses obtained to date from an actively Q-switched Er:YAG laser pumped by a low spectral and spatial brightness laser diode. The 14.5 ns, 6 mJ pulses were obtained using a 1470 nm laser diode end-pumped co-planar folded zigzag slab architecture. We also present an analytical model that accurately predicts the pulse energy-duration product achievable from virtually all Q-switched Er:YAG lasers and high repetition rate quasi-three-level Q-switched lasers in general.

OCIS codes: (140.3500) Lasers, erbium; (140.3540) Lasers, Q-switched; (140.3070) Infrared and far-infrared lasers; (140.3580) Lasers, solid-state.

References and links

1. S. D. Setzler, M. P. Francis, Y. E. Young, J. R. Konves, and E. P. Chicklis, "Resonantly pumped eyesafe erbium lasers," IEEE J. Sel. Top. Quantum Electron. **11**, 645–657 (2005).
2. W. Koechner, *Solid-State Laser Engineering* (Springer, 2013).
3. W. G. Wagner and B. A. Lengyel, "Evolution of the giant pulse in a laser," J. Appl. Phys. **34**, 2040–2046 (1963).
4. J. J. Degnan, "Theory of the optimally coupled Q-switched laser," IEEE J. Quantum Electron. **25**, 214–220 (1989).
5. J. J. Degnan, "Optimization of passively Q-switched lasers," IEEE J. Quantum Electron. **31**, 1890–1901 (1995).
6. P. Li, Q. Wang, and D. Gao, "Maximum peak power generation from Q-switched lasers," Opt. Laser Technol. **31**, 247–250 (1999).
7. V.E. Kisel, A.S. Yasukevich, N.V. Kondratyuk and N.V.Kuleshov, "Diode-pumped passively Q-switched high-repetition-rate Yb microchip laser" Quantum Electron. **39**, 1018 (2009).
8. R. J. Beach, "Optimization of quasi-three-level end-pumped Q-switched lasers," IEEE J. Quantum Electron. **31**, 1606–1613 (1995).
9. R. C. Stoneman, R. Hartman, E. A. Schneider, A. I. Malm, S. R. Vetorino, C. G. Garvin, J. V. Pelk, S. M. Hannon, and S. W. Henderson, "Eyesafe 1.6 μm Er: YAG transmitters for coherent laser radar," in *Proceedings of 14th Coherent Laser Radar Conference (CLRC XIV)* (2007).
10. R. D. Stultz, V. Leyva, and K. Spariosu, "Short pulse, high-repetition rate, passively Q-switched Er: yttrium-aluminum-garnet laser at 1.6 microns," Appl. Phys. Lett. **87**, 1118 (2005).
11. J. Kim, J. Sahu, and W. Clarkson, "High-energy Q-switched operation of a fiber-laser-pumped Er: YAG laser," Appl. Phys. B **105**, 263–267 (2011).
12. S. D. Setzler, Y. E. Young, K. J. Snell, P. A. Budni, T. M. Pollak, and E. P. Chicklis, "High-peak-power erbium lasers resonantly pumped by fiber lasers," Proc. SPIE **5332**, 85–96 (2004).
13. M. Wang, J. Meng, X. Hou, and W. Chen, "In-band pumped polarized, narrow-linewidth Er: YAG laser at 1645 nm," Appl. Opt. **53**, 7153–7156 (2014).
14. N. Chang, N. Simakov, D. Hosken, J. Munch, D. Ottaway, and P. Veitch, "Resonantly diode-pumped continuous-wave and Q-switched Er: YAG laser at 1645 nm," Opt. Express **18**, 13673–13678 (2010).
15. I. Kudryashov and A. Katsnelson, "1645-nm Q-switched Er: YAG laser with in-band diode pumping," in *SPIE Defense, Security, and Sensing*, (SPIE, 2010), pp. 76860B–76860B.
16. J. Richards and A. McInnes, "Versatile, efficient, diode-pumped miniature slab laser," Opt. Lett. **20**, 371–373 (1995).
17. J. Eggleston, L. Frantz, and H. Injeyan, "Deviation of the Frantz-Nodvik equation for zig-zag optical path, slab geometry laser amplifiers," IEEE J. Quantum Electron. **25**, 1855–1862 (1989).
18. R. B. Kay and D. Poulios, "Q-switched rate equations for diode side-pumped slab and zigzag slab lasers including gaussian beam shapes," IEEE J. Quantum Electron. **41**, 1278–1284 (2005).
19. R. B. Kay, D. Poulios, D. B. Coyle, P. R. Stysley, and G. B. Clarke, "Derivation of the Frantz-Nodvik equation for diode-side-pumped zigzag slab laser amplifiers with gaussian laser mode and pump beam shapes," IEEE J. Quantum Electron. **47**, 745–749 (2011).

Optics EXPRESS

1. Introduction

Compact and efficient lasers that produce short duration, high energy pulses are required for a variety of field-based laser radar applications, including âĂŸrange-findersâĂŹ for which the pulse duration determines the range resolution and the peak power determines the maximum range. Direct generation of such pulses at 1617 nm or 1645 nm using Q-switched Er:YAG lasers would allow replacement of sources that currently use non-linear materials to frequency down-convert short-duration pulses at 1 μm to the eye-safe band (1.5-1.8 μm). However, short durations are difficult to achieve using Er:YAG because it has inherently low gain as the ions in the upper lasing state are spread between seven relatively closely spaced Stark-shifted levels [1].

There have been many theoretical studies of Q-switched lasers [2-11] but generally they have focused on optimizing the efficiency rather than minimizing the pulse duration. Equations describing the operation of Q-switched lasers were first outlined by Wagner and Lengyel [3]. However, these equations are transcendental and required complicated numerical solutions. Degnan [4, 5] generalized the equations to quasi-three-level lasers by including an inversion reduction factor and used Lagrange multipliers to obtain simpler expressions for the pulse properties for the case where the laser has the optimum output coupling. Li et al. [6] recast Degnans approach to consider the effect of optimizing the reflectivity of the output coupler to maximize the peak output power and showed that it could be increased. Kisel et al. [7] linearized the equations developed for passive Q-switching to develop analytical solutions for pulse repetition frequency of such a laser in the high pulse repetition frequency limit. Beach [8] adopted a different approach and developed equations that did not insist on optimum output coupling and could be evaluated easily using numerical techniques so that design sensitivity studies could be performed. In this paper we study the case of Er:YAG lasers that are actively Q-switched and derive a simple relationship between pulse energy and duration that is applicable to any actively Q-switched Er:YAG lasers and any actively Q-switched quasi-three-level laser operating in the high repetition frequency limit. We used this insight to develop a new laser that produced the shortest duration pulses from an actively Q-switched laser.

The shortest duration pulsed Er:YAG laser reported so far yielded 1.1 ns, 1.6 mJ pulses, produced using an injection-seeded and cavity dumped master-oscillator-power-amplifier system, an architecture that was chosen to prevent optical damage [9]. The gain media were pumped by Er-Yb doped fiber lasers (EDFL) tuned to the 1532 nm absorption line of Er:YAG by an external cavity. Passively Q-switching an EDFL-pumped Er:YAG laser using a ZnSe saturable absorber yielded 6.8 ns, 0.24 mJ pulses [10]. This short pulse duration was achieved because the passive Q-switch was very small, enabling the use of an extremely compact resonator. However, the damage threshold of ZnSe is low, which limits the power scaling of this approach.

The shortest pulses produced by an actively Q-switched oscillator have used EDFL-pumping, yielding pulse durations and energies of 20 ns and 30.5 mJ [11] and 21 ns and 3.4 mJ [12]. It would thus appear that passively Q-switched Er:YAG lasers can generate ca. 7 ns pulses but perhaps only with low energies, and the shortest pulse duration for an actively Q-switched Er:YAG laser is ca. 20 ns.

Compact and efficient Q-switched Er:YAG lasers should be achievable using direct laser-diode pumping but short duration and high energy pulses from such systems have yet to be demonstrated. An acousto-optically-Q-switched Er:YAG laser pumped using a fiber-coupled bandwdith-narrowed 1532 nm laser diode produced 95 ns, 12 mJ pulses [13]. Diode pumping using a close-coupled broadband 1470 nm diode has also been used to demonstrate 100 ns, 2.3 mJ pulses at 250 Hz Pulse Repetition Frequency (PRF) with a total optical-to-optical efficiency of 2.5% [14]. Diode pumping using a spectrally narrowed 1470 nm laser diode has been demonstrated to produce 27 ns, 10.5 mJ pulses at 20 Hz PRF [15].

We report the results of an investigation of Q-switched Er:YAG lasers with an emphasis on minimizing the pulse duration, rather than optimizing the efficiency. Our approach provides a

Research Article | Vol. 24, No. 14 | 11 Jul 2016 | OPTICS EXPRESS 15343
Optics EXPRESS

new simple expression for the pulses produced by short-duration Q-switched lasers with quasi-three-level gain media. Importantly, we validate these expressions and demonstrate the shortest duration pulses yet achieved from an actively Q-switched Er:YAG laser at 1.6 μm.

A laser gain medium architecture with high gain was crucial to obtaining these results as it allowed the use of low reflectance output couplers which reduces the ratio of intra-cavity power to output power and hence allowed us to avoid optical damage. Thus, we used a folded zigzag slab architecture [16], which allows end-pumping and thus low doping. Zigzag slabs offer additional advantages, including reduced thermal lensing, increased gain and easier mounting [2]. However, they also add some theoretical complexity because of the overlapping laser fields. Eggleston et al. [17] addressed this issue by using a so-called âĂIJaverage flux approximationâĂİ. Kay et al. used this technique for non-uniformly-pumped zigzag slabs, developing both a numerical approach [18] and an analytical expression [19] for calculating the output energy assuming a Gaussian-intensity profile pulse. We assume uniform pumping, as the pump absorption bleaches due to the low doping and thus the population inversion is more uniformly distributed along the gain medium. We also introduce an âĂIJoverlap factorâĂİ than can be adjusted to suit the gain medium architecture.

The Er:YAG laser we describe here is a compact electro-optically-Q-switched laser that is pumped using a broadband single-bar 1470 nm diode and produces 14.5 ns, 6 mJ pulses.

The outline of the paper is as follows: in Section 2 we present a new model that gives a simple analytical relationship between pulse energy and duration. In Section 3 we describe the laser system that was used to validate this new model and demonstrate short pulses from an actively Q-switched laser. We compare the properties of observed pulses with predictions of the model in Section 4.

2. Theory

The Q-switched laser model we present in this section is an extension of the work by Degnan [4]. It assumes that the gain medium has only two energy manifolds whose combined population is constant, ie $N_{eff} \equiv N_1 + N_2$ where N_1 and N_2 are the population densities of lower and upper lasing manifolds respectively. This is a valid assumption for resonant pumping if the effect of energy transfer processes and excited state absorption are negligible due to low dopant concentrations, in which case N_{eff} is the total dopant concentration. The aforementioned assumption can still hold if energy transfer processes are significant during the pumping time but insignificant during evolution of the Q-switch pulse which is much shorter. In this case N_{eff} will be less than the total dopant concentration.

The time dependent behavior of the photon number density of the spatially averaged laser mode traveling in one direction within the resonator (Eq. 1 of [4]) is given by

$$\frac{d\phi}{dt} = \left(\frac{\sigma L(f_2 N_2 - f_1 N_1)}{t_r} - \frac{1}{t_c}\right)\phi \tag{1}$$

where σ is the cross section of the lasing transition, L is the round-trip path length within the gain medium, t_r is the resonator round-trip time, f_2 and f_1 are the Boltzmann factors for the upper and lower lasing states, and the cavity lifetime t_c is given by

$$t_c = -\frac{t_r}{\delta + \ln(R)} \tag{2}$$

where R is the reflectivity of the output coupler, $\delta = \ln(1 - L_i)$ and L_i is the fractional round trip loss within the resonator

The evolution of the population densities during a Q-switched pulse is

$$\frac{dN_2}{dt} = -\frac{dN_1}{dt} = -\sigma B c \phi (f_2 N_2 - f_1 N_1) \tag{3}$$

where c is the speed of light in a vacuum and we have introduced a new factor B that accounts for the laser mode overlapping with itself in the gain medium and therefore the effective intensity that interacts with the population inversion. We expect $B = 1$ for a non-zigzag ring resonator, $B = 2$ for a non-zigzag linear resonator and $B = 4$ for a zigzag linear resonator.

Combining Eq. (1) and Eq. (3) gives

$$\frac{d\phi}{dN_2} = -\frac{L}{Bct_r} + \frac{1}{\sigma Bc(f_2N_2 - f_1N_1)t_c} \tag{4}$$

Integrating Eq. (4), defining $N_2 = N_i$ at the start of the pulse and assuming $\phi(N_2 = N_i) = 0$, gives

$$\phi(N_2) = \frac{(N_i - N_2)L}{Bct_r} - \frac{1}{t_c\sigma Bc(f_1 + f_2)} \ln\left(\frac{f_2N_i + f_1N_i - f_1N_{eff}}{f_2N_2 + f_1N_2 - f_1N_{eff}}\right) \tag{5}$$

At the end of the pulse $\phi = 0$ and $N_2 = N_f$. Thus

$$0 = (N_i - N_f) - \frac{t_r}{\sigma Lt_c(f_1 + f_2)} \ln\left(\frac{f_2N_i + f_1N_i - f_1N_{eff}}{f_2N_f + f_1N_f - f_1N_{eff}}\right) \tag{6}$$

At the peak of the pulse the round-trip gain is 1 and hence $\frac{d\phi}{dt} = 0$ and $N_2 = N_t$, the threshold population density. Thus Eq. (1) gives

$$N_t = \frac{f_1}{f_1 + f_2}N_{eff} + \frac{\delta - \ln(R)}{\sigma L(f_1 + f_2)} = N_{trans} + \frac{\delta - \ln(R)}{\sigma L(f_1 + f_2)} \tag{7}$$

where N_{trans} is the upper state population density at which the gain medium becomes transparent to the laser radiation.

Equation (6) is transcendental and must be solved numerically to determine N_f for a given N_i. However, if the initial population density of the upper manifold (N_i) is moderately larger than the threshold population density (N_t) then, as shown in Appendix A,

$$N_t - N_f = N_i - N_t \tag{8}$$

which can be written $\Delta N_f = \Delta N_i$ where $\Delta N_i = N_i - N_t$ and $\Delta N_f = N_t - N_f$.

A typical numerical solution of Eq. (6) and Eq. (7), for the parameters shown in Table 1, is plotted in Fig. 1 (left). This figure shows, as expected, that if ΔN_i is small then Eq. (8) holds. The range of N_i for which this approximation is valid will increase as the reflectivity of the output coupler decreases, as $N_t - N_{trans}$ increases.

If $N_i >> N_t$ then the final population density (N_f) asymptotes towards N_{trans}, the smallest value of N_f for which Eq. (6) is real valued (ie $f_2N_f + f_1N_f - f_1N_{eff} > 0$).

Table 1. **Parameters used in the numerical simulation**

Parameter	Value	Parameter	Value
σ_{1645}	2.7×10^{-20} cm ^{2}	R	0.4
t_r	1.33 ns	L_i	0.1
A	2.6×10^{-3} cm ^{2}	B	4
f_1	0.02	f_2	0.21
L	10.7 cm		

We now determine the output power, pulse energy and duration by considering the evolution of the pulse. The output power is related to the photon density (Eq. A.12 of [4]) by

$$P(N_2) = -h\gamma Ac\ln(R)\phi(N_2) \tag{9}$$

Research Article | Vol. 24, No. 14 | 11 Jul 2016 | OPTICS EXPRESS 15345
Optics EXPRESS

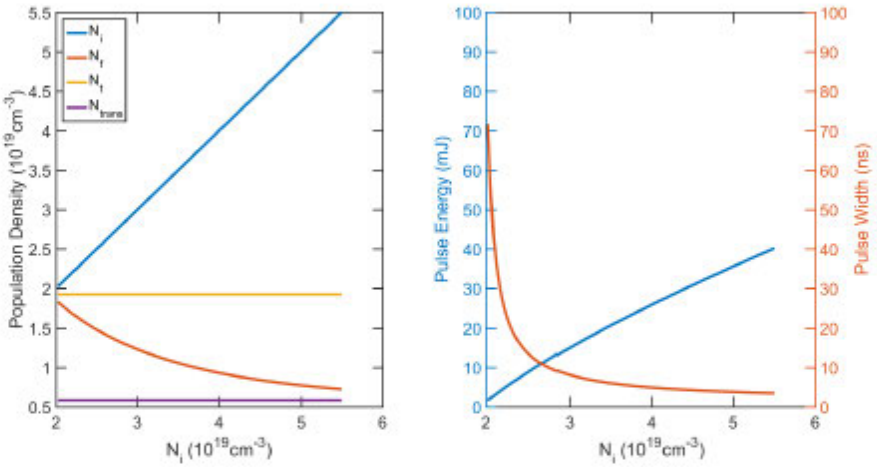

Fig. 1. Left: A plot of the upper manifold population densities at the start (N_i) and end (N_f) of the pulse for a given initial population density (N_i). Right: A plot of the dependence of the pulse energy and width on the initial population density.

where $\phi(N_2)$ is given by Eq. (5) , h is Planck's constant and γ is the frequency of the laser light. The energy of the output pulse is obtained by integrating Eq. (9) , giving

$$E = \int_{N_i}^{N_f} P(N_2)dN_2 = -\frac{h\gamma A \ln(R)}{\sigma B(f_1+f_2)} \ln\left(\frac{f_2N_i + f_1N_i - f_1N_{eff}}{f_2N_f + f_1N_f - f_1N_{eff}}\right) \tag{10}$$

This equation can be simplified by combining it with Eq. (6) giving

$$E = \frac{-h\gamma AL\ln(R)}{B}\frac{N_i - N_f}{\delta - \ln(R)} \tag{11}$$

The peak power occurs when $N_2 = N_t$ and hence is given by

$$P_p = \frac{-h\gamma A\ln(R)}{B} \times \left(\frac{(N_i - N_t)L}{t_r} - \frac{1}{\sigma t_c(f_1+f_2)} \ln\left(\frac{f_2N_i + f_1N_i - f_1N_{eff}}{f_2N_t + f_1N_t - f_1N_{eff}}\right)\right) \tag{12}$$

This equation can be simplified by using a series expansion in the small ΔN_i regime, giving

$$P_p = \frac{-\ln(R)}{\delta - \ln(R)} \frac{h\gamma A\sigma L^2(f_2+f_1)(N_i - N_t)^2}{2Bt_r} \tag{13}$$

A characteristic pulse width (Δt) can be calculated, following [4], by dividing the pulse energy by the peak power. The dependence of the pulse energy and width on the initial population density in the upper manifold is plotted in Fig. 1 (Right).

In the small ΔN_i limit

$$E \times \Delta t = \frac{E^2}{P_{peak}} = \frac{-8h\gamma A\ln(R)t_c}{B(f_1+f_2)\sigma} = \frac{8h\gamma At_r}{B(f_1+f_2)\sigma}\frac{-\ln(R)}{\delta - \ln(R)} \tag{14}$$

and thus $\Delta t^{-1} \propto E$ and $E \times \Delta t / A \propto t_r$

The inverse pulse width and the pulse energy are plotted in Fig. 2 for the complete numerical solution and the small ΔN_i solution, using the parameters listed in Table 1. Fig. 2 shows that the small ΔN_i approximation is accurate to within 10 % to an output energy of 30 mJ. An output energy that is significantly higher than the damage threshold for this laser.

Optics EXPRESS

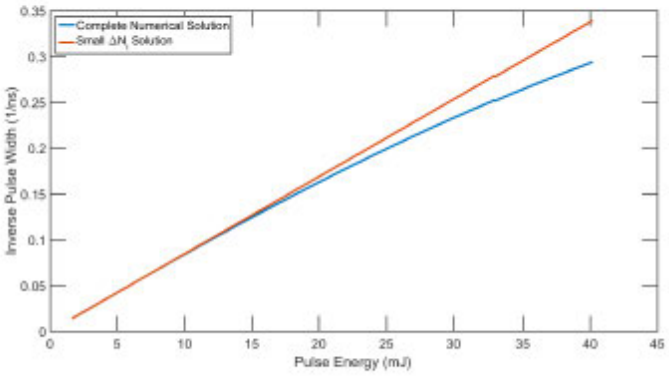

Fig. 2. Comparison of the pulse duration versus pulse energy for the complete numerical solution and the small ΔN_i solution described in Eq. (14)

3. Laser description

A schematic of the laser is shown in Fig. 3. The 0.5 at.% Er:YAG gain medium uses a coplanar-folded-zigzag-slab (CPFS) architecture [16], which has Brewster-angled entrance and exit faces. This geometry maximizes the gain-length product for a given absorbed pump density because the laser mode passes the same volume four times. It also allows close-coupled end pumping that conveniently separates the lasing mode and the pump light without the need for dichroic optical coatings on the slab. Two slab lengths were used: 21 mm and 35 mm. Both slabs were 2.0 mm wide (in zigzag plane), 4.0 mm high and were mounted in a laser head consisting of two water-cooled copper blocks. Indium was placed between the slab and copper blocks to provide stress relief and facilitate cooling.

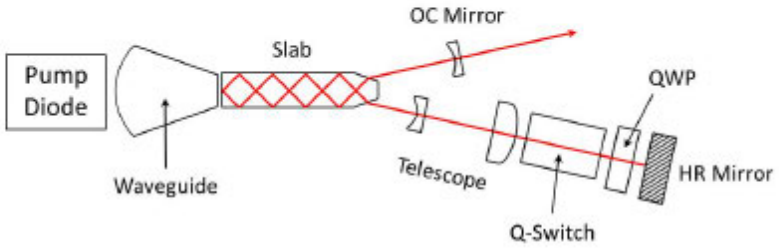

Fig. 3. Schematic of the Q-switched laser incorporating the CPFS slab.

The roundtrip loss of these slabs were measured using a 1319 nm wavelength CW laser. This wavelength was used to separate the scattering loss from the ground state re-absorption that occurs when a wavelength of 1.6 μm is used. It was found that the round-trip loss at this wavelength was 10% for the shorter 21 mm slab and 14% for the longer 35 mm slab. This relatively high loss was attributed to the high number of internal bounces (21 for short slab and 35 for long slab) required for this geometry.

The gain medium was pumped by a single-array fast-axis-collimated diode, the output of which was guided into the slab using a tapered lens duct, producing a 0.6 mm high pumped region. The laser resonator used a flat HR mirror and 20 cm radius-of-curvature output coupler (OC). A telescope is used to expand the intra-cavity mode and decrease the fluence at the RTP Q-switch and quarter-wave plate (QWP).

Research Article | Vol. 24, No. 14 | 11 Jul 2016 | OPTICS EXPRESS 15347
Optics EXPRESS

The laser was initially tested in long-pulse mode using 10 ms pump pulses at 12 Hz repetition rate with peak pump powers of up to 60 W, corresponding to a 600 mJ pump pulse. A comparison of the output pulse energy for both slabs against a range of output coupler reflectivities is shown in Fig. 4 and 5.

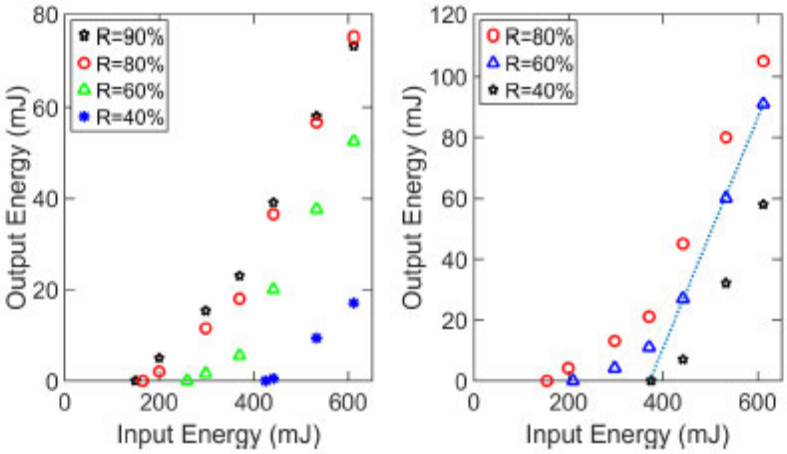

Fig. 4. Plot of the output energy versus incident energy for the laser in long-pulse mode for the short 21mm slab (Left) and the long slab 35 mm slab (Right). The slope of the solid line corresponds to a slope efficiency of 40%.

The threshold pump energy is relatively large for both slabs due to the quasi-three-level nature of Er:YAG. A significant fraction of this energy is needed to make the Er:YAG transparent, the remainder is used to overcome output coupling and scatter losses. Both systems have similar threshold energies because the short slab does not absorb all of the pump light.

The additional gain and stored energy in the longer slab allowed the use of a less reflective output coupler, resulting in increased efficiency, as shown in Fig. 5. The highest slope efficiency was achieved using a R = 60% output coupler as shown by the solid line in Fig. 4 (Right); the 40% slope efficiency compared to the energy emitted by the pump source is only slight less than that reported by Setzler [12] and yet was achieved using a cheap low spectral and spatial brightness laser diode pump source rather than an EDFL pump source.

It is thus apparent that the CPFS architecture enables a high-round-trip gain and higher output coupling with minimal loss of slope efficiency. Unfortunately, the extra-gain of the long CPFS slab will not significantly reduce the duration of the Q-switched pulses compared to rod architectures [12] as the resonator round-trip time is also increased.

Thus, we chose to use a R = 40% output coupler in the Q-switched laser to further reduce the intra-cavity peak power and enable increased pulse energy. The shortest duration pulses were achieved using the short slab, with duration of 14.5 ± 0.2 ns and average pulse energy of 6 mJ at 12 Hz pulse repetition frequency. A plot of this pulse is shown in Fig. 6. A plot of the pulse duration and output energy versus input energy for this slab is included as Fig. 7

Er:YAG lasers can operate at either 1617 nm or 1645 nm, as determined by the upper manifold population density at the start of the pulse. The 1617 nm transition has a higher cross section but higher re-absorption losses, which reduce as ions are removed from the ground state. Thus, lasing occurs at 1617 nm when the average upper manifold population density exceeds

$$N = \frac{N_{eff}(\sigma_{1617} f_{1@1617} - \sigma_{1645} f_{1@1645})}{\sigma_{1645}(f_{2@1645} + f_{1@1645}) - \sigma_{1617}(f_{2@1617} + f_{1@1617})} \quad (15)$$

Optics EXPRESS

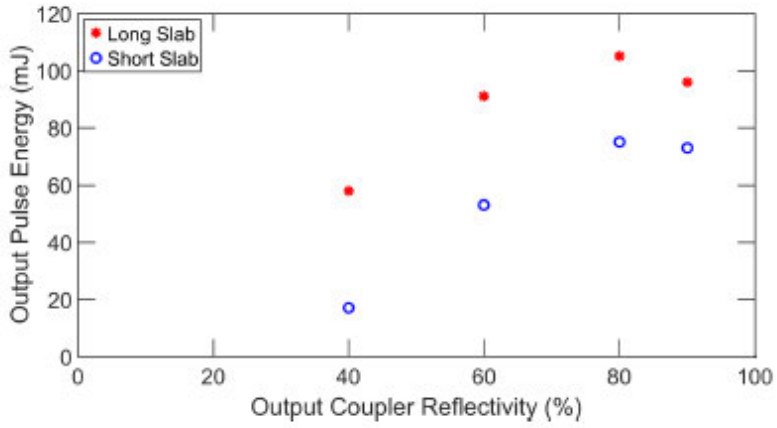

Fig. 5. Output pulse energy in long pulse-mode for both slabs versus output coupler reflectivity for an input pump pulse energy of 600 mJ.

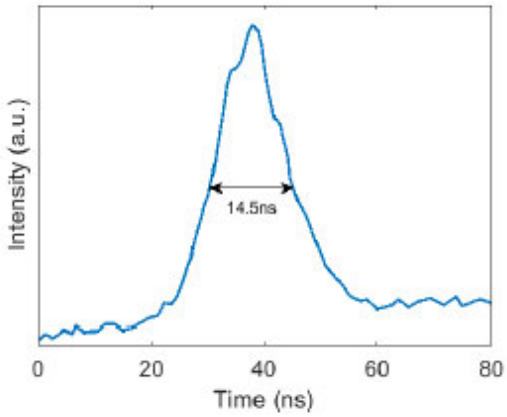

Fig. 6. Plot of the shape of the shortest duration pulse. The pulse shape was measured using an InGaAs photodiode with a 200 ps rise time and a 200 MHz bandwidth oscilloscope.

The required gain at threshold is dominated by the output coupling fraction when its value is high. In this case the shorter slab requires a greater population inversion to achieve the same gain since its length is reduced. Hence it will lase at 1617 nm whilst the longer slab will tend to lase at 1645 nm.

4. Comparison of measured and predicted results

The pulse energy (E) and duration (Δt) were measured for R = 40% and a variety of pump powers, slab lengths and cavity round-trip times, which was varied by moving the HR mirror. The inverse relationship between pulse energy and pulse duration is demonstrated in Fig. 8(left) by plotting $1/\Delta t$ versus E for a range of round trip times (t_r) when using the longer slab. The solid lines are linear fits.

The accuracy of the model is further demonstrated in Fig. 8(right), in which $E\Delta t/A$ is plotted as a function of cavity round trip. The $E\Delta t$ product was obtained by varying the pump energy so that a range of pulse energy and pulse duration combinations were obtained and the results were

Research Article | Vol. 24, No. 14 | 11 Jul 2016 | OPTICS EXPRESS 15349
Optics EXPRESS

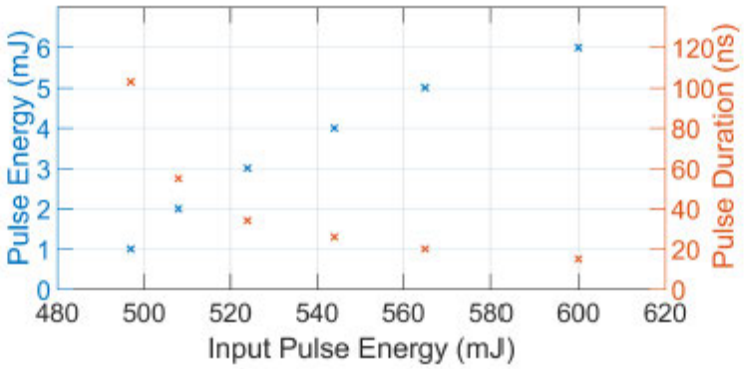

Fig. 7. Plot of the output energy and pulse duration versus input energy for the laser operated in Q-switched mode for the short 21 mm slab.

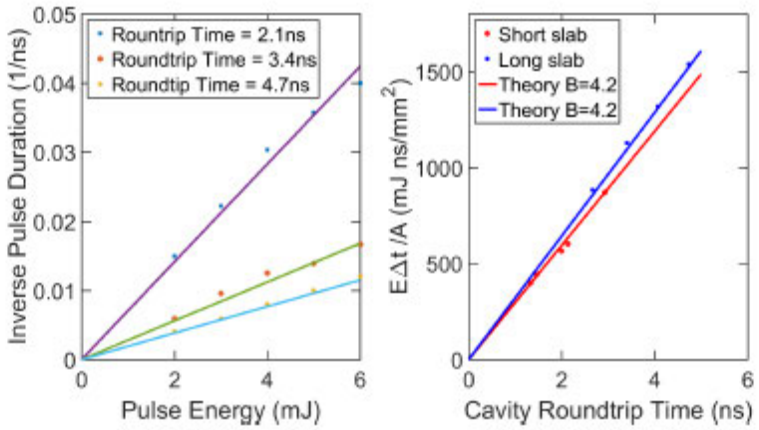

Fig. 8. Left: Plot of the inverse of pulse duration versus pulse energy for a range of different cavity round trip times. Right: Plot of the $E\Delta t/A$ versus t_r for the two different slab lengths. The solid lines are predicted by Eq. (14) with the only free parameter being the beam overlap factor B

averaged. The error on the mean of these quantities was 5% or less. The mode area was obtained using a Gaussian resonator beam modeling package. Since the longer slab will lase at 1645 nm we used the parameters given in Table 1. For the shorter slab we use the parameters for 1617 nm which are $\sigma = 2.9 \times 10^{-20}$ cm ^{2} and $f_1 = 0.036$. The only free parameter in the solid line in Fig. 8(right) was the beam overlap factor, B. To obtain an excellent fit we required the value of B to 4.2 rather than the expected value of 4. This difference can be explained by a 5% error in either the cross sections, area of the mode or the calibration of the power meter.

5. Conclusion

We have described a compact single-gain medium actively Q-switched Er:YAG laser that produced 14.5 ns, 6 mJ pulses. The laser used a CPFS gain medium end-pumped by a low spectral and spatial brightness 1470nm laser diode. Shorter pulses and the associated increase in their pulse energy were prevented by optical damage to the laser crystal.

We have also presented and experimentally validated a simple analytical theory that demonstrates that the product of pulse energy and duration of an actively Q-switched quasi-three-level lasers is constant when operated near threshold. This approximation is valid for most Er:YAG lasers because of the high pump intensity required to achieve threshold, and most quasi-three-level lasers that are operated at a high repetition rate.

Unfortunately, the model predicts that shorter duration pulses necessarily have higher fluence, which will result in laser induced damage. The only way to get shorter duration pulses is to further reduce the round trip time of the resonator.

A. Derivation of Eq. (8)

The transcendental Eq. (6) can be combined with the definition of N_t (see Eq. (7)) to form the following equation:

$$0 = (N_i - N_f) - \frac{(f_2 + f_1)N_t - f_1 N_{eff}}{(f_1 + f_2)} \ln\left(\frac{f_2 N_i + f_1 N_i - f_1 N_{eff}}{f_2 N_f + f_1 N_f - f_1 N_{eff}}\right) \tag{16}$$

By introducing $\Delta N_i = N_i - N_t$ and $\Delta N_f = N_t - N_f$, substituting them into Eq. (16) and then performing a second order Taylor's series expansion about $\Delta N_f = \Delta N_i = 0$, Eq. (16) can be re-written as:

$$0 = \frac{\Delta N_i^2 - \Delta N_f^2}{2(N_t(f_2 + f_1) - f_1 N_{eff})} = \frac{(N_i + N_f - 2N_t)(N_i - N_f)}{2(N_t(f_2 + f_1) - f_1 N_{eff})} \tag{17}$$

Eq. (17) is only valid above threshold ($N_i > N_f$) if $N_i + N_f - 2N_t = 0$.

Acknowledgments

The authors acknowledge Martin O'Connor and Gerry Smith from BAE Systems Australia (Holden Hill) for useful discussions. This work was financially supported by BAE Systems Australia and the Australian Research Council under ARC Linkage Grant LP110200734

Optics Letters

Compact cavity-dumped Q-switched Er:YAG laser

LACHLAN HARRIS, MYLES CLARK, PETER VEITCH, AND DAVID OTTAWAY*

Department of Physics and the Institute of Photonics and Advanced Sensing (IPAS), The University of Adelaide, South Australia 5005, Australia
**Corresponding author: david.ottaway@adelaide.edu.au*

Received 13 June 2016; accepted 15 August 2016; posted 25 August 2016 (Doc. ID 267739); published 13 September 2016

We report a compact cavity-dumped Q-switched Er:YAG laser that produces pulses with 4.5 ns full width at half-maximum duration and 10 mJ energy. To the best of our knowledge, the resulting 2 MW peak power is the highest reported to date from a 1645 nm Er:YAG laser.

OCIS codes: (140.3500) Lasers, erbium; (140.3480) Lasers, diode-pumped; (140.3538) Lasers, pulsed.

http://dx.doi.org/10.1364/OL.41.004309

High peak power lasers that emit in the "eye-safe" wavelength band (1.4–1.8 μm) are required for a variety of remote sensing applications. For example, high-precision, long-distance range-finding applications demand pulses with a high peak power and a short duration. Practical considerations in the detection system often mean that it is not possible to benefit from the increase in peak power achieved when the pulse durations are reduced below a few nanoseconds. Thus, high-energy pulses are also required. Currently, eye-safe range-finders use pulses produced by frequency-shifting the 1064 nm output of a Q-switched Nd:YAG laser using an optical parametric oscillator.

Er:YAG lasers, by contrast, can emit directly at 1617 or 1645 nm. However, it is difficult to achieve short duration pulses because Er:YAG is an inherently low gain system: stark splitting of the upper lasing level means that only 21% of its population is available at any time which limits the gain. Further, ground state absorption means that a significant upper-level population density is required. This is made more challenging because energy transfer upconversion (ETU) processes remove ions from the upper lasing level [1].

These limitations are particularly important when trying to achieve short duration pulses using Q-switching [2]. The shortest duration pulses from a passively Q-switched Er:YAG laser were 7 ns with a peak power of only 35 kW [3], while the shortest actively Q-switched Er:YAG lasers pulses had durations of 14 and <20 ns [4,5] with peak powers of 400 kW and 1.5 MW, respectively.

The laser reported in [4] used a compact resonator and a co-planar folded zigzag slab (CPFS) gain medium [6], as it provides the highest gain-length product for a given absorbed pump power and, thus, enabled the production of short-duration Q-switched pulses. Additionally, [4] showed that the pulse duration is inversely proportional to the pulse energy in a laser optimized for the production of short duration pulses. Thus, shorter duration pulses will necessarily have higher energy. Unfortunately, the surfaces of the CPFS gain medium at which the lasing mode is reflected via total internal reflection proved to be vulnerable to very high intra-cavity peak powers. This necessitated a change of approach to cavity-dumped Q-switched lasers.

Cavity-dumped Q-switched lasers are less common than Q-switched lasers, but have three important advantages. First, the lasing threshold is reduced, since there is no output coupling during the growth of the giant pulse within the resonator. Second, the pulse duration can be as short as the round-trip time of the resonator, relaxing the requirement on the length of the resonator and the round-trip gain. Finally, the intra-cavity peak power is no greater than the output peak power because the entire pulse is switched out, rather than being the result of transmission through a partially reflecting mirror. The main drawbacks of cavity dumping are the need for an additional intra-resonator polarizer and the need for a higher speed control of the high voltage required for the Pockels cell (PC) Q-switch.

Cavity-dumped lasers have been used to produce short duration pulses from a variety of gain media using both electro-optic PC [7,8] and acousto-optic-modulator switches (AOM) [9]. The latter is limited by the rise time of the AOM due to the speed of sound in the crystal. Hence, electro-optical switches are used to produce the shortest pulses. The shortest duration, high peak power pulses reported to date from an Er:YAG laser had a pulse duration of 1.1 ns and a peak power of 1.5 MW [8]. These pulses were produced by cavity dumping a partially evolved Q-switched pulse from an injection-seeded fiber-laser-pumped Er:YAG ring oscillator, yielding pulses with an energy of 0.22 mJ. These pulses were subsequently amplified to 1.6 mJ using a double-pass amplifier.

We report the development of a compact cavity-dumped Q-switched Er:YAG laser that is pumped by an inexpensive, broadband 1.47 μm laser diode array, and produces pulses with an energy of 10 mJ per and duration of 4.5 ns at 1645 nm from a single oscillator To the best of our knowledge, this is the highest peak power reported at this wavelength.

A schematic of the cavity-dumped Q-switched laser is shown in Fig. 1. A CPFS gain medium [6] was used, as it does not require any optical coatings because the lasing mode enters and exits the slab at a Brewster's angle, and can be confined within the slab by total internal reflection at the side and

0146-9592/16/184309-03 Journal © 2016 Optical Society of America

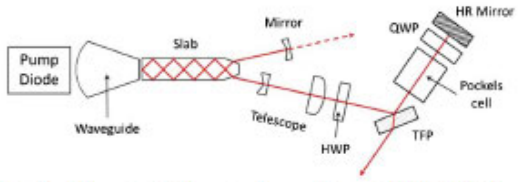

Fig. 1. Schematic of the cavity-dumped *Q*-switched Er:YAG laser. The red line represents the path of the laser mode. HWP, half-wave plate; TFP, thin-film polarizer; QWP, quarter-wave plate; HR, high reflectance. The mirror was slightly transmitting to allow convenient diagnostics of the stored energy evolution using the dashed beam.

end surfaces if the slab is cooled through the top and bottom surfaces. Additionally, it can provide a long pump absorption length if end-pumped, as shown, thus allowing the use of broadband low-brightness pump sources and low-concentration Er dopings.

The gain medium is end-pumped by a fast-axis-collimated broadband 1.47 μm InGaAsP laser diode that is mounted on a water-cooled copper block. The diode produces 10 ms duration pulses with peak power of up to 60 W at a 12 Hz pulse repetition frequency. A glass lens duct was used to guide the pump light into the slab. In the fast-axis (vertical) direction, the height of the pumped region was 0.7 mm. In the slow-axis (horizontal) direction, the rapidly diverging pump light is trapped within the slab by total internal reflection at the slab surfaces.

Initial tests used the 0.5 at. % Er-doped slab used for the earlier *Q*-switched laser development [4]. However, the high threshold pump density and the small size of the laser mode limited the pulse energy to a few millijoules before laser-induced damage occurred.

The results presented here were obtained using a 0.25 at. % doped slab, which reduced losses due to ETU and allowed a larger lasing mode, but also required the use of a longer slab. The Er:YAG slab was 67.2 mm long, 4.0 mm wide, and 4.0 mm high. It was mounted in a laser head consisting of two water-cooled copper blocks that were mounted to the top and bottom surfaces. Stress relief and excellent thermal contact was achieved by placing indium sheets between the Er:YAG slab and the copper blocks.

The resonator incorporates a telescope to reduce the fluence incident on the half-wave plate (HWP), a thin-film polarizer (TFP), a rubidium–titanyl–phosphate PC and quarter-wave plate (QWP) to minimize the possibility of laser-induced damage. All of these components were anti-reflection coated.

The HWP is used to rotate the polarization of the lasing mode from π polarization in the gain medium to σ polarization at the TFP, where it is reflected. This configuration maximizes the efficiency of the *Q*-switched laser as TFPs generally are more efficient at reflecting σ polarization than transmitting π polarization.

The combination of the TFP, PC, and QWP enables both *Q*-switching and the cavity dumping. The orientation of the QWP was adjusted to provide high-output coupling during pumping without any voltage applied to the PC. The high-output coupling during pumping prevents lasing and allows the buildup of a significant population inversion. Once pumping is complete, the cavity is *Q*-switched to a low loss mode by applying a quarter-wave voltage (1.1 kV here) to the PC. This reduces the output coupling to zero and allows the rapid buildup of the intra-resonator energy, limited only by the losses in the cavity. Once the desired stored laser mode energy is achieved, it is "dumped" (out-coupled) through the TFP by rapidly removing the voltage applied to the PC.

The temporal variation in the energy stored in the resonator, as observed through the mirror, is plotted in Fig. 2. The asymmetry in this pulse shape is due to low output coupling which leads to a rapid rise time and a slower fall time.

The maximum pulse energy and peak power will occur if the cavity is dumped near the peak. However, the stored energy can also be dumped before the peak is reached to yield a so-called partially evolved *Q*-switched pulse. This results in a small reduction in output energy, but significantly reduces the fluence to which the laser components are exposed and, thus, reduces the likelihood of laser-induced damage. Note that Fig. 2 shows the case in which 52 W peak pump power was used as this plot cannot be obtained when the maximum pump power (57 W) is used since laser-induced damage will result.

The effective operation of a cavity-dumped laser requires electronics that can rapidly switch the high voltage on the PC. In particular, it must be capable of a switch-off time much less than the resonator round-trip time, in this case 4.5 ns. We used a custom Starfire HV pulser from Quantum Technology. A typical cavity-dumped pulse is plotted in Fig. 3. We attribute the slight plateau and oscillation at the end of the pulse to ringing in the photodetector.

The threshold peak pump power for a cavity-dumped *Q*-switched operation was approximately 34 W, corresponding to a pump-pulse energy of 340 mJ. The energy of the laser pulses is plotted as a function of time delay after *Q*-switching for several pump powers in Fig. 4. As would be expected, increasing the pump pulse energy decreases the pulse buildup time. All of the pulses had a wavelength of 1645 nm.

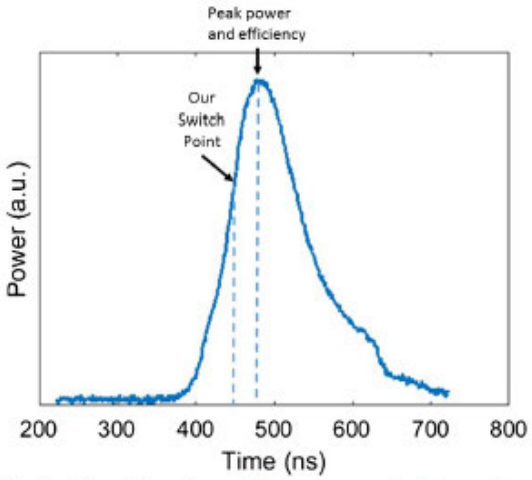

Fig. 2. Plot of the evolution of the energy stored in the cavity laser mode, as observed through the partially transmitting mirror when 52 W of pump power is used, and the intracavity mode is not dumped through the TFP.

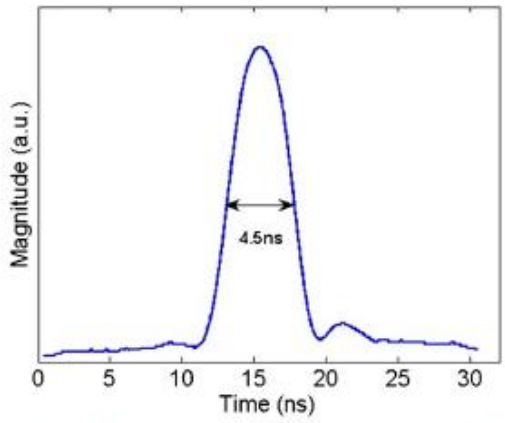

Fig. 3. Plot of a typical cavity-dumped pulse with 4.5 ns FWHM duration. The detector used had a rise time of 180 ps, and the oscilloscope had a bandwidth of 200 MHz with a sample rate of 2 Gs/s.

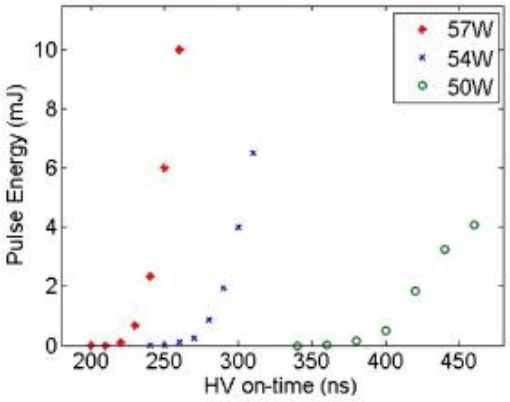

Fig. 4. Plot of pulse energies as a function of time delay after *Q*-switching for several pump powers.

The maximum output pulse energy was a 10 mJ, with a 4.5 ns full width at half-maximum duration, corresponding to a peak power of 2.0 MW. A typical beam profile with fits to a TEM_{00} Gaussian is shown as Fig. 5. The ellipticity of the laser mode is due to the asymmetry of the laser slab geometry.

In summary, we have demonstrated a compact cavity-dumped *Q*-switched Er:YAG laser that can produce pulsed TEM_{00} beams at 1645 nm with 10 mJ of pulse energy and a 4.5 ns duration. The 2.0 MW peak power is the highest reported for an Er:YAG laser at 1645 nm. Additionally, the peak power could be doubled simply by polarization combining an additional laser diode array and increasing the area of the pumped gain volume. Thus, this system would be competitive with the OPO-shifted *Q*-switched Nd:YAG systems currently used in range-finder lidar systems.

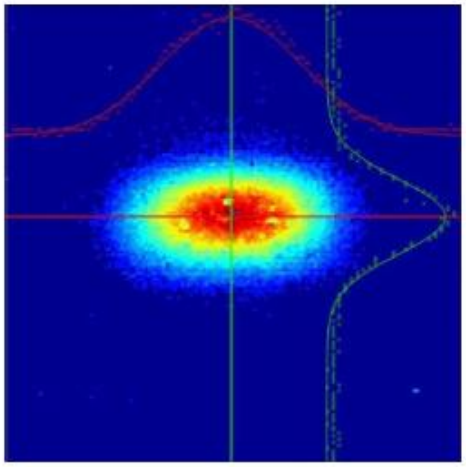

Fig. 5. Typical beam profile of the output of the cavity-dumped laser output showing the fits to Gaussian.

Funding. Australian Research Council (ARC) (LP110200734); BAE Systems Australia (Holden Hill).

Acknowledgment. The authors acknowledge Martin O'Connor and Gerry Smith from BAE Systems Australia (Holden Hill) for useful discussions. We also acknowledge technical support from Bob Chivell from the University of Adelaide, School of Physical Sciences workshop.

REFERENCES

1. S. D. Setzler, M. P. Francis, Y. E. Young, J. R. Konves, and E. P. Chicklis, IEEE J. Sel. Top. Quantum Electron. **11**, 645 (2005).
2. N. P. Barnes, B. M. Walsh, F. Amzajerdian, D. J. Reichle, G. E. Busch, and W. A. Carrion, IEEE J. Quantum Electron. **49**, 238 (2013).
3. R. D. Stultz, V. Leyva, and K. Spariosu, Appl. Phys. Lett. **87**, 241118 (2005).
4. D. J. Ottaway, L. Harris, and P. J. Veitch, Opt. Express **24**, 15341 (2016).
5. J. Kim, J. Sahu, and W. Clarkson, Appl. Phys. B **105**, 263 (2011).
6. J. Richards and A. McInnes, Opt. Lett. **20**, 371 (1995).
7. Y. F. Ma, J. W. Zhang, H. Li, and X. Yu, Laser Phys. Lett. **9**, 561 (2012).
8. R. C. Stoneman, R. Hartman, E. A. Schneider, A. I. Malm, S. R. Vetorino, C. G. Garvin, J. V. Pelk, S. M. Hannon, and S. W. Henderson, in *Proceedings of 14th Laser Radar Conference* (2007).
9. B. Yao, S. Hongwei, D. Tongyu, S. Zuochun, J. Youlun, C. Guoqing, and W. Yuezhu, Appl. Opt. **53**, D29 (2014).

Appendix B: Technical drawings

Schematics of the Er:YAG CPF slabs polished by BAE Systems Australia (Holden Hill)

FIGURE B1: 35.6 mm long 0.5% Er:YAG CPF slab:

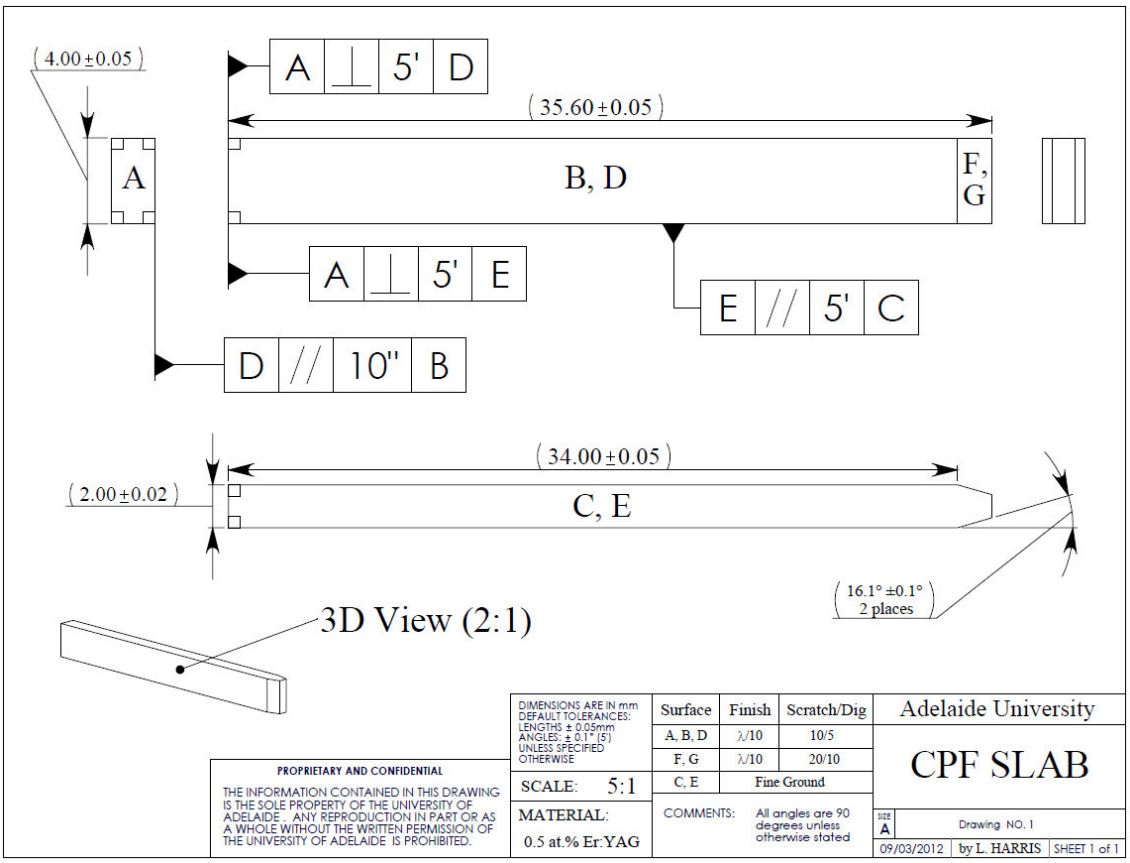

FIGURE B2: 21.6 mm short 0.5% Er:YAG CPF slab:

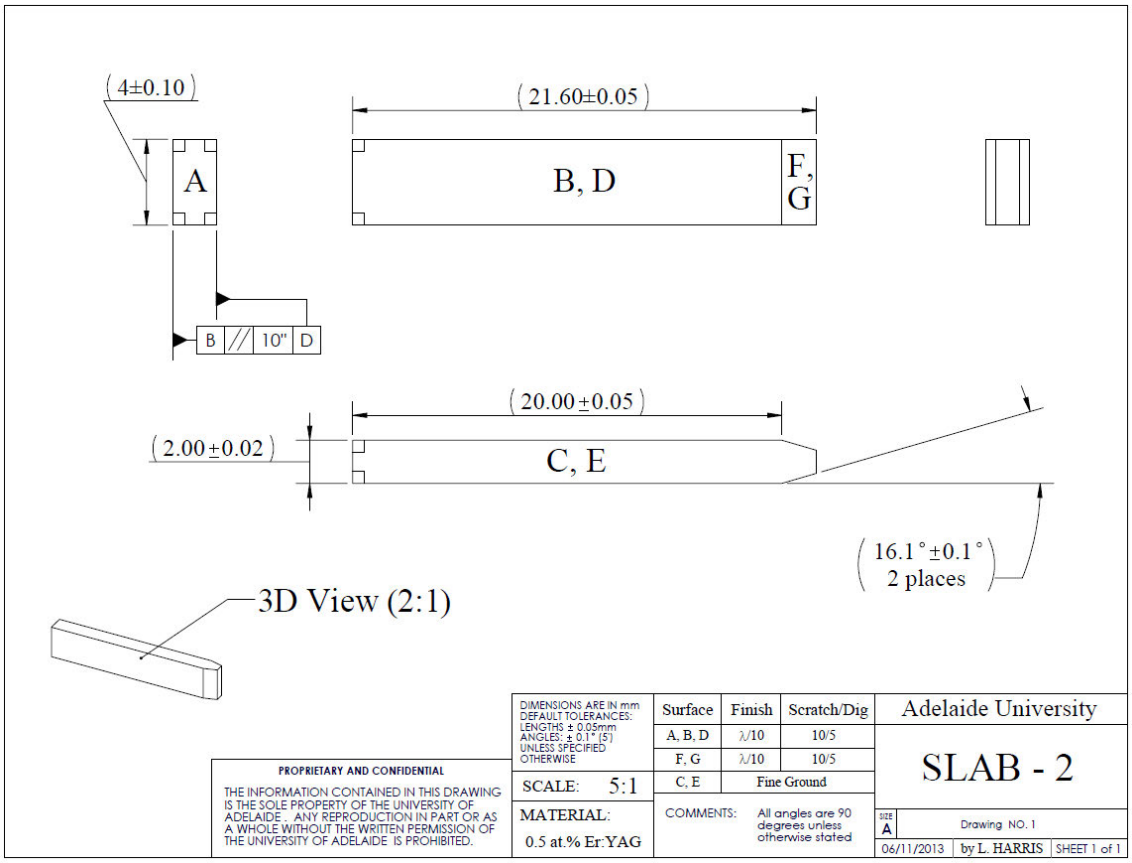

FIGURE B3: Technical drawing of the BK7 glass lens duct used in Q-switched lasers:

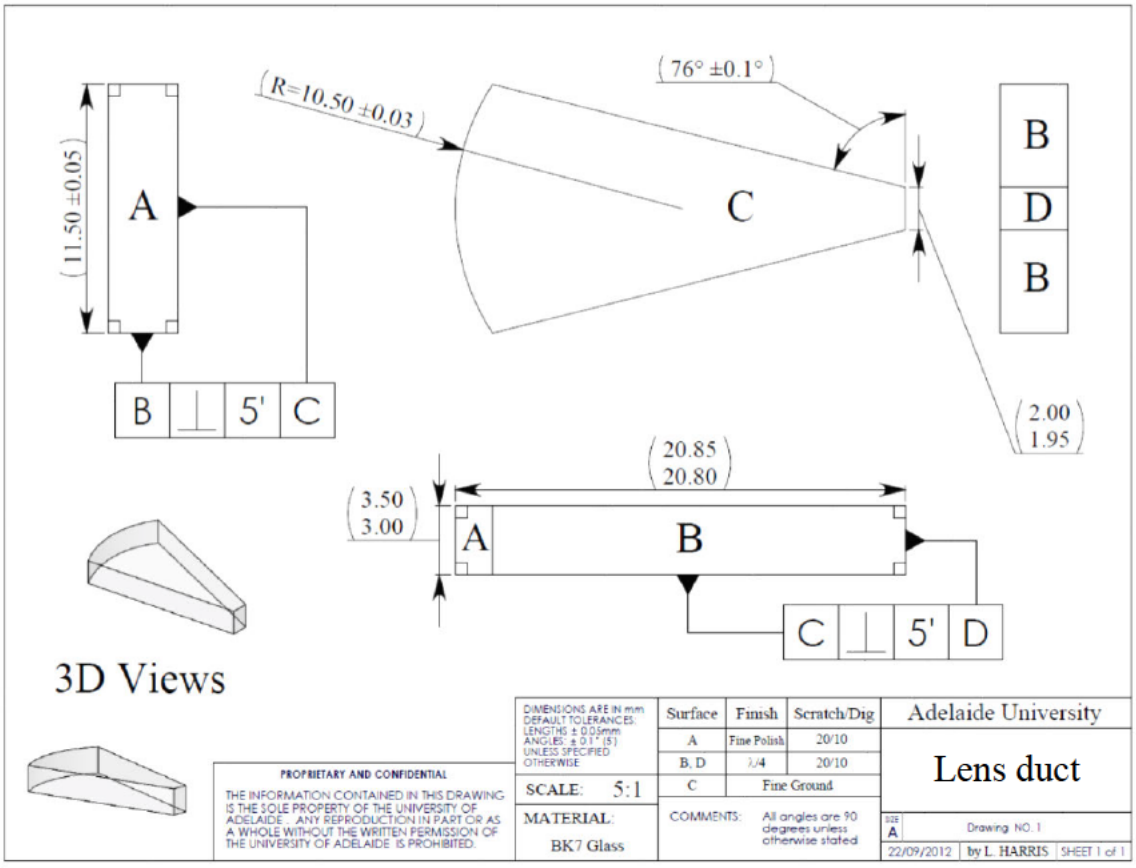

FIGURE B4: The copper pump diode mount (made by the School of Physics workshop):

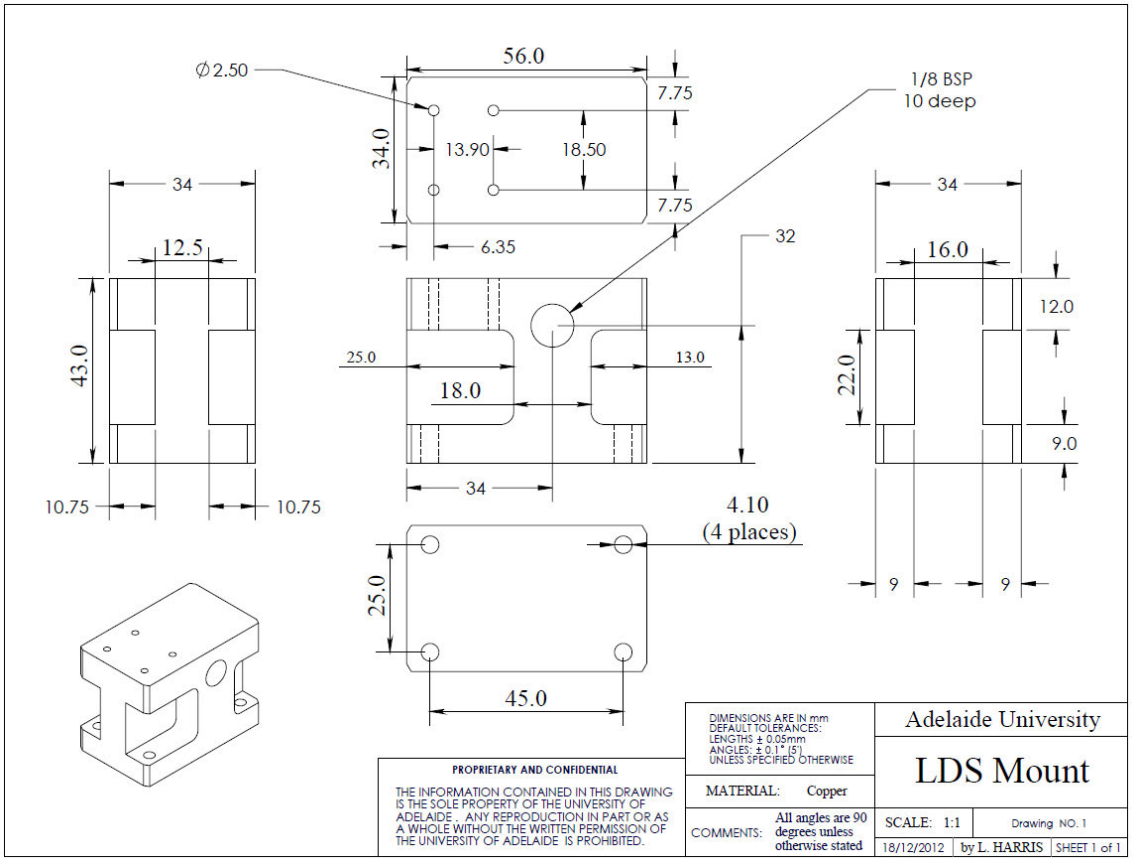

FIGURE B5: Schematic of the tilt stage used to mount the pump diode mount:

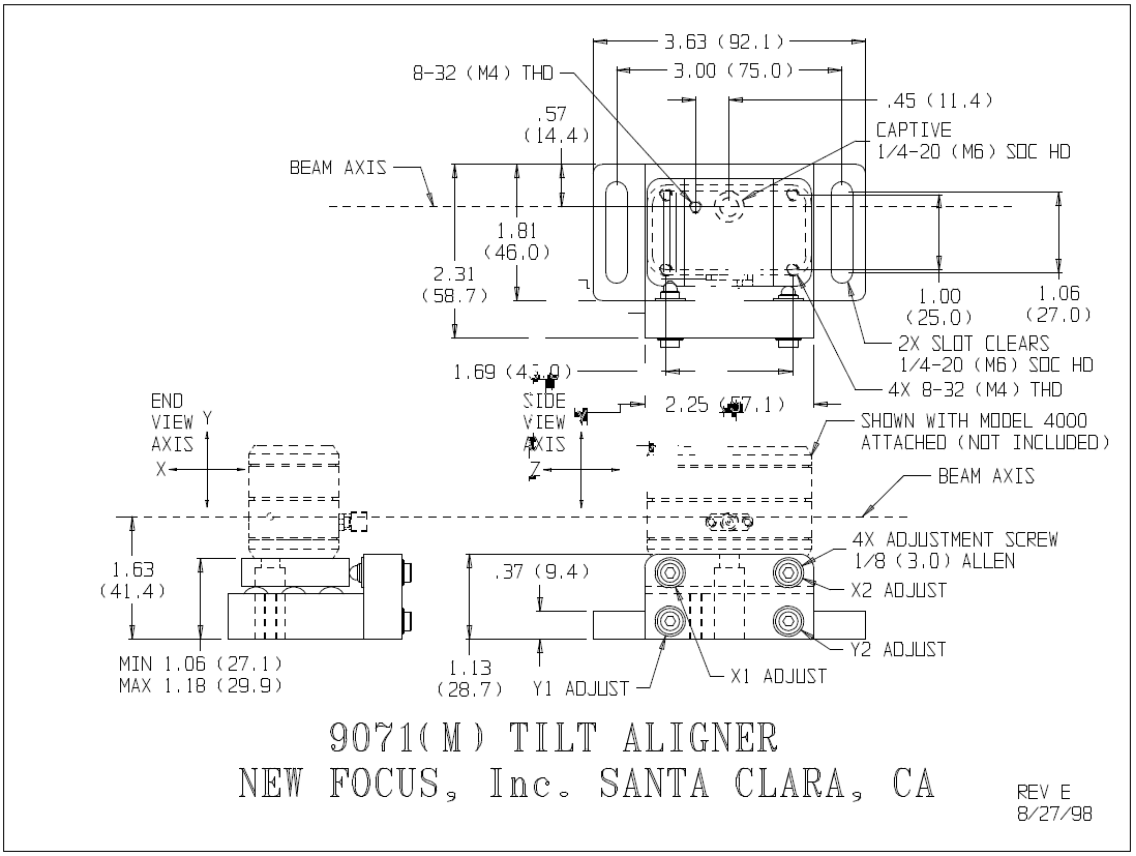

FIGURE B6: Drawing of the aluminium spacer (made by the School of Physics workshop) on to which the tilt stage was attached:

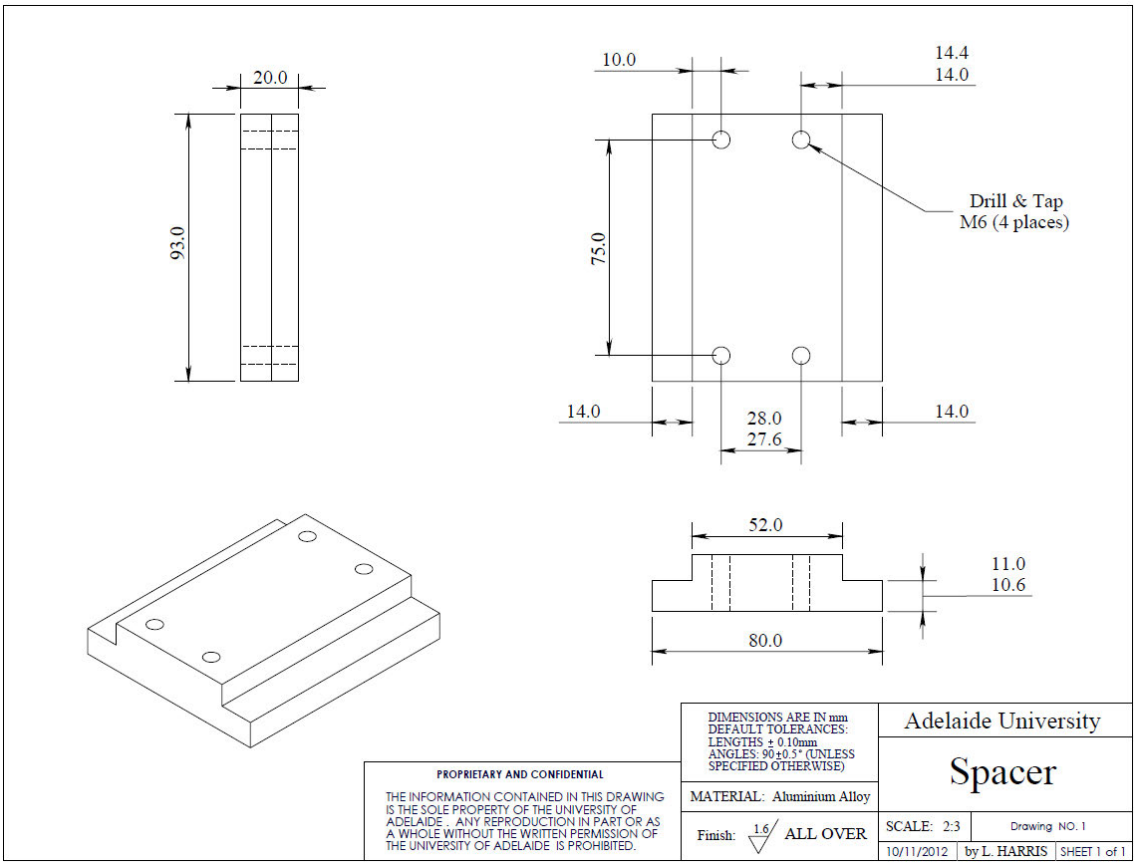

FIGURE B7: Platform of aluminium laser head used in the Q-switched laser:

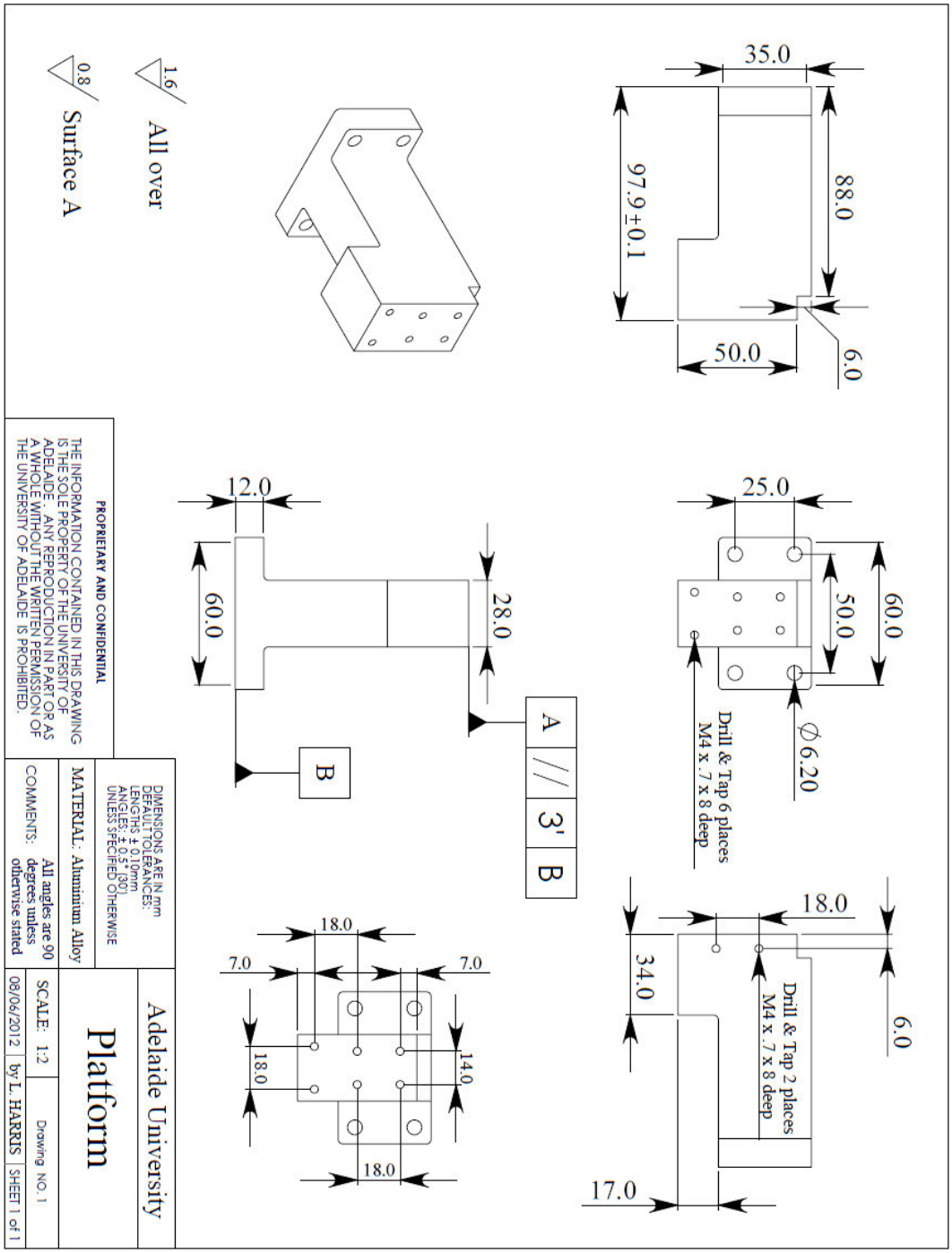

FIGURE B8: Copper base and top blocks of the water-cooled laser head (Toolcraft):

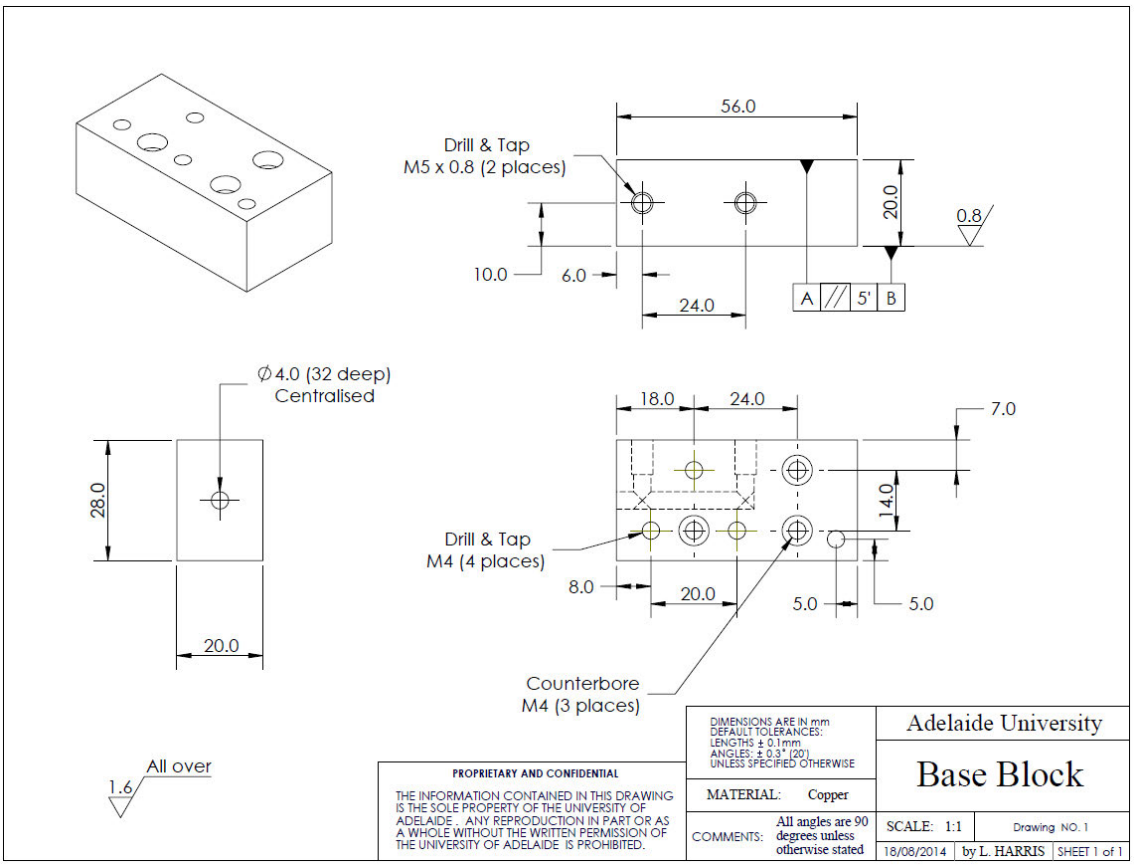

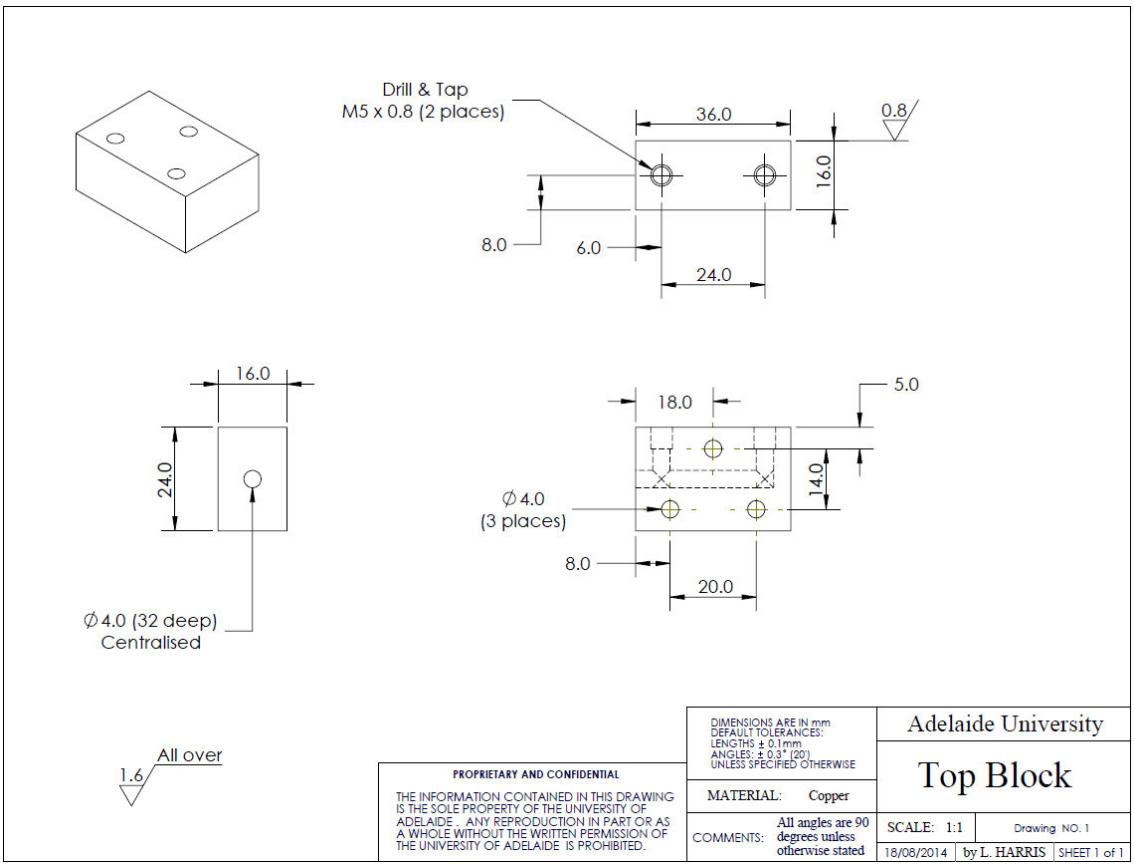

FIGURE B9: Schematic of the 0.25% Er:YAG CPF slab used in the cavity-dumped laser:

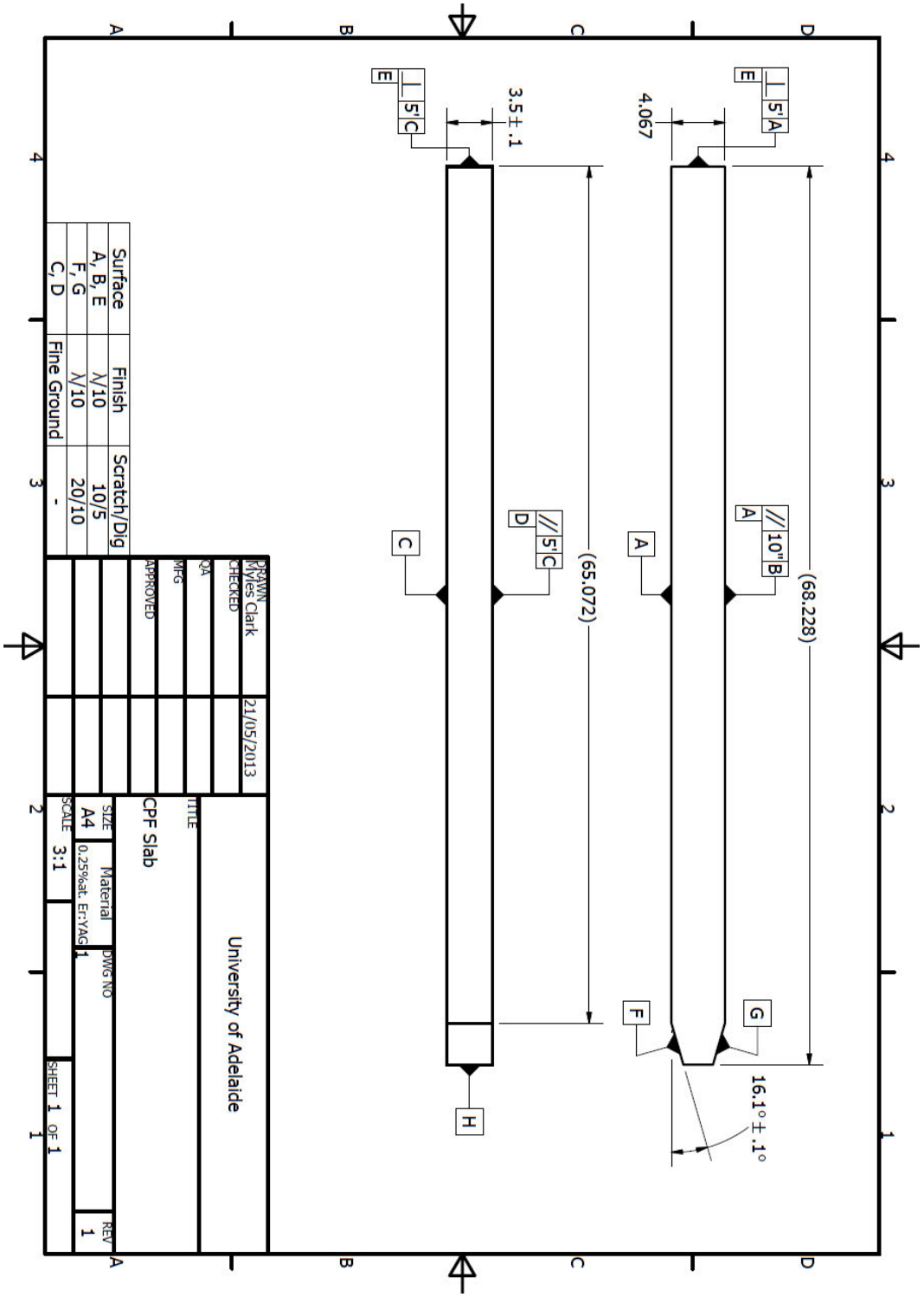

FIGURE B10: The lens duct used in the cavity-dumped laser:

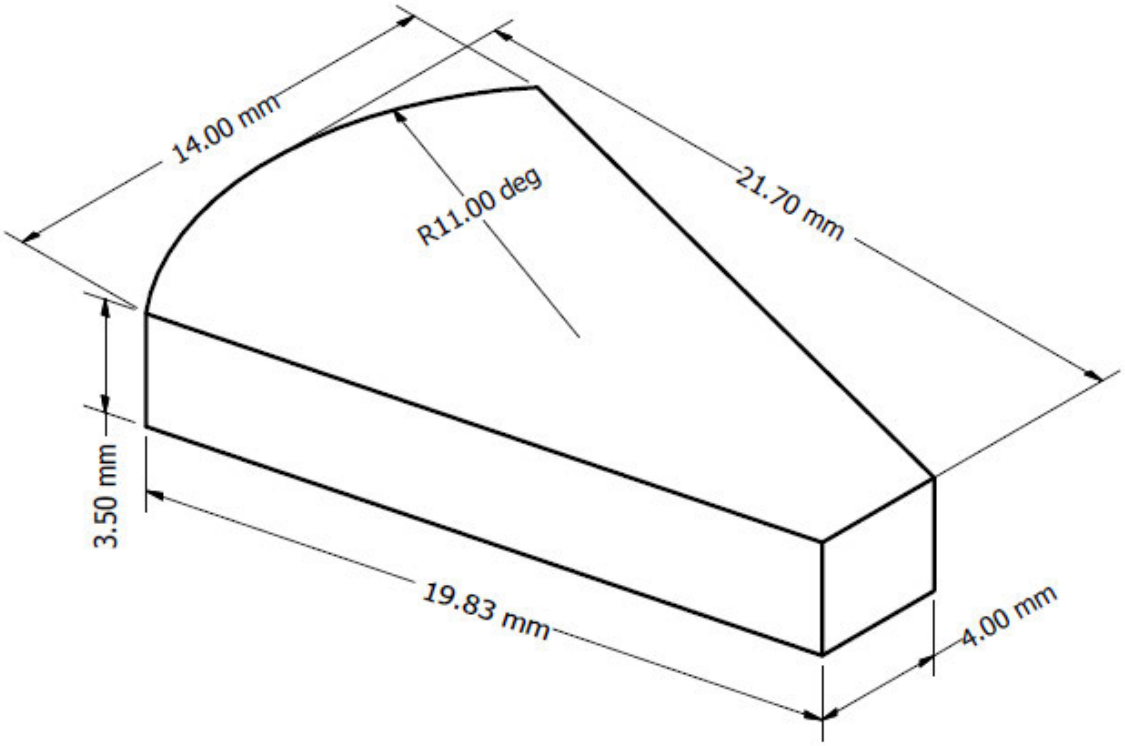

FIGURE B11: The water-cooled copper blocks used in the cavity-dumped laser head:

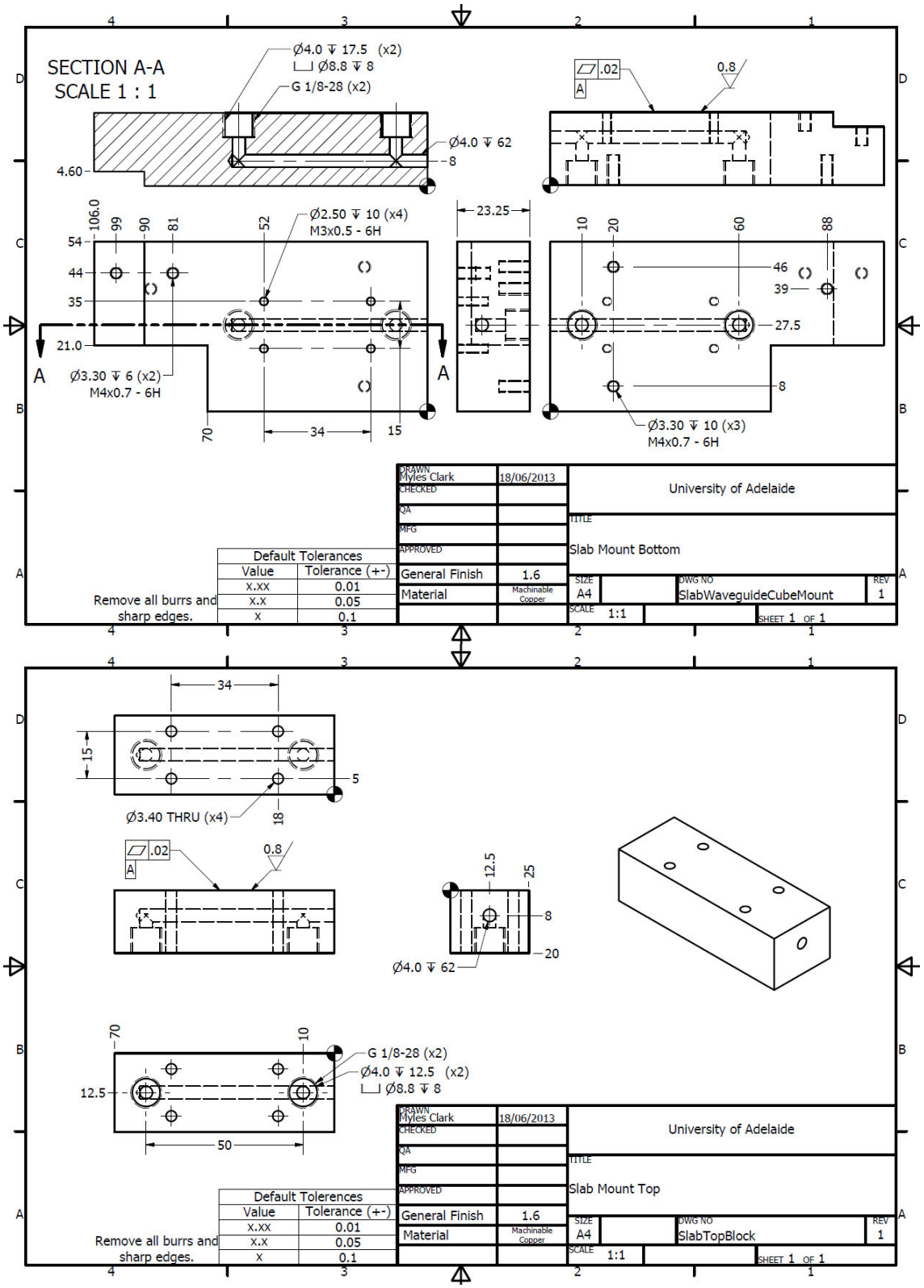

Appendix C: MATLAB codes

C1: Er:YAG gain medium modelling; programs to model the Er:YAG CPFS:

Er_YAG_CW_Dimension.m:

```
% A function to model the population levels in Er:YAG including
% upconversion and bleaching
close all
clear all

% Alter Default Graphic Settings to make plots better
set(0,'DefaultAxesFontSize',14);
set(0,'DefaultAxesFontWeight','normal');
set(0,'DefaultTextFontSize',14);
set(0,'DefaultTextFontWeight','normal');
set(0,'DefaultUicontrolFontSize',16);
set(0,'DefaultUicontrolFontWeight','normal');
set(0,'DefaultAxesTickLength',[0.025 0.015]);
set(0,'DefaultAxesLineWidth', 1.0);
set(0,'DefaultLineLineWidth', 2.0);

% Load the parameters for the model
situation = 'BAE_params';
Er_YAG_parameters
nx_points = 20;    % Number of points along the crystal length
NC = a.doping.*1.4e20;  % 1.4e20 is the concentration for 1%
options = [];
tspan = 5e-2;

N0 = zeros(5*nx_points,1);
N0(1:nx_points) = ones(nx_points,1)*NC;

width_v = linspace(0.1,0.18,17);
area_v = 10*width_v;
clength_v = linspace(2,6,17);

[width_m,clength_m] = meshgrid(clength_v,width_v);
[area_m,clength_m] = meshgrid(clength_v,area_v);

for ii = 1:length(width_v)
   for jj = 1:length(clength_v)
       [ii,jj]
       a.clength = clength_v(jj);   % Length of crystal
       a.plength = a.clength*2*sqrt(2);  % The paths within the gain medium

       xx = linspace(0,a.clength,nx_points);
       delta_x = a.clength/nx_points;
```

```
        a.pump_dia_v = width_v(ii);    % pump diameter in vertical
        a.pump_dia_h = width_v(ii);    % pump diameter in horizontal
        lasing_mode_area = (a.pump_dia_h*a.pump_dia_v);
        pump_area = (2*abs(xx-a.pump_waist_loc)*a.pump_div_v + a.pump_dia_v)...
           .*(2*abs(xx-a.pump_waist_loc)*a.pump_div_h + a.pump_dia_h);

        energy_scaling = a.h*a.c/lambda_l*delta_x*lasing_mode_area/(fl_upper + fl_lower);

        pump = 20;
        a.pump_in = pump*[1,1,1,1,1]/5;
        Er_Pop = @(t,N) Er_Pop_Model_Spatial_Spectral(N,a);
        [t_cycle,Ntemp] = ode45(Er_Pop,[0,tspan],N0);

        delta_n = delta_x*sum(Ntemp(length(t_cycle),(1:nx_points))*a.f1...
            - Ntemp(length(t_cycle),(nx_points+1):2*nx_points)*a.f2);
        pump_out20(ii,jj) = sum(a.pump_in.*exp(-a.abs_c*delta_n));
        gol = sigma_l*sum(Ntemp(length(t_cycle),(nx_points+1):2*nx_points)*fl_upper...
            -Ntemp(length(t_cycle),(1:nx_points))*fl_lower)*delta_x;
        gain20(ii,jj) = exp(2*gol*a.plength/a.clength);
        energy_available20(ii,jj) = -sum(Ntemp(length(t_cycle),(1:nx_points))*fl_lower...
            - Ntemp(length(t_cycle),(nx_points+1):2*nx_points)*fl_upper)*energy_scaling;
        %energy_available_thresh20(ii,jj) = (-sum(Ntemp(length(t_cycle),
(1:nx_points))*fl_lower - Ntemp(length(t_cycle),(nx_points+1):2*nx_points)*fl_upper)...
        %    - log(1/a.oc_refl)/(2*a.plength*sigma_l))*energy_scaling;

        pump = 50;
        a.pump_in = pump*[1,1,1,1,1]/5;
        Er_Pop = @(t,N) Er_Pop_Model_Spatial_Spectral(N,a);
        [t_cycle,Ntemp] = ode45(Er_Pop,[0,tspan],N0);

        delta_n = delta_x*sum(Ntemp(length(t_cycle),(1:nx_points))*a.f1...
            - Ntemp(length(t_cycle),(nx_points+1):2*nx_points)*a.f2);
        pump_out50(ii,jj) = sum(a.pump_in.*exp(-a.abs_c*delta_n));
        gol = sigma_l*sum(Ntemp(length(t_cycle),(nx_points+1):2*nx_points)*fl_upper...
            -Ntemp(length(t_cycle),(1:nx_points))*fl_lower)*delta_x;
        gain50(ii,jj) = exp(2*gol*a.plength/a.clength);
        energy_available50(ii,jj) = -sum(Ntemp(length(t_cycle),(1:nx_points))*fl_lower...
            - Ntemp(length(t_cycle),(nx_points+1):2*nx_points)*fl_upper)*energy_scaling;
        %energy_available_thresh50(ii,jj) = (-sum(Ntemp(length(t_cycle),
(1:nx_points))*fl_lower - Ntemp(length(t_cycle),(nx_points+1):2*nx_points)*fl_upper)...
        %    - log(1/a.oc_refl)/(2*a.plength*sigma_l))*energy_scaling;
    end
end


figure(1)
pcolor(area_m,clength_m,pump_out20)
title('Transmitted Pump for 20 Watts')
xlabel('Slab Length (cm)')
ylabel('Pumped Area (mm^2)')
colormap jet
colorbar

%figure(2)
%pcolor(width_m,clength_m,energy_available_thresh20)
%title('Energy Available when CW pumped with 20 W (Threshold)')
%xlabel('Slab Length (cm)')
%ylabel('Slab Width (cm)')
%colorbar

figure(3)
pcolor(area_m,clength_m,energy_available20)
title('Energy Available when CW pumped with 20 W')
xlabel('Slab Length (cm)')
ylabel('Pumped Area (mm^2)')
colormap jet
colorbar

figure(4)
pcolor(area_m,clength_m,gain20)
title('Gain when CW pumped with 20 W')
xlabel('Slab Length (cm)')
ylabel('Pumped Area (mm^2)')
colormap jet
colorbar
```

```
figure(5)
pcolor(area_m,clength_m,pump_out50)
title('Transmitted Pump for 50 Watts')
xlabel('Slab Length (cm)')
ylabel('Pumped Area (mm^2)')
colormap jet
colorbar

%figure(6)
%pcolor(width_m,clength_m,energy_available_thresh50)
%title('Energy Available when CW pumped with 50 W (Threshold)')
%xlabel('Slab Length (cm)')
%ylabel('Slab Width (cm)')
%colorbar

figure(7)
pcolor(area_m,clength_m,energy_available50)
title('Energy Available when CW pumped with 50 W')
xlabel('Slab Length (cm)')
ylabel('Pumped Area (mm^2)')
colormap jet
colorbar

figure(8)
pcolor(area_m,clength_m,gain50)
title('Gain when CW pumped with 50 W')
xlabel('Slab Length (cm)')
ylabel('Pumped Area (mm^2)')
colormap jet
colorbar
```

fpop_ErYAG.m:

```
function [f_lower,f_upper] = fpop_ErYAG(sub_level_lower,sub_level_upper,T)

% sub_level_lower is the sub level of the lower state
% sub_level_upper is the sub level of the upper state
% T is the temperature in Kelvin

h = 6.62e-34;
c = 3e8;
lower_band_states = [0,19,57,76,414,424,523,568];
upper_band_states = [6544,6596,6602,6779,6800,6818,6879]-6544;
k = 1.38e-23;

energy_upper = 100*upper_band_states*h*c;
energy_lower = 100*lower_band_states*h*c;

Z_upper = sum(exp(-(energy_upper)./(k*T)));
Z_lower = sum(exp(-(energy_lower./(k*T))));

f_upper = exp(-energy_upper(sub_level_upper)./(k*T))./Z_upper;
f_lower = exp(-energy_lower(sub_level_lower)./(k*T))./Z_lower;

end
```

Er_Pop_Model_Spatial_Spectral.m:

```
function Ndot = Er_Pop_Model_Spatial_Spectral(N,a)
% A function with the ODEs that solve the IVP for the population of Er:YAG
% N is a vector of n positions throughout the crystal for each of
% the energy levels
% Unpack the structure

h = a.h;
lambda = a.lambda;
lifetime = a.lifetime;
abs_c = a.abs_c;
c = a.c;
clength = a.clength;
doping = a.doping;
f2 = a.f2;
f1 = a.f1;
w21 = a.w21;
w31 = a.w31;
w32 = a.w32;
w41 = a.w41;
w42 = a.w42;
w43 = a.w43;
w51 = a.w51;
w52 = a.w52;
w53 = a.w53;
w54 = a.w54;
Cup = a.Cup;
Cup2 = a.Cup2;
pump_in = a.pump_in;

% Derived Quantities

M = round(length(N)/5);
delta_x = clength/M;
xx = linspace(0,clength,M);

if strcmp(a.pump_shape,'circle')
   areav = transpose(pi*(abs(xx-a.pump_waist_loc)*a.pump_div + a.pump_dia/2).^2);
elseif strcmp(a.pump_shape,'square')
   areav = transpose(4*(abs(xx-a.pump_waist_loc)*a.pump_div + a.pump_dia/2).^2);
elseif strcmp(a.pump_shape,'rectangle')
   areav = transpose((2*abs(xx-a.pump_waist_loc)*a.pump_div_v + a.pump_dia_v)...
       .*(2*abs(xx-a.pump_waist_loc)*a.pump_div_h + a.pump_dia_h));
else
   error('Incorrectly specificed a.pump_shape')
end

delta_n = cumsum(N(1:M)*f1 - N((M+1):2*M)*f2);
pump(:,1) = pump_in(1)*exp(-delta_x*abs_c(1)*delta_n);
pump(:,2) = pump_in(2)*exp(-delta_x*abs_c(2)*delta_n);
pump(:,3) = pump_in(3)*exp(-delta_x*abs_c(3)*delta_n);
pump(:,4) = pump_in(4)*exp(-delta_x*abs_c(4)*delta_n);
pump(:,5) = pump_in(5)*exp(-delta_x*abs_c(5)*delta_n);


freq = c/lambda;

Rm(:,1) = ((pump(:,1)./areav)/(h*freq))*abs_c(1);
Rm(:,2) = ((pump(:,2)./areav)/(h*freq))*abs_c(2);
Rm(:,3) = ((pump(:,3)./areav)/(h*freq))*abs_c(3);
Rm(:,4) = ((pump(:,4)./areav)/(h*freq))*abs_c(4);
Rm(:,5) = ((pump(:,5)./areav)/(h*freq))*abs_c(5);

R = sum(Rm,2);
N1 = N(1:M);
N2 = N((M+1):2*M);
N3 = N((2*M+1):3*M);
N4 = N((3*M+1):4*M);
N5 = N((4*M+1):5*M);

% The ODEs set
Ndot1 = N2*w21 + N3*w31 + N4*w41 + Cup*N2.^2 + R.*(N2*f2-N1*f1) + Cup2*N2.*N3;
Ndot2 = -N2*w21 + N3*w32+N4*w42 - 2*Cup*N2.^2 - R.*(N2*f2-N1*f1)- Cup2*N2.*N3;
Ndot3 = N4*w43-N3*(w32+w31) - Cup2*N2.*N3;
Ndot4 = Cup.*N2.^2-N4*(w43+w42+w41) + N5*w54;
Ndot5 = -N5*w54 + Cup2.*N2.*N3;

Ndot = [Ndot1;Ndot2;Ndot3;Ndot4;Ndot5];

end
```

Er_YAG_parameters.m:

```
% A function to model the population levels in Er:YAG including
% upconversion and bleaching

% Alter Default Graphic Settings to make plots better
set(0,'DefaultAxesFontSize',14);
set(0,'DefaultAxesFontWeight','normal');
set(0,'DefaultTextFontSize',14);
set(0,'DefaultTextFontWeight','normal');
set(0,'DefaultUicontrolFontSize',16);
set(0,'DefaultUicontrolFontWeight','normal');
set(0,'DefaultAxesTickLength',[0.025 0.015]);
set(0,'DefaultAxesLineWidth', 1.0);
set(0,'DefaultLineLineWidth', 2.0);

if strcmp(situation,'BAE_params')
   T = 295;
   pump_in = 50;
   sigma_l = 2.7e-20;
   [fl_lower,fl_upper] = fpop_ErYAG(7,3,T);
   lambda_l = 1.645e-6;   % The lasing wavelength
   laser_mode_diam = 0.08;   % Laser mode diameter
   a.pump_shape = 'rectangle';
   a.oc_refl = 0.8;   % The output coupler reflectivity
   a.clength = 3;    % Length of crystal
   a.plength = a.clength*2*sqrt(2);   % The paths within the gain medium
   a.pump_dia_v = 0.08;   % pump diameter in vertical (0.1)
   a.pump_div_v = 0;    % pump divergence in vertical
   a.pump_dia_h = 0.2;   % pump diameter in horizontal (0.15)
   a.pump_div_h = 0;    % pump divergence in horizontal

   a.pump_waist_loc = 0.4;   % pump waist location relative to the input coupler
   a.doping = 0.5;    % 0.5% Er:YAG
   a.Cup = 3.6e-18;   % Upconversion rates?
   a.f2 = 0.080;   % Normalized Boltzmann factors
   a.f1 = 0.25;   % Normalized Boltzmann factors
   a.lambda = 1.47e-6;   % Laser pump wavelength
   NC = a.doping.*1.4e20;   %1.4e20 is the concentration for 1%
   abs_c = [0.9,0.5,0.9,0.3,0.9]/a.f1;
   a.abs_c = abs_c/NC;   % Absolute absorption coefficient

else
    error('Incorrectly specified test_params')
end

a.h = 6.62e-34;    % Planck's constant
a.lifetime = 6.8e-3;   % Lifetime of the upper lasing state of Er:YAG
a.c = 3e8;     % Speed of light

a.w21 = 1/a.lifetime;   % Rate of decay state 2-> 1 (s^-1)
a.w31 = 118;   % Rate of decay state 3->1 (s^-1)
a.w32 = 1/5e-4;   % A guess at the non-radiative decay rate based on Tellurite
a.w41 = 51;   % Rate of decay state 4 ->1 (s^-1)
a.w42 = 57;   % Rate of decay state 4 ->2 (s^-1)
a.w43 = 1e5;   % Too slow but fast enough to dominate other processes
a.w51 = 1484;   % Rate of decay state 5 ->1 (s^-1)
a.w52 = 608;   % Rate of decay state 5 ->2 (s^-1)
a.w53 = 44;   % Rate of decay state 5 ->3 (s^-1)
a.w54 = 66;   % Rate of decay state 5 ->4 (s^-1)

a.Cup2 = 0;   % Upconversion rates
a.pump_in = pump_in*[1,1,1,1,1]/5;   % Pump Power in each of the bands
```

C2: Laser mode plot, graphics generation and component ABCD matrices:

Telescope.m:

```
% *Prototype telescopic resonator*

% Driver program for beam propagation in CPF Slab. Define each component of the
% optic system, then propagates a Gaussian beam through the system.
% Finds waist locations and widths, and can calculate eigenmode (cavity mode) of
% the system. Requires the following files to run properly:
% Graphics: eigenmode.m, propagate.m, Gauss_addgraphics.m
% Components: GRIN_lens.m, mirror.m, free_space.m, curv_surf.m, thin_lens.m

clear all

for j = 1:4   % loop for 4 different absorbed pump powers
wavelength = 1.645e-4;   % Laser wavelength [cm]
plot_units = 'mm';   % Units for beam width. Use 'cm', 'mm' or 'um'
fill_factor = 'on';   % Calculate fill-factor for slabs if 'on'

slab_length = 3.5; n = 1.813;
theta = 61.12;   % Brewster angle
in_angle = asind(sind(theta)/n);
path_length = 2*sqrt(2)*slab_length;
dist1 = 6;
fcoll = 10; fdiv = -5;
delta_x = 1.5;
dist2 = 2;
dist3 = 14;
OC_RoC = 20;   % OC curvature radius

% Define optical elements
HR = mirror(Inf);
sp1 = free_space(dist1);
poslens = thin_lens(fcoll,fcoll);
scope = free_space(fdiv+fcoll+delta_x);
neglens = thin_lens(fdiv,fdiv);
sp3 = free_space(dist2);
in_face = curv_surf(1,n,Inf,0,theta);
slab1 = GRIN_lens(4.92,n,0,0);
slab2 = GRIN_lens(4.92,n,0,0);
out_face = curv_surf(n,1,Inf,0,90-theta);
sp4 = free_space(dist3);
OC = mirror(OC_RoC);

% Define the system of components in sequence
system = {HR,sp1,poslens,scope,neglens,sp3,in_face,slab1,slab2,out_face,sp4,OC};

%init_q = 1i*pi*init_w0^2/wavelength; % define initial q from initial waist
%init_q2 = 1i*pi*init_w0_2^2/wavelength; % initial q for secondary axis
[init_q,stab_v(j)] = eigenmode(system);   % look for eigenmodes of the system
[init_q2,stab_h(j)] = eigenmode(system,2);   % look for eigenmodes of the system
                                             % in the secondary axis

%%%%%%%%%%%%%%%%%%%%%%%%%%%%%%%%%%%%%%%%%%%%%%%%%%%%%%%%%%%%%%%%%%%%%%%%%%%%%%%
scaling = 1;
if strcmp(plot_units,'cm'); scaling = 1;
elseif strcmp(plot_units,'mm'); scaling = 10;
end;

% Call propagate.m for primary axis and calculate R and w
[q,d,waist_loc,waist_size,graphics] =...
    propagate(wavelength,init_q,system,1);
q_inv = 1./q;
R_system = 1./real(q_inv);   % Beam radii of curvature
w_system = sqrt(-wavelength./(pi*imag(q_inv)))*scaling;   % Beam widths
```

```
% Call propagate.m for secondary axis and calculate R and w
[q2,d2,waist_loc2,waist_size2,graphics2] =...
    propagate(wavelength,init_q2,system,2);
q_inv2 = 1./q2;
R_system2 = 1./real(q_inv2);   % Beam radii of curvature
w_system2 = sqrt(-wavelength./(pi*imag(q_inv2)))*scaling;   % Beam widths

ax_label = 'Length [cm]';
if isequal(fill_factor, 'on')
    % Determine the fill factor within the GRIN lens (i.e. laser slab)
    startloc = graphics.startloc;
    endloc = graphics.endloc;
    stepsize = d(startloc+5)-d(startloc+4);
    % Integrate to find total area swept out by beam
    areainbeam_vert = sum(real(w_system(startloc:endloc-1)))*stepsize;
    areainbeam_horiz = sum(real(w_system2(startloc:endloc-1)))*stepsize;
    % Total pumped area, assuming rectangular pumped region
    pumped_area_vert = (d(endloc)-d(startloc))*...
        max(real(w_system(startloc:endloc)));
    pumped_area_horiz = (d(endloc)-d(startloc))*...
        max(real(w_system2(startloc:endloc)));
    % Fill factor of the pumped region by laser beam (higher order modes
    % have widths proportional to that of fundamental Gaussian)
    eff_vert = areainbeam_vert/pumped_area_vert;
    eff_horiz = areainbeam_horiz/pumped_area_horiz;
    ax_label = {'Length [cm]'};
end

% Plot beam profile(s)
figure(1)
plot(d,w_system,d,-w_system,'color','g')    % vertical beam
hold on
plot(d2,w_system2,d2,-w_system2,'color','r')    % horizontal beam
xlabel(ax_label)
if strcmp(plot_units,'um'); plot_units = '\mum'; end;
ylabel(['Beam width [' plot_units ']'])

% Axes limits
ax_max = max(max(real(w_system)),max(real(w_system2)))*1.2;
axis ([-max(d)*0.05 max(d)*1.05 -ax_max*1.05 ax_max*1.05])
% Add component locations and waist locations to graph
Gauss_addgraphics(ax_max,graphics,waist_loc,waist_size*scaling,...
    waist_loc2,waist_size2*scaling)
hold off
end

stab_h(1)
stab_v(1)
```

QSLaser.m:

```
% *Final Q-switched Laser*

% Driver program for beam propagation in CPF Slab. Define each component of the
% optic system, then propagates a Gaussian beam through the system.
% Finds waist locations and widths, and can calculate eigenmode (cavity mode) of
% the system. Requires the following files to run properly:
% Graphics: eigenmode.m, propagate.m, Gauss_addgraphics.m
% Components: GRIN_lens.m, mirror.m, free_space.m, curv_surf.m, thick_lens.m

clear all

for j = 1:4   % loop for 4 different absorbed pump powers
wavelength = 1.617e-4;   % Laser wavelength [cm]
plot_units = 'mm';   % Units for beam width. Use 'mm' or 'um'
fill_factor = 'on';    % Calculate fill-factor for slabs if 'on'

slab_length = 2.1; n = 1.813;
theta = 61.12;   % Brewster angle
in_angle = asind(sind(theta)/n);
path_length = 2*sqrt(2)*slab_length;
dist1 = 1.5;
fcoll = 5; fdiv = -3;
delta_x = 0.25;
dist2 = 0.8;
dist3 = 1.2;
OC_RoC = 30;
Length = dist1+3.5+(2+delta_x)+dist2+10.67+dist3;

% Define optical elements
HR = mirror(Inf);
sp1 = free_space(dist1);
RTP = free_space(1.14,1.76);
sp0 = free_space(0.5,1);
poslens = thick_lens(0.53,1.5,-2.58,9999999);
scope = free_space(fdiv+fcoll+delta_x);
neglens = thick_lens(0.2,1.5,9999999,-1.55);
sp2 = free_space(dist2);
in_face = curv_surf(1,n,Inf,0,theta);
slab1 = GRIN_lens(2.94,n,0,0);
slab2 = GRIN_lens(2.94,n,0,0);
out_face = curv_surf(n,1,Inf,0,90-theta);
sp3 = free_space(dist3);
OC = mirror(OC_RoC);

% Define the system of components in sequence
system = {HR,sp1,RTP,sp0,poslens,scope,neglens,sp2,in_face,slab1,slab2,out_face,sp3,OC};

%init_q = 1i*pi*init_w0^2/wavelength; % define initial q from initial waist
%init_q2 = 1i*pi*init_w0_2^2/wavelength; % initial q for secondary axis
[init_q,stab_v(j)] = eigenmode(system);   % look for eigenmodes of the system
[init_q2,stab_h(j)] = eigenmode(system,2);   % look for eigenmodes of the system
                                             % in the secondary axis

%%%%%%%%%%%%%%%%%%%%%%%%%%%%%%%%%%%%%%%%%%%%%%%%%%%%%%%%%%%%%%%%%%%%%%%%%%%%%%%
scaling = 1;
if strcmp(plot_units,'cm'); scaling = 1;
elseif strcmp(plot_units,'mm'); scaling = 10;
end;

% Call propagate.m for primary axis and calculate R and w
[q,d,waist_loc,waist_size,graphics] =...
    propagate(wavelength,init_q,system,1);
q_inv = 1./q;
R_system = 1./real(q_inv);   % Beam radii of curvature
w_system = sqrt(-wavelength./(pi*imag(q_inv)))*scaling;   % Beam widths
```

```
% Call propagate.m for secondary axis and calculate R and w
[q2,d2,waist_loc2,waist_size2,graphics2] =...
    propagate(wavelength,init_q2,system,2);
q_inv2 = 1./q2;
R_system2 = 1./real(q_inv2);  % Beam radii of curvature
w_system2 = sqrt(-wavelength./(pi*imag(q_inv2)))*scaling;   % Beam widths
ax_label = 'Length [cm]';
if isequal(fill_factor, 'on')
    % Determine the fill factor within the GRIN lens (i.e. slab)
    startloc = graphics.startloc;
    endloc = graphics.endloc;
    stepsize = d(startloc+5)-d(startloc+4);
    % Integrate to find total area swept out by beam
    areainbeam_vert = sum(real(w_system(startloc:endloc-1)))*stepsize;
    areainbeam_horiz = sum(real(w_system2(startloc:endloc-1)))*stepsize;
    % Total pumped area, assuming rectangular pumped region
    pumped_area_vert = (d(endloc)-d(startloc))*...
        max(real(w_system(startloc:endloc)));
    pumped_area_horiz = (d(endloc)-d(startloc))*...
        max(real(w_system2(startloc:endloc)));
    % Fill factor of the pumped region by laser beam (higher order modes have widths
    % proportional to that of fundamental Gaussian)
    eff_vert = areainbeam_vert/pumped_area_vert;
    eff_horiz = areainbeam_horiz/pumped_area_horiz;
    ax_label = {'Length [cm]'}
end

% Plot beam profile(s)
figure(1)
plot(d,w_system,d,-w_system,'color','g')   % vertical beam
hold on
plot(d2,w_system2,d2,-w_system2,'color','r')   % horizontal beam
xlabel(ax_label)
if strcmp(plot_units,'um'); plot_units = '\mum'; end;
ylabel(['Beam width [' plot_units ']'])

% Axes limits
ax_max = max(max(real(w_system)),max(real(w_system2)))*1.2;
axis ([-max(d)*0.05 max(d)*1.05 -ax_max*1.05 ax_max*1.05])
% Add component locations and waist locations to graph
gauss_addgraphics(ax_max,graphics,waist_loc,waist_size*scaling,...
    waist_loc2,waist_size2*scaling)
hold off
end

stab_h(1)
stab_v(1)
Length
```

CDLaser.m:

```
% Cavity-dumped laser resonator

% Driver program for beam propagation in CPF Slab. Define each component of the optic
system, then propagates a Gaussian beam through the system.
% Finds waist locations and widths, and calculates eigenmode (cavity mode) of the
system. Requires the following files to run properly:
% Graphics: eigenmode.m, propagate.m, Gauss_addgraphics.m
% Components: GRIN_lens.m, mirror.m, free_space.m, curv_surf.m, thick_lens.m

clear all

for j = 1:4    % loop for 4 different absorbed pump powers
wavelength = 1.645e-4;   % Laser wavelength [cm]
plot_units = 'mm';   % Units for beam width. Use 'mm' or 'um'
fill_factor = 'on';   % Calculate fill-factor for slabs if 'on'

slab_length = 6.7; n = 1.813;
theta = 61.12;   % Brewster angle
in_angle = asind(sind(theta)/n);
path_length = 2*sqrt(2)*slab_length;
dist1 = 4;
dist2 = 16;
fcoll = 7.5; fdiv = -5;
delta_x = 1;
dist3 = 1.7;
dist4 = 3;
OC_RoC = 30;   % OC curvature radius
Length = 6+dist2+(2.5+delta_x)+dist3+34+dist4;

% Define optical elements
HR = mirror(Inf);
sp1 = free_space(dist1);
RTP = free_space(2,1.76);
sp2 = free_space(dist2);
poslens = thick_lens(0.41,1.5,-7.66,7.66);
scope = free_space(fdiv+fcoll+delta_x);
neglens = thick_lens(0.2,1.5,999999,-2.58);
sp3 = free_space(dist3);
in_face = curv_surf(1,n,Inf,0,theta);
slab1 = GRIN_lens(9.4,n,0,0);
slab2 = GRIN_lens(9.4,n,0,0);
out_face = curv_surf(n,1,Inf,0,90-theta);
sp4 = free_space(dist4);
OC = mirror(OC_RoC);

% Define the system components in sequence
system = {HR,sp1,RTP,sp2,poslens,scope,neglens,sp3,in_face,
slab1,slab2,out_face,sp4,OC};

%init_q = 1i*pi*init_w0^2/wavelength; % define initial q from initial waist
%init_q2 = 1i*pi*init_w0_2^2/wavelength; % initial q for secondary axis
[init_q,stab_v(j)] = eigenmode(system);   % look for eigenmodes of the system
[init_q2,stab_h(j)] = eigenmode(system,2);  % look for eigenmodes of the
                                    % system in secondary axis

%%%%%%%%%%%%%%%%%%%%%%%%%%%%%%%%%%%%%%%%%%%%%%%%%%%%%%%%%%%%%%%%%%%%%%%%%%%%%%%
scaling = 1;
if strcmp(plot_units,'cm'); scaling = 1;
elseif strcmp(plot_units,'mm'); scaling = 10;
end;

% Call propagate.m for primary axis and calculate R and w
[q,d,waist_loc,waist_size,graphics] = propagate(wavelength,init_q,system,1);
q_inv = 1./q;
R_system = 1./real(q_inv);   % radii of curvature of beam
w_system = sqrt(-wavelength./(pi*imag(q_inv)))*scaling;   % beam widths
```

```
% Call propagate.m for secondary axis and calculate R and w
[q2,d2,waist_loc2,waist_size2,graphics2] =...
   propagate(wavelength,init_q2,system,2);
q_inv2 = 1./q2;

R_system2 = 1./real(q_inv2);   % radii of curvature of beam
w_system2 = sqrt(-wavelength./(pi*imag(q_inv2)))*scaling;   % beam widths

ax_label = 'Length [cm]';
if isequal(fill_factor, 'on')
   % Determine the fill factor within the GRIN lens (i.e. laser slab)
   startloc = graphics.startloc;
   endloc = graphics.endloc;
   stepsize = d(startloc+5)-d(startloc+4);
   % Integrate to find total area swept out by beam
   areainbeam_vert = sum(real(w_system(startloc:endloc-1)))*stepsize;
   areainbeam_horiz = sum(real(w_system2(startloc:endloc-1)))*stepsize;
   % Total pumped area, assuming rectangular pumped region
   pumped_area_vert = (d(endloc)-d(startloc))*...
       max(real(w_system(startloc:endloc)));
   pumped_area_horiz = (d(endloc)-d(startloc))*...
       max(real(w_system2(startloc:endloc)));
   % Fill factor of the pumped region by laser beam (higher order modes have
widths proportional to that of fundamental Gaussian)
   eff_vert = areainbeam_vert/pumped_area_vert;
   eff_horiz = areainbeam_horiz/pumped_area_horiz;
   ax_label = {'Length [cm]'};
end

% Plot beam profile(s)
figure(2)
plot(d,w_system,d,-w_system,'color','g')    % Vertical beam
hold on
plot(d2,w_system2,d2,-w_system2,'color','r')    % Horizontal beam
xlabel(ax_label)
if strcmp(plot_units,'um'); plot_units = '\mum'; end;
ylabel(['Beam width [' plot_units ']'])

% Axes limits
ax_max = max(max(real(w_system)),max(real(w_system2)))*1.2;
axis ([-max(d)*0.05 max(d)*1.05 -ax_max*1.05 ax_max*1.05])
% Add component locations and waist locations to graph
Gauss_addgraphics(ax_max,graphics,waist_loc,waist_size*scaling,...
   waist_loc2,waist_size2*scaling)
hold off
end
```

eigenmode.m:

```
function [init_q,stability] = eigenmode(system,axis)
% For use in Gaussian_beams.m.
% Calculates the eigenmode (self-consistent mode) of the system, i.e. cavity modes.
% Multiplies the ABCD matrices of each component in system (both forwards and backwards
% directions) and finds the self-consistent solution. Returns an initial q = 0 if no
% mode is found (unstable). For systems that differ in the two axes, define axis
% variable - 1 for primary (uses the .mat matrix of each component), 2 for secondary
% (uses the .mat2 matrix of each component if defined, else assumes the component is
% identical in both and uses .mat matrix).

ABCD = [1,0;0,1];
if nargin == 1;axis = 1;end
for i = 1:length(system)   % forward propagation through system
    if strcmp(system{i}.type,'thick lens')
       % special provisions required for thick lens due to asymetry.
       surf1 = curv_surf(1,system{i}.n_inner,system{i}.R1);
       inside_lens = free_space(system{i}.length,system{i}.n_inner);
       surf2 = curv_surf(system{i}.n_inner,1,system{i}.R2);
       ABCD = surf2.mat*inside_lens.mat*surf1.mat*ABCD;
    else
       % component ordering begins from the right
       if (axis == 2)&&(isfield(system{i}, 'mat2'))
           ABCD = system{i}.mat2*ABCD;
```

```
        else
            ABCD = system{i}.mat*ABCD;
        end
    end
end
for i = length(system):-1:1   % backward propagation through system
    if strcmp(system{i}.type,'thick lens')
        % special provisions required for thick lens due to asymetry.
        surf2 = curv_surf(1,system{i}.n_inner,-system{i}.R2);
        inside_lens = free_space(system{i}.length,system{i}.n_inner);
        surf1 = curv_surf(system{i}.n_inner,1,-system{i}.R1);
        ABCD = surf1.mat*inside_lens.mat*surf2.mat*ABCD;
    elseif strcmp(system{i}.type,'curved surface')
        % special provisions required for curved surfaces due to asymetry.
        R = -system{i}.RoC;
        n1 = system{i}.n_i;
        n0 = system{i}.n_f;
        AoI1 = system{i}.AoI1_deg;
        AoR1 = asind(n1/n0*sind(AoI1));
        AoI2 = system{i}.AoI2_deg;
        AoR2 = asind(n1/n0*sind(AoI2));
        surf = curv_surf(n0,n1,R,AoR1,AoR2);
        if (axis == 2)&&(isfield(system{i}, 'mat2'))
            ABCD = surf.mat2*ABCD;
        else
            ABCD = surf.mat*ABCD;
        end
    elseif strcmp(system{i}.type,'mirror')
        % only single "pass" through mirrors - skip for backward propagation
    else
        if (axis == 2)&&(isfield(system{i}, 'mat2'))
            ABCD = system{i}.mat2*ABCD;
        else
            ABCD = system{i}.mat*ABCD;
        end
    end
end

A = ABCD(1,1);
B = ABCD(1,2);
C = ABCD(2,1);
D = ABCD(2,2);
re_part = (D-A)/(2*B);              % finds real part of initial q value
im_part = sqrt(4-(A+D)^2)/(2*B);    % finds imaginary part of initial q value
% stability parameter - cos(theta) (see Kogelnik and Li)
stability = 0.5*(A+D);

if isreal(im_part)
    if im_part > 0
        im_part = -im_part;    % if +ve solution is +ve, use -ve solution
    end
    init_q = 1/(re_part + 1i*im_part);
else   % no solution (unstable resonator)
    init_q = 0;
end
```

propagate.m:

```
function [q,d,waist_loc,waist_size,graphics] =...
    propagate(wavelength,init_q,system,axis)
% For use in Gaussian_beams.m.
% Analyses the system, going through the components one by one to calculate the value of
q throughout the system, as well as the waist size and locations. Initial beam q defined
by init_q. All components of non-zero length (free space, GRIN lenses, thick lenses) are
divided into segments and q is obtained for each segment. Other components are assumed
to have zero length. Waist locations are determined when inside free space only. Returns
q, d, waist locations and size, and locations of components
% (used in Gauss_addgraphics.m)

q = init_q;  % initial beam q parameter. Elements are appended to the
             % end of q as the beam is propagated through the system.
d = 0;    % propagation distance vector. Elements are appended to the
          % end of d as the beam is propagated through the system.
graphics.stops = 0;   % locations of each non-zero-length component
segm = 500;   % number of segments for free space and GRIN lenses.
                    % (divided by 5 for thick lens due to smaller lengths)
graphics.x_b = [0;0;0;0];   % location of any grey boxes (n > 1 regions)
waist_loc = [];
waist_size = [];
if nargin == 3;axis = 1;end   % assumes primary axis if none defined

% propagate beam (calculate q and d) for each component in the system
for i = 1:length(system)
    % dividing components of non-zero length into segments
    if strcmp(system{i}.type,'free space')
        waist_dist = -real(q(length(q)));   % distance to waist
        % if a waist lies in this section, record the location and size
        if ((waist_dist >= 0)&&...
                (system{i}.refInd*waist_dist < system{i}.length))
            waist_loc = [waist_loc,system{i}.refInd*waist_dist+...
                graphics.stops(length(graphics.stops))];
            w_size = sqrt(imag(q(length(q)))*wavelength/pi());
            waist_size = [waist_size,w_size];
        end
        for j = 1:segm
            % propagate beam through free space.
            q = [q,q(length(q))+system{i}.mat(1,2)/segm];
            d = [d,d(length(d))+system{i}.length/segm];
        end
        % graph-related - mark for greying if n > 1
        if system{i}.refInd > 1
            graphics.x_b = [graphics.x_b,...
                [graphics.stops(length(graphics.stops));...
                graphics.stops(length(graphics.stops));...
                graphics.stops(length(graphics.stops))+system{i}.length;...
                graphics.stops(length(graphics.stops))+system{i}.length]];
        end
        % graph-related - marks location of end of free space
        graphics.stops = [graphics.stops,system{i}.length+...
            graphics.stops(length(graphics.stops))];

    elseif strcmp(system{i}.type,'GRIN lens')
        % marks start of GRIN lens in array; used for determining fill
        % factor - applicable for laser crystals. Placed inside graphics
        % for convenience
        graphics.startloc = length(q);

        % dividing GRIN lens into segments and calculating individually
        l_segment = system{i}.length/segm;
        n0 = system{i}.n0;
        n2 = system{i}.n2(axis);
        if (axis == 2)&&(length(system{i}.n2) == 2) % for secondary axis
            n2 = system{i}.n2(2);
        end
        % recalculate lensing for each segment
        A = cos(l_segment*sqrt(n2/n0));
        B = sin(l_segment*sqrt(n2/n0))/sqrt(n0*n2);
```

```
        if n2 == 0; B = l_segment/n0;end    % for n2 = 0 case
        C = -sqrt(n0*n2)*sin(l_segment*sqrt(n2/n0));
        D = cos(l_segment*sqrt(n2/n0));
        for j = 1:segm
            % propagate beam through GRIN lens
            q = [q, (A*q(length(q)) + B)/(C*q(length(q)) + D)];
            d = [d,d(length(d))+l_segment];
        end
        % graph-related - marks GRIN lens for greying
        graphics.x_b = [graphics.x_b,...
            [graphics.stops(length(graphics.stops));...
            graphics.stops(length(graphics.stops));...
        graphics.stops(length(graphics.stops))+system{i}.length;...
        graphics.stops(length(graphics.stops))+system{i}.length]];
        graphics.endloc = length(q);  % marks end of GRIN lens in array
        % graph-related - marks location of end of GRIN lens
        graphics.stops = [graphics.stops,...
            graphics.stops(length(graphics.stops))+system{i}.length];

    elseif strcmp(system{i}.type,'thick lens')
        % separates thick lens into the 3 parts - curved interfaces and
        % free space propagation within the thick lens

        % beam passing through curved interface into thick lens
        surf1 = curv_surf(1,system{i}.n_inner,system{i}.R1);
        q = [q, (surf1.mat(1,1)*q(length(q)) + surf1.mat(1,2))/...
            (surf1.mat(2,1)*q(length(q)) + surf1.mat(2,2))];
        d = [d,d(length(d))];

        % beam propagating within the lens
        inside_lens = free_space(system{i}.length,system{i}.n_inner);
        for j = 1:segm/5   % divide into segments, 5x less than free space
            % propagate beam through thick lens
            q = [q,q(length(q))+inside_lens.mat(1,2)*5/segm];
            d = [d,d(length(d))+inside_lens.length*5/segm];
        end
        % beam passing through curved interface out of thick lens
        surf2 = curv_surf(system{i}.n_inner,1,system{i}.R2);
        q = [q, (surf2.mat(1,1)*q(length(q)) + surf2.mat(1,2))/...
            (surf2.mat(2,1)*q(length(q)) + surf2.mat(2,2))];
        d = [d,d(length(d))];

        % graph-related - marks thick lens for greying
        graphics.x_b = [graphics.x_b,...
            [graphics.stops(length(graphics.stops));...
            graphics.stops(length(graphics.stops));...
            graphics.stops(length(graphics.stops))+system{i}.length;...
            graphics.stops(length(graphics.stops))+system{i}.length]];
        % graph-related - marks location of end of thick lens
        graphics.stops = [graphics.stops,system{i}.length + ...
            graphics.stops(length(graphics.stops))];

    else    % components with zero length
        A = system{i}.mat(1,1);
        B = system{i}.mat(1,2);
        C = system{i}.mat(2,1);
        D = system{i}.mat(2,2);
        if (axis == 2)&&(isfield(system{i}, 'mat2'))
            % use matrix for secondary axis if it exists, else use primary
            A = system{i}.mat2(1,1);
            B = system{i}.mat2(1,2);
            C = system{i}.mat2(2,1);
            D = system{i}.mat2(2,2);
        end
        % calculate q change due to component
        q = [q, (A*q(length(q)) + B)/(C*q(length(q)) + D)];
        d = [d,d(length(d))];
    end
end
```

Gauss_addgraphics.m:

```
function Gauss_addgraphics(ax_max,graphics,waist_loc,waist_size,...
    waist_loc2,waist_size2)
% For use in Gaussian_beams.m.
% Takes the "graphics" and beam waist data from propagate.m and applies to
% current plot. "Graphics" corresponds to thick red lines that represent
% component locations and greying of areas with n > 1.

% draw semi-transparent boxes around areas with n > 1
a = size(graphics.x_b);
y_box = [-ax_max;ax_max;ax_max;-ax_max];
y_b = [0;0;0;0];
for i = 1:a(2)-1
    y_b = [y_b,y_box];
end
patch(graphics.x_b,y_b,'k','LineStyle','none','FaceAlpha',0.1)

line([0,max(graphics.stops)],[0,0],'Color','k')   % centre line

% draw thick red lines representing component locations at "stop" locations
for i = 1:length(graphics.stops)
    line([graphics.stops(i),graphics.stops(i)],[ax_max,...
        -ax_max],'Color','b','LineWidth',1.5);
end

% draw dotted lines at the beam waists (inside free space components only)
if nargin > 2
    for i = 1:length(waist_loc)
        line([waist_loc(i),waist_loc(i)],...
            [waist_size(i),-waist_size(i)],'LineStyle',':','Color','k');
    end
end
if nargin > 4
    for i = 1:length(waist_loc2)
        line([waist_loc2(i),waist_loc2(i)],...
            [waist_size2(i),-waist_size2(i)],'LineStyle',':','Color','k');
    end
end
```

curv_surf.m:

```
function cf = curv_surf(n0,n1,R,AoI1,AoI2)
% For use in Gaussian_beams.m.
% Defines an interface object, with the beam passing from n0 to n1, with radius of
curvature R [m]. Defaults as normal incidence for both angles; define one or both angles
[degrees] to override.
% Note: This is unnecessary for flat interfaces at normal incidence.

cf.type = 'curved surface';
cf.RoC = R;
cf.n_i = n0;
cf.n_f = n1;

if nargin == 3; AoI1 = 0; AoI2 = 0; end   % angle of incidence
if nargin == 4; AoI2 = 0; end
cf.AoI1_deg = AoI1;
cf.AoI2_deg = AoI2;
AoI1 = AoI1*pi()/180;   % degrees to radians
AoI2 = AoI2*pi()/180;
AoR1 = asin(n0/n1*sin(AoI1));   % angle of refraction
AoR2 = asin(n0/n1*sin(AoI2));

% The following matrix form is from Paraxia.
dn1 = (n1*cos(AoR1)-n0*cos(AoI1))/(cos(AoR1)*cos(AoI1));
dn2 = (n1*cos(AoR2)-n0*cos(AoI2))/(cos(AoR2)*cos(AoI2));

cf.mat = [cos(AoR1)/cos(AoI1),0;dn1/R,cos(AoI1)/cos(AoR1)];
if (AoI1 ~= AoI2)
    cf.mat2 = [cos(AoR2)/cos(AoI2),0;dn2/R,cos(AoI2)/cos(AoR2)];
end
```

free_space.m:

```
function space = free_space(L,n)
% For use in Gaussian_beams.m.
% Defines a free space propagation object of length L [m] and refractive index n.
Defaults to vacuum (n = 1) if no refractive index is passed.

space.type = 'free space';
space.length = L;
if nargin == 1;
    space.refInd = 1;
elseif nargin == 2;
    space.refInd = n;
end
space.mat = [1,L/space.refInd;0,1];
```

mirror.m:

```
function mirror = mirror(R)
% For use in Gaussian_beams.m.
% Defines a mirror object of radius of curvature R [m]. Defaults to a flat mirror when
no arguments are passed.

mirror.type = 'mirror';
if nargin == 1;
    mirror.RoC = R;
else
    mirror.RoC = Inf;
end
mirror.mat = [1,0;-2/mirror.RoC,1];
```

GRIN_lens.m:

```
function quad = GRIN_lens(l,n0,n2,n2_2)
% For use in Gaussian_beams.m.
% Defines a gradient index (GRIN) lens object of length l [m], central
% refractive index n0, and quadratically reducing refractive index with radius with
equation: n(r) = n0 - 0.5*n2*r^2. Define both n2 (primary axis) and n2_2 (secondary
axis) for astigmatic lenses.

quad.type = 'GRIN lens';
quad.length = l;
quad.n0 = n0;
quad.n2 = n2;
if n2 == 0   % for n2 = 0, revert to free space.
    quad.mat = [1,l/n0;0,1];
else
    quad.mat = [cos(l*sqrt(n2/n0)),sin(l*sqrt(n2/n0))/sqrt(n0*n2);...
        -sqrt(n0*n2)*sin(l*sqrt(n2/n0)),cos(l*sqrt(n2/n0))];
end
if nargin == 4;   % if the lens is astigmatic
    quad.n2(2) = n2_2;
    if n2_2 == 0    % for n2_2 = 0, revert to free space.
       quad.mat2 = [1,l/n0;0,1];
    else
       quad.mat2 = [cos(l*sqrt(n2_2/n0)),...
          sin(l*sqrt(n2_2/n0))/sqrt(n0*n2_2);...
          -sqrt(n0*n2_2)*sin(l*sqrt(n2_2/n0)),cos(l*sqrt(n2_2/n0))];
    end
end
```

thick_lens.m:

```
function thick = thick_lens(l,n2,R1,R2)
% For use in Gaussian_beams.m.
% Defines a thick lens object with a thickness of l [m], a refractive
% index of n2, front radius of curvature R1 [m] and a back radius of
% curvature of R2 [m].
% Note: For a convex-convex lens, R1 < 0 and R2 > 0.

thick.type = 'thick lens';
thick.length = l;
n_outer = 1;   % Refractive index outside the lens
thick.n_inner = n2;
thick.R1 = R1;
thick.R2 = R2;

% Defines the thick lens as two curved surfaces with a medium inside
surf1 = curv_surf(n_outer,thick.n_inner,thick.R1);
inside_lens = free_space(l,thick.n_inner);
surf2 = curv_surf(thick.n_inner,n_outer,thick.R2);
thick.mat = surf2.mat*inside_lens.mat*surf1.mat;
```

thin_lens.m:

```
function th_lens = thin_lens(f,f2)
% For use in Gaussian_beams.m.
% Defines a thin lens object of focal length f [m]. Define both f (primary axis) and f2
(secondary axis) for astigmatic lenses.

th_lens.type = 'thin lens';
th_lens.f = f;
th_lens.mat = [1,0;-1/f,1];
if nargin == 2;   % if the lens is astigmatic
    th_lens.f2 = f2;
    th_lens.mat2 = [1,0;-1/f2,1];
end
```

C3: Beam imaging programs; these interpret the output from the CCD camera:

GaussPictures.m:

```
close all
clear all

%% The the files to analyse
filename = 'Test5.bmp';
backname = 'Bkgrnd.bmp';
position = 23;

%% Import the picture and its background file
background = ImportPicture(backname);
picture = ImportPicture(filename);
M = 2*(picture - background);

%% Now try to find out about the pictures (size, centroid, etc...)
D4sigmaFit %M is manipulated in here

dx = sizeX / 2 - round(xCent);
dy = sizeY / 2 - round(yCent);

%% Now create the new centered and cropped image
picture = ImportPicture(filename);
M = 2*(picture - background);

sizeXnew = sizeX - abs(dx);
sizeYnew = sizeY - abs(dy);

if dx >= 0
    if dy >= 0
        Mnew = M((dx+1):end, (dy+1):end);
    else
        Mnew = M((dx+1):end, 1:(sizeY-abs(dy)));
    end
else
    if dy >= 0
        Mnew = M(1:(sizeX-abs(dx)), (dy+1):end);
    else
        Mnew = M(1:(sizeX-abs(dx)), 1:(sizeY-abs(dy)));
    end
end

%% Make the size of the image square for fitting

if sizeXnew > sizeYnew
    dX = ceil((sizeXnew - sizeYnew)/2);

    imageSize = sizeXnew - (2*dX);

    Z = rot90(Mnew(dX:(sizeXnew-dX-1), 1:imageSize));
else
    dY = ceil((sizeYnew - sizeXnew)/2);

    imageSize = sizeYnew - (2*dY);

    Z = rot90(Mnew(1:imageSize, dY:(sizeYnew-dY-1)));
end

%% Fit to the beam to find the width

pixelPitch = 9.1e-6;   %(previously 40 um)

% parameters are: [Amplitude, x0, sigmax, y0, sigmay, angle(in rad)]
x0 = [150, 0, 10, 0, 10, 0.126]; %Inital guess parameters

FitForOrientation = 1; % 0: fit for orientation. 1: do not fit for orientation
plot3DImage = 0;

MainD2GaussFitRot %uses the image store in Z (must be square)

%% Spit out some parameters of the picture

% The position relative to the table markings
posStart = 16;
objPlaneDist = 0; % Unknown at this point
Md = ((posStart - position) * 25) - objPlaneDist;

display(['Position: ', num2str(Md), ' mm'])
display(['X Width: ', num2str(xWidth, '% 100.2f'), ' um'])
display(['Y Width: ', num2str(yWidth, '% 100.2f'), ' um'])
```

ImportPicture.m:

```
function beamImage = ImportPicture(fileToRead1)
%IMPORTFILE(FILETOREAD1) % Import the file
%  Imports data from the specified file
%  FILETOREAD1:  file to read

rawData1 = importdata(fileToRead1);

% For some simple files (such as a CSV or JPEG files), IMPORTDATA might
% return a simple array.  If so, generate a structure so that the output
% matches that from the Import Wizard.
[~,name] = fileparts(fileToRead1);
newData1.(genvarname(name)) = rawData1; %#ok<DEPGENAM>

% Create new variables in the base workspace from those fields.
vars = fieldnames(newData1);

% for i = 1:length(vars)
%     assignin('base', vars{i}, newData1.(vars{i}));
% end

beamImage = double(rot90(newData1.(vars{1})(1:220,:,1)));
```

D4sigmaFit.m:

```
%% Process the image store in M

M = M - background;   % Subtract the background

% Pull the dimensions
sizeX = size(M, 1);
sizeY = size(M, 2);

% Kill the negative numbers
for y = 1:sizeY
    for x = 1:sizeX
        if M(x, y) < 0
            M(x, y) = 0;
        end
    end
end

%% Smooth the data
smooth = 3;
[M, noise] = wiener2(M, [smooth smooth]);
M = wiener2(M, [smooth smooth], noise);

M = M - min(mean(M));

%% Calculate the common sum for the denominators

Msum = sum(sum(M,1),2);

%% Calculate the x and y centroids

tempX = 0;
tempY = 0;

for y = 1:sizeY
    for x = 1:sizeX
        tempX = tempX + M(x, y) * x;
        tempY = tempY + M(x, y) * y;
    end
end

xCent = tempX / Msum;
yCent = tempY / Msum;

%% Calculate the x and y D4sigmas

tempX = 0;
tempY = 0;

for y = 1:sizeY
    for x = 1:sizeX
        tempX = tempX + M(x, y) * (x - xCent)^2;
        tempY = tempY + M(x, y) * (y - yCent)^2;
    end
end

xD4 = 4 * sqrt(tempX / Msum);
yD4 = 4 * sqrt(tempY / Msum);
```

MainD2GaussFitRot.m:

```
%% Fit a 2D Gaussian function to data
%% ---------User Input----------------------
MdataSize = size(Z, 1);  % Size of nxn data matrix
x = [250,0,3,0,2,+0.02*2*pi];  %centroid parameters
noise = 0;  % noise in of centroid peak value (x(1))
InterpolationMethod = 'nearest';  % 'nearest','linear','spline','cubic'

%% ---Generate centroid to be fitted-------------------------------------
xin = x;
noise = noise/100 * x(1);
[X,Y] = meshgrid(-MdataSize/2 + 1:MdataSize/2);
xdata = zeros(size(X,1),size(Y,2),2);
xdata(:,:,1) = X;
xdata(:,:,2) = Y;
[Xhr,Yhr] = meshgrid(linspace(-MdataSize/2,MdataSize/2,300)); % generate high res grid for plot
xdatahr = zeros(300,300,2);
xdatahr(:,:,1) = Xhr;
xdatahr(:,:,2) = Yhr;
%---Generate noisy centroid---------------------
% Z = D2GaussFunctionRot(x,xdata);
% Z = Z + noise*(rand(size(X,1),size(Y,2))-0.5);

%% --- Fit---------------------
if FitForOrientation == 0
    % define lower and upper bounds [Amp,xo,wx,yo,wy,fi]
    lb = [0,-MdataSize/2,0,-MdataSize/2,0,-pi/4];
    ub = [realmax('double'),MdataSize/2,(MdataSize/2)^2,MdataSize/2,(MdataSize/2)^2,pi/4];
    [x,resnorm,residual,exitflag] = lsqcurvefit(@D2GaussFunctionRot,x0,xdata,Z,lb,ub);
else
    x0 =x0(1:5);
    xin(6) = 0;
    lb = [0,-MdataSize/2,0,-MdataSize/2,0];
    ub = [realmax('double'),MdataSize/2,(MdataSize/2)^2,MdataSize/2,(MdataSize/2)^2];
    [x,resnorm,residual,exitflag] = lsqcurvefit(@D2GaussFunction,x0,xdata,Z,lb,ub);
    x(6) = 0;
end

%% ---------Plot 3D Image-------------
if plot3DImage == 1
    figure(1)
    C = del2(Z);
    mesh(X,Y,Z,C)  %plot data
    hold on
    surface(Xhr,Yhr,D2GaussFunctionRot(x,xdatahr),'EdgeColor','none')  %plot fit
    %%%axis([-MdataSize/2-0.5 MdataSize/2+0.5 -MdataSize/2-0.5 MdataSize/2+0.5 -noise noise+x(1)])
    alpha(0.2)
    hold off
end

%% -----Plot profiles----------------
hf2 = figure(2);
set(hf2, 'Position', [20 20 950 900])
alpha(0)
subplot(4,4, [5,6,7,9,10,11,13,14,15])
imagesc(X(1,:),Y(:,1)',Z)
set(gca,'YDir','reverse')
colormap('jet')

xWidth = x(3)*4*pixelPitch*1e6;
yWidth = x(5)*4*pixelPitch*1e6;

string1 = ['       Amplitude','    X-Coordinate', '    X-Width','    Y-Coordinate','    Y-Width','
string2 = ['Set     ',num2str(xin(1), '% 100.3f'),'             ',num2str(xin(2), '% 100.3f'),'
string3 = ['Fit     ',num2str(x(1), '% 100.3f'),'             ',num2str(x(2), '% 100.3f'),'

%%%%% text(-MdataSize/2*0.9,+MdataSize/2*1.15,string1,'Color','red')
%%%%% text(-MdataSize/2*0.9,+MdataSize/2*1.2,string2,'Color','red')
%%%%% text(-MdataSize/2*0.9,+MdataSize/2*1.25,string3,'Color','red')

%% -----Calculate cross sections-------------
% generate points along horizontal axis
m = -tan(x(6));  % Point slope formula
b = (-m*x(2) + x(4));
xvh = -MdataSize/2:MdataSize/2;
yvh = xvh*m + b;
hPoints = interp2(X,Y,Z,xvh,yvh,InterpolationMethod);
% generate points along vertical axis
mrot = -m;
brot = (mrot*x(4) - x(2));
yvv = -MdataSize/2:MdataSize/2;
xvv = yvv*mrot - brot;
vPoints = interp2(X,Y,Z,xvv,yvv,InterpolationMethod);

hold on  % Indicate major and minor axis on plot
```

```
85
86      % plot points
87      % plot(xvh,yvh,'r.')
88      % plot(xvv,yvv,'g.')
89
90      % plot lines
91 -    plot([xvh(1) xvh(size(xvh))],[yvh(1) yvh(size(yvh))],'r')
92 -    plot([xvv(1) xvv(size(xvv))],[yvv(1) yvv(size(yvv))],'g')
93
94 -    hold off
95      %%%axis([-MdataSize/2-0.5 MdataSize/2+0.5 -MdataSize/2-0.5 MdataSize/2+0.5])
96
97 -    ymin = - noise * x(1);
98 -    ymax = x(1)*(1+noise);
99 -    xdatafit = linspace(-MdataSize/2-0.5,MdataSize/2+0.5,300);
100 -   hdatafit = x(1)*exp(-(xdatafit-x(2)).^2/(2*x(3)^2));
101 -   vdatafit = x(1)*exp(-(xdatafit-x(4)).^2/(2*x(5)^2));
102 -   subplot(4,4, [1:3])
103 -   xposh = (xvh-x(2))/cos(x(6))+x(2);  % correct for the longer diagonal if fi~=0
104 -   plot(xposh,hPoints,'r.',xdatafit,hdatafit,'black')
105     %%%axis([-MdataSize/2-0.5 MdataSize/2+0.5 ymin*1.1 ymax*1.1])
106 -   subplot(4,4,[8,12,16])
107 -   xposv = (yvv-x(4))/cos(x(6))+x(4);  % correct for the longer diagonal if fi~=0
108 -   plot(vPoints,xposv,'g.',vdatafit,xdatafit,'black')
109     %%%axis([ymin*1.1 ymax*1.1 -MdataSize/2-0.5 MdataSize/2+0.5])
110 -   set(gca,'YDir','reverse')
111 -   figure(gcf)  % bring current figure to front
112
```

D2GaussFunction.m:

```
1   function F = D2GaussFunction(x,xdata)
2   %% Original function
3 - F = x(1)*exp(-((xdata(:,:,1)-x(2)).^2/(2*x(3)^2) + (xdata(:,:,2)-x(4)).^2/(2*x(5)^2)));
```

D2GaussFunctionRot.m:

```
1   function F = D2GaussFunctionRot(x,xdata)
2   %% x = [Amp, x0, wx, y0, wy, fi]
3   %[X,Y] = meshgrid(x,y)
4   %  xdata(:,:,1) = X
5   %  xdata(:,:,2) = Y
6   % Mrot = [cos(fi) -sin(fi); sin(fi) cos(fi)]
7   %%
8 - xdatarot(:,:,1)= xdata(:,:,1)*cos(x(6)) - xdata(:,:,2)*sin(x(6));
9 - xdatarot(:,:,2)= xdata(:,:,1)*sin(x(6)) + xdata(:,:,2)*cos(x(6));
10 - x0rot = x(2)*cos(x(6)) - x(4)*sin(x(6));
11 - y0rot = x(2)*sin(x(6)) + x(4)*cos(x(6));
12
13 - F = x(1)*exp(-((xdatarot(:,:,1)-x0rot).^2/(2*x(3)^2) + (xdatarot(:,:,2)-y0rot).^2/(2*x(5)^2)));
```

Appendix D: Pump diode data

20W, 1470nm Conduction Cooled Diode Laser Single Bar

DILAS
The diode laser company.

Features

- Very low smile
- Available as non-collimated (MN Series) or fast-axis collimated unit (MY Series)
- Different heatsink geometries available

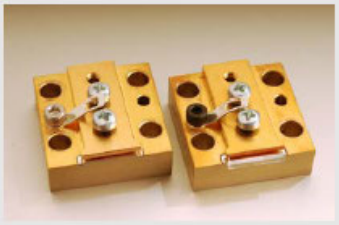

Device Specification

Optical[1]	Units	
Center Wavelength Range[3]	nm	1470
Center Wavelength Tolerance	nm	±20
Output Power	W	20
Number of Emitters	#	19
Emitter Size	µm	100
Fill Factor	%	20
Spectral Width (FWHM)	nm	≤12
Slope Efficiency	W/A	≥0.47
Fast Axis Divergence[6] (90%)	degree	<70
Slow Axis Divergence (90%)	degree	<18
Wavelength Temp. Coefficient[3]	nm/°C	~ 0.35
Electrical Parameters		
Power Conversion Efficiency	%	≥35
Threshold Current (I_{TH})	A	<8
Operating Current (I_{OP})	A	55
Operating Voltage (V_{OP})	V	<1.5
Thermal Parameters[1]		
Operating Temperature Range[3, 4]	°C	+20 to 30
Storage Temperature Range[4]	°C	0 to 55
Recommended Heatsink Capacity Per Bar	W	≥70

[1]Data at 20°C cold plate temperature, unless otherwise stated.
[2]Reduced lifetime if used above nominal operating conditions.
[3]Others available upon request.
[4]A non-condensing environment is required for storage and operation below the ambient dew point.
[6]For fast axis collimation using FAC lens: divergence <8mrad.

DILAS
The diode laser company.

Operating instructions for diode laser elements M1N/M1Y-series

Caution!

Safety of Laser Products: Reference DIN EN ISO 60825-1:2008-05! This diode laser element is registered as a Class 4 laser product. According to these regulations the operator is bound to careful and responsible use of the diode laser equipment.
Laser warning signs are to be attached on the product where this diode laser element is built-in.

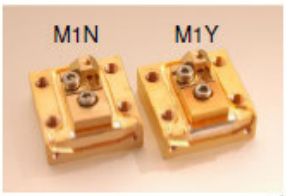

Technical data

Find technical data for your diode laser element in the enclosed measuring data sheet, the power diagram and the overleaf dimensional drawing.

Connectors / components

(refer to overleaf drawings)
1 = Cathode (N-Terminal, - connection), thread M4x5
2 = Anode (P-Terminal, + connection), thread M4x6
3 = Drill hole for customer specific temperature sensor
4 = Collimation lens (only for M1Y-type)

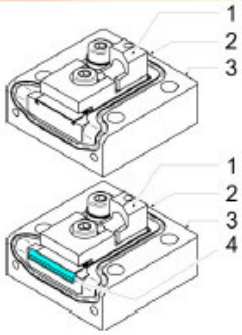

Transportation and handling precautions

Follow ESD rules for handling of electronic parts!
Avoid condensation! Keep away from diode laser element: humidity, dust, waste, oil, and any other waste source! Do not alter modules mechanically!
Ensure shorting clip is properly secured to electrodes for transport and storage. Pack element only into ESD conformal packing (see packing as delivered). Use dust proof, vibration- and impact-protected packaging. Whenever possible use original DILAS packaging for transportation of the elements! After any transportation allow an acclimatization time of at least one hour to avoid any condensation on the diode laser element.

Set-up

This diode laser element is designed for usage within diode laser applications mounted onto corresponding platform for cooling. For mounting the diode laser element onto the platform use 4 screws (M3, M4). Tighten screws crosswise.
Tightening torques: ***45 Ncm*** *for mechanical fixation*

Cooling interface installation

Cooling the diode laser element is performed via the non-potential-free cooling interface plate on bottom side of module, by use of thermo-electric or water-cooled cooling plate provided by customer.
Required cooling capacity is ≥ 100W. Consider surface finish (RZ≤ 4), flatness (<0.01 mm) and dimension of cooling surface!
Minimize thermal contact resistance by using appropriate heat conducting foil (Recommendation: T-GON 805).
Notice: Avoid use of heat conduction paste, because it may lead to destruction of the laser diode element!

Maximum element temperature = 35 °C/95 °F, measured in defined drill hole (refer to overleaf drawings).

DILAS
The diode laser company.

Electrical connection

Consider the necessary cable diameters for Imax (see type plate).
Ensure correct polarity of voltage! Avoid voltage peaks caused by loose connections!
Ensure current stability <+10% (within µs-range).
For power supply connection only use wiring rated for the high power of the diode laser element.

Tightening torques: ***60 Ncm***

Notice: Secure electrical leads by use of appropriate lock washers.

Notice: Risk of short circuit!
Consider electrical isolation against environment.

Dimensional drawings

For M1N:

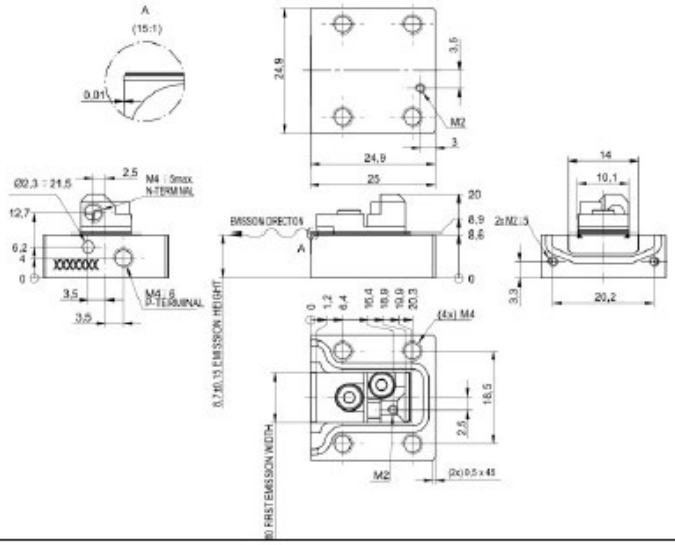

For M1Y:

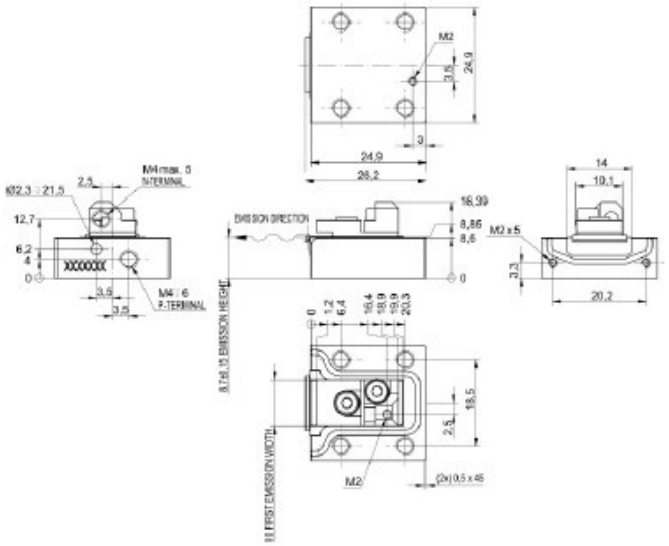

Appendix E: Pockels cell data

QUANTUM TECHNOLOGY, INC.
TEST DATA SHEET
Q-SWITCH

CUSTOMER : Univ.of Adelaide, Badger Labs
MODEL : RT-3-1.64um
SERIAL NO.: Q130-055
W/O NO. : 130-055
DATE : 02/17/2014
CRYSTAL PARAMETERS
MATERIAL : RTP
APERTURE (mm.) : 3 mm
TERMINALS : 4-40 Terms TT ___ 0.080 pin jacks √
HOUSING : WHITE DELRIN
CAPACITANCE pf. : 3 pF
CUSTOMER DRAWING NO. : N/A

OPTICAL QUALITY CONTROL
TRANSMISSION AT 1640nm. : >98% est.
CONTRAST RATIO : >100:1
HALF-WAVE VOLTAGE @ 632.8 nm. (KV.): 0.860 volts
HALF-WAVE VOLTAGE @ 1640nm KV.): 2.280

PHYSICAL PARAMETERS
INDEX MATCHING FLUID: N/A DECALIN OTHER

AR COATING (nm.) : WINDOWS INPUT OUTPUT N/A
: CRYSTAL INPUT OUTPUT 1.64um

COMMENTS: Quarter wave voltage @ 1.64um is ~ 1.114KV

TESTED BY: Sanjay Adhav Date: 02/17/2014

TESTDATA CRYSTALS\1 BLANK SHG & QSW TDS FORMS\Q130-055 Univ of Adelaide-Badger.doc

DATA SHEET STARFIRE-5XX-24 PULSER MODULE

Date: 02/14/2014 Work order: 130-055

Ser. No.: 130-055 Customer: BADGER LABS., UNIV. OF ADELAIDE

Model no: STARFIRE-2DMA-CD
___(STARFIRE-9DM -HRM, -VRB, -HSM, -RAM, -SRM, -SHM, -F-)
___(STARFIRE-5 -HRM, -VRB, -HSM, -RAM, -SRM, -SHM, -F-)

PARAGRAPH	TEST	RESULT
1.	LEADING EDGE RISE TIME	9 NSEC
2.	TRAILING EDGE FALL TIME	1 NSEC
3a.	Min/Max PULSE WIDTH TYPICAL	100 / .30 nsec/msec
4.	MAX Vpp OUT	2.5 KV
5.	MAX PULSE RATE CONTINUOUS	3.0 KHZ
6.	FORCED AIR COOLED (-F-)	N/A OK
7.	REAR MOUNT CONNECTORS (SHV, -SHM, -SRM)	SHV OK
8.	OUTPUT CABLE SHV-PT-RG62-LC-2'	√ OK

Power Section:

Volts input: PS 24V @ 2 Amps
Bias Volts: input No Load V 315 Full Load REG V 314
RAW No Load REG V N/A
Internal HV Current Trip @ -0.6 Volts for 0.6 mA
Remote HV adj. √ 0-2.5kV √ 0-10VDC
HV monitor 1V per 1kV cal. √ ok
HV limit 2.5 kV HV trip 2.5 kV

NOTES: Shipped with RT-3-1645nm Q-Switch. CAUTION: PLEASE KEEP DUTY CYCLE OF HV PULSE WIDTH-REP RATE TO < 1% (0.5% TYPICAL) FOR LONG LIFE TIME OF RTP POCKELS CELL.

SIGNATURE: J. FERGUSON

Appendix F: YAG Sellmeier equation

The refractive index of YAG is higher than many laser hosts. The Sellmeier equation of YAG takes the form:

$$n^2 = 1 + \frac{C\lambda^2}{\lambda^2 - \lambda_0^2} \tag{F1}$$

where $C = 2.2779$ and $\lambda_0 = 107$ nm, corresponding to the UV opacity of YAG [112]. The refractive index curve is plotted below in Figure F1:

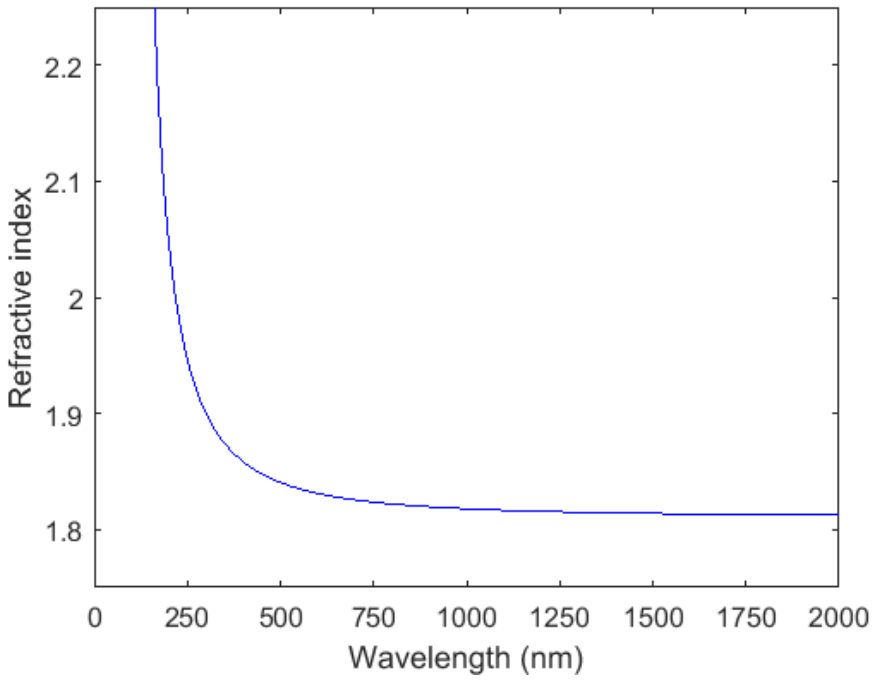

FIGURE F1: The refractive index of YAG as a function of wavelength.

References:

[1] R. P. Farnsworth and R. W. Wyeth, *"Digital range measuring system"*, United States Patent #3,666,367 (1970)

[2] D. W. Coffey and V. J. Norris, *"YAG:Nd^{+3} Laser Target Designators and Range Finders"*, Applied Optics, vol. 11, no. 5, pp. 1013-1018 (1972)

[3] T. Wilkerson, G. Schwemmer, K. Ritter, U. Singh and R. Mahon, *"Applications of Laser and Lidar Spectroscopy to Meteorological Remote Sensing"*, Laser Spectroscopy VIII, vol. 55 (1987)

[4] G. Goyer and R. Watson, *"The Laser and its Application to Meteorology"*, Bulletin of the American Meteorological Society, vol. 44, no. 9, pp. 564-575 (1963)

[5] D. D. Arslanov, M. Spunei, J. Mandon, S. M. Cristescu, S. Persijn and F. Harren, *"Continuous-wave optical parametric oscillator based infrared spectroscopy for sensitive molecular gas sensing"*, Laser & Photonics Reviews, vol. 7, no. 2, pp. 188-206 (2012)

[6] C. Bellecci, M. Francucci, P. Gaudio, M. Gelfusa, S. Martellucci, M. Richetta and T. Lo Feudo, *"Application of a CO_2 dial system for infrared detection of forest fire and reduction of false alarm"*, Applied Physics B, vol. 87, no. 2, pp. 373-378 (2007)

[7] N. Menyuk, D. K. Killinger and W. E. DeFoe, *"Remote sensing of NO using a differential absorption lidar"*, Applied Optics, vol. 19, no. 19, pp. 3282-3286 (1980)

[8] According to measurements performed by Joshua Pease, using 100 ns pulses to measure a 300 m distance with an uncertainty of ±1.3 m.

[9] R. D. Peterson and K. L. Schepler, *"Timing modulation of a 40-MHz laser-pulse train for target ranging and identification"*, Applied Optics, vol. 42, no. 36, pp. 7191-7196 (2003)

[10] T. G. Bergman, *"Design for a Laser Rangefinder"*, U.S. Naval Ordnance Test Station, Instrument Development Division (1964)

[11] W. J. Smith, *Modern Optical Engineering* (4th edition), McGraw-Hill, (2008)

[12] D. H. Sliney, *Selected Papers on Laser Safety*, SPIE Milestone Series, vol. MS-117, Bellingham, Washington (1995)

[13] MPE vs. wavelength & pulse duration: https://en.wikipedia.org/wiki/Laser_safety

[14] J. Daly, *"The Nd:YAG Laser Rangefinder/Designator"*, Scientific and Engineering Applications of Commercial Laser Devices, pp. 68-71 (1986)

[15] L. R. Marshall, J. Kasinski and R. Burnham, *"Diode-pumped eye-safe laser source exceeding 1% efficiency"*, Optics Letters, vol. 16, no. 21, pp. 1680-1682 (1991)

[16] OPO: http://www.ru.nl/tracegasfacility/research/laser-sources/optical-parametric/

[17] Z. Chu, U. Singh and T. Wilkerson, *"A self-seeded SRS system for the generation of 1.54 μm eye-safe radiation"*, Optics Communications, vol. 75, no. 2, pp. 173-178 (1990)

[18] Z. Chu, U. Singh and T. Wilkerson, *"Multiple Stokes wavelength generation in H_2, D_2 and CH_4 for lidar aerosol measurements"*, Applied Optics, vol. 30, no. 30, pp. 4350-4357 (1991)

[19] A. Sabella, J. A. Piper and R. P. Mildren, *"Efficient conversion of a 1.064 μm Nd:YAG laser to the eye-safe region using a diamond Raman laser"*, Optics Express, vol. 19, no. 23, pp. 23554–23560 (2011)

[20] A. McKay, O. Kitzler and R. P. Mildren, *"Simultaneous brightness enhancement and wavelength conversion to the eye-safe region in a high-power diamond Raman laser"*, Laser & Photonics Review, vol. 8, no. 3, pp. L37-L41 (2014)

[21] N. P. Barnes, B. M. Walsh, F. Amzajerdian, D. J. Reichle, G. E. Busch and W. A. Carrion, *"Up conversion measurements in Er:YAG; comparison with 1.6 μm laser performance"*, Optical Materials Express, vol. 1, no. 4, pp. 678-685 (2011)

[22] J. W. Kim, J. I. Mackenzie and W. A. Clarkson, *"Influence of energy-transfer-upconversion on threshold pump power in quasi-three-level solid-state lasers"*, Optics Express, vol. 17, no. 14, pp. 11935-11943 (2009)

[23] A. E. Siegman, *Lasers*, University Science Books (1986)

[24] B. J. Dinerman and P. F. Moulton, *"CW Laser Operation from Er:YAG, Er:GGG and Er:YSGG"*, OSA/ASSL, pp. 152-155 (1992)

[25] S. Nikolov and L. Wetenkamp, *"Lasing characteristics of a 1.644 μm Er^{3+}:YAG monolith pumped at 647 nm, 787 nm and 964 nm"*, Laser in Engineering (1994)

[26] T. Schweizer, T. Jensen, E. Heumann and G. Huber, *"Spectroscopic properties and diode pumped 1.6 μm laser performance in Yb-codoped Er:$Y_3Al_5O_{12}$ and Er:Y_2SiO_5"*, Optics Communications, vol. 118, pp. 557-561 (1995)

[27] J. Kim, D. Shen, J. Sahu and W. Clarkson, *"Fiber-Laser-Pumped Er:YAG Lasers"*, IEEE Journal of Quantum Electronics, vol. 15, no. 2, pp. 361-371 (2009)

[28] W. Koechner, *Solid-State Laser Engineering* (6th edition), Springer (2006)

[29] Z. Mierczyk, K. Kopczynski, M. Kwasny, T. Lukasiewicz, Z. Frukacz and Z. Galazka, *"Investigations of YAG:Er^{3+},Yb^{3+} and YAG:Co^{2+} crystals for laser applications"*, International Conference on Solid State Crystals (2000)

[30] S. D. Setzler, M. P. Francis, Y. E. Young, J. R. Konves and E. P. Chicklis, *"Resonantly Pumped Eyesafe Erbium Lasers"*, IEEE Journal of Selected Topics in Quantum Electronics, vol. 11, no.3, pp. 645-657 (2005)

[31] L. D. da Vila, L. Gomes, L. V. G. Tarelho, S. J. L. Ribeiro and Y. Messadeq, *"Mechanism of the Yb–Er energy transfer in fluorozirconate glass"*, Journal of Applied Physics, vol. 93, no. 7, pp. 3873-3880 (2003)

[32] E. Snitzer and R. Woodcock, *"Yb^{3+}–Er^{3+} GLASS LASER"*, Applied Physics Letters, vol. 6, no. 3, pp. 45-46 (1965)

[33] R. J. Mears, L. Reekie, I. M. Jauncey and D. N. Payne, *"Low-noise erbium-doped fibre amplifier operating at 1.54 μm"*, Electronics Letters, vol. 23, no. 19, pp. 1026-1028 (1987)

[34] M. Heintze, F. Jeanneret, J. Munch, D. Ottaway and P. Veitch, *"Development of an Er:Yb:Glass Coherent Laser Radar"*, AIP 18th National Congress (2008)

[35] Z. Meng, J. Kamebayashi, M. Higashihata, Y. Nakata, T. Okada, Y. Kubota, N. Nishimura and T. Teshima, *"1.55-μm Ce-Er-ZBLAN Fiber Laser Operation Under 980-nm Pumping: Experiment and Simulation"*, IEEE Photonics Technology Letters, vol. 14, no. 5, pp. 609-611 (2002)

[36] X. Peng, F. Song, S. Jiang, N. Peyghambarian, M. Kuwata-Gonokami and L. Xu, *"Fiber-taper-coupled L-band Er^{3+}-doped tellurite glass microsphere laser"*, Applied Physics Letters, vol. 82, no. 10, pp. 1497-1499 (2003)

[37] M. C. Heintze, *"Development and Testing of an Er:Yb:Glass Coherent Laser Radar for Wind Field Mapping"*, The University of Adelaide, School of Chemistry and Physics (2010)

[38] Brochure, *"Laser Materials Er:YAG"*, Scientific Materials Corporation (2010)

[39] Brochure, *"Laser Damage Thresholds of Optical Coatings (UV to near-IR)"*, CVI Technical Optics

[40] J. E. Geusic, H. M. Marcos and L. G. Van Uitert, *"Laser oscillations in Nd-doped yttrium aluminum, yttrium gallium and yttrium gadolinium garnets"*, Applied Physics Letters, vol. 4, no. 10, pp. 182-184 (1964)

[41] L. F. Johnson, J. E. Geusic and L. G. Van Uitert, *"Coherent Oscillations from Tm^{3+}, Ho^{3+}, Yb^{3+} and Er^{3+} ions in Yttrium Aluminum Garnet"*, Applied Physics Letters, vol. 7, no. 5, pp. 127-129 (1965)

[42] K. White and S. Schleusener, *"Coincidence of Er:YAG laser emission with methane absorption at 1645.1 nm"*, Applied Physics Letters, vol. 21, no. 9, pp. 419-420 (1972)

[43] E. Zharikov, V. Zhekov, L. Kulevskii, T. Murina, V. Osiko, A. Prokhorov, A. Savel'ev, V. Smirnov, B. Starikov and M. Timoshechkin, *"Stimulated emission*

from Er^{3+} ions in yttrium aluminum garnet crystals at λ = 2.94 μm", Soviet Journal of Quantum Electronics, vol. 4, no. 8, pp. 1039-1040 (1975)

[44] E. Georgiou, F. Kiriakidi, O. Musset and J-P. Boquillon, *"1.65-μm Er:Yb:YAG diode-pumped laser delivering 80-mJ pulse energy"*, Optical Engineering, vol. 44, no. 6, pp. 064202,1-10 (2005)

[45] N. Barnes, R. Allen, L. Esterowitz, E. Chicklis, M. Knights and H. Jenssen, *"Operation of an Er:YLF Laser at 1.73 μm"*, IEEE Journal of Quantum Electronics, vol. 22, no. 2, pp. 337-343 (1986)

[46] H. Stange, K. Petermann, G. Huber and E. Duczynski, *"Continuous Wave 1.6 μm Laser Action in Er Doped Garnets at Room Temperature"*, Applied Physics B, vol. 49, no. 3, pp. 269-273 (1989)

[47] V. V. Osiko, V. B. Sigachev, V. I. Strelov and M. I. Timoshechkin, *"Erbium gadolinium gallium garnet crystal laser"*, Soviet Journal of Quantum Electronics, vol. 21, no. 2, pp. 159-160 (1991)

[48] Q-switching representation: https://www.rp-photonics.com/q_switching.html

[49] W. Koechner, *Solid-State Laser Engineering* (6^{th} edition), Springer (2006)

[50] Website: https://www.rp-photonics.com/saturable_absorbers.html

[51] A. Aubourg, J. Didierjean, N. Aubry, F. Balembois and P. Georges, *"Passively Q-switched diode-pumped Er:YAG solid-state laser"*, Optics Letters, vol. 38, no. 6, pp. 938-940 (2013)

[52] D. Y. Shen, J. K. Sahu and W. A. Clarkson, *"Electro-optically Q-switched Er:YAG Laser In-band Pumped by an Er,Yb Fiber Laser"*, OSA/ASSP (2006)

[53] R. D. Stultz, V. Leyva and K. Spariosu, *"Short pulse, high-repetition rate, passively Q-switched Er: yttrium-aluminum-garnet laser at 1.6 microns"*, Applied Physics Letters, vol. 87, no. 24, pp. 241118,1-2 (2005)

[54] I. Kudryashov and A. Katsnelson, *"1645 nm Q-switched Er:YAG laser with in-band diode pumping"*, Laser Technology for Defense and Security VI, SPIE, vol. 7686 International Society for Optics and Photonics (2010)

[55] S. D. Setzler, M. P. Francis, Y. E. Young, J. R. Konves and E. P. Chicklis, *"Resonantly Pumped Eyesafe Erbium Lasers"*, IEEE Journal of Selected Topics in Quantum Electronics, vol. 11, no.3, pp. 645-657 (2005)

[56] J. W. Kim, J. K. Sahu and W. A. Clarkson, *"High-energy Q-switched operation of a fiber-laser-pumped Er:YAG laser"*, Applied Physics B, vol. 105, no. 2, pp. 263-267 (2011)

[57] I. Kudryashov and D. Garbuzov, *"Volume Bragg Grating improves characteristics of resonantly diode pumped Er:YAG 1.65-μm DPSSL"*, SPIE, vol. 6451 (2007)

[58] M. Wang, J. Meng, X. Hou and W. Chen, *"In-band pumped polarized, narrow-linewidth Er:YAG laser at 1645 nm"*, Applied Optics, vol. 53, no. 30, pp. 7153-7156 (2014)

[59] M. Wang, L. Zhu, W. Chen and D. Fan, *"High-energy directly diode-pumped Q-switched 1617 nm Er:YAG laser at room temperature"*, Optics Letters, vol. 37, no. 17, pp. 3732-3734 (2012)

[60] W. Koechner, *Solid-State Laser Engineering* (6th edition), Springer (2006)

[61] N. W. Chang, D. J. Hosken, J. Munch, D. Ottaway and P. Veitch, *"Stable, Single Frequency Er:YAG Lasers at 1.6 μm"*, IEEE Journal of Quantum Electronics, vol. 46, no. 7, pp. 1039-1042 (2010)

[62] N. W. Chang, N. Simakov, D. J. Hosken, J. Munch, D. Ottaway and P. Veitch, *"Resonantly diode-pumped, continuous-wave and Q-switched Er:YAG laser at 1645 nm"*, Optics Express, vol. 18, no. 12, pp. 13673-13678 (2010)

[63] L. McDonagh, R. Wallenstein and R. Knappe, *"47 W, 6 ns constant pulse duration, high-repetition-rate cavity-dumped Q-switched TEM_{00} Nd:YVO_4 oscillator"*, Optics Letters, vol. 31, no. 22, pp. 3303-3305 (2006)

[64] A. A. Vuylsteke, *"Theory of Laser Regeneration Switching"*, Journal of Applied Physics, vol. 34, no. 6, pp. 1615-1622 (1963)

[65] J. C. van den Heuvel and F. J. M. van Putten, *"Short-Pulse, Eye-Safe Nd:YAG Laser Using Cavity-Dumping"*, Journal of Quantum Electronics, vol. 34, no. 5, pp. 920-925 (1998)

[66] H. Hitotsuya, N. Shimojo, S. Matsubara, M. Inoue and S. Kawato, *"High Efficiency Laser-Diode-Pumped Cavity-Dumped Ytterbium-Doped $Y_3Al_5O_{12}$ Laser"*, MNK Publication, vol. 2, no. 1, pp. 450-453 (2013)

[67] Y. F. Ma, J. W. Zhang, H. Li and X. Yu, *"High stable electro-optical cavity-dumped Nd:YAG laser"*, Laser Physics Letters, vol. 9, no. 8, pp. 561-563 (2012)

[68] G. Cai, Y. Ju, B. Yao, W. Liu, X. Duan and T. Dai, *"Acousto-optically cavity dumped Tm:YAG laser with 54 ns pulses at 200 kHz repetition rate"*, Optics Express, vol. 22, no. 8, pp. 9942-9947 (2014)

[69] R. Stoneman, R. Hartman, E. Schneider, A. Malm, S. Vetorino, C. Garvin, J. Pelk, S. Hannon and S. Henderson, *"Eyesafe 1.6-μm Er: YAG transmitters for coherent laser radar"*, 14th Coherent Laser Radar Conference (2007)

[70] S. D. Setzler, M. P. Francis, Y. E. Young, J. R. Konves and E. P. Chicklis, *"Resonantly Pumped Eyesafe Erbium Lasers"*, IEEE Journal of Selected Topics in Quantum Electronics, vol. 11, no.3, pp. 645-657 (2005)

[71] A. McQuarrie, *Statistical Mechanics*, University Science Books, California (2000)

[72] A. Sennaroglu (editor), *Solid-State Lasers and Applications*, CRC Press (2006)

[73] S. A. Pollack, D. B. Chang and N. L. Moise, *"Upconversion-pumped infrared erbium laser"*, Journal of Applied Physics, vol. 60, no. 12, pp. 4077-4086 (1986)

[74] O. Toma and S. Georgescu, *"Pump wavelengths for an up-conversion pumped Er:YAG green-emitting laser"*, Romanian Journal of Physics, vol. 51, no. 5-6, pp. 649-661 (2005)

[75] N. P. Barnes, B. M. Walsh, F. Amzajerdian, D. J. Reichle, G. E. Busch and W. A. Carrion, *"Measurement of Up Conversion in Er:YAG and Influence on Laser Performance"*, Journal of Quantum Electronics, vol. 49, no. 2, pp. 238-246 (2013)

[76] J. W. Kim, J. Sahu and W. A. Clarkson, *"Impact of energy-transfer-upconversion on the performance of hybrid Er:YAG lasers"*, SPIE 6871, Photonics West, pp. 1-8, https://eprints.soton.ac.uk/50691/ (2008)

[77] M. O. Iskandarov, A. Nikitichev and A. Stepanov, *"Quasi-two-level $Er^{3+}:Y_3Al_5O_{12}$ laser for the 1.6 μm range"*, Journal of Optical Technology, vol. 68, no. 12, pp. 885-888 (2001)

[78] J. Kim, D. Shen, J. Sahu and W. Clarkson, *"Fiber-Laser-Pumped Er:YAG Lasers"*, IEEE Journal of Quantum Electronics, vol. 15, no. 2, pp. 361-371 (2009)

[79] J. W. Kim, I. O. Musgrave, M. J. Yarrow and W. A. Clarkson, *"Simple technique for measuring the energy-transfer-upconversion parameter in solid-state laser materials"*, Optoelectronics Research Centre, University of Southampton (2007)

[80] J. Kim, D. Shen, J. Sahu and W. Clarkson, *"Fiber-Laser-Pumped Er:YAG Lasers"*, IEEE Journal of Quantum Electronics, vol. 15, no. 2, pp. 361-371 (2009)

[81] F. C. Maciuc, C. I. Stere and A-R. P. Sterian, *"Rate equations for an erbium laser system: a numerical approach"*, SPIE proceedings vol. 4430, ROMOPTO 2000, Sixth Conference on Optics (2001)

[82] J. W. Kim, J. I. Mackenzie and W. A. Clarkson, *"Influence of energy-transfer-upconversion on threshold pump power in quasi-three-level solid-state lasers"*, Optics Express, vol. 17, no. 14, pp. 11935-11943 (2009)

[83] N. W. Chang, *"Eye-Safe Er:YAG Lasers for Coherent Remote Sensing"*, The University of Adelaide, School of Chemistry and Physics (2012)

[84] J. Richards and A. McInnes, *"Versatile, efficient, diode-pumped miniature slab laser"*, Optics Letters, vol. 20, no. 4, pp. 371-373 (1995)

[85] D. J. Hosken, *"Deployable Stable Lasers for Gravitational Wave Interferometers"*, The University of Adelaide, School of Chemistry and Physics (2008)

[86] W. Koechner, *Solid-State Laser Engineering* (6th edition), Springer (2006)

[87] R. Beach and W. Benett, *"Lensing duct"*, United States Patent #5,307,430 (1994)

[88] N. Coluccelli, *"Non-sequential modelling of laser diode stacks using Zemax: simulation, optimization and experimental validation"*, Applied Optics, vol. 49, no. 22, pp. 4237-4245 (2010)

[89] Laser diode "smile": https://www.rp-photonics.com/diode_bars.html

[90] H. Kogelnik and T. Li, *"Laser Beams and Resonators"*, Applied Optics, vol. 5, no. 10, pp. 1550-1567 (1966)

[91] D. J. Hosken, *"Deployable Stable Lasers for Gravitational Wave Interferometers"*, The University of Adelaide, School of Chemistry and Physics (2008)

[92] E. Hecht, *Optics* (4th edition), Addison Wesley (2002)

[93] A. E. Siegman, *Lasers*, University Science Books (1986)

[94] W. Koechner, *Solid-State Laser Engineering* (6th edition), Springer (2006)

[95] H. Albrecht, P. Villeval and C. Bonnin, *"Study of RTP crystal used as Electro-Optic Modulator"*, OSA/ASSP, pp. 3-5 (2006)

[96] RTP properties: http://raicol.com/products/rtp-products

[97] Brochure, *"RTP Crystal Based EO Devices"*, Raicol Crystals

[98] A. E. Siegman, *Lasers*, University Science Books (1986)

[99] A. Sennaroglu (editor), *Solid-State Lasers and Applications*, CRC Press (2006)

[100] R. M. Wood, *"Laser induced damage thresholds and laser safety levels. Do the units of measurement matter?"*, Optics and Laser Technology, vol. 29, no. 8, pp. 517-522 (1998)

[101] B. T. Do and A. V. Smith, *"Bulk optical damage thresholds for doped and undoped, crystalline and ceramic yttrium aluminum garnet"*, Applied Optics, vol. 48, no.18, pp. 3509-3514 (2009)

[102] J-F. Bisson, Y. Feng, A. Shirakawa, H. Yoneda, J. Lu, H. Yagi, T. Yanagitani and K-I. Ueda, *"Laser Damage Threshold of Ceramic YAG"*, Japanese Journal of Applied Physics, vol. 42, part 2, no. 8B, pp. L1025-L1027 (2003)

[103] N. Bloembergen, *"Role of Cracks, Pores and Absorbing Inclusions on Laser Induced Damage Threshold at Surfaces of Transparent Dielectrics"*, Applied Optics, vol. 12, no. 4, pp. 661-664 (1973)

[104] Website: https://www.semrock.com/ldt-calculator.aspx

[105] C. W. Carr, H. B. Radousky and S. G. Demos, *"Wavelength Dependence of Laser-Induced Damage: Determining the Damage Initiation Mechanisms"*, Physical Review Letters, vol. 91, no. 12, pp. 127402, 1-4 (2003)

[106] Website: https://www.thorlabs.com/tutorials.cfm

[107] A. E. Siegman, *Lasers*, University Science Books (1986)

[108] J. J. Carvajal, P. Segonds, A. Pena, J. Zaccaro, B. Boulanger, F. Diaz and M. Aguilo, *"Structural and optical properties of $RbTiOPO_4$:Nb crystals"*, Journal of Physics: Condensed Matter, vol. 19, 116214, pp. 1-15 (2007)

[109] J. J. Degnan, *"Theory of the Optimally Coupled Q-Switched Laser"*, IEEE Journal of Quantum Electronics, vol. 25, no. 2, pp. 214-220 (1989)

[110] S. Matsubara, T. Ueda, M. Inoue, M. Tanaka, K. Otani, S. Kawato and T. Kobayashi, *"High efficiency cavity dumped Yb:YAG laser at room temperature"*, Conference on Lasers and Electro-optics (2005)

[111] T. P. Rutten, P. J. Veitch and J. Munch, *"Efficient Pulse Stretching of Q-switched Lasers"*, IEEE Journal of Quantum Electronics, vol. 44, no. 10, pp. 911-915 (2008)

[112] E. Filer, C. Morrison, G. Turner and N. Barnes, *"Theoretical Branching Ratios for the $^5I_7 - {}^5I_7$ Levels of Ho^{3+} in the Garnets $A_3B_2C_3O_{12}$ (A = Y, La, Lu, Gd; B = Al, Lu, Sc, Ga; C = Al, Ga)"*, Advanced Solid State Lasers, vol. 6, pp. 354-362, Optical Society of America (1990)